Photonic Nanostructures for Light Management and Sensing

Zur Erlangung des akademischen Grades eines

DOKTORS DER INGENIEURWISSENSCHAFTEN (Dr.-Ing)

von der KIT-Fakultät für
Elektrotechnik und Informationstechnik
des Karlsruher Instituts für Technologie (KIT)

genehmigte

DISSERTATION

von

M.Sc. Qihao Jin

geb. in Shaoxing, V.R. China

Tag der mündlichen Prüfung:	21.02.2024
Hauptreferent:	Prof. Dr. rer. nat. Uli Lemmer
Korreferent:	Prof. Dr. rer. nat. Wilhelm Stork

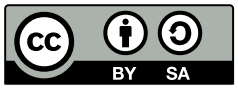

Abstract

Photonic structure for optical applications is an interdisciplinary research frontier encountering new opportunities with the development of modern science and technologies. It includes control and manipulation of light properties in order to fulfill specific requirements and functions. Boosted by nanoresearch and nanofabrication, different fields actively engage with each other, making studying photonic nanostructures a hot research spot and a holistic subject. The applications can be found in light management, optical imaging and sensing, biomedical diagnoses, optical and quantum communications, material analysis, energy harvesting, etc. In this work, inspired by real-life challenges, different photonic nanostructures are fabricated using developed fabrication processes. Furthermore, the precise control of the light responses of the fabricated optical components is realized. The physical fundamentals of the work comprise optical interference and scattering. Three application fields have been investigated and demonstrated: optical filters, smart windows, and Raman sensors.

The first part of the work focuses on inkjet-printed optical interference filters. The motivation is to fully inkjet print optical interference filters and precisely control their optical properties. The physical fundamental of the work is optical interference. In this part, an inkjet printing process has been developed. In contrast to the conventional fabrication approaches of producing optical interference filters, this work has managed to print filters in ambient conditions directly. It is done through layer-by-layer deposition. The long-lasting bottleneck of reproducibility and reliability in fabricating multilayer optical filters by solution processing is tackled. A filter with 39 single layers has been demonstrated to have adequate optical performance for practical applications. Longpass, shortpass, bandpass, and dichroic filters are fabricated with the developed printing process and ink formulations. This is the first time a high-end optical interference filter has been realized using inkjet printing. In addition, upscaling of printed optical filters is demonstrated with a DIN A4 size (210 x 297 mm^2). Furthermore, the lateral patterning of optical filters is also realized, showing a good technical advantage of inkjet printing in maskless patterning in contrast to the conventional approaches. Using inkjet printing technology, the design and fabrication of the filters benefit from rapid prototyping, a high degree of freedom, high affordability, etc.

The second part of the work concentrates on dynamic light scattering manipulation in a smart window. The motivation is to introduce the pixel character into the smart window using locally generated optical scattering. The physical fundamental of this work is elastic light scattering. Using inkjet printing, surface etching masks are printed directly on polydimethylsiloxane slices. After plasma treatment, nano- and microstructures are introduced on the surface as scattering centers. Thanks to the capability of flexible lateral patterning of inkjet printing, the photonic structures can be generated in a manner that is

uniquely tailored from one site to another. This allows for the control of light scattering locally and at various levels, realizing the pixelation of the light scattering. The fabricated smart window is mechanoresponsive. This means that the entire optical response of the smart window can be tuned by the applied stress. Combining these two properties, i.e., global tunability of the optical response and the pixelized light scattering, the developed smart window is suitable for the high dynamic range signage application. The work also developed a method of depositing an ultra-thin buffer layer for surface property adjustment, which can be applied universally to the inkjet printing process.

The third part of the work focuses on surface-enhanced Raman scattering (SERS) for chemical sensing. The motivation for this work is to tailor the localized surface plasmon responses (LSPR) in a 3D photonic nanostructure. It aims to match the LSPR peaks with the excitation laser wavelength to achieve an ultrahigh sensitivity for analyte detection. The physical fundamental of this work is Raman scattering, a type of inelastic light scattering. By controlling the growth of gold nanoparticles in a 3D nanoporous silicon network, the LSPR peaks are precisely manipulated. This allows the LSPR peak to match the excitation laser wavelength to reach a significantly amplified localized electrical field and LSPR. The amplified LSPR further enhances the Raman scattering of the targeting molecule, i.e., methylene blue. Through this, an ultra-high enhancement factor is obtained in the order of 10^9. It demonstrates the ultra-high sensitivity of the SERS sensor, which is capable of detecting a single-molecule concentration.

The core of the work in this dissertation is light management and sensing enabled by photonic nanostructures. Different fabricating processes are developed to achieve the goal. Additionally, the details of design and fabrication are described. The obtained results are discussed comprehensively.

Kurzfassung

Photonische Strukturen für optische Anwendungen sind ein interdisziplinäres Forschungsgebiet, das mit der Entwicklung von moderner Wissenschaft und Technologie neue Möglichkeiten eröffnet. Es umfasst die Kontrolle und Manipulation von Lichteigenschaften, um spezifische Anforderungen und Funktionen zu erfüllen. Durch die Nanoforschung und Nanofabrikation werden verschiedene Bereiche aktiv miteinander verknüpft, was die Untersuchung photonischer Nanostrukturen zu einem wichtigen Forschungsbereich und einem ganzheitlichen Thema macht. Anwendungen finden sich in beispielsweise den Bereichen Lichtmanagement, optische Bildgebung und Sensorik, biomedizinische Diagnosen, optische und Quantenkommunikation, Materialanalyse, und Energiegewinnung. In dieser Arbeit werden, inspiriert durch die Bewältigung realer Herausforderungen, verschiedene photonische Nanostrukturen mithilfe neu entwickelter Herstellungsverfahren hergestellt. Darüber hinaus wird die präzise Kontrolle der Lichtreaktionen in den hergestellten optischen Komponenten realisiert. Die physikalischen Grundlagen der Arbeit umfassen optische Interferenz und Streuung. Es wurden drei Anwendungsbereiche untersucht und demonstriert: optische Filter, Smart windows und Raman-Sensoren.

Der erste Teil der Arbeit beschäftigt sich mit optischen Interferenzfiltern, die mittels Tintenstrahldruck hergestellt werden. Die Motivation besteht darin, diese Filter vollständig im Tintenstrahldruckverfahren zu produzieren und dabei ihre optischen Eigenschaften präzise zu kontrollieren. Die physikalische Grundlage dieser Arbeit bildet die optische Interferenz. Im Verlauf der Studie wurde ein Tintenstrahldruckverfahren entwickelt, das im Gegensatz zu herkömmlichen Methoden zur Herstellung optischer Interferenzfilter ermöglicht, diese direkt unter Umgebungsbedingungen zu drucken. Dies erfolgt durch eine schichtweise Deposition der Lagen. Der langjährige Engpass in Bezug auf Reproduzierbarkeit und Zuverlässigkeit bei der Produktion flüssigprozessierbarer mehrschichtiger optischer Filter wird in dieser Arbeit angegangen. Die Ergebnisse zeigen, dass ein Filter mit 39 Einzelschichten eine für praktische Anwendungen ausreichende optische Leistung erzielt. Mit dem entwickelten Druckverfahren und den Tintenformulierungen werden Langpass-, Kurzpass-, Bandpass- und dichroitische Filter hergestellt. Zum ersten Mal wurde ein hochwertiger optischer Interferenzfilter erfolgreich mittels Tintenstrahldruck hergestellt. Darüber hinaus wird die Hochskalierung von gedruckten optischen Filtern bis zur Größe DIN A4 (210 x 297 mm^2) demonstriert. Eine zusätzliche Innovation besteht in der lateralen Strukturierung von optischen Filtern, was einen deutlichen technischen Vorteil des Tintenstrahldrucks gegenüber konventionellen Methoden ohne Einsatz von Masken zeigt. Die Anwendung der Tintenstrahldrucktechnologie ermöglicht schnelles Prototyping, einen hohen Grad an Freiheit, und geringe Kosten bei Design und Herstellung der Filter.

Der zweite Teil der Arbeit beschäftigt sich mit der dynamischen Beeinflussung der Lichtstreuung in einem Smart window. Die Motivation besteht darin, den Pixelcharakter

in das Smart window durch lokal erzeugte optische Streuung zu induzieren. Die physikalische Grundlage für diese Arbeit ist die elastische Lichtstreuung. Mithilfe des Tintenstrahldrucks werden Oberflächenätzmasken direkt auf Polydimethylsiloxan-Scheiben gedruckt. Nach einer Plasmabehandlung entstehen auf der Oberfläche Nano- und Mikrostrukturen als Streuzentren. Dank der flexiblen lateralen Strukturierungsfähigkeit des Tintenstrahldrucks können die photonischen Strukturen auf einzigartige Weise ortsaufgelöst erzeugt werden. Auf diese Weise lässt sich die Lichtstreuung lokal und auf verschiedenen Ebenen steuern, was zu einer Pixelung der Lichtstreuung führt. Das hergestellte Smart window ist mechanoresponsiv. Das bedeutet, dass die gesamte optische Reaktion des Smart window durch eine angelegte mechanische Spannung eingestellt werden kann. Durch die Kombination dieser beiden Eigenschaften – der globalen Abstimmbarkeit der optischen Antwort und der pixelisierten Lichtstreuung – eignet sich das entwickelte Smart window für die Anwendung von Signalen mit einem hohen Dynamikbereich. Im Rahmen der Arbeit wurde auch eine Methode zur Abscheidung einer ultradünnen Pufferschicht zur Einstellung der Oberflächeneigenschaften entwickelt, die universell auf den Tintenstrahldruckprozess angewendet werden kann.

Der dritte Teil der Arbeit befasst sich mit der oberflächenverstärkten Raman-Streuung (SERS) in der chemischen Sensorik. Die Motivation dieser Arbeit liegt in der Anpassung der lokalisierten Oberflächenplasmonenreaktionen (LSPR) innerhalb einer photonischen 3D-Nanostruktur. Das Ziel ist es, die LSPR-Peaks mit der Wellenlänge des Anregungslasers abzustimmen, um eine ultrahohe Empfindlichkeit beim Nachweis von Analyten zu erreichen. Die physikalische Grundlage dieser Arbeit bildet die Raman-Streuung, eine Form der inelastischen Lichtstreuung. Durch die gezielte Kontrolle des Wachstums von Goldnanopartikeln in einem nanoporösen 3D-Siliziumnetzwerk werden die LSPR-Peaks präzise manipuliert. Dadurch kann der LSPR-Peak an die Wellenlänge des Anregungslasers angepasst werden, um ein deutlich verstärktes lokales elektrisches Feld and LSPR zu erzeugen. Diese verstärkte LSPR wiederum intensiviert die Raman-Streuung des Zielmoleküls Methylenblau. Auf diese Weise wird ein ultrahoher Verstärkungsfaktor in der Größenordnung von 10^9 erreicht. Dies unterstreicht die ultrahohe Empfindlichkeit des SERS-Sensors, der in der Lage ist, Konzentrationen von Einzelmolekülen zu erkennen.

Der Kern dieser Dissertation liegt im Lichtmanagement und -sensing durch photonische Nanostrukturen. Zur Realisierung dieses Ziels werden verschiedene Herstellungsverfahren entwickelt und im Detail beschrieben. Die erzielten Ergebnisse werden umfassend diskutiert.

List of Publications and Contributions to Conferences

Peer-reviewed publications (* shared first author)

1. **Qihao Jin**, Qiaoshuang Zhang, Christian Rainer, Hang Hu, Junchi Chen, Tim Gehring, Jan Dycke, Roja Singh, Ulrich. W. Paetzold, Gerardo Hernández-Sosa, Rainer Kling, and Uli Lemmer. "Inkjet-Printed Optical Interference Filters". In: *Nature Communications* 15, 3372 (2024). doi: 10.1038/s41467-024-47086-x

2. **Qihao Jin**, Qiaoshuang Zhang, Junchi Chen, Tim Gehring, Santiago Eizaguirre, Robert Huber, Guillaume Gomard, Uli Lemmer, and Rainer Kling. "High Dynamic Range Smart Window Display by Surface Hydrophilization and Inkjet Printing". In: *Advanced Materials Technologies* 7.5 (2022), p. 2101026. doi: 10.1002/admt. 202101026

3. Rihan Wu*, **Qihao Jin***, Catherine Storey, Jack Collins, Guillaume Gomard, Uli Lemmer, Leigh Canham, Rainer Kling, and Andrey Kaplan. "Gold nanoplasmonic particles in tunable porous silicon 3D scaffolds for ultra-low concentration detection by SERS". In: *Nanoscale Horizons* 6.10 (2021), pp. 781–790. doi: 10.1039/D1NH00228G

4. Qiaoshuang Zhang, **Qihao Jin**, Adrian Mertens, Christian Rainer, Robert Huber, Jan Fessler, Gerardo Hernandez-Sosa, and Uli Lemmer. "Fabrication of Bragg Mirrors by Multilayer Inkjet Printing". In: *Advanced materials* 34.33 (2022), e2201348. doi: 10.1002/adma.202201348

5. Junchi Chen, **Qihao Jin**, Yidenekachew Donie, Dmitry Busko, Bryce S. Richards, and Uli Lemmer. "Enhanced Photoluminescence of a Microporous Quantum Dot Color Conversion Layer by Inkjet Printing". In: *Nano Research* 17 (2024), doi: 10.1007/s12274-024-6671-9

6. Qiaoshuang Zhang, Maximilian Schambach, **Qihao Jin**, Michael Heizmann, and Uli Lemmer. "A Compact Multispectral Light Field Camera Based on an Inkjet-printed Microlens Array and Color Filter Array". Submitted.

7. Yi Wang, Tim Gehring, **Qihao Jin**, Jan Dycke, and Rainer Kling. "Characterization of Argon/Hydrogen Inductively Coupled Plasma for Carbon Removal over Multilayer Thin Films". In: *Coatings* 13.2 (2023), p. 368. doi: 10.3390/coatings13020368

8. Tim Gehring, Santiago Eizaguirre, **Qihao Jin**, Jan Dycke, Manuel Renschler, and Rainer Kling. "On the Temperature and Plasma Distribution of an Inductively Driven Xe-I2-Discharge". In: *Plasma* 4.4 (2021), pp. 745–754. doi: 10.3390/plasma4040037

9. Qiaoshuang Zhang, Maximilian Schambach, Stefan Schlisske, **Qihao Jin**, Adrian Mertens, Christian Rainer, Gerardo Hernandez–Sosa, Michael Heizmann, and Uli Lemmer. "Fabrication of Microlens Arrays with High Quality and High Fill Factor by Inkjet Printing". In: *Advanced Optical Materials* 10.14 (2022), p. 2200677. ISSN: 2195-1071. doi: 10.1002/adom.202200677

10. Junchi Chen, Dominik Theobald, Abdullah Bin Shams, **Qihao Jin**, Adrian Mertens, Guillaume Gomard, and Uli Lemmer. "Silver-Nanoparticle-Based Metallodielectric Wavelength-Selective Reflectors for Quantum-Dot-Enhanced White-Light-Emitting Diodes". In: *ACS Applied Nano Materials* 5.1 (2022), pp. 87–93. ISSN: 2574-0970. doi: 10.1021/acsanm.1c02885

11. Christian Rust, Pavel Shapturenka, Manuel Spari, **Qihao Jin**, Han Li, Andreas Bacher, Markus Guttmann, Ming Zheng, Tehseen Adel, Angela R. Hight Walker, Jeffrey A. Fagan, and Benjamin S. Flavel. "The Impact of Carbon Nanotube Length and Diameter on their Global Alignment by Dead-End Filtration". In: *Small* 19.10 (2023), e2206774. doi: 10.1002/smll.202206774

12. Rihan Wu, Thibaut Mathieu, Catherine J. Storey, **Qihao Jin**, Jack Collins, Leigh T. Canham, and Andrey Kaplan. Localized Plasmon Field Effect of Gold Clusters Embedded in Nanoporous Silicon". In: *Advanced Optical Materials* 9.9 (2021), p. 2002119. ISSN: 2195-1071. doi: 10.1002/adom.202002119

13. Santiago Eizaguirre Cabrera, Tim Gehring, Fabian Denk, **Qihao Jin**, Jan Dycke, Manuel Renschler, Marc Hiller, Uli Lemmer, and Rainer Kling. "SiC-Based Resonant Converters With ZVS Operated in MHz Range Driving Rapidly Variable Loads: Inductively Coupled Plasmas as a Case of Study". In: *IEEE Transactions on Power Electronics* 37.7 (2022), pp. 7775–7788. ISSN: 0885-8993. doi: 10.1109/TPEL.2022.3147947

14. Yang Li, Julie Roger, Isabel Allegro, Jan C. Fischer, **Qihao Jin**, Uli Lemmer, Ian A. Howard, and Ulrich W. Paetzold. "Lasing from Laminated Quasi–2D/3D Perovskite Planar Heterostructures". In: *Advanced Functional Materials* 32.27 (2022), p. 2200772. ISSN: 1616-301X. doi: 10.1002/adfm.202200772

15. Junchi Chen, Guocan Jiang, Elias Hamann, Henning Mescher, **Qihao Jin**, Isabel Allegro, Philipp Brenner, Nikolai Gaponik, Alexander Eychmueller, and Uli Lemmer. "Organosilicon-based Ligand Design for High-Performance Perovskite Nanocrystal Films for Color Conversion and X-Ray Imaging". In: *ACS Nano*, 18 (14), 10054–10062. doi: 10.1021/acsnano.3c11991

16. Kai Xia, Zheqin Dong, Qing Sun, Rafaela Debastiani, Sida Liu, **Qihao Jin**, Yang Li, Ulrich W. Paetzold, Peter Gumbsch, Uli Lemmer, Yolita M. Eggeler, Pavel A. Levkin, and Gerardo Hernandez–Sosa. "Electrical Conductivity and Photodetection in 3D–Printed Nanoporous Structures via Solution–Processed Functional Materials". In: *Advanced Materials Technologies* (2023). ISSN: 2365-709X. doi: 10.1002/admt.202300408

17. Isabel Allegro, Víctor Bonal, Emil R. Mamleyev, José M. Villalvilla, José A. Quintana, **Qihao Jin**, María A. Díaz-García, and Uli Lemmer. "Distributed Feedback Lasers by Thermal Nanoimprint of Perovskites Using Gelatin Gratings". In: *ACS applied materials & interfaces* 15.6 (2023), pp. 8436–8445. doi: 10.1021/acsami.2c22920

18. Christian Rust, Han Li, Georgy Gordeev, Manuel Spari, Markus Guttmann, **Qihao Jin**, Stephanie Reich, and Benjamin S. Flavel. "Global Alignment of Carbon Nanotubes via High Precision Microfluidic Dead–End Filtration". In: *Advanced Functional Materials* 32.10 (2022), p. 2107411. ISSN: 1616-301X. doi: 10.1002/adfm.202107411

19. Hang Hu, Somayeh Moghadamzadeh, Raheleh Azmi, Yang Li, Milian Kaiser, Jan C. Fischer, **Qihao Jin**, Julia Maibach, Ihteaz M. Hossain, Ulrich W. Paetzold, and Bahram Abdollahi Nejand. "Sn–Pb Mixed Perovskites with Fullerene–Derivative Interlayers for Efficient Four–Terminal All–Perovskite Tandem Solar Cells". In: *Advanced Functional Materials* 32.12 (2022), p. 2107650. ISSN: 1616-301X. doi: 10.1002/adfm.202107650

20. Hang Hu, David B. Ritzer, Alexander Diercks, Yang Li, Roja Singh, Paul Fassl, **Qihao Jin**, Fabian Schackmar, Ulrich W. Paetzold, and Bahram Abdollahi Nejand. "Void-free buried interface for scalable processing of p-i-n-based FAPbI3 perovskite solar modules". In: *Joule* (2023). ISSN: 25424351. doi: 10.1016/j.joule.2023.05.017

21. Hang Hu, Sophie X. An, Yang Li, Seyedamir Orooji, Roja Singh, Fabian Schackmar, Felix Laufer, **Qihao Jin**, Thomas Feeney, Alexander Diercks, Fabrizio Gota, Somayeh Moghadamzadeh, Ting Pan, Bahram Abdollahi Nejand, and Ulrich W. Paetzold. "Triple-Junction Perovskite–Perovskite–Silicon Solar Cells with Power Conversion Efficiency of 24.4%". Under review.

Contributions to Conferences

1. **Qihao Jin**, Qiaoshuang Zhang, Junchi Chen, Tim Gehring, Santiago Eizaguirre Cabrera, Robert Huber, Guillaume Gomard, Uli Lemmer, and Rainer Kling. Pixelated Smart Window for High Dynamic Range Signage Displaying Applications. 2021

2. Qiaoshuang Zhang, **Qihao Jin**, Adrian Mertens, Robert Huber, Jan Fessler, Gerardo Hernandez-Sosa, and Uli Lemmer. Fabrication of patterned, flexible and largescale Bragg mirrors by inkjet printing (Conference Presentation). PC12202. 2022. doi: 10.1117/12.2633359

3. Tim Gehring, **Qihao Jin**, Jan Dycke, Biruk Alemu, Raghuraman Anantharaman, and Rainer Kling. Induktive UV-Strahler: Simulation und Vermessung. 2023, Juli 7. 27. Symposium der Deutschen Akademie für Photobiologie und Phototechnologie (DAfP 2023), Quedlinburg, Deutschland, 6.–7. Juli 2023

4. Tim Gehring, Santiago Eizaguirre Cabrera, **Qihao Jin**, Jan Dycke, Yi Wang, and Rainer Kling. Plasma Water Activation with an Inductive Plasma Torch at Atmospheric Pressure. 2023. doi: 10.5445/IR/1000157521

5. Biruk Alemu, Tim Gehring, Robert Huber, Raghuraman Anantharaman, **Qihao Jin**, and Rainer Kling. Kapazitiv gekoppelte Plasmastrahler zur Erzeugung von 222 nm Excimerstrahlung mit gedruckten Elektrodenstrukturen : Krypton-Chlorid- Flachlampen zur flächigen Erzeugung von UV-Strahlung. 2023, Juli 6. 27. Symposium der Deutschen Akademie für Photobiologie und Phototechnologie (DAfP 2023), Quedlinburg, Deutschland, 6.–7. Juli 2023.

Supervised Student Theses and Work

Master theses

1. Hanlin Zheng, "Multi-layer Thin Film Stack for Passive and Radiative cooling", Abbe School of Photonics of Friedrich Schiller University Jena, 2023
2. Weimu Xu, "Fabrication of Plasmonic Color Based on Metal-Embedded and Phase-Separated Nano-Structures", Master thesis, Karlsruhe School of Optics and Photonics, 2022
3. Xiang Zhao, "Tunable Plasmons on Nanostructured Polymers via Material Sputtering", Master thesis, Materialwissenschaft und Werkstofftechnologie, 2021
4. Yuhao Wang, "Plasma Treated Light Extracting Nanostructures for OLEDs", Master thesis, Karlsruhe School of Optics and Photonics, 2020
5. Shuo Li, "Design a Capacitively Coupled Plasma Chamber for Surface Nanostructuring", Master thesis, Mechatronics and Information Technology, 2019

Internships and study modules

1. Hanlin Zheng, "Single-Layer Anti-refractive Coatings", Research Labwork, Abbe School of Photonics of Friedrich Schiller University Jena, 2023
2. Uyen Nguyen, "RGB Extraction from An Image", Research Project, Karlsruhe School of Optics and Photonics, 2022
3. Yogitaa, "Multispectral Imaging Based on Color Filters," Research Project, Karlsruhe School of Optics and Photonics, 2022
4. Weimu Xu, "Micro-structuring by Optical Lithography", Internship, Karlsruhe School of Optics and Photonics, 2021

Symbols and Abbreviations

- A: Absorptance
- a: Radius of nanosphere
- B: Magnetic flux density
- c_0: Velocity of light in free space
- **D**: Electric displacement
- d: Physical thickness of the layer
- $\boldsymbol{E}$: Electric vector in the electromagnetic field
- E: Electric field amplitude
- $\mathfrak{E}$: Irradiance vector
- $\boldsymbol{H}$: Magnetic vector in the electromagnetic field
- H: Magnetic field amplitude
- k: Extinction coefficient
- k_B: Boltzmann's constant
- N: Complex refractive index
- n: The real part of refractive index
- P: Radiated power
- $\boldsymbol{p}$: Induced dipole
- R: Reflectance
- r: Amplitude reflection coefficient
- τ: Amplitude transmission coefficient
- T: Transmittance
- T: Thermodynamic temperature
- v: Velocity

- Y: Optical admittance
- Υ: Tilted optical admittance
- y_0: Optical admittance in free space
- η: Ink viscosity for inkjet printing
- κ: Wave number
- λ: Wavelength of light
- λ_0: Wavelength of light in free space
- ω: Angular frequency
- σ: Electric conductivity
- ε: Permittivity
- ε_0: Permittivity of free space
- μ: Permeability
- μ_0: Permeability of free space
- δ: Phase difference
- ρ: Density
- γ: Surface tension

Contents

List of Figures

List of Tables

1 Introduction

In this chapter, the background of research that focuses on the development and applications of photonic nanostructures is presented. Additionally, it provides the motivations for the work conducted in this dissertation. Towards the end of this chapter, the structure of the dissertation is outlined.

Nanostructure-based research is a promising and exciting area that has received a lot of attention in recent years. This interdisciplinary field provides new possibilities to tackle challenges ranging from basic research to practical applications. Many research fields involving nanostructures are well-established, such as nanophotonics, nanomaterials, nanobiology, nanomechanics, nanobiotechnology, quantum computing, etc.

Research on photonic nanostructures has stimulated the advance of nanoscience and nanofabrication [1]. The main focus of this research field is to study the interactions between light and matter and how matter can be used to manipulate light [2]. With the help of advanced fabrication techniques, photonic nanostructures of one, two, or three dimensions have been extensively studied and implemented in various fields [3].

In this dissertation, the work focuses on light management and optical sensing by photonic nanostructures. The physical fundamentals of the work are based on optical interference and scattering. Relying on the developed fabrication methods, precise control of the optical responses of the devices is achieved for different applications.

Inkjet-printed optical interference filters

The optical interference filters are essential components widely used in most modern optical instruments [4]. In Figure 1.1, filters with different spectral functionalities can be found in the left image, while the right image shows a general concept of the optical filters, i.e., spectral selection. The optical interference filters are designed and fabricated in a multilayer thin film structure to achieve the required optical responses. As can be easily known from the name, these filters rely on optical interference. The energy absorption can be near zero for dielectric interference filters, which is a strong contrast to the color filters based on absorptive materials [5]. In research and industry, the common high-end optical interference filters include longpass, shortpass, bandpass, and dichroic filters. Nowadays, nearly all of these high-end optical interference filters are fabricated in cost-intensive vacuum chambers. Thermal evaporation, plasma-assisted deposition, and atomic layer deposition are the common technologies used for fabricating these filters. Although these manufacturing processes are well-established nowadays, they are rigid in rapid prototyping, customization, fast iterations, etc. Furthermore, the evolution of technologies triggers numerous emerging applications that require novel fabrication

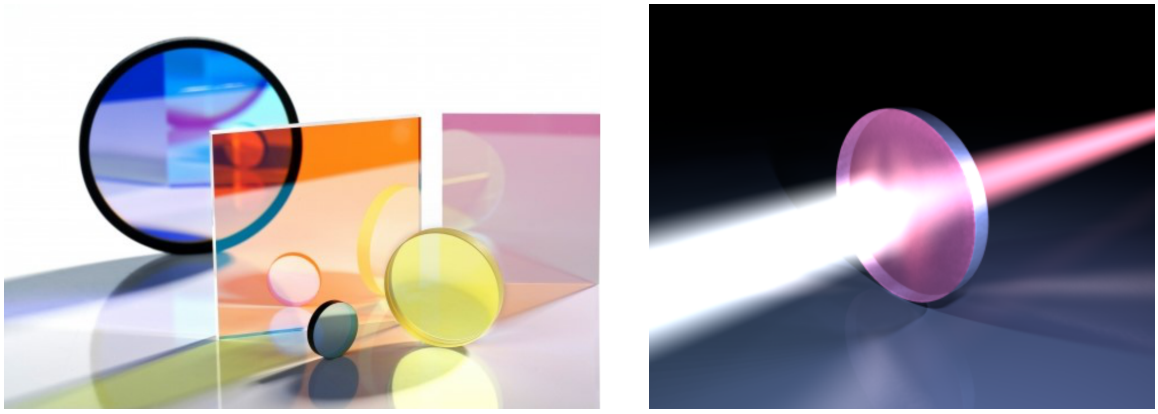

Figure 1.1: Optical interference filters. Source: Alluxa and MEETOPTICS.

techniques, for instance, filters fabricated on flexible substrates, in different sizes ranging from micro to meter scale, lateral combinations of different filters, direct on-sensor printing, etc.

In this dissertation, a new fabrication method is developed to inkjet print optical interference filters directly. Inkjet printing is a technique that is widely used in additive manufacturing. It is based on layer-by-layer deposition. This technology can be applied in ambient conditions without any vacuum requirements. Therefore, it leads to a more affordable and sustainable fabrication process. In addition, inkjet printing offers ultra-high resolution in layer thickness control and a high degree of freedom in lateral pattering. These advantages make inkjet printing stand out for producing high-quality optical filters. Enabled by inkjet printing, more complicated filter designs can be realized, such as a filter array, a gradient filter, etc. However, the inkjet printing process for such filters is yet to be developed. To tackle this, the work in this dissertation has investigated ink formulation, printing process development, and post-treatment. It demonstrates using inkjet printing to realize photonic structures, i.e., optical filters, to achieve precise light manipulation, i.e., spectral selection.

Dynamic control of light scattering in smart windows

Elastic optical scattering is a type of scattering in which the incident and the scattered light show no difference in energy. Macroscopically, the light is deflected after hitting an object. The application based on elastic scattering covers a broad field [6], such as material characterization, medical imaging, bioanalysis, remote sensing, surface inspection, display technology, etc. In many applications, it is very attractive to control the elastic scattering on demand, i.e., the active control of the light scattering. In this dissertation, the work focuses on optical information conveyed, e.g., signage application, through the dynamic control of the elastic light scattering from photonic structures. Based on this concept, a smart window is designed and fabricated. This device contains surface structures for optical response control. One of the technical advantages of smart windows is the optical response of the device can be actively tuned. This denotes the number of op-

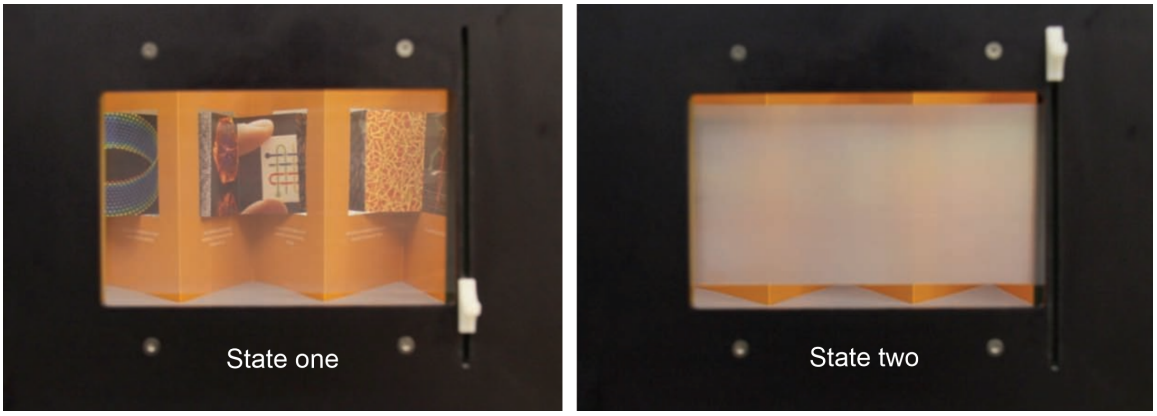

Figure 1.2: Smart window in different states. Transparent and opaque [8].

tical states of the device is at least two. In certain cases, the number of optical states can be unlimited with a proper design.

There are different types of smart windows based on individual mechanisms [7]. The mechanoresponsive smart window is a common one that is highly suitable for manipulating light scattering. One of the bottlenecks in mechanoresponsive smart windows is that the switch of the state usually happens globally, as seen in Figure 1.2. In other words, the optical response of the entire smart window is often the same from site to site. To improve this, some groups have introduced a mask during fabrication to create patterns or letters in the smart windows [8]. However, the amount of conveyed information is limited. In addition, fabricating and employing masks during surface treatment requires additional effort. In this dissertation, the concept of a pixelated smart window is introduced. Masks are inkjet printed directly on the surface to be treated. Attributed to digitally controlled printing and drop-on-demand deposition, a high degree of freedom for surface nanostructuring is realized. By the inkjet-printed masks, a property called locally variable optical haze is achieved and discussed. Therefore, the optical scattering level is controlled in each small pixel, resulting in a very high dynamic range. Consequently, the developed smart window is enabled with a display function for signage applications.

Manipulation of LSPR in SERS for optical sensing

Besides the elastic scattering, the work in this dissertation also explores inelastic scattering. In contrast to elastic scattering, inelastic scattering results in an energy difference between the incident and outgoing optical waves. In many sensing applications, Raman scattering is one of the inelastic scattering often used for material detection. The signal level of the natural Raman scattering is fairly weak, typically in an order of $10^{-}7$ compared to the incident light. Therefore, additional techniques are required to enhance the Raman signal level for a better qualitative and quantitative analysis [9]. In this dissertation, surface-enhanced Raman scattering (SERS) in a 3D nanoporous silicon network has been studied, and the corresponding spectroscopy is conducted for molecule sensing.

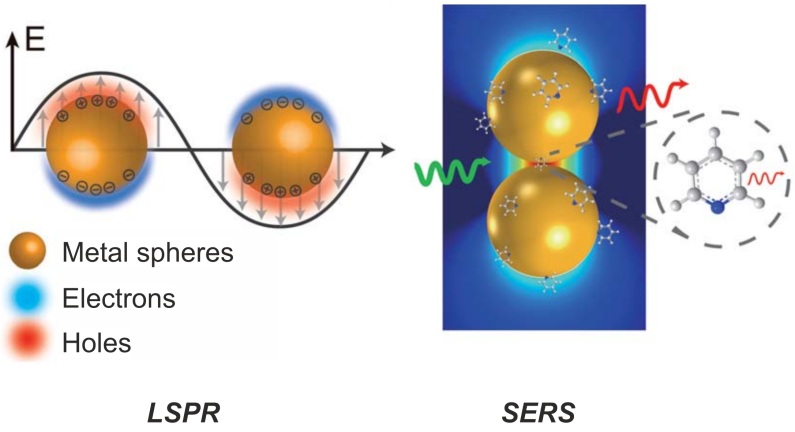

Figure 1.3: Localized surface plasmon resonance (LSPR) and surface-enhanced Raman scattering (SERS) [12].

The goal of the SERS measurement is to obtain a largely enhanced Raman signal. One strategy is to increase the density of the hot spot in the SERS substrate [10]. Here, the hot spot is a nanoscale region where the electromagnetic field is significantly enhanced. On the other side, a practical challenge in measurement comes from the excitation laser source, where the wavelength of the laser source is often "fixed". Although there are many different laser sources, the emitting wavelength of the laser source does not always match the SERS substrate. This leads to the issue that the amplitude of the localized electric field needed is not always optimum. This is because the SERS substrate is based on localized surface plasmon resonance (LSPR). The LSPR is a collective oscillation of electrons with the external electromagnetic waves, as seen in Figure 1.3. The SERS signal is predominantly enhanced by LSPR and reaches the maximum only when the laser line wavelength matches the LSPR. Ideally, the LSPR occurs at an intermediate wavelength value between the excitation wavelength and Raman scattering wavelength [11]. Although one can use a continuously tunable laser source for SERS measurement, it is, unfortunately, cost-intensive, and the tunable range of the laser is usually limited.

In this dissertation, novel 3D SERS substrates are developed with carefully manipulated LSPR peaks. This is achieved by controlling gold nanoparticle deposition in the 3D nanoporous silicon network. A high hot spot density has been reached, which is attributed to the 3D nanostructure that has been fabricated. In different SERS samples, different hot spot densities, particle sizes, and interparticle distances are realized by optimized processing parameters. Enabled by these facts, the LSPR peaks are proven to be controllable. From the measurement, an ultra-high SERS enhancement factor is obtained and validated, allowing the detection of analytes at a single molecule level. It is a step forward for developing highly sensitive SERS detectors for various practical optical sensing.

Structure of the dissertation

The work in this dissertation aims to investigate light management in photonic structures for real-life applications, such as optical filters and material sensing. The reliant

fundamentals are optical interference and scattering. In addition, different processes are developed to fabricate individual devices. The dissertation is structured as follows:

- Chapter 2: fundamentals of optical interference and scattering are presented and discussed. It provides the basic theory background of this dissertation.
- Chapter 3: the state of the art is presented. The results of this work contain three parts, i.e., inkjet-printed optical interference filters, dynamic light scattering modulation in a smart window, and surface-enhanced Raman scattering for chemical sensing. Therefore, three fields are overviewed, and the essential status quo is presented individually.
- Chapter 4: inkjet printing technology is presented and discussed. Inkjet printing is a major fabrication method that is applied in the work of this dissertation. An overview of the utilization of inkjet printing in different research fields is presented. Additionally, the mechanism of the technology and a discussion on ink fluid theory are presented.
- Chapter 5: materials, methods, and characterizations applied in this work are listed and discussed.
- Chapter 6: the work of inkjet-printed optical interference filters is presented and discussed. The chapter gives a detailed description of how high-end optical interference filters have been first-ever fabricated by inkjet printing. Through careful designs, longpass, shortpass, bandpass, and dichroic filters have been printed. Furthermore, it shows the laterally patterned filters, upscaling filters to a DIN A4 size, etc. Results on optical quality characterization are also given in the chapter.
- Chapter 7: the work of dynamic optical scattering control in a mechanoresponsive smart window is presented and discussed. The chapter first shows the initial step of introducing an essential ultra-thin buffer layer for subsequent inkjet printing. After that, plasma surface structuring with printed etching masks is demonstrated. Subsequently, the process of how dynamic optical scattering is induced and controlled is elaborated. Quantitative analysis of the optical scattering, i.e., haze, is revealed in detail.
- Chapter 8: the work of surface-enhanced Raman scattering (SERS) for optical sensing is presented and discussed. Localized surface plasmon responses (LSPR) peaks are carefully manipulated by gold nanoparticle deposition in a 3D nanoporous silicon network. The successful matching of the LSPR and the excitation laser wavelength is realized, obtaining an ultrahigh sensitivity for analyte sensing. The chapter offers details on the fabrication of the SERS substrate and the conducted spectrometry.
- Chapter 9: the conclusion and the outlook of the work are provided.

2 Fundamentals

In this chapter, the fundamental physical aspects of electromagnetic waves interacting with matter are described, comprising interference and scattering. First, the theory of thin film interference is presented. It gives the essential background of how interference is raised and numerically resolved for different boundaries and thin film structures. Subsequently, the fundamentals of optical scattering are elaborated. First, the elastic optical scattering is explained and resolved by Mie theory. This provides a fundamental understanding of how a photonic structure results in the deflection of electromagnetic waves. In addition, optical scattering spectroscopy is discussed for the quantitative measurement of the elastically scattered optical power. Eventually, the inelastic optical scattering process, surface-enhanced Raman scattering, is introduced. The mechanism of this type of scattering is explained from the fundamentals to applications. The affiliated spectroscopy is discussed, including important parameters and factors in the application field.

2.1 Fundamentals of electromagnetic waves

To understand light propagation in materials, the basics of the electromagnetic theory are discussed in the following, starting with Maxwell's equations:

$$\nabla \times \boldsymbol{E} = -\frac{\partial \boldsymbol{B}}{\partial t} \qquad \nabla \times \boldsymbol{H} = j + \frac{\partial \boldsymbol{D}}{\partial t}$$
$$\nabla \cdot \boldsymbol{D} = \rho \qquad \nabla \cdot \boldsymbol{B} = 0$$

where **E** denotes the electric field, **H** the magnetic field, **D** the electric displacement, **B** the magnetic induction, ρ the free charge density and j the current density. These equations are often used to describe the properties of electromagnetic fields.

In this work, the multilayer interference is considered to take place in the media without free charges and currents. Therefore, ρ and j are equal to zero. The Maxwell's equations then become

$$\nabla \times \boldsymbol{E} = -\frac{\partial \boldsymbol{B}}{\partial t} \qquad \nabla \times \boldsymbol{H} = \frac{\partial \boldsymbol{D}}{\partial t}$$
$$\nabla \cdot \boldsymbol{D} = 0 \qquad \nabla \cdot \boldsymbol{B} = 0$$

where,

$$\boldsymbol{D} = \varepsilon \boldsymbol{E} \qquad \boldsymbol{B} = \mu \boldsymbol{H} \tag{2.1}$$

with

$$\varepsilon = \varepsilon_r \varepsilon_0 \qquad \mu = \mu_r \mu_0 \tag{2.2}$$

where ε_0 and ε_r are vacuum permittivity and relative permittivity, μ_0 and μ_r are vacuum permeability and relative permeability, respectively. Therefore, the equations $\nabla \times \boldsymbol{E}$ and $\nabla \times \boldsymbol{H}$ can be rewritten as

$$\nabla \times \boldsymbol{E} = -\mu \frac{\partial \boldsymbol{H}}{\partial t} \tag{2.3}$$

$$\nabla \times \boldsymbol{H} = -\varepsilon \frac{\partial \boldsymbol{E}}{\partial t} \tag{2.4}$$

Applying the curl calculation on equation 2.3 yields

$$\nabla \times (\nabla \times \boldsymbol{E}) = -\mu \frac{\partial (\nabla \times \boldsymbol{H})}{\partial t} = -\mu \frac{\partial}{\partial t} (\sigma \boldsymbol{E} + \varepsilon \frac{\partial \boldsymbol{E}}{\partial t}) \tag{2.5}$$

where σ is the electric conductivity. Since

$$\nabla \times (\nabla \times \boldsymbol{E}) = \nabla (\nabla \cdot \boldsymbol{E}) - \nabla^2 \boldsymbol{E} \tag{2.6}$$

and there is no free charge in the space, i.e., $\nabla \cdot \boldsymbol{E} = 0$, it yields

$$\nabla^2 \boldsymbol{E} = \mu \varepsilon \frac{\partial^2 \boldsymbol{E}}{\partial t^2} + \mu \sigma \frac{\partial \boldsymbol{E}}{\partial t} \tag{2.7}$$

Considering the media consisting of dielectric materials, i.e., the electric conductivity $\sigma = 0$, the wave equation 2.7 becomes

$$\nabla^2 \boldsymbol{E} = \mu \varepsilon \frac{\partial^2 \boldsymbol{E}}{\partial t^2} \tag{2.8}$$

And a similar expression is derived for the magnetic field,

$$\nabla^2 \boldsymbol{H} = \mu \varepsilon \frac{\partial^2 \boldsymbol{H}}{\partial t^2} \tag{2.9}$$

Since $c^2 = 1/(\varepsilon_0 \mu_0)$, where c is the speed of light in free space, equations 2.8 and 2.9 can be rewritten as

$$\nabla^2 \boldsymbol{E} = \frac{1}{c^2} \frac{\partial^2 \boldsymbol{E}}{\partial t^2} \tag{2.10}$$

$$\nabla^2 \boldsymbol{H} = \frac{1}{c^2} \frac{\partial^2 \boldsymbol{H}}{\partial t^2} \tag{2.11}$$

Above are the wave equations used for describing the electromagnetic wave propagating in a non-conducting and isotropic medium. From these, a plane wave oscillating in the x direction can be obtained as

$$\boldsymbol{E} = E_0 \exp[i\omega(t - \frac{z}{v})] \tag{2.12}$$

where the wave propagates along the z-axis in the media with a velocity v.

2.2 Optical interference in thin film structures

Thin film interference occurs when the electromagnetic wave travels in space with a specific phase relation. It is important to know the refractive index of the space. As known, the complex refractive index N of the media is the ratio between the c and v, which can be written as

$$N = \frac{c}{v} = n - ik \tag{2.13}$$

where n is the real part called the refractive index, and k is the imaginary part called the extinction coefficient. With equation 2.13 and the angular frequency $\omega = 2\pi\nu$, equation 2.12 can be written as

$$\boldsymbol{E} = E_0 \exp\left[i\left(\omega t - \frac{2\pi N z}{\lambda}\right)\right] \tag{2.14}$$

Considering the case that a plane wave with a wavelength of λ propagates in the direction possessing x, y, z components, the equation 2.14 becomes

$$\boldsymbol{E} = E_0 \exp\left[i\left(\omega t - \frac{2\pi N(\alpha x + \beta y + \gamma z)}{\lambda}\right)\right] \tag{2.15}$$

Here, the concept of optical admittance is introduced. The optical admittance of the medium Y is defined as the ratio between the magnetic and electric fields:

$$Y = \frac{H}{E} = N y_0 \tag{2.16}$$

The optical admittance is a characteristic of the optical medium, where y_0 is the optical admittance of the free space.

Reflection and transmission at the interface

First, the normal incident case is considered here. If the wave has its electric and magnetic field direction parallel to the incident interface, the electric and magnetic field vectors are continuous across the boundary.

$$\boldsymbol{E_i} + \boldsymbol{E_r} = \boldsymbol{E_t} \tag{2.17}$$

where $\boldsymbol{E_i}$, $\boldsymbol{E_r}$, and $\boldsymbol{E_t}$ are electric field vectors of incidence, reflection, and transmission. Similarly,

$$\boldsymbol{H_i} - \boldsymbol{H_r} = \boldsymbol{H_t} \tag{2.18}$$

where $\boldsymbol{H_i}$, $\boldsymbol{H_r}$, and $\boldsymbol{H_t}$ are magnetic field vectors of incidence, reflection, and transmission. It is noted that a minus sign appears in the magnetic field case. This is due to the manual definition of its direction with respect to wave propagation. According to equation 2.16, which provides the relation between electric and magnetic field, equation 2.18 can be written as

$$Y_0 \boldsymbol{E_i} - Y_0 \boldsymbol{E_r} = Y_1 \boldsymbol{E_t} \tag{2.19}$$

where Y_0 and Y_1 are the optical admittance of the two media along the boundary, respectively. Here, it is defined that the wave propagates from media 0 to media 1. Eliminating $\boldsymbol{E_t}$ using equation 2.17,

$$Y_0(\boldsymbol{E_i} - \boldsymbol{E_r}) = Y_1(\boldsymbol{E_i} + \boldsymbol{E_r}) \tag{2.20}$$

it can be obtained that

$$\frac{\boldsymbol{E_r}}{\boldsymbol{E_i}} = \frac{Y_0 - Y_1}{Y_0 + Y_1} = \frac{n_0 - n_1}{n_0 + n_1} \tag{2.21}$$

where the medium is assumed to have no absorption, i.e., $k = 0$. When eliminating $\boldsymbol{E_r}$ using equation 2.17,

$$\frac{\boldsymbol{E_t}}{\boldsymbol{E_i}} = \frac{2Y_0}{Y_0 + Y_1} = \frac{2n_0}{n_0 + n_1} \tag{2.22}$$

$\frac{E_r}{E_i}$ and $\frac{E_t}{E_i}$ are the ratio of amplitudes, where the former is called amplitude reflection coefficient r. The latter is called amplitude transmission coefficient τ. Therefore,

$$r = \frac{\boldsymbol{E_r}}{\boldsymbol{E_i}} = \frac{Y_0 - Y_1}{Y_0 + Y_1} = \frac{n_0 - n_1}{n_0 + n_1} \tag{2.23}$$

$$\tau = \frac{\boldsymbol{E_t}}{\boldsymbol{E_i}} = \frac{2Y_0}{Y_0 + Y_1} = \frac{2n_0}{n_0 + n_1} \tag{2.24}$$

The reflectivity R and transmittance T are defined by the power ratio. Therefore, the Poynting vector, which defines the irradiance $\mathfrak{E}$ should be applied, where the irradiance is a physical measure of optical power over a unit area.

$$\mathfrak{E} = \frac{1}{2}\mathrm{Re}(\boldsymbol{E} \times \boldsymbol{H}^*) \tag{2.25}$$

where the symbol * indicates the complex conjugate. The irradiance $\mathfrak{E}$ here is a vector whose direction is the same as the flow of energy of the electromagnetic wave. Since the electric and magnetic field vectors are perpendicular to each other, the intensity equation can also be written in a scalar form,

$$\mathfrak{E} = \frac{1}{2}\mathrm{Re}(EH^*) \tag{2.26}$$

From equations 2.17, 2.19, and boundary conditions, it yields

$$\mathfrak{E}_i = \frac{1}{2} Y_0 \boldsymbol{E}\boldsymbol{E}^* \tag{2.27}$$

$$\mathfrak{E}_r = r^2 \frac{1}{2} Y_0 \boldsymbol{E}\boldsymbol{E}^* = r^2 \mathfrak{E}_i \tag{2.28}$$

$$\mathfrak{E}_t = \frac{Y_1}{Y_0}\frac{1}{2}Y_0 \boldsymbol{E}\boldsymbol{E}^* = \frac{Y_1}{Y_0}t^2\mathfrak{E}_i \tag{2.29}$$

Eventually, R and Tcan be calculated as

$$R = \frac{\mathfrak{E}_r}{\mathfrak{E}_i} = r^2 = \left(\frac{Y_0 - Y_1}{Y_0 + Y_1}\right)^2 = \left(\frac{n_0 - n_1}{n_0 + n_1}\right)^2 \tag{2.30}$$

$$T = \frac{\mathfrak{E}_t}{\mathfrak{E}_i} = \frac{Y_1}{Y_0}\tau^2 = \frac{4Y_0Y_1}{(Y_0 + Y_1)^2} = \frac{4n_0n_1}{(n_0 + n_1)^2} \tag{2.31}$$

Until now, the considered case is for normal incidence. When the incidence is oblique, the case is more complicated. To simplify it, the electromagnetic wave is split into two linearly polarized components, denoted as p- and s-polarized. By applying the boundary conditions again, in the p-polarized case

$$\boldsymbol{E_i}\cos\theta_i + \boldsymbol{E_r}\cos\theta_i = \boldsymbol{E_t}\cos\theta_t \tag{2.32}$$

where θ_i and θ_t are the incident and refraction angles, respectively. For magnetic field vector

$$\boldsymbol{H_i} - \boldsymbol{H_r} = \boldsymbol{H_t} \tag{2.33}$$

i.e.,

$$Y_0\boldsymbol{E_i} - Y_0\boldsymbol{E_r} = Y_1\boldsymbol{E_t} \tag{2.34}$$

Thus

$$r = \frac{\boldsymbol{E_r}}{\boldsymbol{E_i}} = \frac{Y_0\cos\theta_t - Y_1\cos\theta_i}{Y_0\cos\theta_t + Y_1\cos\theta_i} \tag{2.35}$$

$$\tau = \frac{\boldsymbol{E_t}}{\boldsymbol{E_i}} = \frac{2Y_0\cos\theta_i}{Y_0\cos\theta_t + Y_1\cos\theta_i} \tag{2.36}$$

Hence, the power-based reflectivity and transmittance can be written as

$$R = r^2 = \left(\frac{Y_0\cos\theta_t - Y_1\cos\theta_i}{Y_0\cos\theta_t + Y_1\cos\theta_i}\right)^2 \tag{2.37}$$

$$T = \tau^2 = \left(\frac{2Y_0\cos\theta_i}{Y_0\cos\theta_t + Y_1\cos\theta_i}\right)^2 \tag{2.38}$$

The conciseness of the equations can be further improved by introducing the titled optical admittance Υ. The components parallel to the boundary are footnoted as tangential,

$$\Upsilon = \frac{H_{\text{tangential}}}{E_{\text{tangential}}} \tag{2.39}$$

$$\Upsilon_p = \frac{Y}{\cos\theta} \tag{2.40}$$

$$\Upsilon_s = Y \cos\theta \tag{2.41}$$

where p and s denote the p- and s-polarized light, respectively, θ is either the incident angle θ_i or the refraction angle θ_t. These two angles are connected by Snell's law, $N_0 sin\theta_i = N_1 sin\theta_t$. Thus, performing a similar derivation as above, the amplitude reflection and transmission coefficients can be written as

$$r = \frac{\Upsilon_0 - \Upsilon_1}{\Upsilon_0 + \Upsilon_1} \tag{2.42}$$

$$\tau = \frac{2\Upsilon_0}{\Upsilon_0 + \Upsilon_1} \tag{2.43}$$

where Υ denotes either Υ_p or Υ_s. The power-based reflectivity and transmission can be written as

$$R = \left(\frac{\Upsilon_0 - \Upsilon_1}{\Upsilon_0 + \Upsilon_1}\right)^2 \tag{2.44}$$

$$T = \frac{4\Upsilon_0\Upsilon_1}{(\Upsilon_0 + \Upsilon_1)^2} \tag{2.45}$$

When considering the case that the media shows absorption, i.e., k ≠ 0, equations 2.44 and 2.45 become

$$R = \left(\frac{\Upsilon_0 - \Upsilon_1}{\Upsilon_0 + \Upsilon_1}\right)\left(\frac{\Upsilon_0 - \Upsilon_1}{\Upsilon_0 + \Upsilon_1}\right)^* \tag{2.46}$$

$$T = \frac{4\Upsilon_0 \,\mathrm{Re}(\Upsilon_1)}{(\Upsilon_0 + \Upsilon_1)(\Upsilon_0 + \Upsilon_1)^*} \tag{2.47}$$

where Υ_0 is real.

Optical interference in a single thin film

This section addresses optical interference resulting from a thin fil comprisingf two parallel interfaces. The thin film contains an incident interface, defined as boundary a, and an exit interface, defined as boundary b. The tilted optical admittance of the thin film is Υ. First, the tangential components of the electric and magnetic field vectors at boundary b are considered:

$$E_{\text{tangential}} = E^+_{\text{tangential}} + E^-_{\text{tangential}} \tag{2.48}$$

$$H_{\text{tangential}} = H^+_{\text{tangential}} - H^-_{\text{tangential}} \tag{2.49}$$

where the + and - signs denote the wave propagating direction. The wave undergoes a phase shift between boundary a and boundary b. From equation 2.14, it can be known that a phase shift can be added by multiplying a factor of $exp(i\delta)$, where $\delta = 2\pi N d cos\theta/\lambda$. d is

the thickness of the thin film. To enhance the conciseness of the equations, the footnote 'tangential' is omitted from the vector components. It is important to notice that the discussion below addresses the tangential components unless it is especially pointed out.

The equations showing the phase shift can be expressed as

$$E_a = E_b e^{i\delta} \tag{2.50}$$

$$H_a = H_b e^{i\delta} \tag{2.51}$$

Thus,

$$\begin{aligned} E_a &= E_a^+ + E_a^- \\ &= E_b \left(\frac{e^{i\delta} + e^{-i\delta}}{2} \right) + H_b \left(\frac{e^{i\delta} - e^{-i\delta}}{2\Upsilon_1} \right) \\ &= E_b \cos\delta + \frac{H_b i \sin\delta}{\Upsilon_1} \end{aligned} \tag{2.52}$$

$$\begin{aligned} H_a &= H_a^+ + H_a^- \\ &= E_b \left(\frac{e^{i\delta} - e^{-i\delta}}{2} \right) + H_b \left(\frac{e^{i\delta} + e^{-i\delta}}{2\Upsilon_1} \right) \\ &= E_b i\Upsilon_1 \sin\delta + H_b \cos\delta \end{aligned} \tag{2.53}$$

It can be further expressed in a matrix form

$$\begin{bmatrix} E_a \\ H_a \end{bmatrix} = \begin{bmatrix} \cos\delta & (i\sin\delta)/\Upsilon_1 \\ i\Upsilon_1 \sin\delta & \cos\delta \end{bmatrix} \begin{bmatrix} E_b \\ H_b \end{bmatrix} \tag{2.54}$$

where the two-by-two matrix in equation 2.54 is called the characteristic matrix of a thin film.

Optical interference in multilayers

The method applied in the last section is called the transfer-matrix method. The advantage of this method is that the individual matrices can be added to the calculation in order to solve a successive problem. Therefore, for a two-layer structure, where three boundaries exist, *a*, *b*, and *c*, with the layer thickness of d_1 and d_2 causing the phase shift of $e^{(i\delta_1)}$ and $e^{(i\delta_2)}$, the equation can be written as

$$\begin{bmatrix} E_a \\ H_a \end{bmatrix} = \begin{bmatrix} \cos\delta_1 & (i\sin\delta_1)/\Upsilon_1 \\ i\Upsilon_1 \sin\delta_1 & \cos\delta_1 \end{bmatrix} \begin{bmatrix} \cos\delta_2 & (i\sin\delta_2)/\Upsilon_2 \\ i\Upsilon_2 \sin\delta_2 & \cos\delta_2 \end{bmatrix} \begin{bmatrix} E_c \\ H_c \end{bmatrix} \tag{2.55}$$

Equation 2.55 can be further written as

$$\begin{bmatrix} B \\ C \end{bmatrix} = \begin{bmatrix} E_a/E_c \\ H_a/E_c \end{bmatrix} = \begin{bmatrix} \cos\delta_1 & (i\sin\delta_1)/\Upsilon_1 \\ i\Upsilon_1\sin\delta_1 & \cos\delta_1 \end{bmatrix} \begin{bmatrix} \cos\delta_2 & (i\sin\delta_2)/\Upsilon_2 \\ i\Upsilon_2\sin\delta_2 & \cos\delta_2 \end{bmatrix} \begin{bmatrix} 1 \\ \Upsilon_3 \end{bmatrix} \tag{2.56}$$

This is a normalized form, where

$$\begin{bmatrix} B \\ C \end{bmatrix} \tag{2.57}$$

is the characteristic matrix of the thin film assembly. Using this strategy, the multilayer on a substrate can be described as

$$\begin{bmatrix} B \\ C \end{bmatrix} = \left\{ \prod_{r=1}^{q} \begin{bmatrix} \cos\delta_r & (i\sin\delta_r)/\Upsilon_r \\ i\Upsilon_r\sin\delta_r & \cos\delta_r \end{bmatrix} \right\} \begin{bmatrix} 1 \\ \Upsilon_s \end{bmatrix} \tag{2.58}$$

where q denotes the number of layers, Υ_s is the optical admittance of the substrate or emergent medium, and $\delta_r = 2\pi N_r d_r \cos\theta_r/\lambda$. By doing this, the multilayer problem is replaced by a single-surface problem.

$$\begin{bmatrix} B \\ C \end{bmatrix} = [M_1][M_2]\cdots[M_m] \begin{bmatrix} 1 \\ \Upsilon_s \end{bmatrix} \tag{2.59}$$

where Y = C/B is the optical admittance given by the ratio of tangential magnetic and electric fields.

R, T, and A in multilayer thin film assembly

If the wave exits the multilayer at the n-th interface, the irradiance $\mathfrak{E}$ exiting the assembly can be calculated as

$$\mathfrak{E}_n = \frac{1}{2}\mathrm{Re}(E_n H_n^*) = \frac{1}{2}\mathrm{Re}(E_n \Upsilon_m^* E_n^*) = \frac{1}{2}\mathrm{Re}(\Upsilon_m^*) E_n E_n^* \tag{2.60}$$

Let R be the reflectance and $\mathfrak{E}_i$ be the incident irradiance, (1-R)$\mathfrak{E}_i$ is the actual irradiance entering the assembly:

$$(1-R)\mathfrak{E}_i = \frac{1}{2}\mathrm{Re}(BC^*) E_n E_n^* \tag{2.61}$$

It then gives

$$\mathfrak{E}_i = \frac{1}{2(1-R)}\mathrm{Re}(BC^*) E_n E_n^* \tag{2.62}$$

Therefore, the transmittance T is

$$T = \frac{\mathfrak{E}_n}{\mathfrak{E}_i} = \frac{\mathrm{Re}(\Upsilon_s)(1-R)}{ER(BC^*)} \tag{2.63}$$

As already known,

$$R = \left(\frac{\Upsilon_0 - Y}{\Upsilon_0 + Y}\right)\left(\frac{\Upsilon_0 - Y}{\Upsilon_0 + Y}\right)^* \tag{2.64}$$

Through Y = C/B,

$$R = \left(\frac{\Upsilon_0 B - C}{\Upsilon_0 B + C}\right)\left(\frac{\Upsilon_0 B - C}{\Upsilon_0 B + C}\right)^* \tag{2.65}$$

and

$$1 - R = \frac{2\Upsilon_0(BC^* + B^*C)}{(\Upsilon_0 B + C)(\Upsilon_0 B + C)^*} \tag{2.66}$$

From equation 2.63, it yields,

$$T = \frac{4\Upsilon_0 \mathrm{Re}(\Upsilon_s)}{(\Upsilon_0 B + C)(\Upsilon_0 B + C)^*} \tag{2.67}$$

Absorptance $A = 1 - R - T$,

$$A = \frac{4\Upsilon_0 \mathrm{Re}(BC^* - \Upsilon_s)}{(\Upsilon_0 B + C)(\Upsilon_0 B + C)^*} \tag{2.68}$$

2.3 Optical scattering by nanostructures

Scattering is a physical phenomenon that results from the optical wave interacting with matter. The study of light scattering can be traced back to the 17th century with Isaac Newton. It is an area of interest for physicists who seek to understand how the properties of light change when it interacts with molecules, atoms, photons, and other entities.

Fundamentals of optical scattering

Two pillars of optical scattering compromise elastic and inelastic scattering. A primary difference between these two is whether there is an energy (or frequency) shift between the incident and outgoing waves, including scattered components. Here, an overview of different scattering processes is listed in Table 2.1.

Type of scattering	**Process**
Elastic	Rayleigh scattering, Mie scattering
Inelastic	Raman scattering, Bragg scattering, Compton scattering, Brillouin scattering

Table 2.1: An overview of elastic and inelastic scattering.

This dissertation comprises two main parts, focusing on investigating and demonstrating optical scattering manipulation by photonic structures. The first part explores optical scattering from surface nano- and microstructures, particularly elastic scattering. The

second part focuses on Raman scattering enhanced by metallic nanoparticles, representing the domain of inelastic scattering. In the current section, the theory of optical elastic scattering is presented.

Elastic light scattering can be mainly divided into three categories, which are preliminarily defined by a so-called particle size diameter Λ,

$$\Lambda = \frac{\pi D}{\lambda} \tag{2.69}$$

where D is the physical diameter of the particle in analysis and λ is the wavelength of the incident light. Depending on the value of Λ, the scattering is

- Rayleigh scattering, when $\Lambda \ll 1$
- Mie scattering, when $\Lambda \approx 1$
- Geometric scattering, when $\Lambda \gg 1$

The particles being analyzed here are of sub-micrometer size. Therefore, the Mie scattering should be considered here accordingly. From the Mie theory, an incident wave with a complex form can be expressed as

$$\boldsymbol{E}(z,t) = Ee^{i(\kappa z - \omega t)} \tag{2.70}$$

where κ is the wavenumber, which is defined as $\kappa = 2\pi/\lambda$ and ω is the angular frequency. Analogous to the incident plane in the last section of the interference theory, here, a scattering plane is introduced, defined by the surface normal and the wave vector of the scattered wave. $\boldsymbol{E}(z,t)$ can be decomposed into two components, which are orthogonal to each other,

$$\boldsymbol{E} = \boldsymbol{E}_{||} + \boldsymbol{E}_{\perp} \tag{2.71}$$

where $\boldsymbol{E}_{||}$ is parallel and $\boldsymbol{E}_{\perp}$ is perpendicular to the scattering plane. The scattered wave from an arbitrary particle can be written as

$$\begin{bmatrix} \boldsymbol{E}_{||s} \\ \boldsymbol{E}_{\perp s} \end{bmatrix} = \frac{e^{i(\kappa z - \omega t)}}{-i\kappa r} \begin{bmatrix} S_2 & S_3 \\ S_4 & S_1 \end{bmatrix} \begin{bmatrix} \boldsymbol{E}_{||i} \\ \boldsymbol{E}_{\perp i} \end{bmatrix} \tag{2.72}$$

where the footnote s denotes the scattered wave and the i denotes the incident wave. The matrix, consisting of the scalar factor S, defines the amplitude. Therefore, it is also called the amplitude scattering matrix. In the case of a homogeneous and spherical particle, S_3 and S_4 equal 0. Therefore, the amplitude scattering matrix becomes

$$\begin{bmatrix} S_2 & 0 \\ 0 & S_1 \end{bmatrix} \tag{2.73}$$

The Mie solutions give [13]

$$S_1 = \sum_{j=1}^{\infty} \frac{2j+1}{j(j+1)} (a_j \Phi_j + b_j \Psi_j) \tag{2.74}$$

$$S_2 = \sum_{j=1}^{\infty} \frac{2j+1}{j(j+1)} (a_j \Psi_j + b_j \Phi_j) \tag{2.75}$$

where a_j, and b_j are the expansion coefficients of electric and magnetic fields, respectively, which are also called the Mie coefficients.

$$a_j = \frac{N\psi_j(Nx)\psi_j^*(x) - \psi_j(x)\psi_j^*(Nx)}{N\psi_j(Nx)\xi_j^*(x) - \xi_j(x)\xi_j^*(Nx)} \tag{2.76}$$

$$b_j = \frac{\psi_j(Nx)\psi_j^*(x) - N\psi_j(x)\psi_j^*(Nx)}{\psi_j(Nx)\xi_j^*(x) - N\xi_j(x)\xi_j^*(Nx)} \tag{2.77}$$

where Ψ and ξ are Riccati-Bessel functions obtained from spherical Bessel and spherical Hankel functions, respectively. N is the complex refractive index. In equations 2.74 and 2.75, the angle-dependent functions Φ and Ψ are defined as

$$\Phi_j = (\frac{2j-1}{j-1} con\theta)\Phi_{j-1} - \frac{j}{j-1}\Phi_{j-2} \tag{2.78}$$

$$\Psi_j = (jcon\theta)\Phi_j - (j+1)\Phi_{j-1} \tag{2.79}$$

where θ is the angle of scattering, defined as the angle between the surface normal and the wave propagating direction. Hence, the scattering σ_{sca}, extinction σ_{ext}, and absorption σ_{abs} cross sections of the particle can be calculated according to the Mie coefficients [14],

$$\sigma_{sca} = \frac{\lambda^2}{2\pi} \sum_{j=1}^{\infty} (2j+1)(|a_j|^2 + |b_j|^2) \tag{2.80}$$

$$\sigma_{ext} = \frac{\lambda^2}{2\pi} \sum_{j=1}^{\infty} (2j+1)\mathrm{Re}(a_j + b_j) \tag{2.81}$$

$$\sigma_{abs} = \frac{\lambda^2}{2\pi} \sum_{j=1}^{\infty} (2j+1) \left(\mathrm{Re}(a_j + b_j) - (|a_j|^2 + |b_j|^2)\right) \tag{2.82}$$

When considering the electric components only, i.e., remove the b_j,

$$\sigma_{ext,E} = \sigma_{abs,E} + \sigma_{sca,E} \tag{2.83}$$

While the Mie theory is widely acknowledged for explaining the properties of the scattered wave behavior from a spherical particle, it is crucial to recognize that real particles often deviate from perfect spherical shapes. This holds true for the photonic structures fabricated in this dissertation. Additional modifications are necessary to enhance the applicability and accuracy of the Mie theory when dealing with irregularly shaped particles that lack symmetry. Different methods can be used to adapt the Mie theory to a non-spherical particle case, including T-matrix, discrete dipole approximation, finite element method, etc. Detailed descriptions of these methods are tedious and out of the scope of

this dissertation. Here, using the T-matrix to solve the scattering problem is presented as an example.

When the incident wave is expressed in vector spherical wave functions,

$$E_{inc} = \sum_{l=1}^{\infty} \sum_{l}^{j=-l} [a_{lj} \boldsymbol{M}_{lj}^{1}(\kappa \boldsymbol{r}) + b_{lj} \boldsymbol{N}_{lj}^{1}(\kappa \boldsymbol{r})] \tag{2.84}$$

Assuming $\boldsymbol{M}$ and $\boldsymbol{N}$ are two free vector solutions that are orthogonal to each other, the scattered field shows a similar form

$$E_{sca} = \sum_{l=1}^{\infty} \sum_{l}^{j=-l} [p_{lj} \boldsymbol{M}_{lj}^{3}(\kappa \boldsymbol{r}) + q_{lj} \boldsymbol{N}_{lj}^{3}(\kappa \boldsymbol{r})] \tag{2.85}$$

The T-matrix then can be used for relating the expansion coefficients of each field,

$$\begin{bmatrix} p \\ q \end{bmatrix} = \boldsymbol{T} \begin{bmatrix} a \\ b \end{bmatrix} \tag{2.86}$$

Subsequently, the T-matrix can be solved using the null-field method. With a known relation, the scattering behavior can be solved accordingly.

Fundamentals of optical scattering spectroscopy

Measuring the optical scattering requires three basic components, i.e., a radiation source, a detector, and the object of interest. However, the measurement setup in reality, can be very complicated when involving an optical lens system for collimating the light, secondary or more radiation sources, different detectors such as spectrometers, cameras, or other photodetectors, microscopes, scanning stages, etc. To remain clear and concise, the following section discusses a simple setup: a light beam incident on an object, and the scattered light is observed by a photodetector. It must be pointed out that the word "light" is often used for electromagnetic waves with wavelengths between 380 and 780 nm, i.e., the visible range. However, the wavelength range can be extended to ultraviolet and infrared radiation in optical scattering spectroscopy. Therefore, the term such as "Ultraviolet light" is commonly used, while a phrase like "radiation beam" may seem uncommon. Nevertheless, it is crucial to be aware that in the following discussion, the term "light" is expanded to include both ultraviolet and infrared radiation.

The scattering of the optical power can be measured either in a transmitting or reflecting way. In certain cases, the photodetector needs to be placed off the direct transmitted or reflected light path to avoid the strong overlap of the scattered light and the light out of interest. To qualitatively define the extent of scattering performance, optical haze is introduced,

$$\text{haze} = \frac{P_{\text{sca}}}{P_{\text{total}}} \tag{2.87}$$

where the P_{sca} is the optical power that is scattered and the P_{total} is the total optical power that is transmitted or reflected. Here, the total transmitted or reflected optical power

comprises the scattered and non-scattered shares of the optical power. For instance, the total reflected power consists of the spectacular and the scattered shares. The scattered optical power is usually distributed over the spatial angles. Therefore, the total scattered power can be obtained by integrating the scattered intensity over all solid angles:

$$P_{sca} = \iint I_{sca}(\theta, \phi) \sin\theta \, d\theta \, d\phi \tag{2.88}$$

where I_{scat} is the scattered intensity as a function of polar angle θ and azimuthal angle ϕ, respectively, and the integration is performed over the solid angles. In practice, an integrating sphere is used to measure the scattered optical power. The essential point in the measurement is making sure the non-scattered share is eliminated in the results.

2.4 Surface-enhanced Raman scattering

Fundamentals of Raman scattering

Raman scattering is a widely known inelastic light scattering phenomenon. It was theoretically discovered by A. Smekal as early as 1923 and experimentally confirmed in 1928 by C.V. Raman and K.S. Krishnan for liquids. C.V. Raman received the Nobel Prize in 1930 for discovering this effect, which is now named after him. Raman spectroscopy is a label-free and non-destructive optical technique that can be used to detect different species, such as molecules. In this section, the fundamentals of Raman scattering are presented.

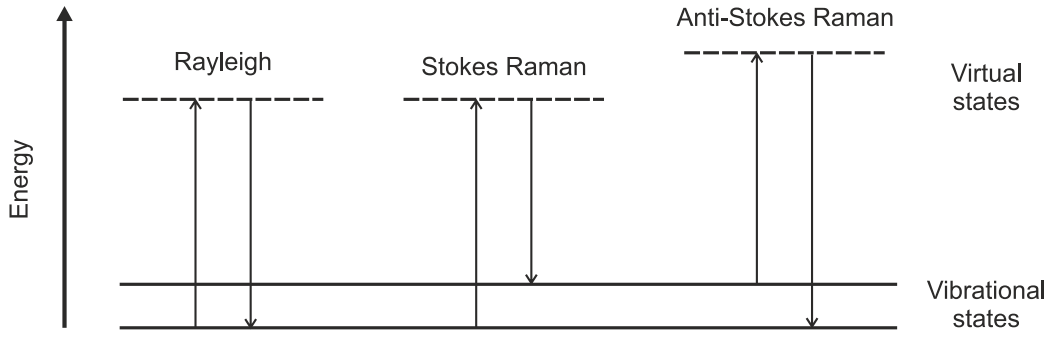

Figure 2.1: Schematic energy diagram. Rayleigh, Stokes Raman, and anti-Stokes Raman scattering.

When an incident photon interacts with a molecule, the electron is excited to a virtual state, which is highly unstable. By releasing itself to the ground state, another photon is emitted. The mechanism can be found in the schematic energy diagram in Figure 2.1. The incident photon can be either elastically or inelastically scattered. The incident photon is predominantly scattered elastically, which is known as Rayleigh scattering. In this case, the energy change of the incident and the scattered photon is zero. Raman scattering is an inelastic process. This denotes that the energy of the incident and scattered photons shows a difference. If the scattered photon has a lower energy, it is called Stokes Raman scattering, while in the case where the scattered photon has a higher energy, it is called

anti-Stokes Raman scattering. The result of the inelastic scattering is that a part of the energy is transferred to the molecule and ends in the form of heat. The energy can be described by Planck's energy–frequency relation in the angular frequency form,

$$\hbar\omega_{\text{Raman-scat}} = \hbar\omega_i \pm \hbar\Delta\omega \tag{2.89}$$

Stokes and anti-Stokes lines are symmetrically positioned with respect to the Rayleigh line. By considering the Boltzmann population distribution, one can derive the correlation between the intensities of Stokes and anti-Stokes lines [15]:

$$\frac{I_s}{I_{as}} = \exp\left(\frac{E}{k_B T}\right) \tag{2.90}$$

where I_s and I_{as} are the light intensity of the Stokes and anti-Stokes Raman signal, respectively, k_B is the Boltzmann's constant, T is the thermodynamic temperature, and $E = \hbar\Delta\omega$ is the vibrational energy.

The (spontaneously) scattered Raman signal is fairly weak, typically in the order of one of millions. It needs to be noted that Raman scattering can be raised either from the rotation or from the vibration of the molecule. However, the energy difference between rotational levels is much smaller than the vibrational levels, which makes the detection of rotational Raman scattering much more difficult since it is very close to the Rayleigh scattering lines. Hence, most reported work is based on vibrational Raman scattering.

Fundamentals of Raman spectroscopy

Raman spectroscopy is a complementary method to infrared absorption spectroscopy, where the vibrational modes lead to a change in the dipole moment. The Raman scattering, on the other hand, depends on a change in the polarizability of a molecule. Raman spectroscopy has been developed over the last decades to qualitatively and quantitatively analyze the chemicals. The methodology involves two primary domains, i.e., linear and nonlinear Raman spectroscopy. The nonlinear Raman spectroscopy uses a higher-order nonlinear process involving two or multi-incident photons interacting with the chemicals to enhance the Raman signal. Examples are coherent anti-Stokes Raman scattering (CARS) and stimulated Raman scattering (SRS).

In this dissertation, the work has been done based on linear Raman spectroscopy, which involves only one laser source incident on the chemicals. In the following, the content focuses on the linear case. The linear Raman spectroscopy process is popular and widely used. The major advantage is that the setup is much simpler than the one used in the nonlinear Raman spectroscopy. However, the obtained light intensity is relatively low, requiring a much longer integration time of the optical signal. Due to this, the scattered Raman photons are much easier to be covered by the background fluorescence signal, which is typically regarded as noise. Therefore, the method is limited in sensitivity for some circumstances.

Nevertheless, linear Raman spectroscopy is the most widely used method in detecting molecules and inspecting crystals. Applying the surface-enhanced Raman scattering (SERS) technique makes it possible to achieve a single-molecule detection level. Using

SERS to realize ultra-low concentration level detection is the main motivation for the (Raman scattering related) work that has been done in this dissertation. Detailed work contents are presented in Chapter 8. In this section, the fundamentals of linear Raman spectroscopy are introduced.

Here, the content needs to be pulled a bit back to the fundamentals of Raman scattering. The linear Raman signal from a molecule relies on the induced dipole $\boldsymbol{p}$ [16],

$$\boldsymbol{p}(\omega_R) = \zeta(\omega_R, \omega_0)\boldsymbol{E}_0(\omega_0) \tag{2.91}$$

where $\zeta(\omega_R, \omega_0)$ is the polarizability tensor. It reflects the ability of a molecule to acquire an electric dipole moment when subjected to an electric field. In other words, it tells the extent of the electron cloud of a molecule to be distorted from its intrinsic shape by an external electric field. The induced dipole $\boldsymbol{p}$ oscillates with the electric field and radiates electromagnetic waves into the far field. When the molecule is isolated in the free space, the total Raman power P_L radiates at a distance L can be expressed as [16]

$$P_L = \frac{1}{2}\omega_R Im[\boldsymbol{p}(\omega_R) \cdot \boldsymbol{E}_0(\omega_R)] \tag{2.92}$$

where $\boldsymbol{E}_0(\omega_R)$ is the local electric field raised by the isolated oscillating dipole in the molecule. The scattering cross-section σ_{scat} can be obtained as the ratio between the total radiated power and intensity of the exciting plane wave,

$$\sigma_{scat} = \frac{\kappa^4}{6\pi\varepsilon_0^2}|\boldsymbol{p}|^2 \tag{2.93}$$

where κ is the wavevector in the surrounding medium. The typical order of the Raman scattering cross-sections per solid angle is 10^{-30} cm^2 sr^{-1} molecule^{-1} [17].

Laser source for excitation

In linear Raman spectroscopy, lasers serve as indispensable photon sources owing to their exceptional monochromatic properties and robust beam fluxes. The process of selecting an optimal laser excitation source for proper Raman detection involves meticulous consideration. A pivotal initial criterion is the choice of laser excitation wavelength. Considering the fourth power dependence of scattering on the frequency, as seen in the next section, the strategic selection of a blue/green visible laser or a UV laser can yield a substantial amplification in scattering intensity. It is roughly a factor of 15 compared to the case using infrared lasers. However, the UV/blue/green lasers often bring in fluorescence issues. On top of this, UV excitation presents an elevated risk of sample degradation. Typically, blue or green lasers prove to be effective as excitation sources for inorganic materials and resonance Raman experiments. Red or near-infrared lasers in the range of 660–1000 nm are particularly suitable for suppressing fluorescence. UV lasers are well-suited for resonance Raman studies involving biomolecules like proteins, DNA, and RNA. Other laser sources, for instance, pulsed lasers, are applied in the investigation of short-lived species. In confocal Raman microscopy, the diameter of the laser spot is defined as 1.22 λ/NA, where λ is the laser wavelength and NA is the numerical aperture of the objective in the microscope.

Fundamentals of surface-enhanced Raman spectroscopy

Since the cross-section of spontaneous Raman scattering is small, the generated signal level is low. To increase the signal, localized surface plasmon resonance (LSPR) needs to be introduced. By coupling the LSPR and the Raman scattering, the Raman signal can be dramatically enhanced. Surface-enhanced Raman spectroscopy utilizes the LSPR to increase the sensitivity of the measurement.

The typical material used in LSPR is metal, such as silver and gold. In many cases, it is in the form of nanostructures, such as nanospheres, nanopillars, nanostars, etc. The complex dielectric constant of a nanosphere with a radius of r can be $\varepsilon(\nu) = \varepsilon'(\nu) + i\varepsilon''(\nu)$, where ν is the frequency. In SERS measurement, the incident laser power is not only scattered but also absorbed by the metallic nanostructures. Therefore, it makes more sense to discuss the overall effect, which is the extinction. From the Mie theory, it is known the optical extinction cross-section σ_{ext} for a spherical metallic nanoparticle is [18]

$$\sigma_{ext} = \frac{24\pi^2 r^3 \varepsilon_0^{3/2} N_e}{\lambda ln(10)} \frac{\varepsilon''(\lambda)}{(\varepsilon'(\lambda) + 2\varepsilon_m)^2 + \varepsilon''(\lambda)^2} \tag{2.94}$$

where r is the radius of the spherical nanoparticle and N_e is the electron density. It can be easily found that the plasmon resonance of metallic nanosphere requires the condition of $\varepsilon'(\nu) = -2\varepsilon_m$. A molecule situated at a distance of d from a sphere is subjected to an electromagnetic field. The superposition of this incident field $\boldsymbol{E_0}$ and the local field originating from a dipole in the nanosphere E_{LSPR} contributes to an enhanced electric field in the vicinity of the metal sphere. The respective amplitude enhancement factor $g_{LSPR}(\nu)$ in a surrounding medium with a dielectric constant of ε_m can be written as

$$g_{\mathrm{LSPR}}(\nu) = \frac{\boldsymbol{E}_{\mathrm{LSPR}}}{\boldsymbol{E}_0} \approx \frac{\varepsilon(\nu) - \varepsilon_m}{\varepsilon(\nu) + 2\varepsilon_m} \left(\frac{r}{r+d}\right)^3 \tag{2.95}$$

Thus, the power enhancement factor is $g_{LSPR}(\nu)^2$. The total enhancement factor of SERS results from a superposition of LSPR and Raman scattering. The Raman scattering will be enhanced if it is in resonance with the LSPR. Therefore, the total power enhancement factor (EF) can be written as [19]

$$\begin{aligned} EF &= |g_{\mathrm{LSPR}}(\nu)|^2 |g_{\mathrm{Raman}}(\nu)|^2 \\ &= \frac{|\boldsymbol{E}_{\mathrm{LSPR}}(\omega_0)|^2}{|\boldsymbol{E}_0(\omega_0)|^2} \cdot \frac{|\boldsymbol{E}_{\mathrm{LSPR}}(\omega_{\mathrm{Raman}})|^2}{|\boldsymbol{E}_0(\omega_0)|^2} \\ &= \frac{|\boldsymbol{E}_{\mathrm{LSPR}}(\omega_0)|^2 \cdot |\boldsymbol{E}_{\mathrm{LSPR}}(\omega_{\mathrm{Raman}})|^2}{|\boldsymbol{E}_0|^4} \end{aligned} \tag{2.96}$$

Above is the theoretical calculation of the SERS EF. It describes the EF as a result of the enhancement of both the incident and Raman scattering field. In practice, it is estimated from measured results. Reported SERS EFs are in the range of 10^3 to 10^{10} [9]. The quantitative analysis of the EF typically consists of the results from two sets of measurements. The first is called the reference measurement, where the sample needs to be "structure-free". That means it measures the Raman signal using the same material but without any

surface structures. The common strategy is to coat a smooth metallic layer on a glass substrate. In the reference measurement, the obtained Raman signal is called I_{ref}, where it is generated from molecules with a number of N_{ref}. The number of molecules is usually determined by the surface area or volume in the irradiance of the laser beam and the molecule density. Therefore, in order to have a proper EF, appropriate focusing of the laser beam in the measurement is crucial. Subsequently, measurement of the SERS signal with a SERS substrate needs to be performed. Analogous to the reference measurement, the SERS signal I_{SERS} is obtained from the molecules with a number of N_{SERS}, which are under the excitation of the laser on the SERS substrate. Eventually, the EF of SERS can be estimated as

$$EF = \frac{I_{\mathrm{SERS}}/N_{\mathrm{SERS}}}{I_{\mathrm{ref}}/N_{\mathrm{ref}}} \tag{2.97}$$

It can be regarded as a ratio of the Raman signal generated per molecule with and without surface enhancement.

3 State of the art

This chapter provides an overview of the latest advancements in optical interference filters, smart windows, and Raman sensing. The first section focuses on multilayer structures that are fabricated by solution processing. The second section discusses different smart windows and the corresponding mechanisms for controlling the light properties of the devices. The third section presents the ongoing research, developing trends, and technical improvements and achievements in Raman spectroscopy.

3.1 Optical interference filters by solution processing

Overview of techniques

Optical interference filters fabricated by solution processing have gone through significant advancements over the last decades [20]. It has been an area of active research, particularly for applications in display technologies, photovoltaics, and optical sensing applications. The major fabrication methods include spin coating and doctor blading [21]. Besides that, inkjet printing is also used for depositing functional layers [22, 23].

	Spin coating	**Doctor blading**	**Inkjet printing**
Fast prototyping	✓	✓	✓
Device cost	✓	✓	–
Scalability	✗	✓	✓
Flexible substrates	✓	✓	✓
Substrate size	✗	✓	✓
Coating rate	✓	✓	✓
Patterning	✗	✗	✓
Thickness upper-limit	✗	✓	✓
Material utilization rate	✗	✓	✓
Unit coating cost	✗	✓	✓

(✗ poor, ✓good, – intermediate)

Table 3.1: Comparison of solution processing techniques for optical filters.

Solution processing in ambient conditions offers many advantages over traditional vacuum deposition techniques, including fast prototyping, low cost, scalability, and compatibility with flexible substrates. The individual method is evaluated in Table 3.1 for comparison. In general, spin coating and doctor blading are regarded as candidates for fabricating optical interference filters. However, each method has its pros and cons. Moreover, due

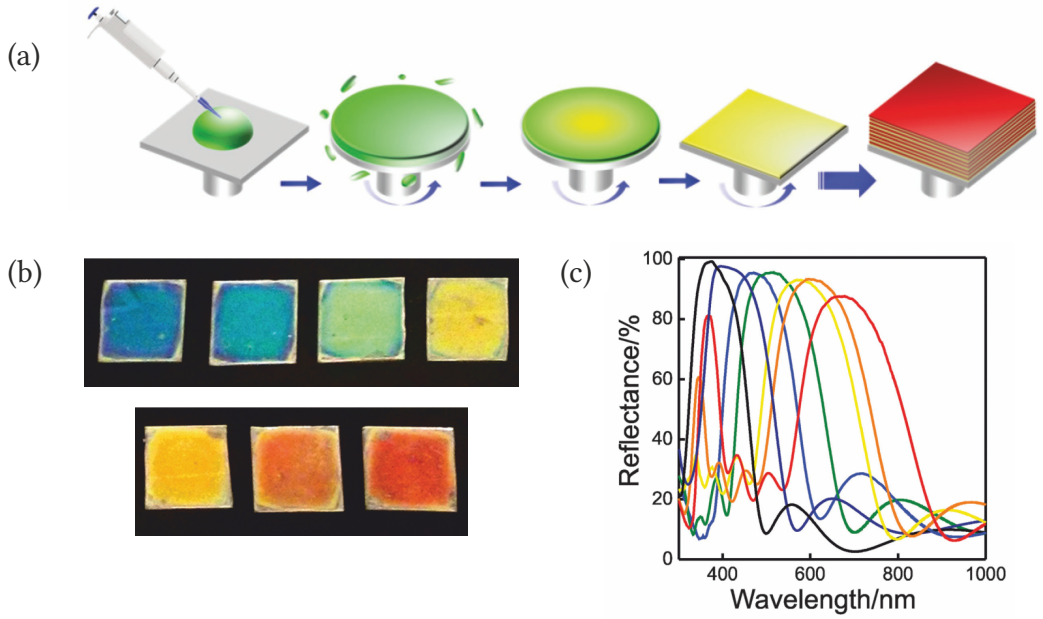

Figure 3.1: Fabrication of Bragg mirrors by spin coating. (a) Schematic of the spin-coating process for Bragg mirror fabrication. (b) Bragg mirrors exhibit different optical responses. (c) Reflection spectra of various Bragg mirrors. Adapted from Ref [20] and Ref [24] with permission from John Wiley & Sons and the Royal Society of Chemistry.

to the different drying mechanisms, the quality of the final thin film can be different. In Table 3.1, a handful of properties of each technique are listed. These are the characteristics of fast prototyping, device cost, scalability, suitability for flexible substrates, coating rate, patterning ability, thickness upper limit, material utilization rate, and unit coating cost. These factors are considered based on both the research and industry aspects.

In the following sections, a comprehensive analysis of the advantages and limitations of each fabricating method is provided. It aims to highlight the strengths and weaknesses of each technique, allowing for a better understanding of their practical applications and potential for improvement.

Spin coating

Spin coating is a popular method of fabricating thin films. It is widely used in research labs and microchip factories. The most obvious advantage of spin coating is the fast prototyping and low device cost. Figure 3.1 (a) shows the basic steps of fabricating the Bragg mirror by spin coating. Through alternate layer-by-layer deposition, a multilayer stack can be produced [20]. The center wavelength, stopband, and reflectance can be tailored by the constituent materials and layer thickness.

Researchers have shown proper control of the optical responses in the fabricated Bragg mirrors [25]. The demonstrated peak wavelengths are mainly distributed in the visible light range. However, due to the nature of the spin coating, the size of the substrate is highly limited [26]. In most of the laboratories, the substrate size is several to tens of

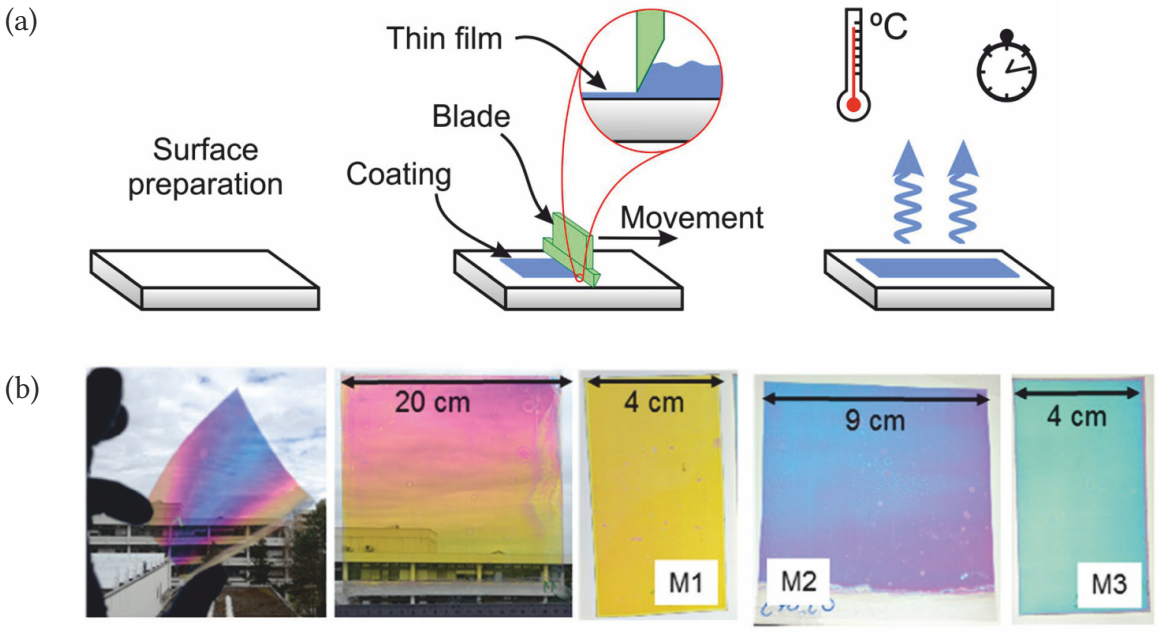

Figure 3.2: Fabrication of Bragg mirrors by doctor blading. (a) Schematic of the doctor blading process for Bragg mirror fabrication. (b) Bragg mirrors exhibit different optical responses. Adapted from Ref [28] and Ref [29] with permission from Springer Nature and John Wiley & Sons.

centimeters in diameter. It is challenging to achieve precise and consistent film thickness across large substrates by spin coating. In addition, the thin film formed by spin coating also suffers from edge effects and comet defects [24]. This can be found in Figure 3.1 (b), which shows the fabricated Bragg mirrors are not satisfactory regarding uniformity and defects. The high material wastage is also a severe problem in spin coating. Therefore, the unit coating cost is high compared to the other technology due to the much higher material usage rate. Despite having several weaknesses, spin coating remains the most viable solution for rapid prototyping and material testing [27].

Doctor blading

Doctor blading is a thin-film deposition technique widely used in applications that require larger size production compared to spin coating [30]. The basic process of fabricating a thin film using doctor blading is shown in Figure 3.2 (a). On either a glass or a foil substrate, a blade tool moves in a direction with a controlled speed. There is a space between the bottom edge of the blade tool and the substrate. Therefore, the coating material will be left behind the blade head, forming a uniform film. Post-treatment, such as annealing, is usually necessary for acquiring a solid thin film [28].

Doctor blading offers several advantages, including straightforward operation, precise thickness control, high scalability, efficient material utilization, and cost-effectiveness in terms of device cost. It is well-suited for the case where bulk production is demanded. Figure 3.2 (b) shows the fabricated Bragg mirror on flexible foils with different sizes. De-

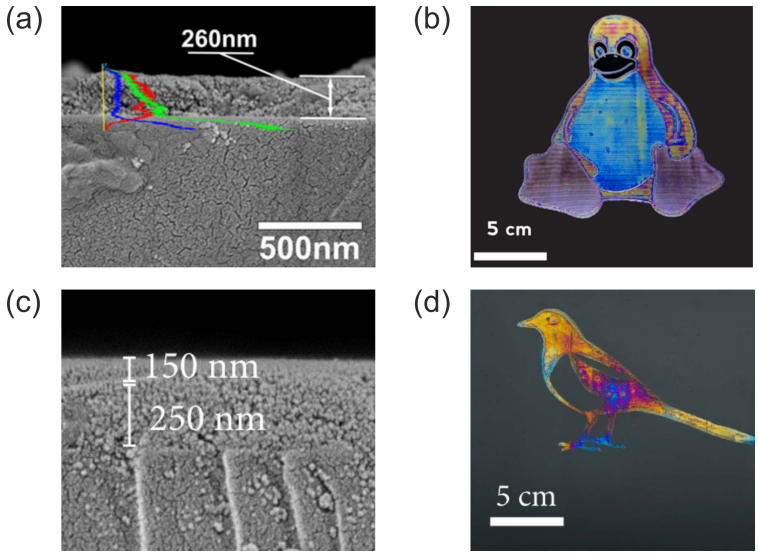

Figure 3.3: Interference color by inkjet printing. (a) SEM cross-section image of one deposited layer and (b) the corresponding color image. (c) SEM cross-section image of two deposited layers and (d) the corresponding color image. Adapted from Ref [33, 34] with permission from American Chemical Society and Springer Nature.

spite its many benefits, doctor blading may not be suitable for all thin-film deposition, especially those involving patterning requirements. The process may also suffer from non-uniformities and edge effects in the coated films, particularly near the blade edges, which can impact the overall film quality [31]. Similar to the Bragg mirrors fabricated by spin coating, challenges such as uniformity and defects are imposed in practical production. Furthermore, achieving uniform film thickness in doctor blading heavily relies on substrate flatness. As a result, more careful substrate preparation is necessary to ensure consistent and high-quality film deposition. Generally, doctor blading remains a powerful and widely used technique, but careful consideration of its advantages and limitations is crucial for successful thin-film fabrication [32].

Inkjet printing

Inkjet printing stands out as a versatile and powerful thin-film deposition method, ideally suited for applications that demand patterning, high spectral resolution, and large-scale fabrication [35, 36]. As mentioned before, there has been no work reporting inkjet-printed optical interference filters so far. The demonstrated work on interference color is from Yakovlev et al. [33, 34]. However, as shown in 3.3, the results are images based on structural color with one or two stacked layers rather than optical filters. Furthermore, the homogeneity of the deposited thin film is insufficient for optical filter purposes. For optical filters, the deviation of each layer thickness should be within 3% [37]. Moreover, high reproducibility and structures with a high stacking number have not been reported. To address the current challenges, processes and ink formulations need to be developed

rationally. Nevertheless, inkjet printing processes have big potential to become a good candidate for fabricating optical interference filters.

Overview of optical filter types fabricated by different techniques

In this section, the results of fabricated optical interference filters by different techniques are presented. The compared fabricating methods include spin coating and doctor blading. It is not intended to cover all the reported work over the last two deceased, but some representative ones to show the state of the art by the end of the year 2020.

Table 3.2 showcases the optical filters fabricated using spin coating and doctor blading. Numerous research groups have successfully demonstrated solution-processed Bragg mirrors using both spin coating and doctor blading, highlighting their simplicity and effectiveness in producing filters with various optical responses. However, it is essential to acknowledge that, as of now, only Bragg mirrors have been reported using these two techniques.

Technique	Filter type	Author	Year
Spin coating[a]	Bragg mirror	Yepuri et al. [27]	2020
		Ma et al. [38]	2019
		Kleine et al. [39]	2018
		Anaya et al. [24]	2016
		Brudieu et al. [26]	2014
		Goldenberg et al. [25]	2013
		Smirnov et al. [40]	2013
		Colodrero et al. [41]	2012
		Calvo et al. [42]	2010
		Sanchez-Sobrado et al. [43]	2010
		Hidalgo et al. [44]	2009
		Kobler et al. [45]	2009
		Puzzo et al. [46]	2009
		Kimura et al. [47]	1979
Doctor blading[a]	Bragg mirror	Bronnbauer et al. [29]	2018
		Gao et al. [32]	2018
		Ramírez Quiroz et al. [31]	2016
		Bronnbauer et al. [30]	2015

[a] (No longpass, shortpass, or bandpass filters have been reported)

Table 3.2: Fabricated optical interference filters by different techniques.

In real-world applications, there is substantial demand for longpass, shortpass, and bandpass filters. Hence, it becomes essential to explore the fabrication of other types of optical filters besides Bragg mirrors. The challenge lies in achieving a highly repeatable and well-controlled depositing process, particularly for elaborate filters such as bandpass filters. Unfortunately, both spin coating and doctor blading encounter limitations in this

aspect, as a highly precise and repeatable printing process for such filter types has not been fully developed and demonstrated using these methods. In contrast, the versatility and ability of inkjet printing make it a potential competitor to meet the demands of various filter types, making it a viable and powerful option for the future fabrication of optical filters.

3.2 Dynamic light scattering modulation in smart windows

It is attractive to control the optical behavior of the optical components dynamically. With the advance of modern science, various types of smart materials and smart structures have been developed. These materials or structures respond to external modulations applied, for instance, heat, voltage, mechanical force, magnetic field, etc. As a result, the optical property is modulated accordingly.

In the past two decades, energy research has gained significant attention, emerging as a prominent area of focus. There is a growing commitment to achieving effective energy management in buildings and facilities, with considerable efforts being dedicated to this endeavor. A smart window is a widely-known optical component that can dynamically modulate the optical property on demand. Some technologies have already been converted into commercial products. With advancements in material and engineering research, novel smart windows have been demonstrated, inspiring enthusiasts for further development. In many cases, the change in the optical behavior in a smart window includes transmission, absorption, reflection, and scattering. Here, a schematic illustration of the light modulation in smart windows is shown in Figure 3.4. Depending on the mechanism of control approaches, the categories of smart windows can be sorted into thermochromic, electrochromic, photochromic, magnetically responsive, mechanoresponsive, and hybrid-technology-based ones.

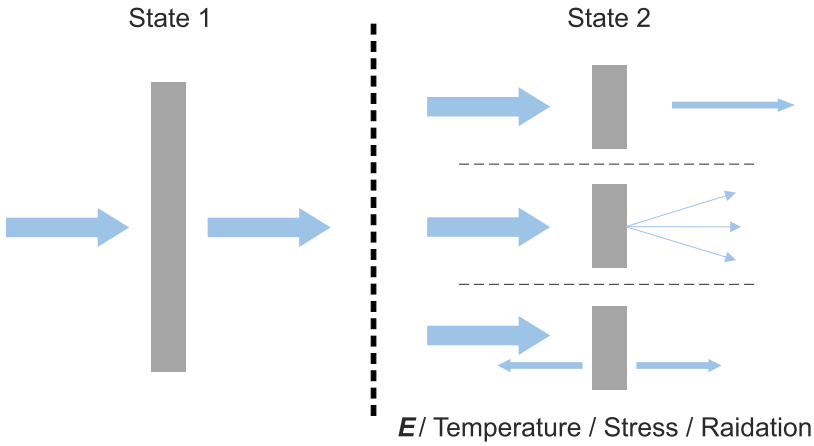

Figure 3.4: Schematic illustration of different light modulations in smart windows. The modulation switches the optical response of the smart window from state one to state two. The typical method involves employing an electric field (***E***), temperature variations, mechanical stress, or radiation.

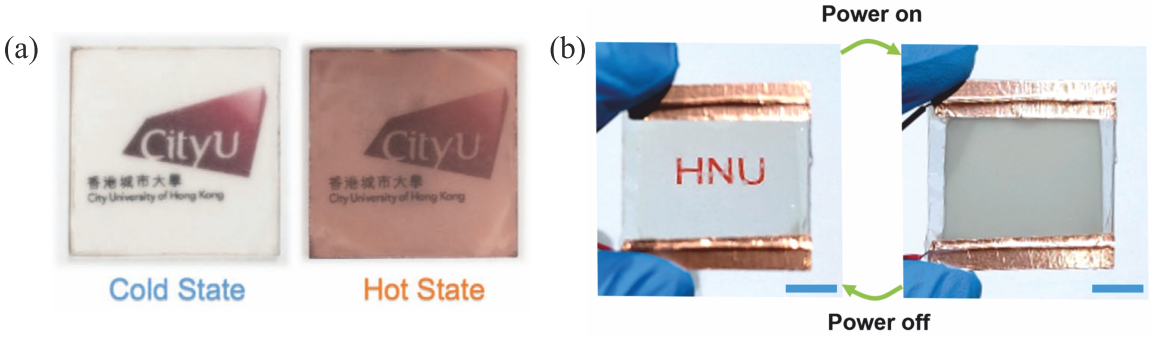

Figure 3.5: Optical transmission modulation in thermochromic and electrochromic smart windows. (a) Thermochromic smart windows in cold and hot states [60]. (b) Electrochromic smart window in power on and off states [61]. Adapted with permission from John Wiley & Sons and American Chemical Society.

Thermochromic smart windows

The common design of a thermochromic smart window is the integration of the thermoresponsive material into the device. Vanadium dioxide (VO_2) is regarded as one of the most promising materials for thermochromic smart windows[48]. The material shows a phase change at around 68°C, resulting in a transmission change from the visible to the infrared wavelength range. An image showing the process of coloration of a fabricated window due to the increased temperature can be seen in Figure 3.5. Some researchers have put efforts into doping the VO_2-based thin films [49, 50] or using nanoparticles [51] to reduce the phase transition temperature. Hybrid compositions, such as single-walled carbon nanotubes with VO_2, were developed for a free-standing ultra-thin optical window [52]. Researchers have also introduced a thermochromic layer into the photovoltaics to regulate the heat and increase the solar cell efficiency [53]. Besides the VO_2, other thermoresponsive materials were developed for thermochromic smart windows. Xie et al. demonstrated a polymer-based window for broadband light modulation[54]. Wei et al. showed a thermally activated smart window based on silver nanorods and hydrogel [55]. Liu et al. showed the potential to use an organic hybrid perovskite material in thermochromic smart windows. Using $W_xV_yO_2$-doped polyvinylpyrrolidone, Liu et al. fabricated a flexible smart window for modulating near-infrared penetration [56]. The radiative cooling function was also revealed in developed windows by Wang et al. [57, 58]. Li et al. reported using a refractive-index-matching strategy to modulate the optical behavior based on the thermoresponsive materials [59].

Electrochromic smart windows

Electrochromic (EC) smart windows usually comprise layered constructions, including an EC material, electrolyte, and ion storage layer enclosed between two transparent conductive electrodes. These windows can dynamically and reversibly adjust their optical characteristics by applying an electric potential, as shown in Figure 3.5(b). The common materials used for the electrodes are indium tin oxide (ITO) or fluorine-doped tin oxide

(FTO) because of their good transparency and electrical conductivity. The optoelectronic characteristics of the EC material are modulated by electrically induced cation insertion or extraction. The typical materials used for the EC, electrolyte, and ion storage layer are listed in Table 3.3 [7, 62].

Category	Materials
EC layer	• Inorganic metal oxides (e.g., WO_3, NiO, Nb_2O_5, TiO_2, V_2O_5, Ta_2O_5, MoO_3, etc.) • Prussian blue • Conductive polymers (e.g., poly-3,4-ethylenedioxythiophene (PEDOT), polypyrrole, polyaniline (PANI), etc.) • Viologens • Transition metal coordination complexes
Electrolyte layer	Li^+, Na^+, K^+, $Mg_2{}^+$, $Ca_2{}^+$, $Al_2{}^+$, $Zn_2{}^+$, H^+ -based ion drives
Ion storage layer	NiO, CeO_2, IrO_2

Table 3.3: Materials used for EC and ion storage layers.

When utilizing the EC smart window as an energy regulator, there is a high demand for independent and selective control of near-infrared and visible light. Wang et al. demonstrated a device that is capable of dual-band modulation as well as for multicolor appearance [63]. Using transition metal phosphates, Lei et al. also showed an EC window that can be modulated in a large dynamic range [64]. To address the slow switching rate in the dual-band EC device, Zhang et al. demonstrated a single-component amorphous and porous tungsten oxide (AP-WO3) cathode [65]. By using the MXene and WO_3 hybrid film, Nguyen et al. realized excellent electrical conductivity that leads to a significantly reduced charge transport barrier and fast coloration/bleaching response rate. A similar achievement was also achieved by Phan et al., who applied NiO nanorods with a large surface area to act as a counter electrode as well as an ion storage layer [66]. Instead of using ITO and FTO as the electrode materials, Yu et al. developed an electrode material comprised of a highly transparent conjugated polymer [67]. Zhang et al. applied Ag@Au core-shell nanowires as flexible transparent electrodes [68]. Patterning of the EC smart window was also investigated by selective photo-sintering of WO_3 Sol precursor [69]. Researchers also realized large area EC windows by applying inkjet printing [70] and wire-bar coating [71]. In addition, a plasmonic EC smart window was also presented by Rao et al. [72] and Zhang et al. [73]. Another big category in the EC windows is the polymer-network-liquid-crystal-based device. Although this type of device is already commercially available, it is still a good research topic toward self-powering, broadband, large scale, and building-integration [74–84].

Mechanoresponsive smart windows

Mechanoresponsive smart windows are sensitive to mechanical stress induced by a variety of stimuli, including mechanical force, electricity, and heat. These stimuli trigger

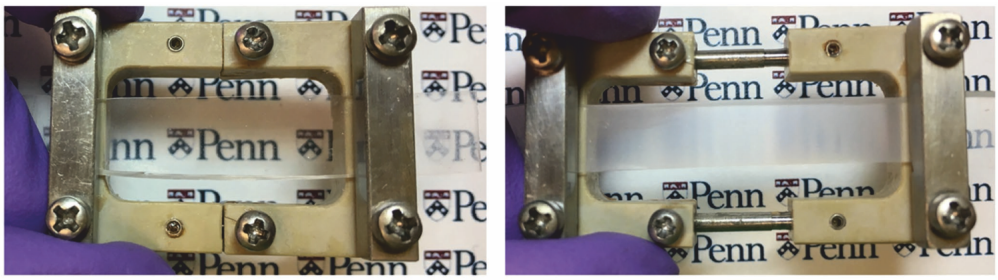

Figure 3.6: Machenoresponsive smart window. The light transmission modulation upon stretching. In the initial or released state, the smart window shows a good transmission. The information below the window can be read. When the window is stretched, the window becomes opaque [86]. Adapted with permission from John Wiley & Sons.

changes in surface morphology or alterations in the interface structure, consequently modulating optical transmittance through light scattering or diffraction, as shown in Figure 3.6. The fabrication of mechanoresponsive smart windows is achievable through diverse mechanisms. One approach involves achieving tunable optical properties using nano/micro-arrays, such as nanospheres [85–87], nanopillars [88], nanoholes [89], and nanogaps [90]. Another strategy involves manipulating light deflection by introducing micro wrinkles. Kim et al. demonstrated the dynamic modulation of optical properties in a smart window by introducing different wrinkling patterns, including stripes, labyrinths, and herringbones [8]. Jiang et al. presented a device with ordered, crack-free wrinkles using polydimethylsiloxane (PDMS) substrates [91]. Son et al. utilized a wrinkled surface as a luminescent solar concentrator by doping a fluorophore in the PDMS [92]. A third common structural approach for mechanoresponsive smart windows involves utilizing micro-cracks. Modulation of light scattering can be achieved by opening and closing these micro-cracks [93]. Mao et al. demonstrated a strain-responsive smart window for display purposes [94]. Mechanical stress can also be induced through an external electric field, change in temperature or humidity, and radiation. Consequently, designing the interface to combine two stimuli offers a powerful strategy to control the light behavior of the smart window precisely [95–98].

Smart windows based on other technologies

With the advancement of innovative materials, smart windows can be operated using alternative approaches, such as materials that respond to magnetic fields or are selectively responsive to light. For example, Gobel et al. developed a technique for creating microplates that were responsive to magnetic fields [99]. They achieved a rapid response rate on the order of hertz. By changing the orientation of the applied magnetic field, the microplates were aligned to achieve the "on" and "off" states. Yang et al. demonstrated a hybrid surface comprising micropillars to control light transmission [100]. Li et al. also synthesized 1D nanochains, where a small applied magnetic field was needed to control the switching of states [101].

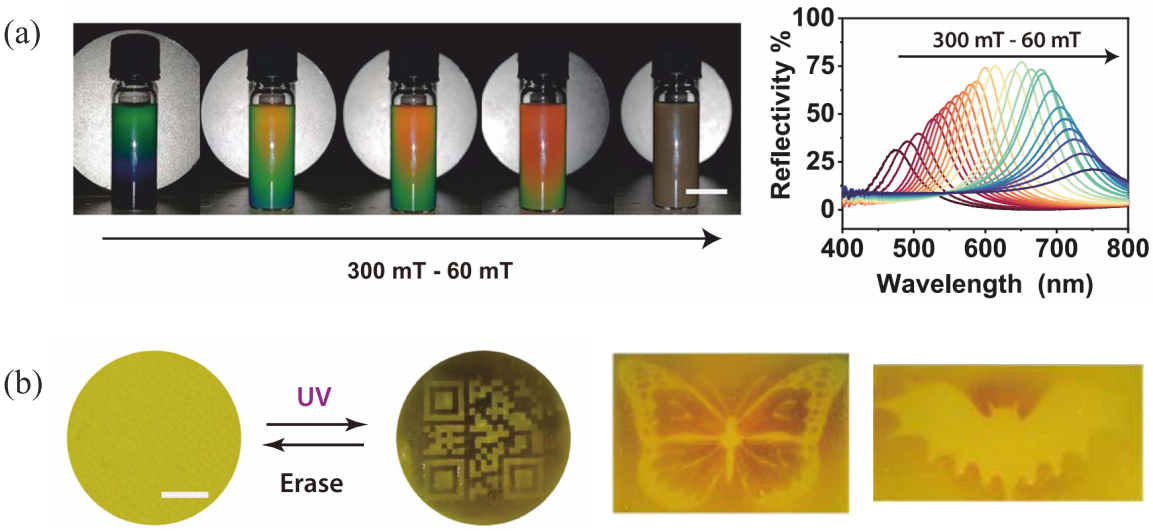

Figure 3.7: Magnetically responsive smart window. (a) The material undergoes spectral transmission variation with the varying magnetic flux density [103]. (b) Using masks, patterns can be generated by near-infrared light radiation. Adapted with permission from Springer Nature.

In addition to magnetically responsive smart windows, Li et al. showed a smart window triggered by near-infrared light based on dynamically reversible wrinkle patterns [102]. Wang et al. developed a hybrid smart material responsive to either light or a magnetic field [103]. The material developed consisted of a co-assembled photoswitchable organogelator and superparamagnetic inorganic nanoparticles (Fe_3O_4@SiO_2) [103]. The material exhibited a reversible transition for light manipulation, independently controllable by both light and magnetic fields. The spectral transmission of this material varied when exposed to different magnetic flux densities, as shown in Figure 3.7 (a). By placing an appropriate mask between the near-infrared light source and the material, a specific pattern was generated. Furthermore, this pattern could be erased, and the process was reversible, as shown in Figure 3.7(b).

3.3 3D SERS platform for low concentration level detection

Research interest on SERS

Surface-enhanced Raman scattering (SERS) is a phenomenon amplifying Raman scattering signals when molecules come close to or are attached to structured metal surfaces or nanoparticles. Discovered in the 1970s, SERS can enhance the Raman signal drastically, allowing precise molecular identification and characterization at ultra-low concentration levels. It is applied extensively for applications in chemical and biological sensing, identifying pollutants, studying biomolecular structures, etc. SERS has revolutionized analytical techniques, propelling advancements in diverse fields through its sensitive and specific molecular detection capabilities.

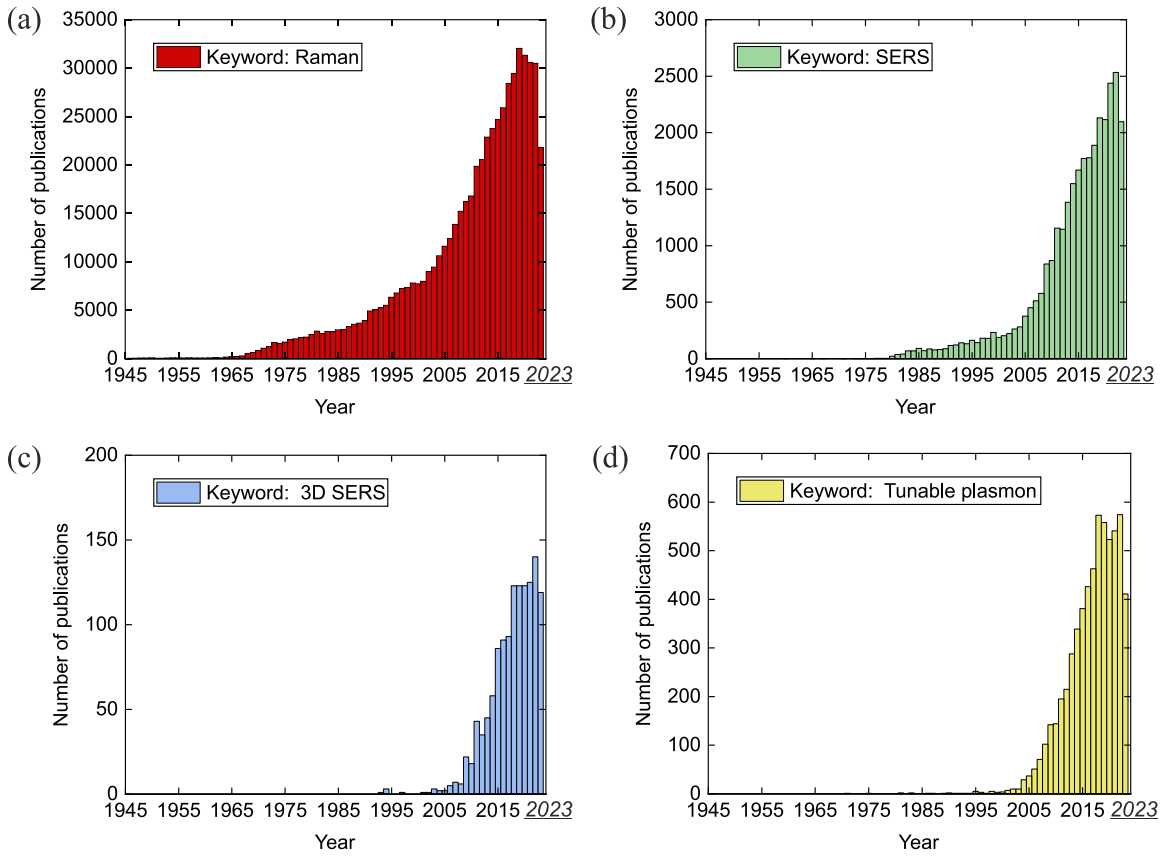

Figure 3.8: Number of publications on SERS-related research over the last 80 years. The results were obtained on the *Web of Science* platform. (a) Using "Raman" as the keyword, (b) Using "SERS" as the keyword, (c) Using "3D SERS" as the keyword, and (c) Using "tunable plasmon" as the keyword.

A substantial amount of research has been dedicated to exploring the physics mechanism and practical applications of SERS. Utilizing statistics sourced from *Web of Science*, a rapidly increasing interest in Raman research is indicated by the increasing publication amount, seen in Figure 3.8. The publications that have been counted include research papers and meeting abstracts. Four keywords, "Raman," "SERS", "3D SERS", and "tunable plasmon" have been employed in the searches. As could be seen, the earliest publications associated with these keywords emerged in the 1940s, 1940s, 1990s, and 1970s, respectively. A notable surge in the number of publications commenced around the year 2000. This exponential growth in the volume of publications related to Raman research signifies heightened activities and enthusiasm in the scientific and technological domains. Particularly, the research on 3D SERS has emerged as a rising star in recent years, as shown in Figure 3.8 (c). The reason is the increasing interest in detecting the material concentration with ultra-low or even single molecule levels. It should be noted that reviewing a broad range of topics on SERS can be lengthy and unnecessary. Based on the work that has been done, the state-of-the-art SERS research focuses on 3D platforms with tailored plasmon resonance for low molecule concentration detection.

3D photonic nanostructure for SERS

The core of detecting the molecules at a (ultra) low concentration is highly based on the design of the sensing platform or substrate. To achieve a highly sensitive SERS substrate, one straightforward strategy is to increase the density of the hot spot. Most of the fabricated SERS substrate is realized by tailoring the 2D surface structure, which results in an intrinsic limit of the sensitivity. Although using the 3D structure is a promising approach to improve the sensitivity, fabricating the SERS substrate with the required nanometer precision has been a long-term obstacle. Generally, in order to ensure practical utilization and reliable functions, a desired SERS platform should possess not only abundant hot spots for high sensitivity but also a uniform distribution of these hot spots to achieve consistent signal reproducibility. In the following, selected work in recent years is presented, mainly focusing on the realization of single-molecule level detection using a developed 3D SERS platform.

Fabrication of the 3D SERS platform is challenging considering the facts mentioned above. However, with the advancement of nanotechnology and material science, the fabrication of 3D SERS substrates can be achieved in versatile approaches. Various chemical synthesis and nanofabrication methods have been employed to fabricate the sophisticated 3D-nanostructured SERS substrates. These methods can be broadly categorized into two, i.e., top-down and bottom-up approaches. The top-down approaches, such as lithography and etching, involve subtractive processes that remove materials or structures. The bottom-up methods, which are primarily additive, encompass direct growth or self-assembly of effective materials such as nanoparticles.

Various surface structures can be demonstrated using the top-down method. This section primarily focuses on the top-down approach for creating a vertically aligned SERS substrate, which is a significant subbranch within 3D SERS platforms. This aligns with the scope of the work conducted in this dissertation. The top-down method typically requires a lithography process, wherein precise patterning of surface etching masks is vital. Several methods have been developed to introduce appropriate masks. For instance, nanosphere lithography utilizes ordered arrays created by spherical particles as masks, facilitating pattern transfer onto the photoresist [104]. Anodic aluminum oxide masks, consisting of nanoscale channels, serve a similar purpose [105]. Another option for masks is block copolymers, which can self-assemble in nanoscale domains [106–108]. After the mask is applied, the etching process can be performed. The integration of masks with etching treatments is critical in generating vertically aligned SERS-active nanostructures. On the other hand, maskless lithography, such as electron-beam and focused ion-beam lithography, offers direct-writing methods without etching [109]. The former achieves high-resolution patterns by exposing an electron-sensitive resist to focused electron beams, while the latter employs ions to etch materials into desired patterns.

Different materials can be used for fabricating the 3D SERS substrates. Silicon (Si) is the most widely utilized semiconductor material. Although it lacks strong plasmonic properties compared to metals, it can be used as a supporting framework for SERS applications. Other than that, various Si nanostructures hold promise for integrated optoelectronic devices. Vertically aligned Si arrays have gained traction as versatile SERS substrates due to their high surface-to-volume ratio, conducive to multiple hot spot creation. These ar-

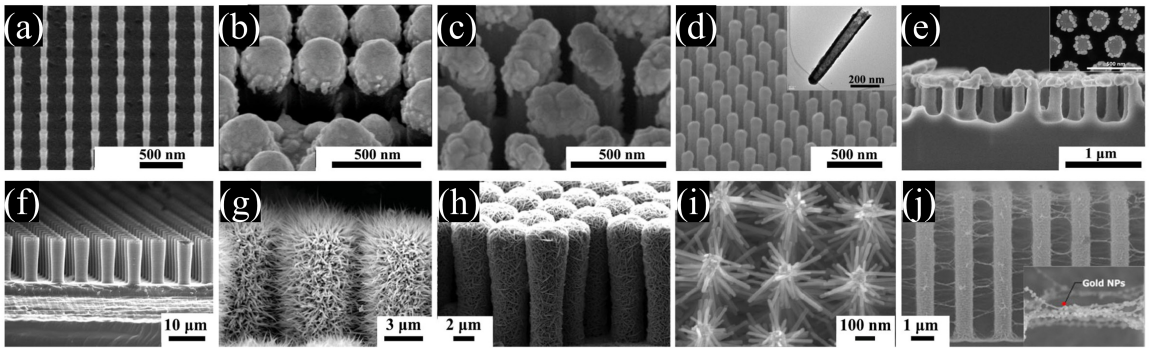

Figure 3.9: Fabricated 3D Silicon SERS substrates. Adapted from Ref [122] with permission from Elsevier B.V..

rays encompass Si nanopillars [110–115], nanohoodoos [116], nanocones [117], nanogrids [118], and etc. The controlled deposition of active nanoparticles onto these Si arrays, especially onto the sidewalls of low-density Si pillars, presents challenges. Strategies involving precise size and uniformity regulation of noble metal nanoparticles (NPs), such as Au NPs, on Si array surfaces have been reported. Hierarchical Si-based structure arrays with large interspaces allow for hierarchical architectures, expanding surface areas and complexity for high-density SERS-active metal NP loading. Plated Si nanoarrays with wide interpillar spacing have been shown to be suitable for uniform analyte dispersion. Research into nanogap behavior between adjacent plasmonic nanostructures is ongoing, aiming at enabling quantitative SERS at the single-molecule level [119–121].

As already discussed above, metallization is a crucial step to make SERS substrates active. Methods like electrochemical deposition [123, 124], electroless plating [125], electrophoretic deposition [126]. Other common methods can also be applied to metalize the platform surface. For instance, spin coating, dip coating, capillary force-assisted coating, physical vapor deposition, etc. The current research would need to develop an SERS substrate that is economical in both the fabrication of the 3D structures and surface activation.

Tunable plasmonic resonance for SERS

Before going deep into the discussion on the current status of tunable plasmonic resonance for SERS, it needs to be pointed out that the discussion on tunability here is confined to the cases that depend on the nanoparticle's intrinsic properties or coupled resonance. This means the discussion rules out scenarios like external electron injection into nanoparticles. The discussion in the following only focuses on the shape, size, material, and interdistance of the nanoparticles that lead to the shift of the resonance peaks.

In general, LSPR is the key to realizing tunability. Therefore, a lot of work has investigated the manipulation of the LSPR for different applications. For instance, the study on the propagating and tunable LSPR for biosensors [128], the synthesis of colloidal nanocrystals for tunable plasmonic [129], tuning the plasmonic for different colors [130], using mechano-approach to tune the plasmonic in colloidal assemblies [131], and explor-

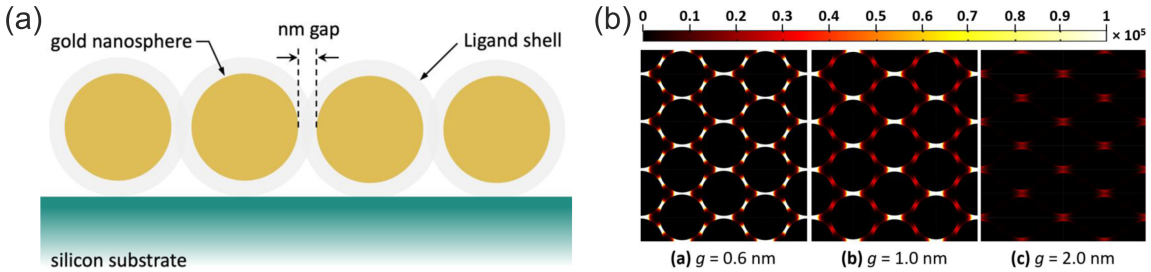

Figure 3.10: Tunable plasmonic for SERS. Adapted from Ref [127] with permission from American Chemical Society.

ing the tunable plasmonic in graphene for optoelectronics [132]. The work mentioned above shows remarkable results in manipulating the LSPR through different strategies.

The motivation of a tunable LSPR for SERS is to match the resonance peak with the incoming excitation light in order to reach a significantly enhanced Raman signal level. Alexander et al. showed that by controlling the distance of nanorod dimers, high sensitivity in the SERS detector could be realized [133]. A similar concept was demonstrated by Bauman et al., as can be seen in Figure 3.10 (a). By covering the gold nanoparticles with a ligand shell, the distance between particles was precisely controlled. The intensity of the localized electric field was significantly enhanced with a subnanometer interparticle distance, as shown in Figure 3.10 (b). Li et al. demonstrated an approach to tuning the interparticle distance using aerosol self-assembly strategy [134]. Besides the interplay of the particles, common approaches such as controlling the particle shape and size were demonstrated [135]. Besides various shapes such as cubes, spheres, prisms, and stars, Joint nanoparticles forming an aggregate can also provide a manipulatable LSPR [136].

The careful design and precise control of the LSPR can address the issue of the excitation laser wavelength practically being off the resonance peak. So far, the precise tailoring of LSPR responding to the excitation laser in a 3D SERS detector has been rarely demonstrated. In addition, a scalable and affordable fabrication method is yet to be developed. There is a high demand for the high enhancement factor provided by the SERS detector. It is challenging, yet highly appealing, to deliver all these demands with a developed SERS detector.

4 Inkjet printing

In this chapter, an introduction to inkjet printing and the related fluid dynamics of ink are provided. Firstly, the current state of inkjet printing, which has been employed in various research fields, is presented. Next, a detailed discussion and explanation of the mechanisms involved in the inkjet printing process is provided. Finally, a basic discussion of the physical parameters and interfacial mechanisms underlying inkjet printing is given in the fluid dynamics section.

4.1 Overview

In the view of broad fields

Inkjet printing is a versatile tool that has been applied in many modern research activities. Nowadays, it is used in fabricating numerous devices, such as electronics [137], biosensors [138], supercapacitors [139], thin-film transistors [140], flexible and wearable electronics [141], ceramic components [142], to name a few. In material science and its extending fields, inkjet printing is a novel method for producing unique components with various materials, for instance, optical materials [143], conductive materials [144], proteins [145], catalysis [146], polymers [147], etc. In the meantime, inkjet printing offers an alternative route for device design and fabrication in many different research areas. These applications contain energy storage [148], solar cells [149], pharmaceuticals [150], synthesis of functional metal oxides [151], carbon-nanotubes and its applications [152], etc. This wide usage of inkjet printing is attributed to the versatility, precision, and scalability of the technology. Inkjet printing continues to advance, with ongoing research focusing on improving printing resolution, developing novel inks and materials, enhancing printing speed, and expanding the range of printable materials and substrates.

In the view of optics and photonics

Significant advancements have been made in optical and photonic applications in recent years. When the focus turns to the application of optics and photonics, inkjet printing has played an increasingly critical role in recent decades. It is not only due to the rapid development of print head technologies but also the extensive research activities in material science that have significantly contributed to its growth. In recent years, numerous breakthroughs have been made in optics and photonics, with inkjet printing playing a significant role. For instance, inkjet printing is used to fabricate optical filters [153] and microlens arrays with a high fill factor [154]. Additionally, printing has been employed to create perovskite quantum dot patterns [155], stretchable optical waveguides [156], direct

patterning of nanocrystals [157], MXene micro-scale devices [158], distributed feedback (DFB) laser gain medium deposited by printing [159], phase-separated nanostructures [160], nanocavities by inkjet printing [161], photonic crystals for imaging [162], sensing [163], as well as anti-counterfeiting patterns [164]. These examples mentioned above are just a few of many in the last decade; some have even been presented very recently, indicating that inkjet printing is a hot research area. What can be foreseen is that inkjet printing will continue to be explored for various applications, including optical communications, display technologies, bioimaging, and nanophotonics. Researchers are constantly pushing the boundaries to improve printing resolution, develop new ink formulations, optimize printing processes, and explore novel materials for enhanced optical and photonic applications.

The main power that drives the inkjet printing technology to become a rising star in modern research and industrial applications comes from its unique properties. To show the details of these properties, the inkjet printing mechanisms are discussed in the next section, which gives a deeper understanding of how this technology becomes a powerful tool in many applications.

4.2 Mechanisms of inkjet printing

There are various technologies employed for ejecting ink droplets in inkjet printing, including thermal, piezoelectric, acoustic, and others. To avoid any potential confusion, it is important to note that the inkjet printing method utilized in this work is exclusively based on piezoelectric technology.

Basic steps in inkjet printing

Generally speaking, inkjet printing includes the steps shown in Figure 4.1. Before the inkjet printing process, the first step is the image or pattern design. Then, the images need to be converted into either binary or greyscale in order to meet the printing requirements. Subsequently, the printing parameters have to be appropriately set, including the size of printed patterns, printing waveform, printing resolution, etc. After the steps mentioned above, the printing task can be performed. Ink droplets are ejected from nozzles under predefined settings. The deposited inks are then dried to form a solidified layer in the following step. However, to increase the stability of the solidified layer, post-treatment, such as UV curing or sintering, is always applied. Depending on the desired features, a single deposition cycle may be insufficient, requiring repetition to achieve the desired specifications. For instance, printing a quarter-wave stack usually requires a certain number of printing cycles.

Drop-on-demand printing

In inkjet printing, the print head is a crucial component. It determines how the ink droplets are ejected and the quality of the material deposition. Two different working modes exist in different print heads. The first is called continuous inkjet printing, as

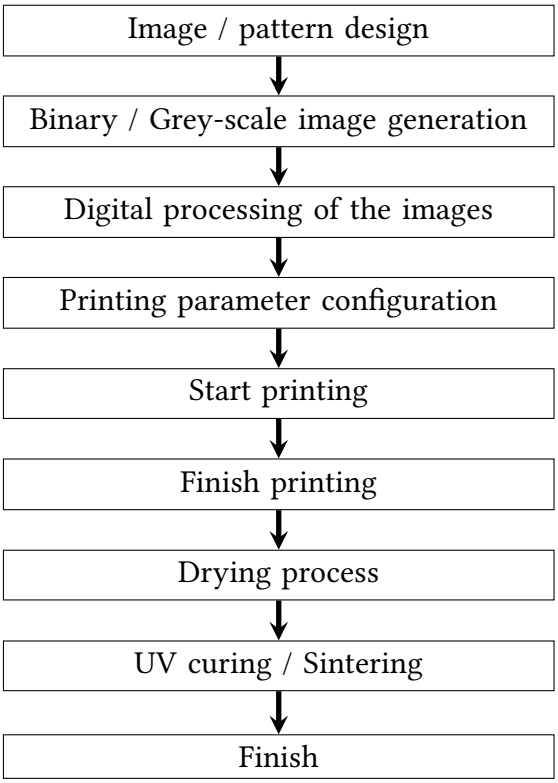

Figure 4.1: Inkjet printing process in a single cycle.

shown in Figure 4.2 (a). The ink flows continuously out of the nozzle, where the droplets are charged before leaving the nozzle. The droplets will pass through a deflector, which is charged and used to deflect the moving direction of the drops. Subsequently, the droplets are directed toward an ink collector when the droplet reflector is activated. Some print heads are designed in the opposite manner, where ink droplets are consistently collected and only deflected when printing is required. In both ways, the collected ink will be recycled. The droplet deflector acts as a switch in the continuous inkjet printing mode for ink deposition.

The second inkjet printing mode is known as the drop-on-demand (DOD) mode, which is widely used in modern printing. In this mode, ink droplets are precisely controlled and ejected individually based on actual demand. This active control of droplet ejection results in a compact design of the print head as well as the precise deposition of inks. Figure 4.2 (b) and (c) show a schematic diagram of two possible DOD modes. With these approaches, droplets are ejected by a pressure pulse created in an ink-filled cavity before the nozzle outlet. In different designs, the pressure pulse can be generated by two mechanisms. Figure 4.2 (b) shows the print head design with a thin-film heater in the cavity. A vapor bubble is formed in the cavity by rapidly heating the heater, which expels the ink droplets from the nozzle. This method is also called thermal inkjet. Another method to eject the ink droplets is mechanical actuation, which is commonly achieved by a piezoelectric transducer. The mechanical deformation leads to pressure change in the ink, resulting in

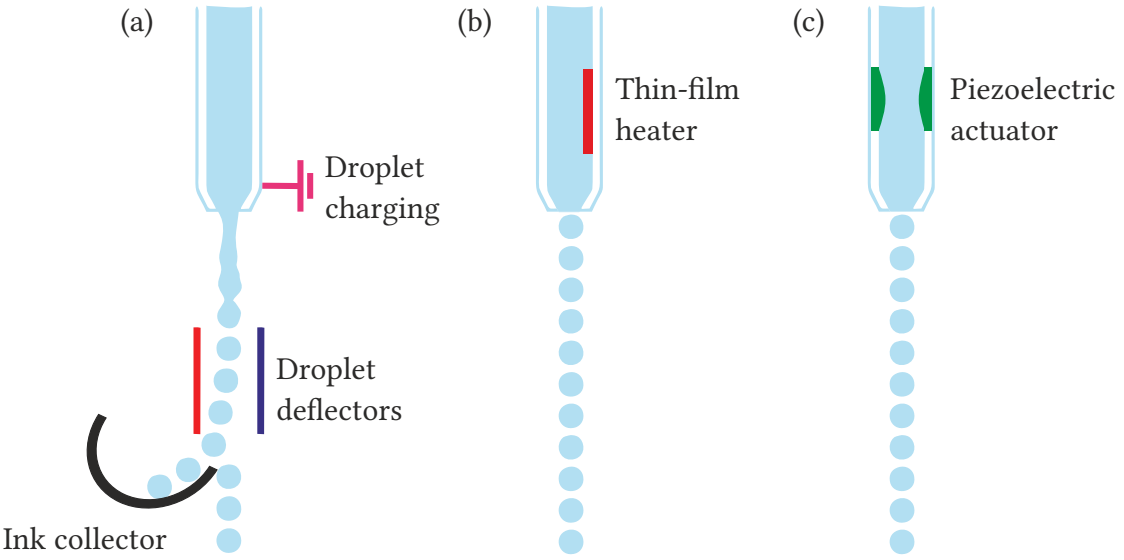

Figure 4.2: Schematic diagram of different inkjet printing modes. (a) Continuous mode. (b) Thermal and (c) Piezoelectric drop-on-demand mode.

droplet ejection. Therefore, it is called piezoelectric inkjet, which is shown in Figure 4.2 (c).

DOD printing brings a more efficient way to deposit ink on the substrate. Choosing between thermal and piezoelectric inkjet is crucial for different inks and applications. Although the thermal inkjet offers some advantages, such as a simple and compact design of the printing head, which makes the device cost-effective, it is also important to realize that ink compatibility is limited under such design due to a high temperature applied to the ink. Ink degradation and nozzle clogging can happen, which leads to frequent maintenance. Piezoelectric inkjet technology utilizes piezoelectric components that change shape when an electric voltage is applied. Without inducing high temperatures, piezoelectric inkjet provides wider ink compatibility, including UV-curable and temperature-sensitive inks. The energy consumption is lower compared to the thermal inkjet. Since the mechanical deformation of the actuator can be controlled precisely, superior control of droplet size can be realized. The common single droplet volume is one to several tens of picoliters. Indeed, the piezoelectric inkjet also has some drawbacks, including higher costs and a more complex manufacturing process. However, with significant developments in recent years, piezoelectric inkjet technology has found widespread use in both industry and research, primarily due to the increased freedom in selecting inks [165].

Related printing parameters

Printing waveform

In inkjet printing, the printing waveform refers to the specific electrical signal that is applied to the print head. In more detail, it consists of the electrical pulse and timing that are applied to control the piezoelectric actuator. In this way, the printing waveform

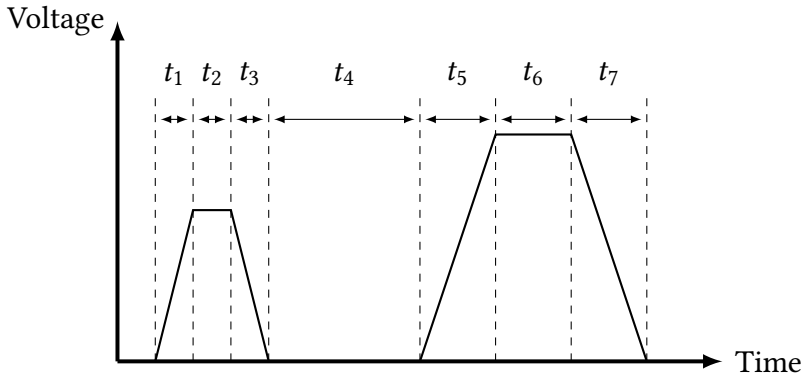

Figure 4.3: Schematic of a simplified waveform in inkjet printing.

effectively controls the ejection of ink droplets, including their shape and velocity as they ejected from the nozzles.

Figure 4.3 shows a simplified printing waveform in a unit period. In a well-controlled case, one droplet is ejected depending on this waveform. By repeating this waveform, individual droplets can be ejected on demand. In a unit time period, one or more pulses can exist to achieve a proper droplet. The pulse consists of a rise time (e.g., t_1 and t_5), a dwell time (e.g., t_2 and t_6), and a fall time (e.g., t_3 and t_7). When there is more than one pulse in a unit period, a slack time (e.g., t_4) is needed. It is also common to apply a negative voltage to facilitate droplet ejection. However, achieving this requires the use of a print head designed for such a purpose. The duration, amplitude, and shape of these pulses can be varied based on the requirement of droplet volume, velocity, and trajectory. With different individual ink formulations, types of print heads, or a combination of both, waveforms can vary significantly. Adjusting the waveform parameters enables the printer to optimize printing quality, addressing factors such as droplet-positioning accuracy, process repeatability, and printing reliability.

Printing resolution

The printing resolution, typically measured in dots per inch (dpi), is an important parameter in inkjet printing. It directly affects the quality of layer morphology, thickness, and even the ink rheology behavior on the substrate. The typical range of dpi in the reported work is from several tens up to ten thousand. Generally, the printing resolution is defined in two dimensions, i.e., x- and y-axis printing resolution. It usually needs to be mentioned that the dpi in different axes is different. During inkjet printing, dots, lines, and layers can be printed by adjusting the printing resolutions.

Printing speed

In an inkjet printer, the printing task is performed by coordinating the movement between the x- and y-axis. In principle, a higher printing speed helps to shorten the total printing time. However, a high printing speed sometimes induces unwanted airflow that impacts the droplet trajectory [166]. It is critical when printing precision optics because optical

filters require a high homogeneity of layers. The local defects caused by the improper printing speed deteriorate the optical quality.

Temperature of the print head

As previously discussed in the section on printing waveforms, the ejection of ink droplets from the nozzles is highly dependent on the control of the piezoelectric component in the print head. Furthermore, the temperature of the printing head, including the temperature of the ink-filled cavity and nozzle, significantly influences droplet formation and ejection. Ink properties such as viscosity are impacted by the change in temperature. Therefore, adjusting the ink properties through temperature modulation of the nozzle is a commonly employed strategy to achieve the desired droplet shape.

Temperature of the substrate

Substrates are typically positioned on the printing platform in an inkjet printer. Advanced inkjet printers often provide the option to regulate the temperature of the platform, allowing for active control of the temperature of the substrate. This capability enables further manipulation of the behavior of the ink deposited on the substrate. For example, adjustments to surface tension and viscosity can be made, enhancing the adhesion, spreading, and overall print quality.

4.3 Ink fluid dynamics in inkjet printing

On the one hand, print heads play an indispensable role in ejecting the ink droplets; on the other hand, the physics and fluid mechanics of the ink liquid determine the generation of the droplets at a decisive level. Moreover, the drying effect of a wet surface, such as the coffee-ring effect, is a continuous topic until today. The study of the behavior of ink droplets has remained vital in recent decades. Both simulating methods and empirical work have been conducted intensively in order to understand the mechanisms behind the subject. Yet, it still has not been fully understood. Therefore, it is important to discuss the fluid mechanics of inkjet printing to clarify the basics and present a clear view of the technical challenges addressed in this work.

Ink physical parameters

The behavior of the ink droplet formation and ejection is dominated by a handful of parameters. These include density, dynamic viscosity, and surface tension of the liquid. Other factors, such as temperature, humidity, and pressure, also influence the behavior of the ink droplets. However, in the discussion below, a laboratory condition is assumed where the ambient condition is under good control.

Density of the ink

Ink density ρ, in the unit of kg/m^3, similar to the density of a liquid, is defined as its mass per unit volume. The difference between ink and liquid is that the former can contain, for instance, different solutes or nanoparticles along with the solvents.

Viscosity of the ink

Ink viscosity η, in the unit of $Pa \cdot s$, represents the resistance of an ink liquid to the shear deformation or a flow [167]. As an essential parameter in fluid mechanics for inkjet printing, viscosity results from the attractive force between the molecule in the ink and the momentum exchange between the molecules and fluid layers adjacent. The viscosity of ink depends highly on the temperature, including the nozzle temperatures. For some print heads, it is possible to control the nozzle temperature actively. Therefore, it helps to stabilize the ink behavior during the printing process.

Surface tension of the ink

Surface tension γ, in the unit of N/m, is defined as the force per unit length along the surface of the liquid. It is similar to the surface energy in the case of a solid surface. Surface tension is raised from the cohesive force, which is the force that must be counteracted to increase the surface area [168]. Surface tension defines the force acting at the interface between the liquid and its surroundings. The unbalanced forces acting on the interface result in its contraction to a minimum surface area. For instance, a water drop in the air always tries to form a spherical shape. Close to the interface, a stronger attraction between molecules is induced compared to the molecules in the bulk, as seen in Figure 4.4. The sum of the cohesive force on any molecule in the bulk of the liquid is zero. However, the net force acting on the molecule at the interface is non-zero, and its direction is toward the bulk liquid. From the energy point of view, the liquid tends to minimize its surface area without the influence of external forces. As a result, a layer of surface molecules forms, resembling a stretched membrane. This membrane effect causes each portion of the liquid surface to exert tension on neighboring portions or objects in contact with it [167].

Surface tension is contributed by two components, i.e., polar and dispersive components. The polar component consists of diverse polar molecular interactions such as hydrogen bonding, dipole energy, and induction energy, while the dispersive component originates from London dispersion attractions. The total surface tension is the sum of these two components.

The surface tension of the ink influences both the droplet ejection process and the formation of droplets, directly impacting the droplet size. Additionally, surface tension plays a crucial role in determining the wettability of inks on the printing surface, significantly affecting the ink contact angle.

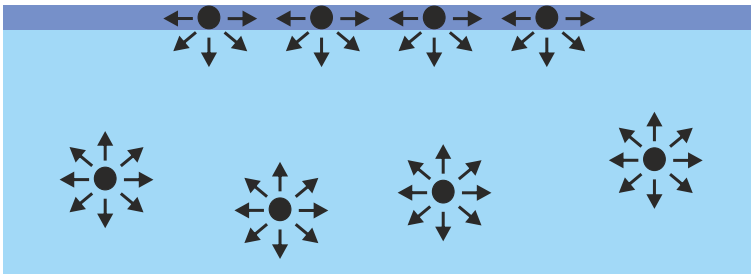

Figure 4.4: Illustration of surface tension. The light blue represents the bulk liquid. The dark blue represents the interface between the liquid and air.

Reynolds, Weber, and Ohnesorge number

Depending on the basic physical parameters mentioned above, three dimensionless numbers are defined, which are Reynolds (*Re*), Weber (*We*), and Ohnesorge (*Oh*) numbers:

$$Re = \frac{v\rho d_n}{\eta} \tag{4.1}$$

$$We = \frac{v^2\rho d_n}{\gamma} \tag{4.2}$$

$$Oh = \frac{\sqrt{We}}{Re} = \frac{\eta}{\sqrt{\gamma\rho d_n}} \tag{4.3}$$

where ρ, η, and γ are the density, viscosity, and surface tension of the fluid, respectively. v (unit: m/s) is the velocity of the droplet, and d_n (unit: m) is the characteristic length, which is the nozzle orifice size in this work. The Reynolds number *Re* shows the ratio of inertial and viscous forces, and the Weber number *We* represents the ratio between inertia and surface tension. Both *Re* and *We* contain the droplet velocity. In order to have an assessment criterion that stays independent from the velocity, the Ohnesorge number *Oh* is defined as in equation 4.3. *Oh* is only related to the physical properties of the liquid and the size of the nozzle. It is important to notice that these three dimensionless numbers are very often used to characterize the behavior of liquid drops, especially in the inkjet printing process. Considerable efforts have been dedicated to understanding these three numbers and using them for assessments of ink printability.

Young's equation

Young's equation describes the relationship between the contact angle θ, surface tension of the liquid γ_{lv}, interfacial tension γ_{sl} between liquid and solid, and the surface free energy γ_{sv} [169],

$$\gamma_{sv} = \gamma_{sl} + \gamma_{lv}\cos\theta \tag{4.4}$$

where, the footnote v denotes the air or gas phase. The equation is valid when the solid and the liquid are in thermodynamic equilibrium conditions. The schematic illustration

of the contact angle and the relations of three interfacial tensions are depicted in Figure 4.5.

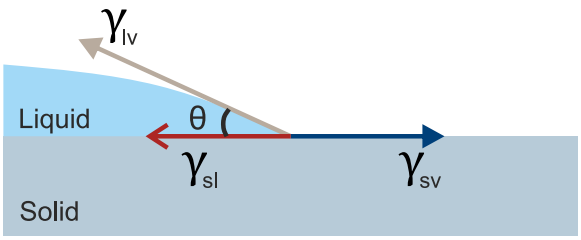

Figure 4.5: Contact angle and relation of interfacial tensions.

Ink printability window

Based on the three dimensionless numbers, *Re*, *We*, and *Oh*, a printability window can be depicted. It is a two-dimensional space diagram defined by four boundary conditions. In order to quantitatively define the boundaries, a fourth number $Z = 1/Oh$ is induced. Z is used to define the first and the second boundaries. If $Z \leq 1$, the ink is too viscous, while $Z \geq 10$ denotes the generation of satellite droplets instead of individual droplets during printing. For the region with $1 < Z < 10$, a stable dropping process is formed [142].

To eject the ink droplet, the liquid droplet has to have sufficient kinetic energy to overcome the air-fluid surface tension at the nozzle surface. This leads to a minimum velocity for droplet ejection [170]

$$v_{\min} = \left(\frac{4\gamma}{\rho d_n}\right) \tag{4.5}$$

When rewriting the equation 4.5 in terms of the *We*,

$$We = \frac{v_{\min}^2 \rho d_n}{\gamma} = 4 \tag{4.6}$$

Therefore, the minimum *We* for droplet ejection is 4 [171]. However, lower *We* is also mentioned in some works [172]. Nevertheless, to show a concept of a general case, the third boundary is set as $We = 4$ in Figure 4.6. This boundary denotes that the printing process with a *We* below cannot eject droplets since the liquid does not acquire enough energy to form a droplet.

The fourth boundary of the printability window is defined by the splashing effect when the droplets are deposited on a surface. When the splashing threshold is reached,

$$We^{1/2} Re^{1/4} = f(R), \tag{4.7}$$

where $f(R)$ is a function of surface roughness. For a flat and smooth surface, $f(R)$ is found to be around 50 [173]. Consequently, an ink printable window is defined by these four boundaries, shown in Figure 4.6. This is a reference region where the ink fluid properties can be optimized for DOD inkjet printing.

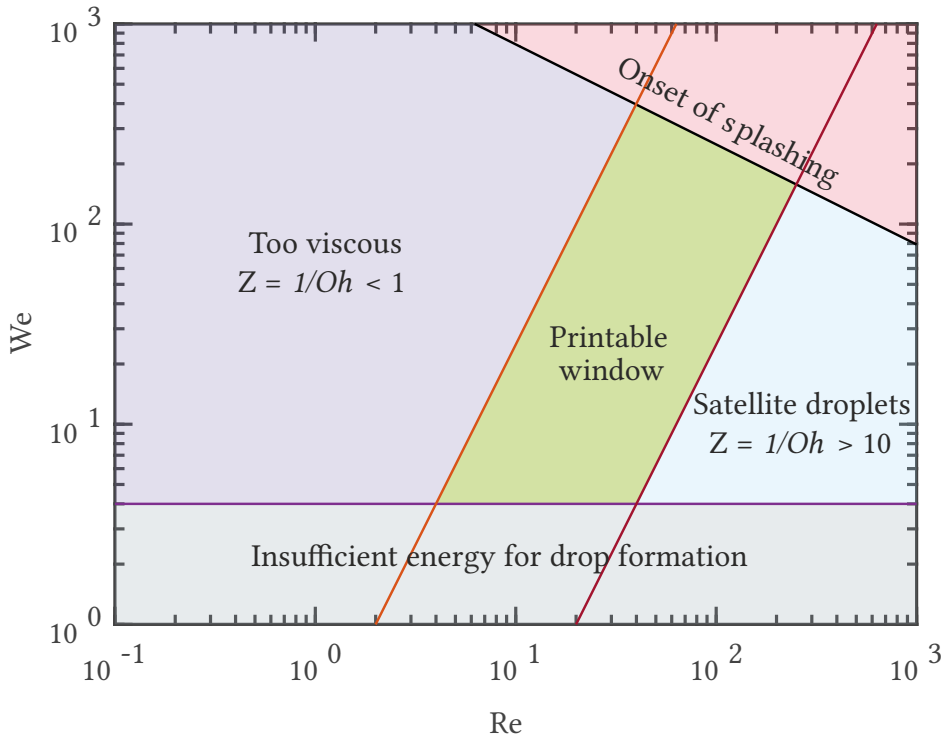

Figure 4.6: Ink printability window. The green region is the printability window, which is defined by four boundary lines in the diagram.

Ink drying and optimization

Coffee-ring effect

After the proper formation of the ink droplets, the drying behavior of the liquid is a further sophisticated subject. The main research activities over the several decades have focused on the suppression of the coffee-ring effect. This effect refers to a phenomenon observed when a liquid evaporates from a surface. As the liquid evaporates, it leaves behind a ring-shaped residue. This results in an inhomogeneous surface morphology after layer drying. Deegan et al. reported in 1997 that the coffee-ring effect is caused by the capillary flow [174]. It is proposed in the work that the criteria of the coffee-ring effect are (1) the deposited liquid on the surface possesses a non-zero contact angle, (2) the contact line is pinned to its initial position, and (3) the solvent evaporates. A schematic illustration in Figure 4.7 shows the formation of the coffee ring. First, a droplet is deposited on a surface. It can be a solution with solutes or ink with nanoparticles. The non-zero contact angle leads to a stronger capillary flow outward from the center to the contact line, which brings the solutes or nanoparticles to the edge. After the solvent evaporation, the solids are concentrated along the drop edge.

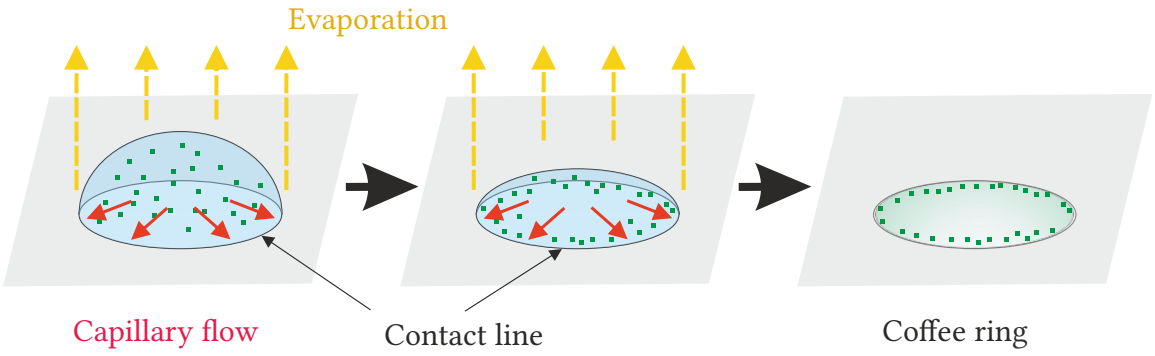

Figure 4.7: Schematic drying process showing coffee-ring effect formation.

Suppression of the coffee-ring effect

To obtain a homogeneous layer, suppressing the coffee-ring effect is essential. Many factors, such as ink surface tension, ink viscosity, substrate surface energy, etc., influence the drying process of liquids. One common way to suppress the coffee-ring effect is introducing Marangoni flow, driven by the surface tension gradient over the center to edge. Figure 4.8 shows the comparison between the cases that are without (left) and with (right) the Marangoni flow. In the case without the Marangoni flow, the capillary flow continuously brings the particles to the edge. After the droplet dries completely, particles concentrate at the edge. Surfactants are commonly used to induce a proper Marangoni flow. The surfactants are usually used to reduce the ink surface tension. Under this circumstance, the surfactants are brought to the droplet edge due to the capillary flow. Therefore, the surface tension on the edge is lower than the bulky center. The Marangoni flow is induced due to the surface tension gradient, and the accumulated particles are pulled back from the edge to the center. Hence, a relatively more homogeneous layer can be formed with the help of the Marangoni flow. It needs to be noted that the capillary flow usually results in radial internal flows while the Marangoni flow causes loops in the ink [175].

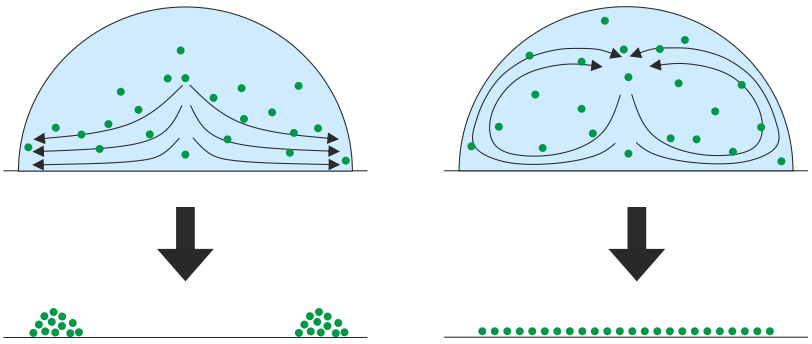

Figure 4.8: Comparison of the formed layer morphology without (left) and with (right) Marangoni flow.

In addition to the Marangoni flow, the strategy based on fast evaporation of the solvents can also be applied [176, 177]. The main concept behind this strategy is to increase the evaporating speed of the liquid part so that the ink viscosity increases rapidly. As a result,

nanoparticles can stay at the quasi-initial dropped location. In some cases, it helps to realize a reduced coffee-ring effect. However, the inhomogeneity of the thin film becomes an issue when the successively printed adjacent lines can not merge properly due to the fast drying.

5 Materials, methods, and characterization

In this chapter, the materials used, methods applied, and characterizations employed in the dissertation are provided and discussed. The first section provides details on materials, including ink formulations and material properties. The second section presents the methods used to fabricate the devices and components in this dissertation. The third section illustrates the principles of the characterizations conducted for analyzing and investigating the results.

5.1 Materials

Silicon dioxide and titanium dioxide

The ink formulations for optical filters consist of silicon and titanium dioxide nanoparticles, respectively. These materials have been chosen because they show no absorption in the visible range, ensuring good optical performance. Additionally, these inorganic materials exhibit high stability against degradation. The refractive index of silicon dioxide is approximately 1.5, while that of titanium dioxide exceeds 2.3, depending on the specific crystallographic structures.

Silver

Silver (Ag) is utilized in the fabrication of a Fabry–Pérot etalon type bandpass filter, where the Ag layer serves as a reflecting layer integrated into the filter. The presence of the Ag layer effectively suppresses residual side peaks in the bandpass filter. On the other hand, the existence of the Ag layer also leads to a decreased total transmittance in the filter because of the absorption and surface plasmon in the interface of the Ag and dielectric layers. The details are illustrated in Chapter 6.

Polydimethylsiloxane

Polydimethylsiloxane (PDMS) is purchased from Dow Inc. The full name of the product is SYLGARD™ 184 silicone elastomer kit. In a raw form, the product consists of two components. The first is the siloxane polymer. The second is the curing agent. The former is a primary polymer consisting of silicon and oxygen atoms interspersed with methyl groups. The latter is a cross-linker, which is vital. The curing agent initiates the chemical reaction with the siloxane polymer, creating cross-links and transforming the polymer into a solid elastomer.

Nanoporous Silicon

The boron-doped silicon (100) wafer is purchased from Sigma-Aldrich. The resistance is measured in the range of 5 - 20 mΩ cm, corresponding to a dopant density of $3{\times}10^{18}$ cm^{-3}. Silicon is made into a nanoporous component and used in surface-enhanced Raman spectroscopy measurements.

Tetrachloroauric(III) acid trihydrate

Tetrachloroauric(III) acid trihydrate ($HAuCl_4{\cdot}3H_2O$) is purchased from Sigma-Aldrich. It is used for generating the gold nanoparticles and nanoclusters in the nanoporous silicon substrate. The embedded gold nano entities create a large number of hot spots for detecting analytes using surface-enhanced Raman spectroscopy.

Methylene blue

Methylene blue (MB) is purchased from Sigma-Aldrich. It is used as the reference analyte in the surface-enhanced Raman spectroscopy measurement. The MB is delivered in the powder form. It is dissolved in ethanol with different concentrations for characterization.

5.2 Methods

Spin coating

Spin coating is applied to coat SiO_2 and TiO_2 inks on the glass substrates to determine the surface free energy of each material. The resulting thickness of each solid layer is around 100 nm. Spin-coating is a method to deposit a liquid (i.e., a solution) onto a substrate. A thin film is formed after a high-speed rotation. The film thinning formation results from the rotational forces (hydrodynamic thinning) and solvent evaporation (evaporative thinning). A number of parameters affect the interplay between hydrodynamic and evaporative thinning, including viscosity, vapor pressure, molecular weight, ambient temperature, ambient humidity, ambient flow condition, as well as the operation parameters such as rotation time, acceleration rate, and rotational rate.

Fabrication of PDMS slice

PDMS slices are fabricated through the initial mixing of the silicone elastomer and a curing agent (Sylgard 184, Dow) at a weight ratio of 10:1. Subsequently, the resulting mixture goes through vacuum degassing within a desiccator for 30 minutes to eliminate entrapped air bubbles. Following this, a specific volume of the mixture is dispensed onto a glass substrate using a syringe. The glass substrate, positioned on a hot plate at room temperature, facilitated the self-leveling of the mixture to cover the entire glass surface. The hot plate temperature was incrementally raised to 50 °C for 10 minutes, followed by a subsequent increase to 95 °C for an additional 10 minutes. The resulting PDMS slice was then carefully detached from the glass substrate, exhibiting an approximate thickness of 1 mm.

PDMS surface modification

PVA aqueous solution is formulated using PVA aqua solution, which is described above. For the surface treatment of polydimethylsiloxane (PDMS), the solution's temperature is increased to 100 °C. A stretched PDMS slice is immersed in the solution for 1 hour. Distilled water is intermittently added during each heating step to maintain the total solution weight. After naturally cooling the solution to room temperature, the PDMS slice is dried using a nitrogen flow and retained in the stretched state for subsequent inkjet printing applications.

Etching mask design

The PMMA etching mask is designed digitally. First, the greyscale of the digital mask is decided. The method to generate the greyscale image is halftone. In this way, the ratio of the surface covered by the PMMA mask is directly determined by the initial greyscale value. The software used to generate the mask image is CorelDRAW (Corel Corporation, Canada)

Plasma treatment

The PDMS slice is treated in oxygen plasma using a UV/Ozone plasma chamber (Femto, Diener electronic) at a pressure of 40 Pa with a power input of 100 W for 6 minutes. Throughout the treatment, only the surface that has been printed with micro etching masks (MEMs) is exposed to the plasma, while the opposite side is affixed to a glass slide and thus remains unexposed to the plasma. Following the release of the PDMS, microgrooves spontaneously formed on the treated surface. It is a consequence of the strain difference between the SiO_x layer and the underlying intact PDMS. In this dissertation, the stretching ratio of the length is maintained at 1.6 for the generation of microgrooves.

Nano-porous silicon fabrication

Nanoporous silicon (np-Si) samples are fabricated by electrochemical anodization of a boron-doped Si(100) substrate with resistivity ranging from 5 to 20 mΩ cm, corresponding to a dopant density of 3×10^{18} cm^{-3}. The anodization process involves the application of an electrolyte solution containing methanol and 40% hydrofluoric acid in a 1:1 ratio, conducted at a current density of 100 mA/cm^2 for 8 seconds. This results in the formation of an np-Si layer approximately 550 nm thick. Subsequently, the wafer is thoroughly rinsed in methanol and subjected to air drying, resulting in a porosity of approximately 65%. The initial structure of the unmodified sample comprises a sponge-like silicon material. The average wall thickness is around 10 nm, and the channel diameter is approximately 50 nm. In this dissertation, efforts are made to maintain a thin layer to ensure consistent penetration of the gold solution into the depth while ensuring sufficient thickness to accommodate the laser penetration depth required for Raman measurements. The developed methodology could potentially be extended to fabricate layers or membranes with

thicknesses exceeding 100 micrometers, offering the chance to design layered materials that facilitate surface-enhanced Raman spectroscopy (SERS).

Gold-nanoparticle cluster embedding

The electroless immersion plating technique, also called electroless deposition, is employed to introduce gold clusters into the nanoporous silicon (np-Si) layer. The immersion solution is prepared by dissolving 9.85 mg of tetrachloroauric acid ($HAuCl_4$) in 50 mL of ethanol, resulting in a concentration of 0.5 mM. Prior to the impregnation process, the np-Si sample underwent a 30-second immersion in a 2% hydrofluoric acid (HF) solution diluted in deionized water to eliminate the native oxide layer formed on the sample surface and within the pores. Subsequently, the np-Si sample is immersed in the pre-prepared $HAuCl_4$ solution and subjected to ultrasonic agitation to facilitate solution infiltration into the pores. Due to the presence of the native pSi surface, which contains a metastable $Si–H_x$ termination, a reaction occurred near the pore interface: $(AuCl_4)^- + H^+ + 3e^- = Au + 4Cl^- + H^+$, resulting in the reduction of Au and the formation of gold nanoparticles. Following a specified time interval, the sample is rinsed in ethanol and air-dried.

5.3 Characterization

Contact angle measurement

The contact angle (CA) is evaluated by a measuring system (OCA 50, DataPhysics Instruments) in a static state under ambient conditions. The temperature and humidity are controlled at 22 ± 1 °C and 50% ± 5%. The analysis of the CA is done through the sessile-drop method and the Laplace-Young equation.

Surface free energy characterization

To determine the surface free energy (SFE) of a specific solid surface, deionized H_2O, ethylene glycol (Sigma-Aldrich), and diiodomethane (Sigma-Aldrich) are employed. The Owens-Wendt-Rabel-Kaelble (OWRK) method is utilized to compute both the polar and dispersive components of the SFE. The solid surface of SiO_2 (TiO_2) used in the CA measurements is created by spin-coating a SiO_2 (TiO_2) nanoparticle dispersion to produce a thin film with an approximate thickness of 100 nm. The procedure is subsequently accompanied by annealing at 250 °C for 5 minutes. The thickness of the thin film is measured using a profilometer (DektakXT, Bruker). On each solid surface, ten distinct sites are employed to measure the CA of a liquid with a single dosing volume of 0.5 µl. The resulting average CA is utilized in the calculation of SFE. Similarly, the average CA of SiO_2 (TiO_2) ink on TiO_2 (SiO_2) surfaces is determined by measuring ten different sites.

Surface tension characterization

The overall surface tension (SFT) of the liquid/ink is determined using an SFT measuring system (OCA 50, DataPhysics Instruments) at ambient conditions. The analysis employs

the pendant-drop method with the Laplace-Young equation. To obtain the polar and dispersive components of the liquids and inks, polyethylene (Thermo Scientific) is utilized as an exclusively dispersive reference surface.

Scanning electron microscopy

Scanning electron microscopy (SEM) images are measured by SUPRA 55 (Carl Zeiss). The accelerating voltage is set to 2 kV. Before the SEM characterization, the sample surface is sputtered with a layer of gold. The thickness of this gold layer is around 5-10 nm.

Focused ion beam milling

To obtain the cross-sectional view of the samples, focused ion beam (Zeiss Crossbeam 1540 EsB) milling is conducted. It uses a focused beam of gallium ions with an energy of 5 keV. The high-energy ion beam enables precise material removal and etching, allowing for the creation of a window for cross-sectional inspection.

Atomic force microscopy

The surface morphology is measured by atomic force microscopy (AFM) (NanoWizard, Bruker Nano), and the surface root-mean-square (RMS) roughness was analyzed with the software Gwyddion. The tapping mode is used during the AFM measurement to avoid damage to the sample surface. The basic working principle of the AFM is described in the following. A cantilever with a sharp tip oscillating in standard frequency scans over the surface of interest. The atomic force causes the cantilever to displace, interacting with the different surface morphologies. A laser beam incident on the tip and reflected to a CCD array. Through this, the deflection of the cantilever is detected in either the direction toward or away from the surface. The movement of the laser spot on the CCD array is then transformed into an electronic signal, which is subsequently utilized for the reconstruction of a detailed surface image. This methodology offers comprehensive insights, both qualitatively and quantitatively, into diverse physical properties, including size, morphology, surface texture, and roughness.

UV-vis-NIR spectrometer

Transmission and reflection are measured with a spectrophotometer (Lambda 1050 UV-vis-NIR, PerkinElmer) equipped with a 150 mm integrating sphere module. This device is a two-beam system. The advantage of this configuration is a much higher accuracy compared to the one-beam system. In addition, the used spectrophotometer is designed as a double-monochromator system, which further increases the reliability of the measured results. The device is able to measure the transmittance and reflectance in the range of 175 to 3300 nm by utilizing different auxiliary modules.

Ellipsometry

Refractive indices and extinction coefficients of the printed layers are measured by an ellipsometer (VASE ellipsometer, J.A. Woollam). The working principle of the general ellipsometer is described in the following. The device uses a monochromatic polarized light to incident a sample surface. The reflected light beam is then measured by a photodiode for further analysis. The polarization state of the reflected light changes upon the sample, where the changes in polarization state are quantified in two ellipsometric parameters, i.e., Ψ and Δ. The former and the latter are the amplitude ratio and the phase difference between the p and s components of the reflected light. Generally, the Ψ and Δ can not be directly converted to the optical constants such as refractive index and extinction coefficient. A model analysis is essential. The obtained Ψ and Δ are used to fit the experimental data, which are already in a database to provide the best-matched optical constants and layer thickness.

Surface-enhanced-Raman-scattering microscopy

In SERS measurement, an 808 nm laser (Changchun New Industries Optoelectronics Tech. Co., Ltd) is used as the excitation laser source. A 40× objective (NA 0.6, Plan-Neofluar, Zeiss) is used to focus the laser spot and collect the SERS signal in the vicinity of the sample surface. The back-scattered Raman signal goes through the objective and subsequently to a notch filter (TECHSPEC 808 notch filter, Edmund Optics Inc., Germany). Detection of the signal is accomplished using a monochromator (Acton Spectra Pro 2500i, Princeton Instruments, Trenton, NJ, USA) equipped with an electron-multiplying charge-coupled device (EMCCD) camera (iXon, Andor, Belfast, UK). The fundamentals of the SERS measurement are presented in Chapter 2, section 2.4.

Bright-field and dark-field microscopy

Microscope Axioplan 2 (Zeiss, Germany) is used in bright and darkfield microscopy. Different objectives are used based on the different requirements of magnification. A CCD camera (AT AxioCam ICc R3, Zeiss, Germany) is used to record the images. The basis parameters, such as exposing time, image contrast, etc, are controlled automately by the software ZEN core (v3.2, Zeiss, Germany). In bright-field microscopy, the image contains both the reflected and scattered light from the sample, while in dark-field microscopy, only the scattered light is recorded.

6 Inkjet-printed optical interference filters

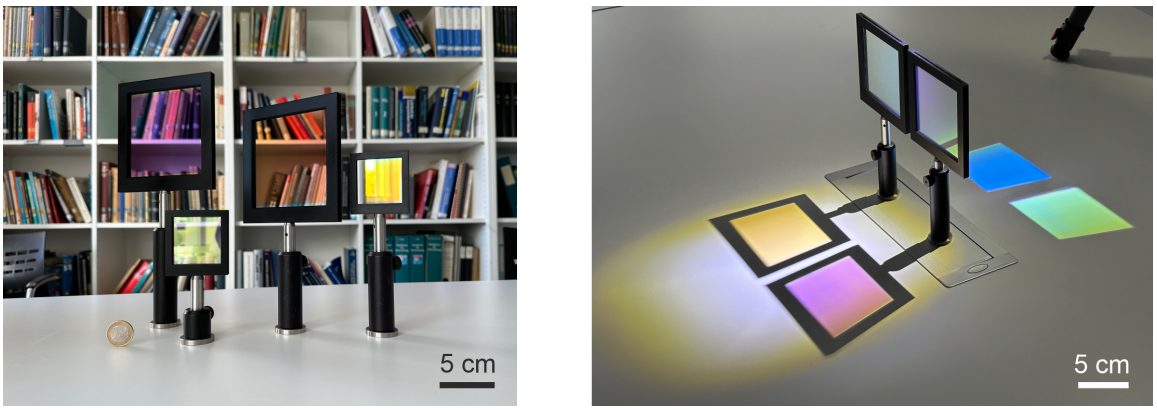

Figure 6.1: Inkjet-printed optical interference filters.

This chapter presents the work on inkjet-printed optical interference filters, covering the ink design, filter fabrication, and characterization. The content of the ink design gives a rational strategy for ink formulation starting from scratch. The part of filter fabrication offers comprehensive work on printing parameter optimization and characterization. It is worth mentioning that the filters fabricated in this dissertation are multilayer interference filters rather than color filters that are based on absorptive materials.

Parts of the results presented in this chapter have previously been published in the journal Nature Communications [178].

Optical interference filters are indispensable components for numerous optical and photonic systems. The broad usage of optical filters is already presented and discussed in Chapter 3. The production of optical interference filters encounters notable challenges due to emerging applications that necessitate new demands that are hard to address by conventional fabrication methods. The present manufacturing techniques are often technically and economically costly to meet the requirements of cutting-edge applications. Therefore, there is a crucial need to find novel approaches to address these challenges. There are high demands for lateral patterning, rapid prototyping, fast multi-round iterations, cost-effectiveness, and the ability to produce components of various sizes ranging from micro to meter size. In response to the open challenges, inkjet printing of optical interference filters is developed and demonstrated in this work. It is the first time that this kind of filter has been realized in a full set, i.e., longpass, shortpass, bandpass, and

dichroic filters. Moreover, laterally patterned and upscaled filters (29.7×21.0 cm^2) have been demonstrated.

The left image in Figure 6.1 shows the inkjet-printed filters mounted in standard holders. The filters are fabricated with different spectral functionalities. For instance, the right side image of Figure 6.1 shows the splitting of a white incident light into two complementary parts of the spectrum.

6.1 Ink formulation and property characterization

Surface free energy of the surfaces and the selection of organic vehicles

Optical interference filters are conventionally produced using vacuum-based technologies, involving the stacking of thin films with alternating high and low refractive indices. SiO_2 and TiO_2 are the two comm materials used in the fabrication of the filters. Both of these materials exhibit excellent optical transparency with negligible absorption in the visible and near-infrared spectral range. Moreover, these are inorganic materials, which are stable at high temperatures and resistant to degradation. Therefore, the inkjet printing in this dissertation uses SiO_2 and TiO_2 nanoparticle dispersions to fabricate optical filters.

In the inkjet printing process, ink droplets are ejected onto the substrate to form a homogeneous layer. The droplet ejection is a process involving a number of physical mechanisms. The vital factors include the surface free energy (SFE) of the solid layer where the ink is applied, as well as the surface tension (SFT), viscosity, and vapor pressure of the ink. In the initial stage of ink design, it is essential to ensure that the ink exhibits a minimal contact angle on the solid surface. Additionally, for the sake of simplifying the fabrication process, it is preferable not to include the pre-surface treatment of the solid layer with UV/ozone plasma or other additional efforts.

The ink comprises the nanoparticle, organic vehicle (i.e., the main liquid component), and essential additives such as humectants. It is apparent that ink designs become more complex with an increased number of chemical components in the ink. The reason is that to disperse the nanoparticles properly in the organic vehicle, it requires particular surface modification. The improper chemical components can affect the modified nanoparticles easily, resulting in aggregation. Nevertheless, selecting an adequate organic vehicle is the first step in ink design.

To find a proper organic vehicle, the SFE of the solid surface needs to be determined first. It can be obtained by characterizing the relation of the liquid, solid, and vapor. Using Young's equation, this relation and the corresponding CA can be expressed as [169]

$$\cos\theta_c = \frac{\gamma_{sv} - \gamma_{sl}}{\gamma_{lv}} \tag{6.1}$$

where γ_{sv}, γ_{sl}, and γ_{lv} are the interfacial tensions of solid-vapor, solid-liquid, and liquid-vapor, respectively, and θ_c is the CA. It can be seen the CA is a result of the three interfacial tensions. The surface tension of the liquid comprises two parts, i.e.,

$$\gamma_{lv} = \gamma_l^P + \gamma_l^D \tag{6.2}$$

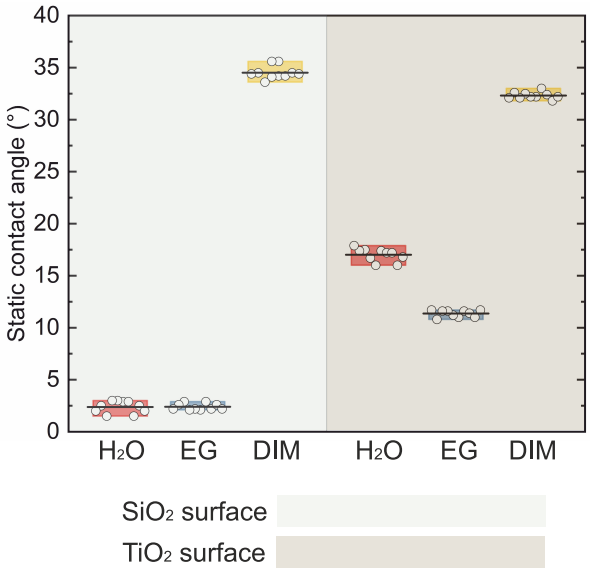

Figure 6.2: Measured static contact angle on SiO_2 and TiO_2 surfaces. The applied reference liquids are deionized water (H_2O), ethylene glycol (EG), and diiodomethane (DIM), respectively.

where, γ_l^P and γ_l^D are the polar and dispersive components, respectively. Therefore, the equation 6.1 can be rewritten as

$$\cos\theta_c = 2\frac{\sqrt{\gamma_s^P \gamma_l^P} + \sqrt{\gamma_s^D \gamma_l^D}}{\gamma_l^P + \gamma_l^D} - 1 \tag{6.3}$$

One can easily find that by measuring the CAs of minimum two reference liquids, whose γ_l^P and γ_l^D are known; hence, γ_s^P and γ_s^D can be calculated. In this dissertation, the SFE of SiO_2 and TiO_2 surfaces are characterized using three reference liquids: deionized water (H_2O), ethylene glycol (EG), and diiodomethane (DIM). The measured CAs on the SiO_2 and TiO_2 solid surface are depicted in Figure 6.2, where the CAs are measured in a static state. For each reference liquid, ten CAs are measured over the same surface but at different sites. Therefore, the results obtained are the mean value. The black bars in the figure represent the corresponding average static CAs. Consequently, the SFE of the surfaces can be calculated accordingly. The results are listed in Table 6.1.

SFE information (mN/m)	**SiO_2 surface**	**TiO_2 surface**
Total average SFE	68.24	66.16
Polar share	35.69	32.57
Dispersive share	32.55	33.59

Table 6.1: Information of surface free energy of SiO_2 and TiO_2 surfaces.

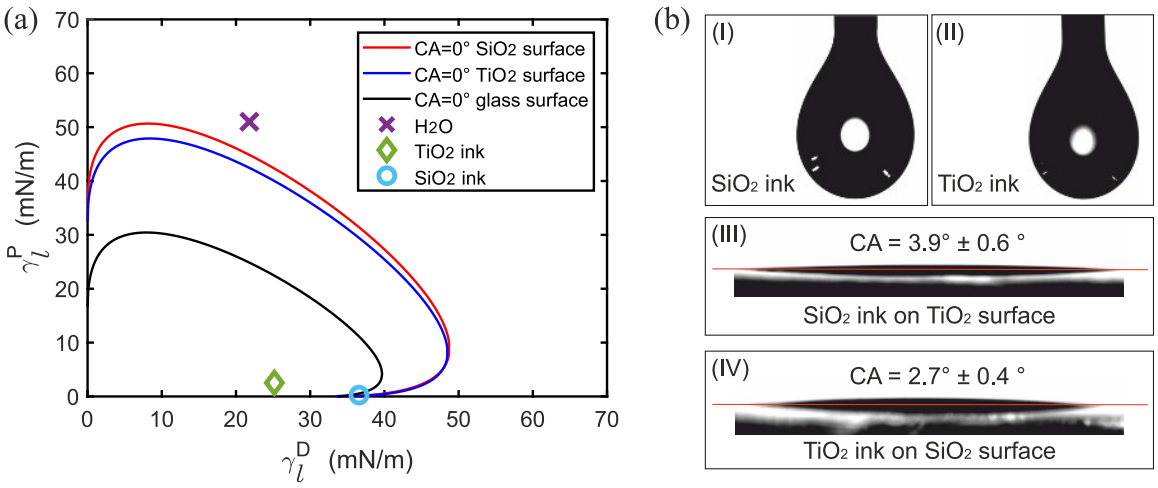

Figure 6.3: Ink property characterization. (a) Wetting envelopes. (b) I and II are ink droplet profiles for surface tension calculation. III and IV are contact angles of ink on respective surfaces.

After the determination of SFE, a wetting envelope can be defined subsequently. The wetting envelope illustrates the surface wetting characteristic of liquids on a specific surface. It is often used to visualize the wetting performance by plotting the corresponding CA lines. Each line represents a specific CA, and more than one line can be plotted in the wetting envelope when needed.

Figure 6.3 (a) shows the wetting envelope diagram. The x- and y-axis are the values of the dispersive and the polar share of a liquid, respectively. There are three envelopes in the figure belonging to SiO_2 (red), TiO_2 (blue), and glass (black) surfaces, respectively. A random point on each individual envelope indicates that on this certain surface, the CA of the liquid is zero. In addition, the corresponding dispersive and polar share of the liquid can be read from the coordinate. Moreover, it is apparent that the total SFT is the sum of the dispersive and polar share. In this work, 1,3-dimethoxybenzene (1,3-d) and 2-propoxyethanol (2-p) are selected as the organic vehicles for dispersing the nanoparticles. The first reason is that these solvents show relatively higher boiling points, which helps to ease the nozzle clogging issue. The second reason is that both the solvents show a very low CA on corresponding surfaces, i.e., 1,3-d on the TiO_2 surface and 2-p on the SiO_2 surface. This is important since the filters are fabricated in a multilayer structure, where the SiO_2 and TiO_2 layers are alternately deposited on each other. Achieving homogeneous layers requires good wetting behavior of the ink droplet on the corresponding material.

Surface tension of the inks

The SFT of the developed SiO_2 and TiO_2 inks are measured using the ink droplet profiles hanging on a needle tip in Figure 6.3 (b) I and II. The results are listed in the Table 6.2. The values are fitted back into the wetting envelopes in Figure 6.3 (a). As can be seen, the wetting behavior of the SiO_2 ink on the TiO_2 surface is satisfactory, as indicated by the blue dot positioned on the envelope, representing a CA equal to zero. Moreover,

the TiO_2 ink shows an even better wetting behavior since the green dot is within the envelope, which implies a complete wetting [179]. For reference, the purple dot represents water, and it performed relatively poorly on all the testing surfaces, particularly on the glass surface. Here, the further the point from the curve, the worse the wettability. This indicates a large contact angle of water on the normal glass surface. Figure 6.3 (b) III and IV show the CAs of SiO_2 and TiO_2 ink on the SiO_2 and TiO_2 solid surfaces. The measured CAs are very low, which are 3.9 ± 0.6 ° and 2.7 ± 0.4 °. These results imply a suitable wetting performance of the inks on solid surfaces, which helps to form a homogeneous thin film.

Surface tension values (mN/m)	**SiO_2 ink**	**TiO_2 ink**
Total	36.84	27.70
Polar share	0.26	2.53
Dispersive share	36.58	25.17

Table 6.2: Information of surface tension of SiO_2 and TiO_2 inks.

Silicon dioxide nanoparticle ink

Silicon dioxide (SiO_2) nanoparticles dispersed in methyl ethyl ketone (MEK) are purchased from Nissan Chemical, Japan. The solid concentration of the nanoparticle dispersion is 40%. The ink eventually used in inkjet printing the optical interference filters in this work is formulated in a way that the organic vehicle (MEK) is replaced by 1,3-dimethoxybenzene (1,3-d). The detailed reason is illustrated in Chapter 6. To replace the organic vehicle, the MEK-based nanoparticle dispersion is added into a glass flask. The glass flask is swirled to spread the liquid over the glass wall. Due to the very high concentration of the dispersion and high volatility of the MEK, the dispersion undergoes fast drying, leaving only the solid nanoparticles in the glass flask. Immediately, 1,3-d is added to the glass flask. The glass flask is swirled again, and the 1,3-d moves inside to collect the nanoparticles. The glass flask is swirled until there are no visible nanoparticle clusters on the wall. After this, the 1,3 d-based nanoparticle dispersion is transferred into a glass vial with a steering bar. The ink is then steered with a rotation speed of 500 revolutions per minute (rpm) for 24 hours. By carefully controlling the volume ratio of the MEK nanoparticle dispersion and the 1,3-d solvent, the 1,3-d-based silicon nanoparticle dispersion can be formulated with a solid concentration of 3%. X-ray diffraction analysis is employed to characterize the phase of the SiO_2 nanoparticles, which are identified as amorphous.

Titanium dioxide nanoparticle ink

Titanium dioxide (TiO_2) nanoparticles dispersed in 2-propoxyethanol (2-p) are purchased from Avantama AG, Switzerland. The solid concentration of the nanoparticle dispersion is 18%. The ink eventually used in inkjet printing the optical interference filters in this work uses the original vehicle, i.e., 2-p. Only the solid concentration is modified to 1.8%.

Using X-ray diffraction analysis, the phase of the TiO_2 nanoparticle is characterized as rutile.

Ink printability evaluation

In inkjet printing, an appropriate SFT allows the droplets to overcome the barrier and be ejected from the nozzle. Other ink properties, such as density and viscosity, play an important role in the ejection process as well. Furthermore, the momentum transferred to the liquid from the channel wall deformation in the printing head affects the droplet velocity [180]. During the last decades, numerous investigations have been performed to understand the interplay of the parameters of inkjet printing. Here, the properties of the developed inks are listed in Table 6.3. The following work on the assessment of the ink printability is based on these values.

Ink properties	**SiO_2 ink**	**TiO_2 ink**
Nanoparticle concentration	3.0%	1.8%
Surface tension (mN/m)	36.84	27.70
Density (g/ml)	1.069	0.934
Viscosity (mPa·s)	2.04	2.5
Droplet velocity (m/s)	2-4	2-4
We	2.50-9.98	2.90-11.60
Re	22.53-45.07	16.05-32.10
Oh	0.07	0.11
Z	14.26	9.43

Table 6.3: Properties of the developed SiO_2 and TiO_2 inks.

Subsequently, a printability window is depicted in Figure 6.4 (a). The general background and theory to explain ink printability are presented in Chapter 4. This is usually illustrated by a printability window of the ink. The boundaries are defined based on the Reynolds, Weber, and Ohnesorge number, i.e., *We*, *Re*, and *Oh*, as well as on *Z* number, which is $1/Oh$. The boundaries in Figure 6.4 (a) are displayed with particular numbers. These values are calculated from the measured ink properties listed in Table 6.3. The droplet velocity is measured by the integrated camera and software of the printer. The applied ink droplet velocity is 2-4 m/s, where the ink droplets are well ejected without any satellites. The red arrow in the image indicates the direction of the increased velocity. Depending on the droplet velocity, the calculated *We* for the SiO_2 and TiO_2 inks are 2.50-9.98 and 2.90-11.60, respectively. It is noted that the minimum *We* in this work is 2.5, which is lower than the 4 in the literature [171]. This means it requires less energy to form the droplet using the developed ink.

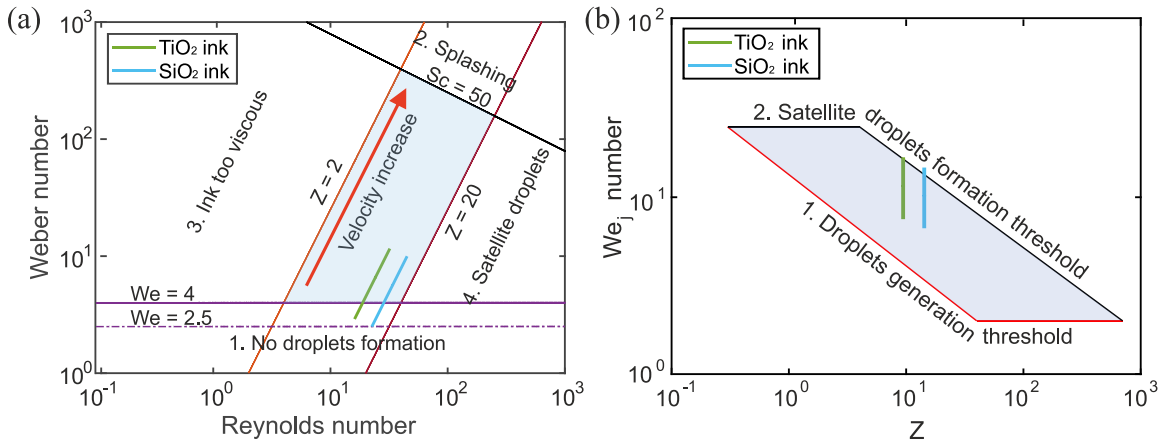

Figure 6.4: Printablity windows of the developed inks. (a) and (b) are printability windows based on different boundary definitions.

The blue and green lines in Figure 6.4 (a) belong to SiO_2 and TiO_2 inks, respectively. The light-blue domain indicates good ink printability, which is defined by four boundaries. It can be found that the inks show a good performance according to the essential criteria. This type of printability window is a very common one and often can be found in different work [181]. The printability domain is defined by *We* and *Re*, which are velocity-based. Researchers have proposed a strategy of using parameters containing no velocity to define a printability window [172]. The boundaries for assessing printability are defined by two dimensionless parameters, i.e., Z and We_j, which demonstrate in a more practical manner when applied to fluids with well-established Newtonian physical properties. The We_j is calculated using the fluid's velocity prior to drop formation, providing a more accurate representation of the mechanisms involved in drop ejection. In addition, Z is also defined by the ink properties purely. As shown in Figure 6.4 (b), the printability window is defined by a range of We_j values ($2 < We_j < 25$), creating a parallelogram that is determined by $Z \approx 2$–20. When We_j is below 2, there is no droplet formed due to the capillary force, while a We_j above 25 leads to a satellite formation. The inclined boundary on the left defines the critical condition of viscosity and the right one gives the minimum We_j where the satellite is formed. Therefore, these four boundaries can be concluded as the red boundaries in Figure 6.4 (b) represent the droplet generation threshold, and the black boundaries specify the satellite droplet formation threshold.

The calculation of the We_j depends on v_j, which is the fluid velocity inside the nozzle channel prior to the droplet formation. We_j can be expressed as [182]

$$We_j = \frac{v_j^2 \rho d}{\gamma} \tag{6.4}$$

where d is the nozzle orifice size. Furthermore, v_j can be calculated by the ejected droplet volume V_j,

$$V_j = \pi \left(\frac{d}{2}\right)^2 \frac{v + \sqrt{v^2 - 4\left(\frac{3\eta}{\rho\Delta t} - \frac{2\gamma}{\rho d}\right)}}{2} \Delta t \tag{6.5}$$

where v is the velocity of the ejected droplet, and Δ t is estimated by the time difference between the nozzle channel starting to deform and the droplet leaves the nozzle,

$$V_j = \int_{t_0}^{t_e} Av \, dt \tag{6.6}$$

where A is the exit area estimated by the nozzle orifice site.

The inclusion of the second printability window aims to cross-check with the validation obtained from the first window, making the results more reliable and convincing. As can be seen in Figure 6.4 (b), the ink lines defined by We_j and Z number are depicted. Both lines are located in the printable region indicated by the light-blue zone. These results demonstrate the printability of the inks for inkjet printing.

6.2 Inkjet printing of thin films

Precise thickness control

Before printing the thin film assembly, inkjet printing a thin film and the optical behavior of the printed layers needs to be validated and characterized. The precise control and high repeatability of printed layer thickness are required for fabricating the optical filters. It is challenging to achieve this in the solution-based process. In this work, using the developed inks and by carefully controlling the printing parameters, precise control of the individual layer thickness is realized. The details are presented in the following. Figure 6.5 (a) shows the increase of TiO_2 layer thickness via controlling the number of droplets printed on a unit area. The x-axis is the measured layer thickness respective to the droplet number divided by 1000, which is the y-axis. For instance, when the number of the printed droplets is 400000, the measured layer thickness is 57.5 nm. Each thickness is an average value out of repeated five times printing. Therefore, a standard deviation is obtained for each number and is added to the graph with a ± sign. It can be seen that with the increase of the droplet number from 400000 to 900000, the thickness measured increases from 57.5 nm to 108 nm accordingly. The red line in the graph is a linearly fitted line of the six thickness values. By calculating the coefficient of determination, R^2, it yields 0.9999. This implies a highly linear relationship between the number of printed droplets and the resulting thickness. In addition to this, the low standard deviations, being less than 1% of each layer thickness, indicate a highly repeatable layer printing process. Based on this strategy, the final layer thickness can be precisely controlled by using the proper printing resolution, i.e., dpi. Therefore, direct and digital control of layer thickness can be realized.

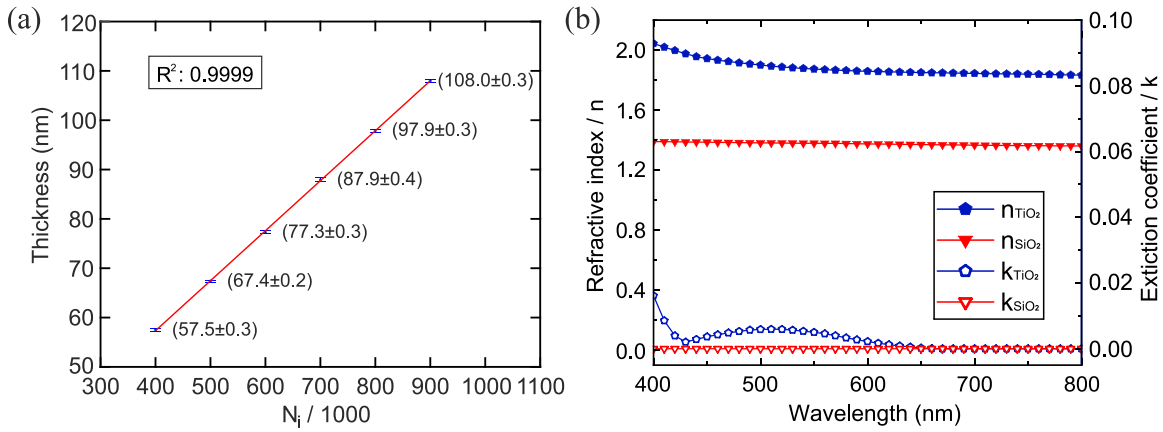

Figure 6.5: Thickness control and optical property of inkjet-printed layers. (a) Layer thickness control via the number of printed droplets. (b) Refractive index and extinction coefficient of printed layers.

Refractive index and extinction coefficient of layers

To design the optical interference filters properly, it is necessary to characterize the refractive index of SiO_2 and TiO_2 layers. This is because the optical thickness is the essential value used in the simulation, where optical thickness equals physical thickness times the refractive index. Figure 6.5 (b) shows the refractive index, n, and the extinction coefficient, κ, of printed SiO_2 and TiO_2 layers. The layer thickness of each material is around 100 nm. The TiO_2 layer shows a refractive index of around 2.0 to 1.8 from 400 to 800 nm. The SiO_2 layer shows a relatively steady value around 1.4 throughout the same wavelength range. The difference in refractive index between these two materials is large enough to be used for designing the optical interference filters.

Besides the refractive index, the extinction of the printed layer is important. As discussed in Chapter 2, the extinction includes absorption and scattering. In optical interference filters, a high extinction leads to deteriorated performance in terms of transmittance or reflectance. In Figure 6.5 (b), the spectral extinction value of SiO_2 is nearly zero in the wavelength range of 400 to 800 nm, indicating good optical behavior. However, the TiO_2 shows a slightly increased extinction in the range below 650 nm. The reason can be assigned to the crystal structures of the used rutile phase TiO_2 nanoparticles [183]. A potential solution will be replacing rutile TiO_2 nanoparticles with amorphous phase nanoparticles. However, there exists a trade-off between the reduced optical scattering and the diminished refractive index difference between SiO_2 and TiO_2 layers, requiring a higher number of total layers to achieve equivalent optical performance. Nevertheless, the extinction of the TiO_2 layer remains small and is almost zero in the longer wavelength range. This guarantees the material to be used for fabricating the optical filters.

Crystallographic structure composition of the solid thin films

X-ray diffraction analysis (XRD) is conducted to reveal the crystallographic structure of the printed thin films. The XRD measurement is performed when the thin films are with

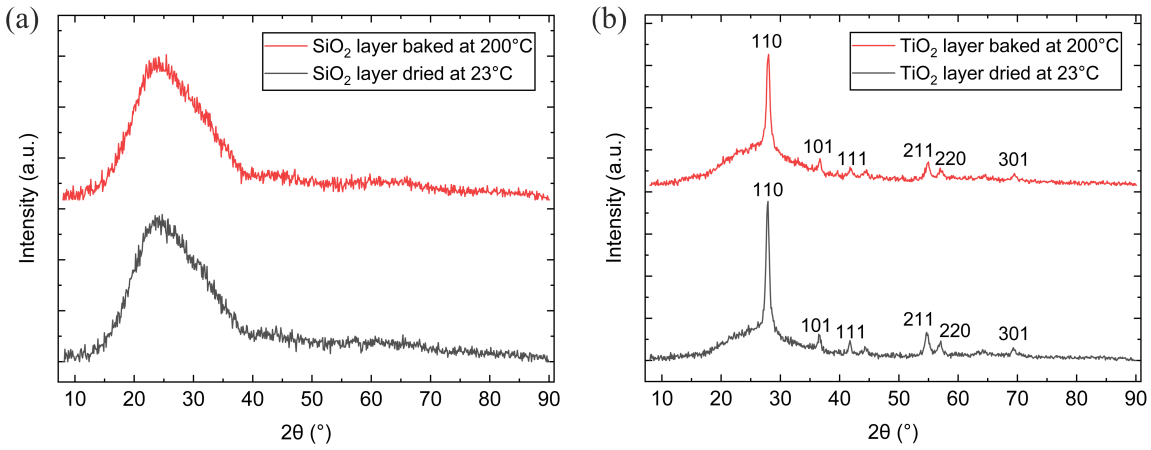

Figure 6.6: Crystallographic phase composition of thin films.

and without annealing. The measured curves are shown in Figure 6.6 (a) and (b), which correspond to the SiO_2 and TiO_2 material, respectively. The printed thin films without annealing are dried at room temperature, i.e., 23 °C. It preserves the original crystallographic structure of the nanoparticles. In the images, SiO_2 nanoparticles present the crystallographic structure of amorphous with a characteristic 2θ angle of 22° [184], while the TiO_2 nanoparticles show the crystallographic structure of rutile with typical 2θ angles of 27.1°, 36.4°, 39.1°, 54.5°, 57.2°, 69.0° corresponding to the reflections from 110, 101, 111, 210, 211, 220, and 301, respectively [185, 186].

After annealing the thin films at 200 °C for 10 minutes. The XRD measurement is conducted again. As can be seen, there is no difference in the measured results before and after the annealing. Therefore, the SiO_2 and TiO_2 layers remain in the amorphous and rutile phase constantly.

Inkjet printing process

Optical interference filters are thin film assemblies consisting of alternately stacked layers. To fabricate these filters, a layer-by-layer printing process is developed in this work. Figure 6.7 (a) shows two materials with different refractive indices are deposited on each other. The substrate can be different materials, including glass, polymers, and metals. The print head uses multiple nozzles during the printing process. Droplets are deposited in the defined area, forming a uniform layer. Figure 6.7 (b) shows a single printing cycle. After printing each layer, the drying process is usually required. Subsequently, an annealing process is conducted. After this, the next layer can be printed on the existing layer. It needs to be noted that this printing cycle applies to the nanoparticle inks used in this work. The printing process must be modified if different inks are used. For instance, when using UV-curable inks, a step of radiation illumination should be included.

As discussed in the previous section, precise control of layer thickness is crucial during the fabrication of optical interference filters. The development of both inks and printing processes must be coordinated to achieve optimal layer quality. The interplay of various parameters, such as printing speed and in-situ drying speed, printing resolution and ink

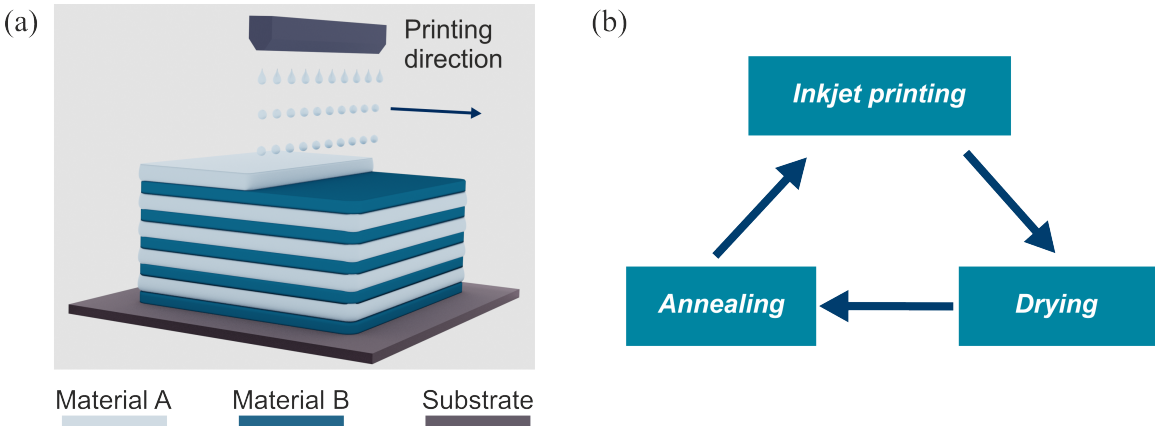

Figure 6.7: Inkjet printing the thin film assembly. (a) Layer-by-layer inkjet printing. (b) Inkjet printing cycle.

merging, and nozzle or substrate temperatures with ink viscosity, requires a comprehensive approach. Properly optimizing the printing process demands a substantial amount of empirical work. In this work, the harmony between various parameters is achieved to realize a successful fabrication of optical interference by inkjet printing.

Ripple suppression by non-periodic structure

One of the highlights of the inkjet-printed filters in this work is that the multilayer assemblies can be printed in a desired manner, which is printing periodic and non-periodic structures on demand. Compared to the periodic filters, non-periodic structures are often used to suppress the sidebands in edge filters, as seen in Figure 6.8. The figure compares the transmission curves of (a) a longpass and (b) a shortpass filter when designed with periodic and non-periodic structures. Here, the longpass filter is a type of filter where the longer wavelengths transmit through, while the shortpass filter is a filter that allows shorter wavelengths to pass. In the pass region of both filters, it can be found that the ripples are suppressed in the non-periodic design compared to the periodic ones. The suppression of the ripples leads to an enhanced optical performance of the filters. In the non-periodic structure, the individual layer thickness needs to be optimized. Typically, the thickness can vary from around ten to several hundred nanometers [187]. Therefore, it requires the printing process to be highly controllable and repeatable. Moreover, this precise thickness control needs to be maintained until the fabrication is finished. To allow the filter to be used in real-world labs and devices, a layer number of several tens to several hundred is expected [188]. With such a high number of layers, even a small deterioration in thickness will lead to a rather poor optical performance of the filter. Therefore, it is even more challenging to fabricate the non-periodic thin film assemblies using a solution-based process. In this dissertation, optical interference filters are inkjet printed with either fully or partially non-periodic structures, contributing to suppressed ripples in pass regions.

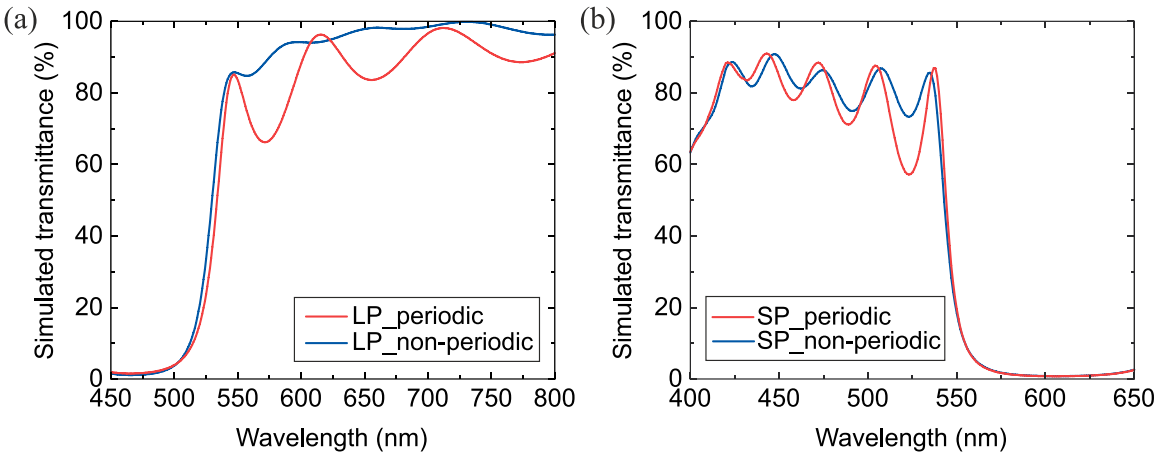

Figure 6.8: Transmission curve comparison of periodic and non-periodic thin film structures. The curves are the simulation results. (a) and (b) are the results of longpass (LP) and shortpass (SP) filters, respectively.

6.3 Inkjet-printed optical interference filters

Inkjet-printed edge filters

Edge filters include longpass and shortpass filters. The transmission or reflection curve of these filters is similar to a step with a sharp edge. Edge filters allow a part of the wavelength range to pass through while reflecting the rest. As described in the previous section, longpass filters allow the transmission of longer wavelengths, while shortpass filters transmit shorter wavelengths. In this section, inkjet-printed longpass and shortpass filters are demonstrated. To suppress the ripples in the pass region in both longpass and shortpass filters, non-periodic strictures are printed.

In the initial phase of fabricating inkjet-printed optical interference filters, simulations are executed to ascertain the optimal thickness of constituent layers. Essential Macleod, a commercial software developed by Thin Film Center Inc., is employed for the optical design. Both periodic and nonperiodic layer structures are generated by configuring the center wavelength and desired transmittance or reflectance. The integrated Optimac method is applied to systematically optimize the thickness of individual layers within the nonperiodic structure. This optimization process, comprising synthesis and refinement stages, is integral to the overall procedure aiming at attaining the final design of the optical filter.

Inkjet-printed longpass filter

Figure 6.9 (a) shows the concept of a longpass filter, where the longer wavelengths transmit through, and the short wavelengths are blocked. Figure 6.9 (b) shows the SEM image of the cross-sectional view of the printed longpass filter. The scale bar is 1 μm. The filter is designed using the simulation software Essential Macleod. With a desired transmission curve, the software gives each layer's thickness based on the material property input. Each layer has a different thickness, which is optimized with the overall optical perfor-

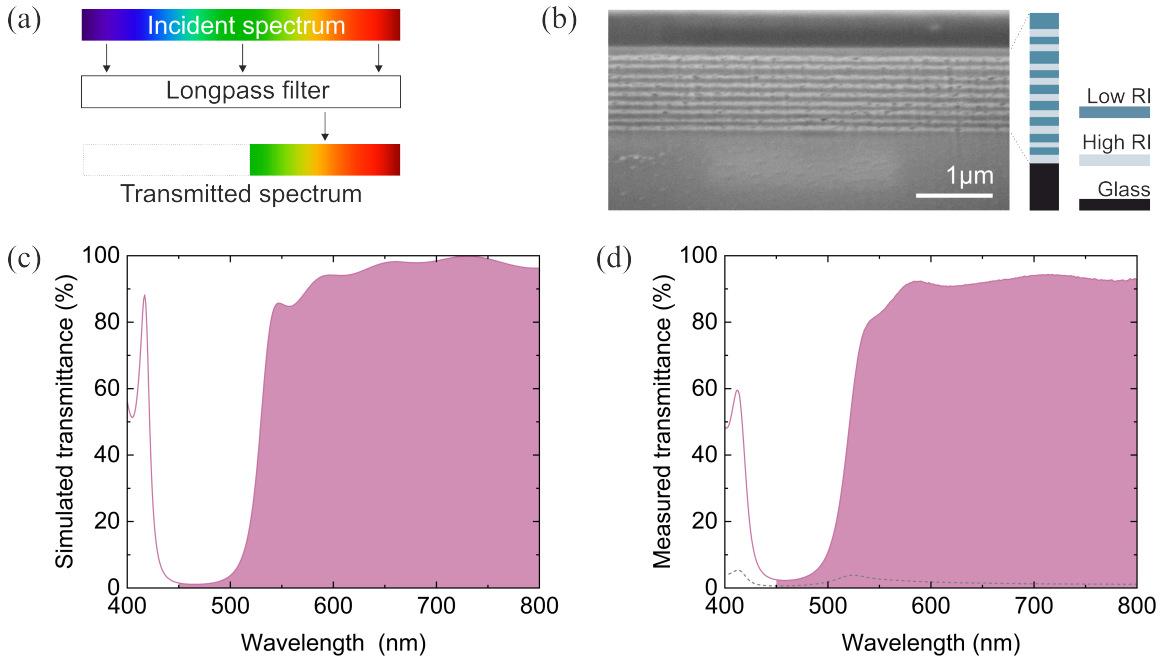

Figure 6.9: Inkjet printed longpass filter. (a) Concept of a longpass filter. (b) SEM image of the cross-section of the printed longpass filter. The color column on the right side indicates the material and layer thickness. (c) and (d) are simulated and measured transmission curves of the printed longpass filter, respectively.

mance of the filter. In the SEM image, layers composed of SiO_2 and TiO_2 nanoparticles are stacked alternately using inkjet printing. Different materials are differentiated by the color column on the right side. The glass substrate is indicated in black. The individual blocks in the color column have different heights, which implies the layer thickness difference.

Figure 6.9 (c) shows the transmission curve obtained from the simulation, where the cut-on wavelength is designed as 529 nm. The cut-on wavelength is typically defined as the wavelength where the transmittance of the filter rises to 50% of the maximum. It can also be used to describe the spectral position of the edge. The cut-on wavelength in longpass filters can vary from UV to IR, where the spectral region is not restricted. It is often used to define a starting point for the transmission window in the filter. However, flattening the transmission curve in the pass region is not easy, where ripples can be suppressed but always exist in the real case. Therefore, fluctuations in the curve cause deviations in defining the maximum transmittance. In this work, the calculation of the cut-on wavelength is optimized accordingly. The maximum transmittance is replaced with an average of the high transmittance in the pass range. Therefore, the obtained result is more practical and representative. For instance, the overall pass region of the designed longpass filter is from 450 to 800 nm. In the simulation, the filter possesses a high transmittance in the range of 540 to 800 nm with an average transmittance of 95.5%. The halve of this average transmittance is 47.8%, which is respective to a cut-on wavelength of 529 nm.

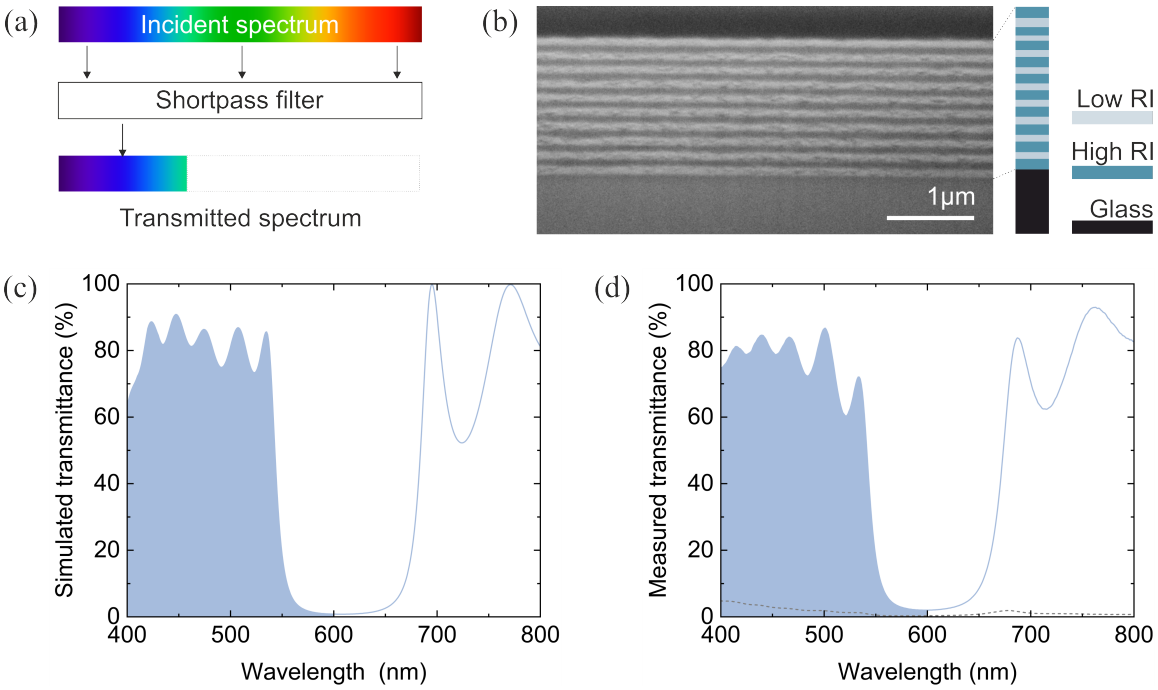

Figure 6.10: Inkjet printed shortpass filter. (a) Concept of a shortpass filter. (b) SEM image of the cross-section of the printed shortpass filter. The color column on the right side indicates the material and layer thickness. (c) and (d) are simulated and measured transmission curves of the printed shortpass filter, respectively.

After the longpass filter is printed, the respective transmission curve is measured and shown in Figure 6.9 (d). It can be seen that the transmission region in the printed filter starts from 450 nm, showing a good realization from the simulation to the fabrication. The cut-on wavelength in this printed filter is calculated the same way as the above. The wavelength range with high transmittance is from 540 to 800 nm, with an average transmittance of 91.7%. Therefore, the respective cut-on wavelength is 532 nm, which is close to the design. Additionally, the ripples in the pass region are found to be effectively suppressed in the printed filter. The scattering performance of the printed filter is characterized as well. The dashed grey line in Figure 6.9 (d) shows the diffuse transmittance remains below 2% between 600 and 800 nm. It exhibits a slight ridge within the 500 to 600 nm range, which can be attributed to the increased extinction of the TiO_2 layer at shorter wavelengths.

Inkjet-printed shortpass filter

Similar to the discussion in the section on the longpass filter, Figure 6.10 (a) shows the concept of a shortpass filter. There exist UV cut-off filters or IR cut-off filters, corresponding to different pass regions. Figure 6.10 (b) is the SEM image of the cross-section view of the printed shortpass filter, where the scale bar is 1 μm. The color column on the right side indicates the different materials used in individual layers. Furthermore, the varying heights of each block imply the non-periodic structure of the printed filter.

In shortpass filters, the cut-off wavelength is used to describe the spectral position of the edge. The value of the cut-off wavelength is defined as the transmittance of the filter declines to 50% of the maximum. Similar to the case in the longpass filter, the cut-off wavelength is not limited in the spectrum. It is a value that defines the cut-off edge of the pass region. Analogous to the method applied in the calculation of the longpass filter, the maximum value for calculating the cut-off wavelength is replaced with an average value, which is based on the high transmittance in the pass range. In this printed shortpass filter, the pass region is designed to be 400 to 600 nm. In the simulation, the wavelength range of 400 to 535 nm is used for calculating the average transmittance, which yields a value of 81.2%. Accordingly, the cut-off wavelength is 544 nm. The transmission curve obtained from the simulation is shown in Figure 6.10 (c). In Figure 6.10 (d), the measured transmission curve of the printed shortpass filters is displayed. The wavelength range used for calculating the average transmittance is from 400 to 533 nm, which mounts to 77.4%. Accordingly, the cut-off wavelength is 544 nm, which is the same as the designed value. In addition, the diffuse transmittance of the printed filter is also measured. It is depicted by the dashed grey line in Figure 6.10 (d), showing a decrease in value from 5% to nearly zero within the wavelength range of 400 to 600 nm.

Inkjet-printed bandpass filters

Type I: stacking architecture

The bandpass filter allows a part of the incident spectrum to pass through the filter. The basic concept of a bandpass filter is depicted in Figure 6.11 (a). The bandwidth of the transmitted spectrum can vary from sub-nanometers to several hundred nanometers. There are different approaches to realizing a bandpass filter. In this work, two common architectures are demonstrated. First is the one in Figure 6.11 (a), where a longpass is stacked on a shortpass filter, using glass as the substrate. The transmission bandwidth of the bandpass filter can be controlled by the overlapped pass region between two filters.

Figure 6.11 (b) is the SEM image of the cross-sectional view of the printed bandpass filter, where the scale bar is 1 μm. The color columns on the right side indicate the different materials and thickness variations. Longpass and shortpass units are marked with red and blue colors. The green unit in between is a thickness-matching layer, which consists of 2 single layers. As can be seen in the SEM image, individual layers are deposited homogeneously over each other. In total, 39 layers are deposited successfully. This structure is by far the only one that reaches such a high number of layers. Most of the work reported by far only realizes less than 3 layers; see in Chapter 3. In addition, it demonstrates the feasibility of inkjet printing an optical interference filter with tailored sub-units. This means the optical quality of the filter can be further improved by printing more units of the existing component if it is required.

Figure 6.11 (c) and (d) are the simulated and measured transmittance, respectively. For a bandpass filter, the characteristic parameters such as peak wavelength, cut-on wavelength, and cut-off wavelengths need to be defined. Similarly, the cut-on and cut-off wavelengths are determined by the 50% rule. In some bandpass filters, the pass region shows a flat top. Therefore, either the maximum or the average value shall be applied.

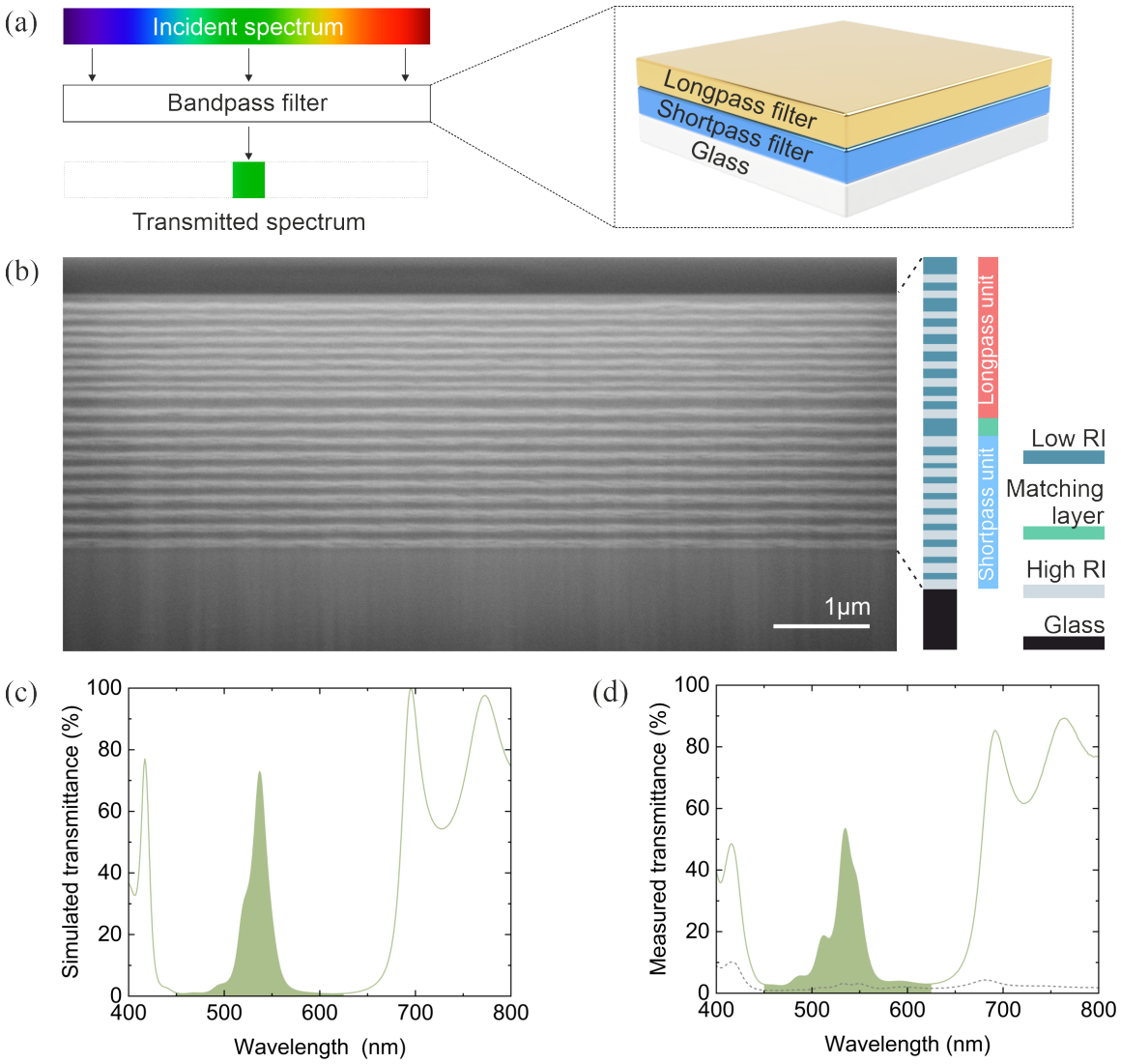

Figure 6.11: Inkjet printed bandpass filter based on stacking architecture. (a) Concept of a bandpass filter, which shows the spectrum selectivity on the left and the designed structure on the right. (b) SEM image of the cross-section of the printed bandpass filter. The color column on the right side indicates the material and layer thickness. (c) and (d) are simulated and measured transmission curves of the printed bandpass filter, respectively.

In this work, the pass region shows a sharp peak, making it easier to find the maximum transmittance. According to the simulation and the measured results, the wavelengths of maximum transmittance are found to be 537 and 535 nm, respectively. In addition, the cut-on wavelengths in the simulation and the printed filter are both 526 nm, and the cut-off wavelengths are 547 and 551 nm. This good realization of the initial design in the real fabricated filter indicates a highly controlled and repeatable printing process. Additionally, the diffuse transmittance was assessed and consistently stays below 3% within the specified region of interest, starting from 450 to 630 nm.

Type II: Fabry-Pérot (FP) etalon architecture

The second approach to designing a bandpass filter is the FP etalon architecture. The filter consists of three components, i.e., two mirrors and a cavity, as shown in Figure 6.12 (a). The incident light goes through a resonance within the cavity, resulting in constructive interference in the transmitted light. In this work, dielectric quarter wave (QW) stacks are printed and utilized as highly reflective mirrors. This is because the optical loss in the dielectric mirrors is low. Therefore, they are very suitable for use in optical resonators. Each QW stack produced in this work consists of seven individual layers. SiO_2 is the material used for the cavity.

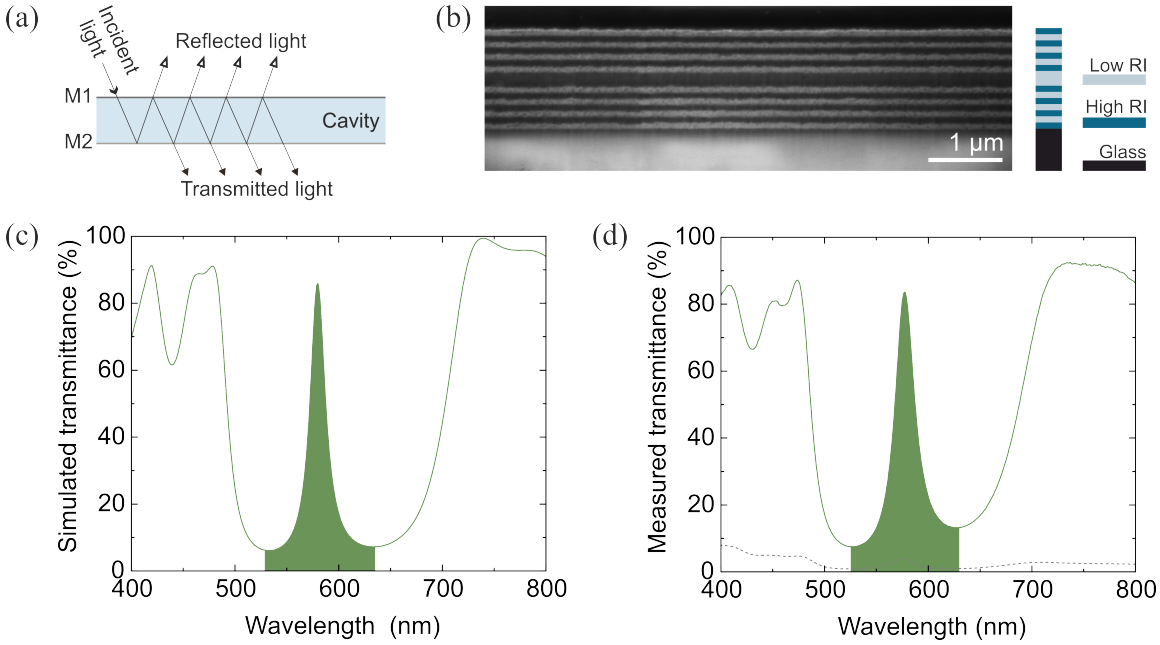

Figure 6.12: Inkjet-printed bandpass filter based on Fabry-Pérot (FP) etalon architecture. (a) The schematic of the filter. (b) SEM image of the cross-section of the printed bandpass filter. The color column on the right side indicates the material and layer thickness. (c) and (d) are simulated and measured transmission curves of the printed bandpass filter, respectively.

Figure 6.12 (b) is the SEM image of the cross-sectional view of the printed bandpass filter based on Fabry-Pérot (FP) etalon architecture, where the scale bar is 1 μm. The color columns on the right side indicate the information on materials and thickness. In the SEM image, it can be seen that the cavity is deposited between the mirror components, showing a sandwiched structure.

Figure 6.12 (c) and (d) are the simulated and measured transmittances, respectively. Sharp peaks can be seen in the images. The respective wavelengths of the peaks are 580 and 577 nm, with a transmittance of 85.9% and 83.7% in the simulated and fabricated filters, respectively. Therefore, the cut-on can be determined as 571 and 566 nm, and the cut-off wavelengths are 589 and 590 nm from the simulation and fabrication, respectively. The

diffuse transmittance is further measured where the values are below 3% in the region of interest, i.e., from 530 to 640 nm.

In the printed FP-type bandpass filter, one may find the residual sidebands in the transmission curve conspicuous. A common strategy is to add a functional layer inside the cavity. To enhance the performance, the printed filter is subsequently integrated with a silver layer. The silver layer is inserted in the middle of the cavity, as shown in Figure 6.13 (a), the SEM image of the cross-sectional view of the printed filter, where the scale bar is 1 μm. The thickness of the silver layer is around 60 nm, and the deposition is conducted by thermal evaporation. The color columns on the right side indicate the information on materials and thickness. The integrated silver layer, which is in the center of the cavity, can be clearly seen in the SEM image.

Figure 6.13 (b) and (c) are the simulated and measured transmittances, respectively. The unwanted sidebands are effectively suppressed in the presence of silver. In this filter, the peak wavelengths are 567 and 577 nm, obtained from the simulated and fabricated filters, respectively. The difference in the peak wavelength is 10 nm, which is larger than other fabricated filters. It is attributed to the thickness deviation of the deposited silver layer. Nevertheless, it can be improved by further optimizing the evaporation parameters. The cut-on wavelengths determined from the simulated and fabricated filters are 560 and 557 nm, respectively, and the respective cut-off wavelengths are 573 and 578 nm. The peak transmittance in the simulated filter is around 60%. However, it is around 40% in the fabricated device. This reduction in transmittance can be attributed to the absorption in the silver [189] and the surface plasmons at the metal-dielectric interfaces [190]. The diffuse transmission of the filter is measured where it remains below 5% in the pass region. Nevertheless, integrating a silver layer into the FP-type filters is a common and effective strategy to suppress the residual sidebands.

Until here, the inkjet-printed optical interference filters, including longpass, shortpass, and bandpass filters, are presented. The optical performance of each filter is characterized. Although it has been listed in the last two sections, Table 6.4 and Table 6.5 are provided to offer a clear comparison of the crucial parameters between the design and fabrication.

Table 6.4 lists the optical parameters of the edge filters. LP and SP represent the longpass and shortpass filters, respectively.

Filter type	**Result type**	**Cut-on wavelength (nm)**	**Cut-off wavelength (nm)**
LP	Simulated	529	/
	Printed	532	/
SP	Simulated	/	544
	Printed	/	544

Table 6.4: Comparison of simulated and fabricated edge filters.

Table 6.5 lists the optical parameters of the bandpass filters. BP represents the bandpass filter, FP-type means the filter based on Fabry-Pérot (FP) etalon architecture, and (Ag) denotes the filter contains an intermediate silver layer.

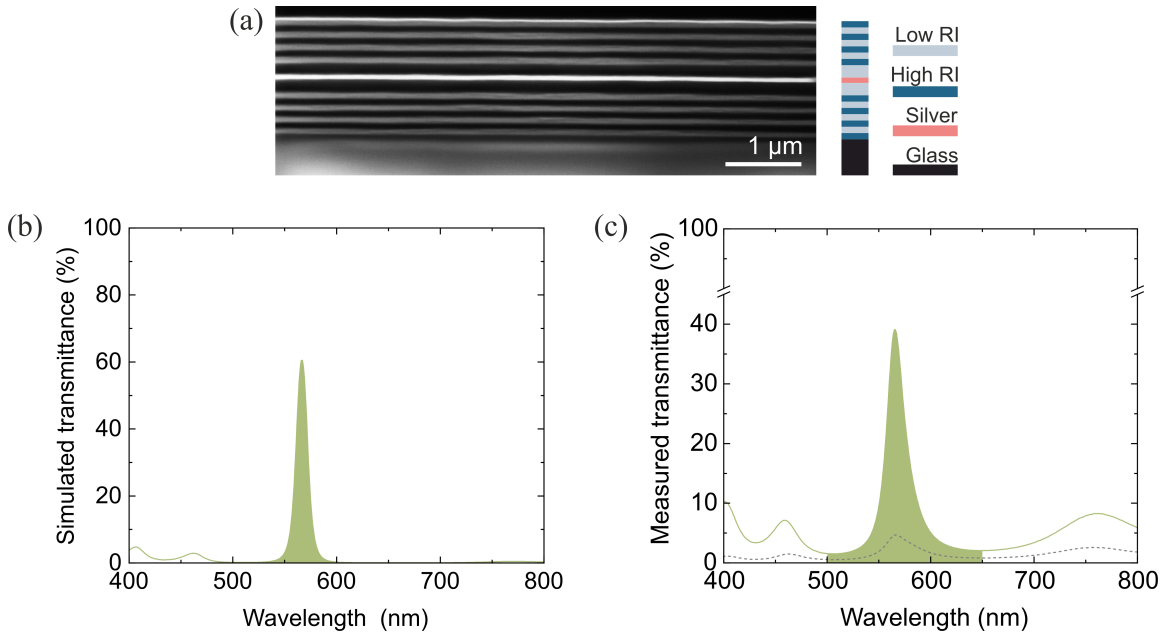

Figure 6.13: Sideband suppression in inkjet-printed bandpass filter based on Fabry-Pérot (FP) etalon architecture. (a) SEM image of the cross-section of the printed bandpass filter. The color column on the right side indicates the material and layer thickness. (b) and (c) are simulated and measured transmission curves of the printed bandpass filter, respectively.

It can be seen the spectral deviation of the optical parameters listed in the tables above is within ±5 nm. This is a number comparable to commercial products, which can be found in online stores such as Edmund Optics (www.edmundoptics.com) and Thorlabs (www.thorlabs.com). It shows the potential of fabricating precision optics by inkjet printing.

Inkjet-printed dichroic filters

Dichroic filters are capable of splitting the incident spectrum into two complementary parts. For instance, when white light hits the dichroic filter, the filter reflects green light and allows red light to pass through, see Figure 6.14 (a). The one-euro coin and a caliper in the image are scale references. These filters are commonly used in fluorescence microscopy and Raman spectroscopy to reflect certain wavelengths. Therefore, such filters are also called dichroic mirrors or Bragg mirrors. The spectral range for reflection can vary significantly from one to another. In some cases, it can be as narrow as several tens of nanometers [191] or as broad as several hundred nanometers [192]. This is a major difference compared to the longpass or shortpass filters.

In this section, printing different dichroic filters with various optical responses is presented. The filters are printed in a relatively large size, i.e., 10×10 cm^2. Each filter consists of nine bi-layers. Figure 6.14 (b) and (c) are the reflection and transmission spectra of a

Filter type	Result type	Peak wavelength (nm)	Cut-on wavelength (nm)	Cut-off wavelength (nm)
BP	Simulated	537	526	547
	Printed	535	526	551
BP FP-type	Simulated	580	571	589
	Printed	577	566	590
BP FP-type (Ag)	Simulated	567	560	573
	Printed	577	557	578

Table 6.5: Comparison of simulated and fabricated bandpass filters.

printed dichroic filter. The reflected green color is observed with a dark background, while the transmitted red color is from a bright background.

Various dichroic filters with distinct spectral properties are manufactured in this work. The center wavelength and the peak reflectance are two important factors that define these filters. Here, filters with center wavelengths varying in the visible light range are realized based on the initial design. In addition, the peak reflectance in all the filters has reached around 95%. Figure 6.14 (d) and (c) display the simulations and the measured results from the printed five filters with different center wavelengths. By precisely controlling the deposited layer thickness, the center wavelength is tuned from 350 nm to 680 nm. The detailed values are listed in Table 6.6. The difference between the simulation and the measured results is less than 1% of the center wavelength, which indicates satisfactory printing quality.

Parameter	Results	Filter 1	Filter 2	Filter 3	Filter 4	Filter 5
Center wavelength (nm)	Simulated	380	480	590	620	680
	Printed	383	479	592	619	678
Peak reflectance	Simulated	99.3%	96.0%	91.8%	91.3%	95.4%
	Printed	95.0%	96.0%	96.5%	94.7%	94.0%

Table 6.6: Center wavelength and peak reflectance of the printed dichroic filter.

The printing process for these large-size dichroic filters is modified. In the inkjet printing process in Figure 6.7 in Section 6.2, the procedure includes a drying step. However, this step is skipped when printing the 10×10 cm^2 size filters. This is achieved by properly adjusting the nozzle jetting frequency and the printing speed so that the wet layer dries during printing. The detailed parameters can be found in Chapter 5. Consequently, the entire printing cycle contains only inkjet printing and annealing. The process is significantly simplified, resulting in a reduction in fabrication time. It is worth mentioning that the large-size fabrication helps to reduce the unit cost of filter production. A similar example is that a larger wafer size is preferable in microchip manufacturing to reduce the

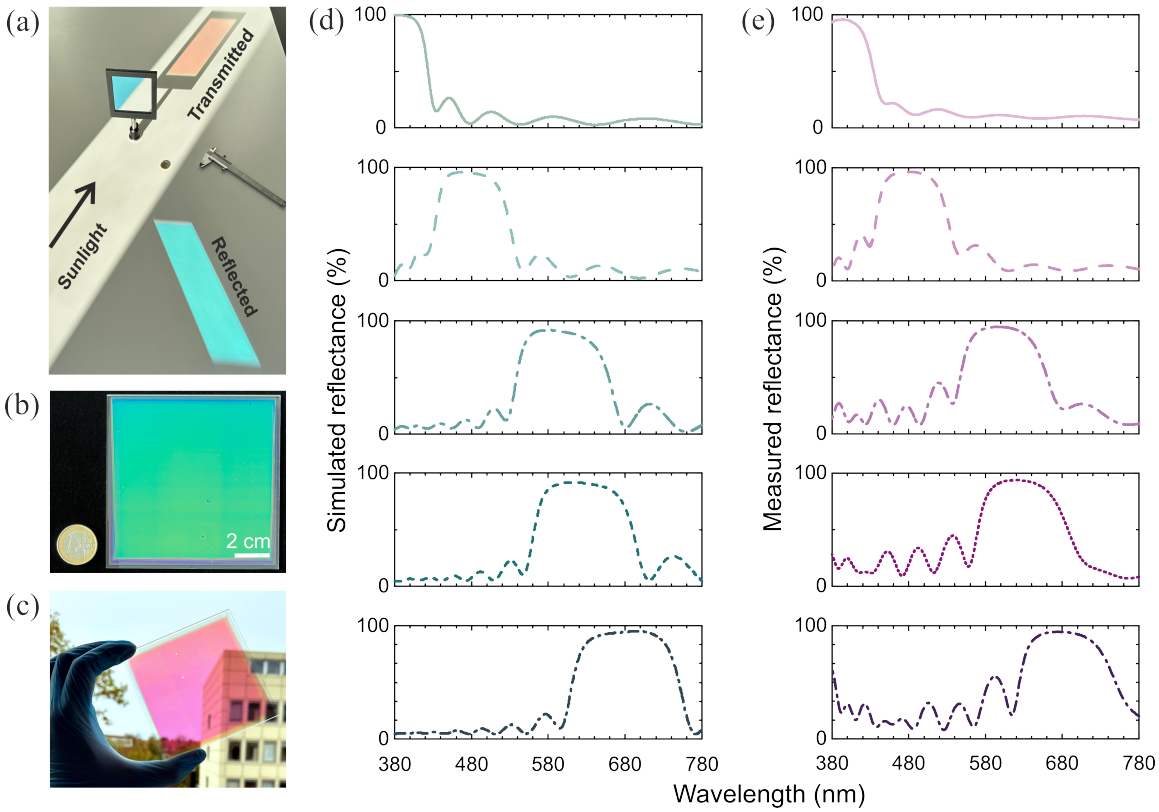

Figure 6.14: Inkjet-printed dichroic filters. (a) Spectrum splitting capability of the dichroic filter. (b) and (c) Inkjet-printed 10×10 cm^2 dichroic filters, in the dark and the bright background, respectively. (d) Designed reflectances of different dichroic filters. (e) Reflectances measured from the printed dichroic filters.

unit price of the product. Therefore, in this dissertation, the filter size is pushed to the maximum size, which is limited by the capability of the device. The details are presented in the next section.

6.4 Upscaling of inkjet-printed dichroic filters

Inkjet-printed dichroic filters in A4 size

Based on the printing process of 10×10 cm^2 size, further optimization of the printing parameters is conducted to achieve an even larger size. The printer used in this work has a printing platform with a size of around 227×327 mm^2. Therefore, the largest size demonstrated in this work is DIN A4 size (210×297 mm^2).

Figure 6.15 shows the inkjet-printed dichroic filter with an A4 size. It consists of 5 bilayers with a center wavelength of 585 nm. The normalized reflection curve is inserted in Figure 6.15. This is by far the largest optical interference filter ever produced by solution processing. Moreover, the printing task is fully conducted in ambient conditions. Nowadays, since the filters are mostly fabricated in vacuum chambers, the sizes are usu-

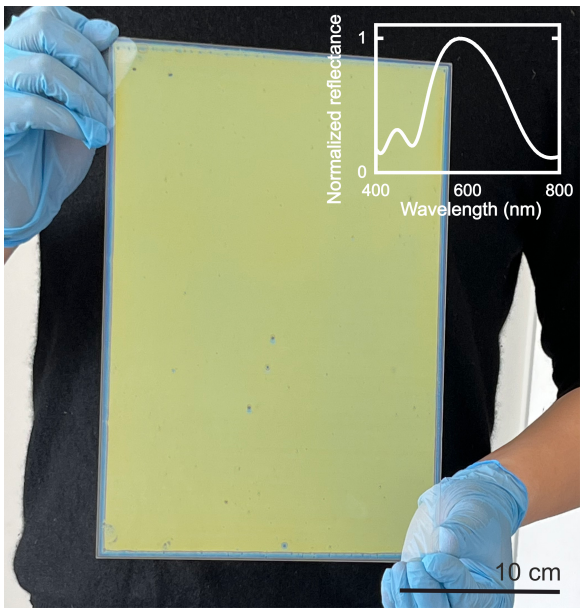

Figure 6.15: Inkjet-printed dichroic filter in A4 size.

ally limited, especially for high-end optical interference filters. Using an inkjet printer with a larger printing platform, it is feasible to print filters with further increased sizes. Therefore, it shows the potential of being applied for large-area and large-scale industrial production.

Some defects can be found in the printed filter, which is probably caused by the dust during the transportation between the printing and annealing stations. The detailed discussion is presented in Chapter 9.

Homogeneity characterization of the A4 size filter

An important factor in the optical quality control of the optical filters is homogeneity. In this work, the essential properties to be characterized are the peak, cut-on, and cut-off wavelengths. Since the printed filter is in A4 size, a large number of measurement points need to be applied. Here, twenty individual sites are selected on the filter, as seen in Figure 6.16 (a). The reflectance is measured on each site. During the measurement, the size of the light spot used is 2 mm in diameter. The lateral and vertical distance between the neighboring sites are 35 and 40 mm, respectively.

In Figure 6.16 (b), the measured results are plotted individually. Besides the three parameters mentioned above, full-width-half-maximum (FWHM) is also included in the assessment. FWHM is the bandwidth of the spectrum, which is calculated as the difference between the cut-on and cut-off wavelength. The value of each parameter can be read from the figure. For the central wavelength, the mean value is 583.9 nm, with a standard deviation of 1.4 nm. The cut-on wavelength shows a mean value of 509.2 nm and a standard deviation of 0.6 nm. The cut-off wavelength has a mean value of 694.8 nm and a standard deviation of 0.9 nm. By calculating the difference between each pair of cut-on and cut-off wavelengths, FWHM values are obtained with a mean of 185.7 nm and a standard devia-

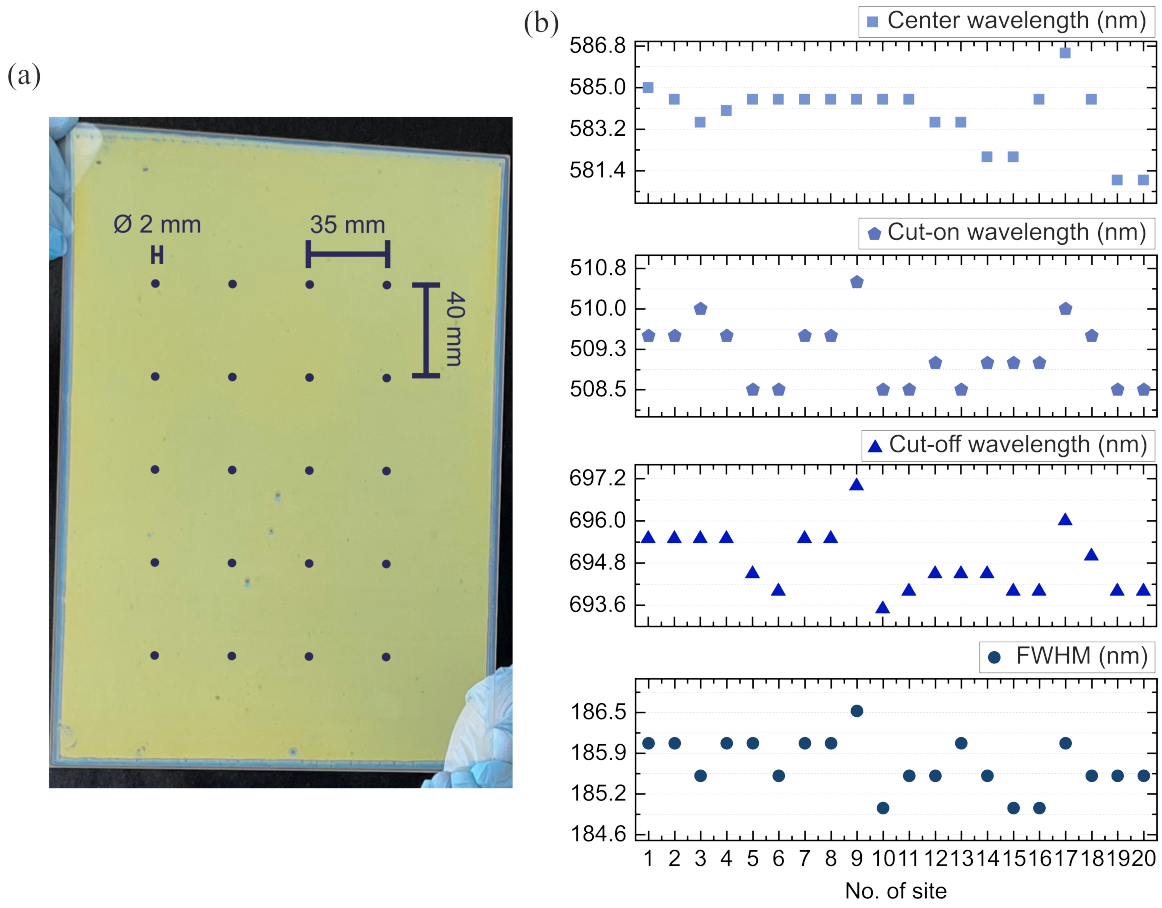

Figure 6.16: Homogeneity characterization in the inkjet-printed dichroic filter.

tion of 0.4 nm. All the standard deviations are surprisingly low, being below 1 nm. This denotes a highly uniform optical property over the A4 size filter. It further indicates a highly homogeneous thickness distribution over the surface in this multilayer structure. It needs to be pointed out that the process and inks developed in this work focus on the upscaling of the filers. Therefore, the edge defects are not considered. In reality, the filter can be cut into desired sizes, such as half or one-inch diameter. Eliminating the edge defects requires a completely different route for both ink and printing process development. However, this is out of the scope of this work. The detailed discussion is presented in the outlook of the future work in Chapter 9.

6.5 Laterally patterned filters

Inkjet printing has a technical advantage known as drop-on-demand, which makes it well-suited for lateral patterning. This means that inkjet printing is highly effective for creating patterns in a lateral direction. The optical filters can be patterned using a digitally controlled printing process. This allows for the creation of different forms, including a filter array or a planar filter with an irregular contour. In the present study, an optical filter is printed in the form of a logo.

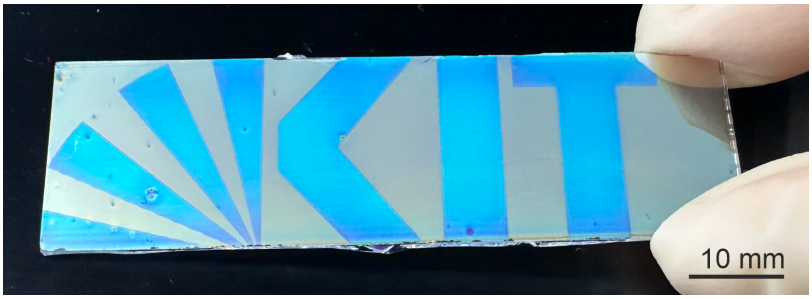

Figure 6.17: Inkjet-printed patterned filter.

Figure 6.17 shows the printed filter with a dimension of 25×75 mm^2. The filter in this work is printed with a pattern that has been designed to incorporate the KIT logo. This filter is comprised of four bi-layers, producing the desired color effect. To produce this filter using traditional methods, a mask must be fabricated and carefully placed over the substrate. The placement of the mask needs to ensure that the positions are correctly aligned. However, using inkjet printing, the logo is directly printed without any additional shielding technology. In this printed filter, the edge of the pattern is sharp. In addition, fine structures such as slashes and corners are well reproduced from the original design.

6.6 Filters printed on flexible substrate

The demonstrated fabricated filters above are printed on glass substrates. However, by properly adjusting the annealing parameters, the printing process has been successfully transferred to a flexible foil. This is another advance in the fabrication of optical filters. The conventional vacuum-based approach often repels the use of polymer substrates since the high temperature during the deposition process damages the polymer and even leads to the contamination of the devices. Therefore, fabrication of filters with low temperatures, i.e., less than around 100 °C, is very attractive for polymer substrates. In this situation, only atomic layer deposition can achieve low temperatures [193]. However, the disadvantage of using atomic layer deposition is the much longer process time compared to other technologies.

In this section, a patterned optical filter printed on polyethylene terephthalate (PET) foil (Puetz Folien) is demonstrated. The size of the filter in Figure 6.18 is 25×75 mm^2 and the size of the foil is 90 × 90 mm^2. The same logo in the previous section is printed. The color of the logo arises from the interference of 4 bi-layers. The lines and corners are printed with good quality. The change in the fabrication process is the annealing temperature. Since the PET foil cannot withstand a high temperature, the annealing temperature is optimized accordingly. Instead of using 200 °C, the foil is annealed at 100 °C. Consequently, the time needed for annealing increases from 10 minutes to one hour. Further optimization can be done in inks to reduce the required annealing time. For instance, using UV-curable ink can shorten the time by photonic curing, which requires only a second-scale time period.

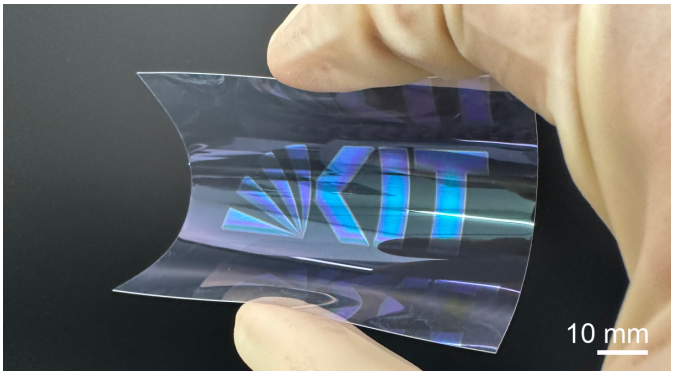

Figure 6.18: Inkjet-printed filter on flexible foil.

The robustness of the printed filter is tested by bending the substrate 100 times as in Figure 6.18. After the test, the filter shows the same color performance as before. Further investigation of micro-cracks is needed to be conducted. Nevertheless, the scope of the work is to demonstrate the transfer of the printing process from glass to foil. Enhancement of the filter mechanical property shall be the future work.

6.7 Printing process of the demonstrated filters

The detailed inkjet printing process for the demonstrated optical filters is as follows: The fabrication of optical interference filters involves the utilization of an inkjet printer, specifically the PixDro LP50 model (SÜSS MicroTec SE), equipped with 10 pL cartridges (FUJIFILM Dimatix, Inc.). The printing process is conducted under standard ambient conditions with a temperature range of 21–22 °C and humidity levels between 40% and 50%. Prior to filling the ink tank, both inks undergo filtration using (full name of PTFE) PTFE filters with a pore size of 0.2 µm. Throughout the printing process, the printhead temperature is consistently maintained at 27 °C, and jetting frequencies are set between 2 and 2.5 kHz. The substrate moves along the y-axis, and the specific printing resolution, ranging from 500 to 900 dpi, is selected based on the desired layer thickness.

Longpass, shortpass, and bandpass filters are fabricated on individual 2.5×2.5 cm^2 glass substrates. The printing velocity varies from 70 to 100 mm/s depending on the chosen dpi, the quality factor is set at 2, and the jetting frequency is set at 2 kHz. The substrate temperature remains constant at 25 °C. TiO_2 layers are naturally dried in the air, while SiO_2 layers are dried at a slightly reduced pressure of 0.8 atm to expedite the drying process. For filters designed in quarter-wave structures, larger glass substrates (10×10 cm^2)) are employed. The printing speed ranges from 100 to 115 mm/s based on dpi, the quality factor is set at 2, and the jetting frequency is set at 2 kHz. The printer substrate temperature is maintained at 25 °C. Both TiO_2 and SiO_2 layers undergo natural drying in the air during the printing process. A filter printed on an A4 glass substrate is also designed in a quarter-wave structure. It is printed at a speed of 125 mm/s with a quality factor of 2 and a jetting frequency of 2.5 kHz. The printer substrate temperature is held constant at 25 °C, similar to the previous processes, and both TiO_2 and SiO_2 layers undergo natural

drying in air. Following the printing of each layer, annealing processes are conducted on a hotplate at a temperature of 200 °C for 10 minutes.

6.8 Comparison with commercial products

In this section, the optical performance of the inkjet-printed filter is compared with that of commercial products, which are purchased from Edmund Optics. Here, the filters compared are the longpass and shortpass filters. The commercial filters purchased show similar spectrum properties as the printed filters. Detailed information on the commercial products is listed in Table 6.7. Both commercial products are produced by the vacuum-based approaches. The cut-on wavelength of the longpass filter is 500 nm, and the cut-off wavelength of the shortpass filter is 450 nm. The size of the commercial products is relatively small, 6×6 mm^2, compared to the inkjet-printed optical filters, which is 20×20 mm^2.

Source	Fabricating method	Filter type	Cut-on/off wavelength	Size (mm^2)	Online store item number
Commercial	Vacuum-based	LP	500 nm	6×6	15234
		SP	450 nm	6×6	15200
This work	Inkjet-printed	LP	532 nm	20×20	/
		SP	544 nm	20×20	/

Table 6.7: Information of the compared filters.

The comparison of the optical performance between the inkjet-printed and commercial products is plotted in Figure 6.19. The two left images present the longpass filters, while the two right images belong to the shortpass filters.

Upon comparison to commercially available longpass filters, the inkjet-printed filter demonstrates a similar level of transmission in the pass region, particularly for the pass range starting from the wavelength of 500 nm. The optical property of the filter in the 430-500 nm range exhibits a satisfactory blocking performance of approximately 3%. However, this result is considered moderate when compared to commercial filters. This difference is attributed to the lower number of layers, indicating potential enhancement through the addition of more layers. Residual transmission (400-450 nm) can be suppressed based on specific application requirements through targeted modifications of the stack design. However, the proper consideration of the optimal performance and the fabrication complexity is essential.

In the comparison of the shortpass filters, the inkjet-printed SP filter demonstrates satisfactory transmission within the pass region. To enhance the transmission characteristics in this region, optimization of layer thicknesses can be employed. It is worth noting that both printed and commercial filters exhibit residual transmission in the longer wavelength range, and the suppression of the unwanted transmission can be achieved through the implementation of more intricate layer stacks. Importantly, this is not always necessary to suppress the transmission in the spectral range that is out of interest. Although

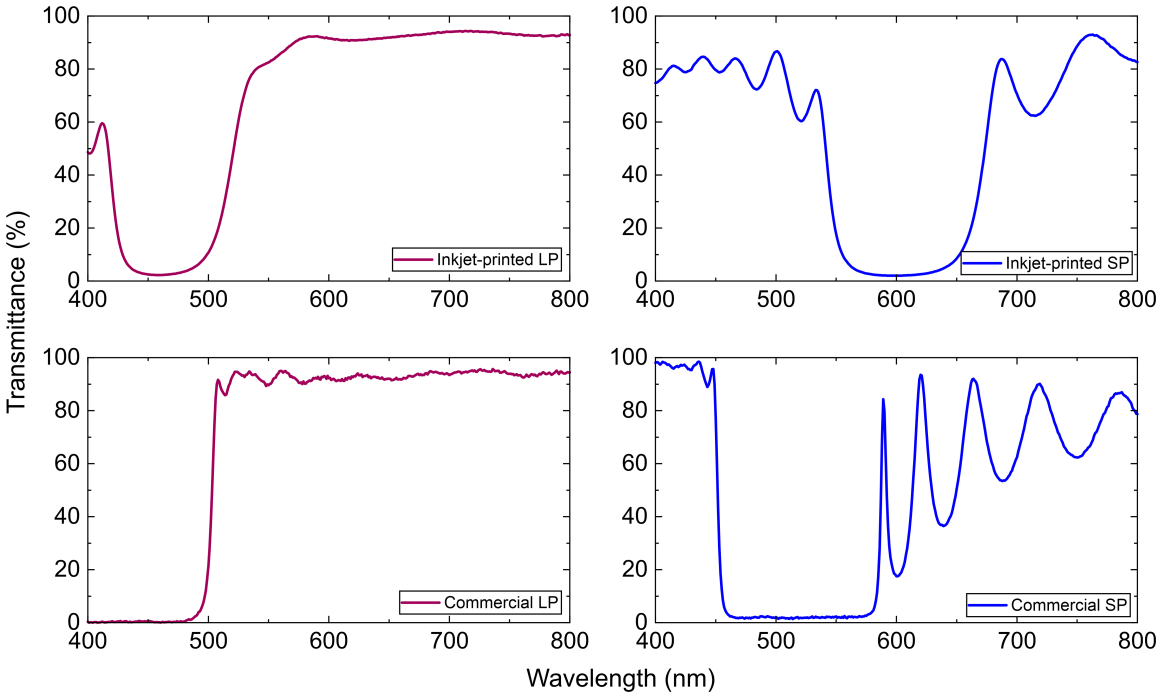

Figure 6.19: Optical performance comparison between the inkjet-printed and commercial filters.

adding more layers or stacks can be achieved based on specific applications, the extra effort and the cost need to be considered at the same time.

Strategy for enhancing the optical performance of printed filters

Residual band suppression

Further optimization can be conducted to enhance the optical performance of the printed filters, for instance, suppression of the unwanted residual bands in the printed long pass filters. In Figure 6.19, the transmission curve of the longpass filters shows a bulge in the wavelength range of 400 to 450 nm. To push the optical quality of the printed filter close to the commercial product, the transmission in the range mentioned above should be suppressed.

In optical filter design, a frequently employed strategy for eliminating undesired transmission is to broaden the optical stopband, which is the band that the transmittance is very low. This objective is usually achieved by incorporating multiple optical cavities. In this study, the printed longpass filter is configured with a cut-on wavelength of 532 nm. To effectively suppress the residual transmittance within the 400 to 450 nm wavelength range, an additional cavity, functioning as another longpass filter, is stacked upon the initial cavity.

Here, the proof of concept for suppressing the undesired transmission is demonstrated in simulated results. In Figure 6.20 (a), the transmission curve of the originally designed single cavity longpass filter is depicted. The residual peak in the range of 400 to 450 nm is

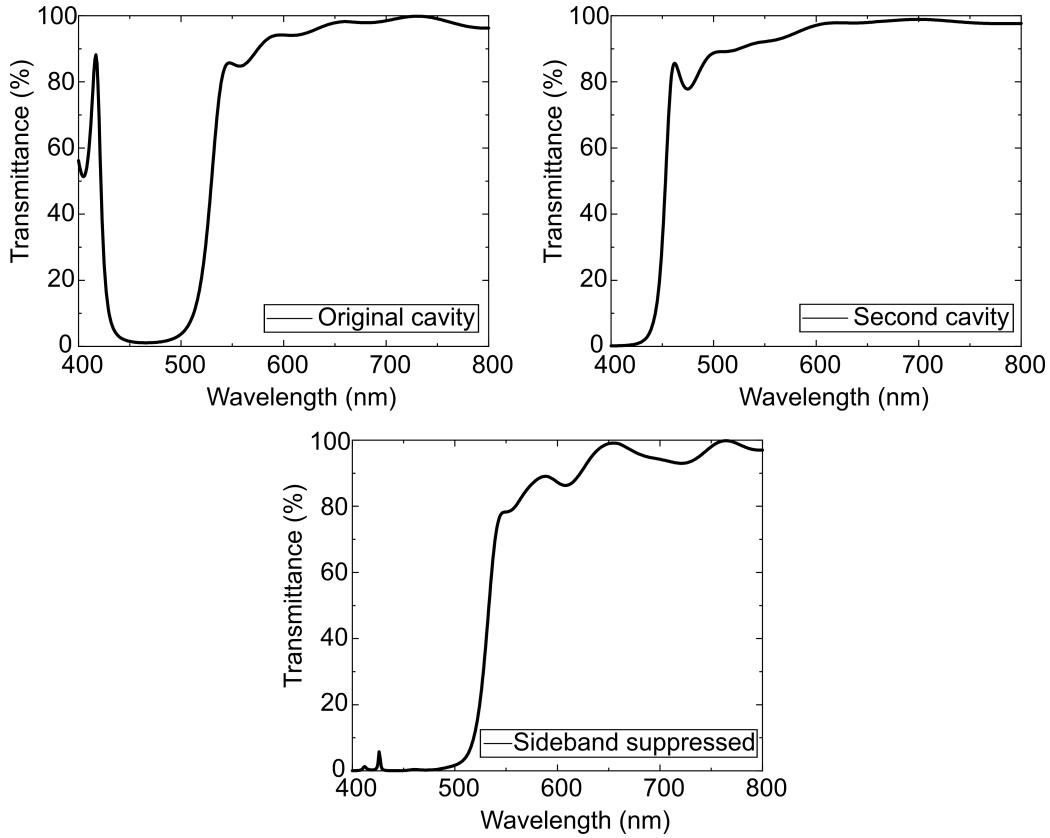

Figure 6.20: Sideband suppression in printed filters. The two diagrams in the upper row belong to the original and designed second cavity, respectively. The diagram in the lower row shows the result of combining these two cavities.

apparent. In Figure 6.20 (b), the transmission curve of a secondary designed cavity is plotted. In this second cavity, the center wavelength of the stopband is shifted 50 nm towards the shorter wavelength direction. Through the strategic stacking of these two cavities, the final filter is obtained. Figure 6.20 (c) demonstrates the effective suppression of residual transmission within the 400 to 450 nm range. This is a straightforward demonstration of how the residual transmission can be suppressed. Additionally, more optimizations can be done to further improve the spectral behavior. For instance, individual layer thickness and the total layer number within two optical cavities can be optimized, treating the stack as an entire entity or including more cavities to suppress the spikes in the curve.

Increase of the optical density

The optical density is the ability of a filter to block the light. It is defined as

$$\text{Optical density} = -\log_{10} T \tag{6.7}$$

where T is the transmittance. An increased optical density indicates an enhanced ability to block light within the spectral range of low transmission. Therefore, to increase the optical density, more layers can be added to the current design. Here, a longpass filter is

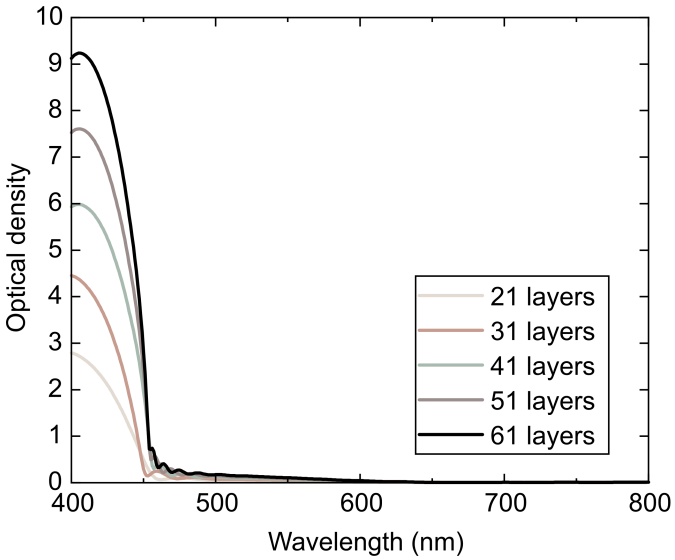

Figure 6.21: Increase of the optical density in printed filters.

used as an example. The filter has a cut-on wavelength of 450 nm, which means the light is intended to be blocked below this wavelength.

Figure 6.21 shows the curves of the simulated results. Different layer numbers are applied in different designs. The number of layers are 21, 31, 41, 51, and 61. It can be seen that with the increase of the total layer number, the optical density in the blocking wavelength increases from 2.8 to over 9. An OD of 9 represents a transmittance of one over a billion, which is an ultra-high value. In some applications, a high optical density is required, such as fluorescence microscopy. Including more layers in the optical filter is an established approach in industry.

6.9 Durability test of printed layers

The durability of the filters is highly important in practical use. The critical properties include layer adhesion and anti-abrasion. There are two standards that can be referred to, i.e., MIL-PRF-13830B and DIN EN ISO 2409. These two standards give detailed testing conditions and parameters. In this work, to assess the durability of the printed filters, adhesion and abrasion tests are conducted accordingly.

Adhesion test

The adhesion test is an overall performance characterization of the adhesion between the deposited layers, as well as between the layer and substrate. Two filters annealed at different temperatures, 200 °C and 500 °C, are tested. Both filters consist of 4 layers on the glass substrates. Before the test, the filters need to be placed in a climate chamber with a temperature of 48 ±3 °C and a relative humidity maintained at 95% to 100% for 24 hours. These parameters are guided by the two standards mentioned above.

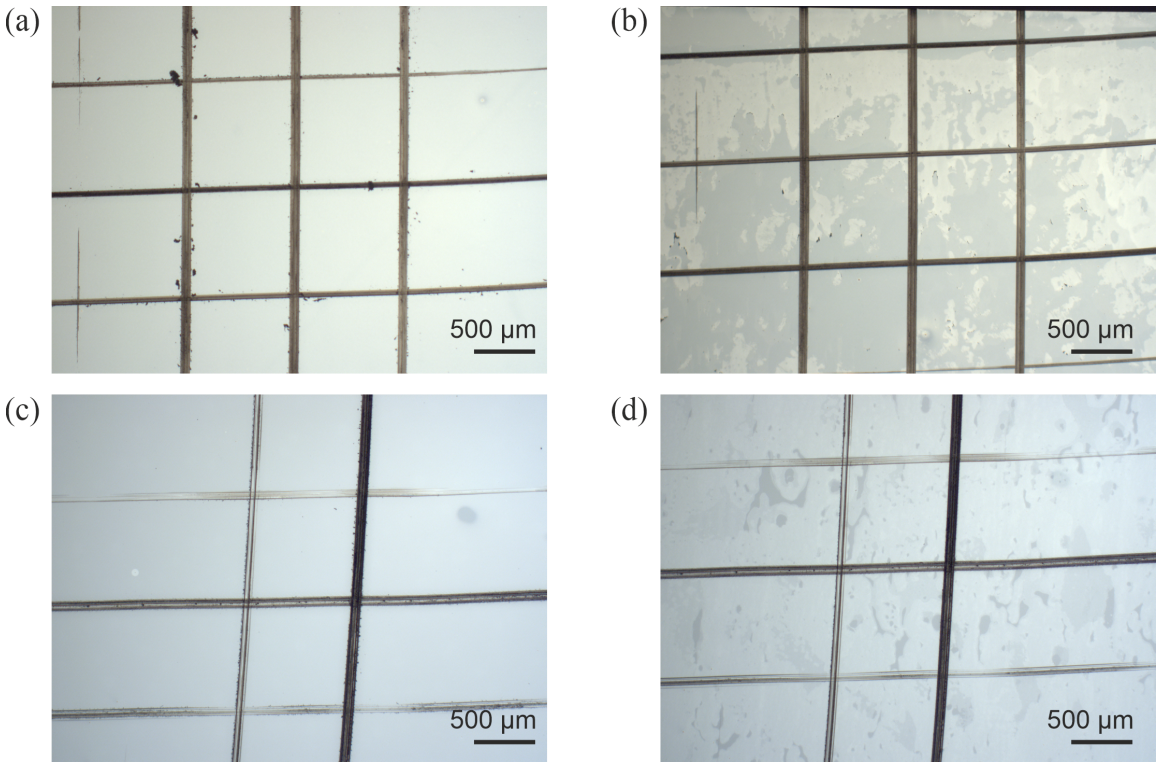

Figure 6.22: Adhesion test based on different annealing temperatures.

After the procedure in the climate chamber, the filters are crosscut by a steel cutter. As required by the standards, cellophane tape is firmly attached to the surface and rapidly removed at an angle that is normal to the surface. The tape will remove the materials if the adhesion is not sufficient. DIN EN ISO 2409 defines the class of quality according to the ratio of the removed area to the total area. The detailed Class definition is listed in Table 6.8.

Figure 6.22 shows the results of the adhesion test, where (a) and (b) are the microscope images of the filter annealed at 200 °C for 10 min before and after applying the tape. The dimmed area in Figure 6.22 (b) is the area that has been removed. The ratio of the removed

	Ratio of the removed area
ISO Class 0	≈0
ISO Class 1	≤5%
ISO Class 2	5%-15%
ISO Class 3	15%-35%
ISO Class 4	35%-65%
ISO Class 5	≥65%

Table 6.8: Adhesion class definition according to DIN EN ISO 2409.

area is calculated in the software Matlab, giving a value of more than 65%. Therefore, the adhesion quality of the filter is in Class 5., which is the lowest. However, After annealing the filter at 500 °C for 10 minutes, the ratio of the removed area decreases to 5%-15%. The results are shown in Figure 6.22 (c) and (d), which are the surfaces before and after applying the tape, respectively. Consequently, the quality is defined as ISO Class 2. Therefore, the enhancement of the adhesion can be achieved by raising the annealing temperature.

Various approaches can be employed to enhance both the adhesion between nanoparticles and substrates and the adhesion among the nanoparticles themselves, such as using oligomers [194], including an interlayer [195], pre-treatment of the substrate [195], modifying surface ligands of nanoparticles [196], and substrate surface roughness control [197].

Abrasion test

The filters in the abrasion test are placed in the climate chamber with the same condition as in the adhesion test. The abrasion test conducted in this work is based on the item "C. 4. 5. 11 Moderate abrasion" in standard MIL-PRF-13830B. The filters undergoing testing are subjected to a gentle abrasion procedure. Initially, the filter surface is rubbed with a clean, dry, laundered cheesecloth pad. The cheesecloth has dimensions of 1/4 inch (6.4 mm) in thickness and 3/8 inch (9.5 mm) in width. Ensuring accurate testing requires securely affixing the cheesecloth pad to the tester, ensuring a complete and repeatable testing process. Subsequently, the tester, equipped with the cheesecloth pad, moves across the filter surface in a back-and-forth motion for a total of 25 complete cycles, equivalent to 50 strokes. Throughout this process, it is crucial to maintain a continuous force of not less than 1.0 pounds (0.45 kg). After this procedure, the filters are observed with the microscope. The dimensions of the surface scratches are measured. According to the standard, the scratch number is defined by the scratch width. The filter quality regarding the anti-abrasion is characterized subsequently.

Figure 6.23 shows the results of the abrasion test. Figure 6.23 (a) is the original surface before the test. Figure 6.23 (b) contains four images. It is a series of zoomed-in microscope images from image I to image IV. From the images, the width of the induced scratch after the test is within 5 μm. Standard MIL-PRF-13830B defines a parameter called scratch number based on the scratch width. It is used to classify the surface quality of a filter against the abrasion.

Table 6.9 shows the scratch number and the corresponding scratch width. A smaller scratch number belongs to a small scratch width, which indicates a better surface quality. In this work, the observed scratch width is below 5 μm. Therefore, the surface quality of the printed filter is classified as Scratch number 5, denoting the highest surface quality.

6.10 Summary and discussion

In this chapter, the work of inkjet-printed optical interference filters is presented. Inks with different refractive indices are formulated. Moreover, inkjet printing processes for different filters are developed. The strong interplay between the inks and the printing

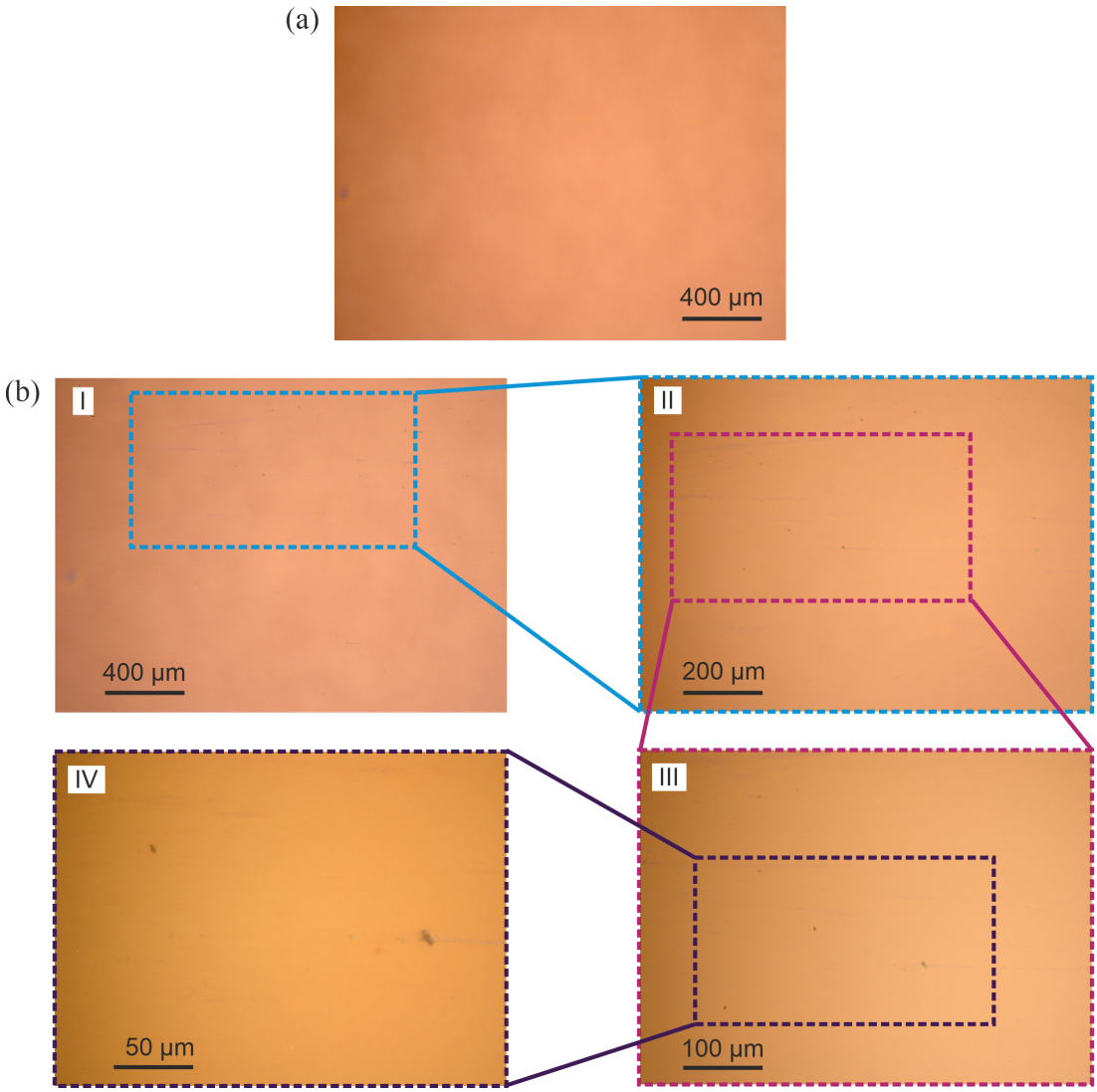

Figure 6.23: Optical images of printed filters before and after the abrasion test.

process is well-controlled. Consequently, longpass, shortpass, bandpass, and dichroic filters are fabricated by inkjet printing in ambient conditions. The optical responses of the individual filters are precisely realized from the designs, where the maximum shift of the center wavelength between each other is below 1% of the center wavelength. In addition, upscaling of the inkjet printing process and the filters are demonstrated. Dichroic filters are printed with well-replicated optical properties. Tuning of the center of the stopband is achieved. Subsequently, the size of the dichroic filter is upscaled to A4 size (210×297 mm^2). Importantly, the drying step is eliminated from the inkjet printing cycle of large-size fabrication. Therefore, the printing process is largely simplified, containing only the printing and annealing steps. The homogeneity of the printed A4 size filter is characterized. The small standard deviations of the central, cut-on, and cut-off wavelength validate a uniform optical property. Additionally, patterned filters are fabricated both on glass and foils. The latter is achieved by properly adjusting the post-treatment process.

Scratch number	Scratch width (mm)
5	0.005
10	0.010
20	0.020
40	0.040
60	0.060
80	0.080
120	0.120

Table 6.9: Scratch number and the corresponding scratch width according to standard MIL-PRF-13830B.

After the fabrication is accomplished, the filters are compared with commercial products. Optical transmittance in printed long pass and short pass filters are compared with products purchased from Edmund Optics. The solution of enhancement of the inkjet-printed optical filters is discussed and presented. Moreover, the durability of the printed optical filters is characterized. The tests contain adhesion and abrasion. The obtained results imply a satisfactory surface quality of inkjet-printed filters.

7 Mechanoresponsive smart windows - Pixelated haze by inkjet printing

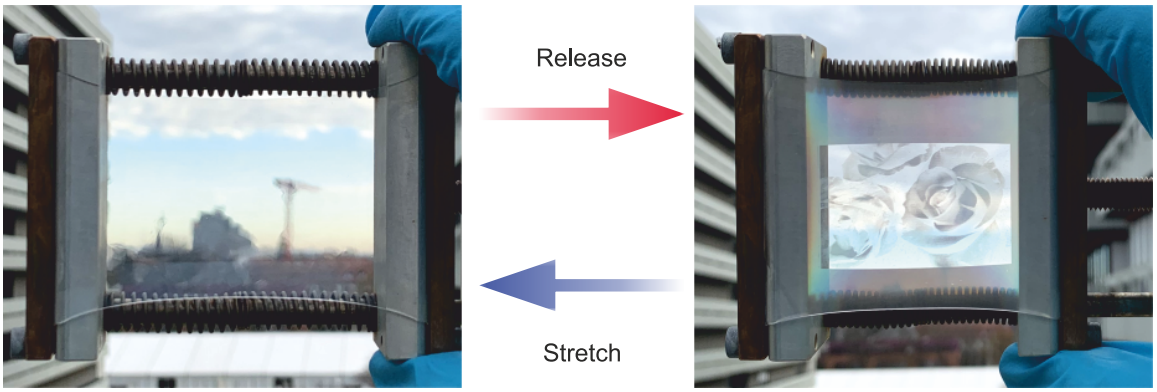

Figure 7.1: Fabricated mechanoresponsive smart window.

In recent years, significant research efforts have been dedicated to the development of mechanoresponsive smart windows due to their promising applications in signage and versatile light management. However, incorporating display functionality into these smart windows remains a notable challenge, primarily due to the intricate nature of pixelation within such devices. Furthermore, mechanoresponsive smart windows with a high dynamic range of haze levels have been rarely demonstrated. The lack of work in this regard can be attributed to the complexities associated with fabrication processes and the subsequent increase in costs.

In the present chapter, the aforementioned challenges are addressed through the design of a novel surface modification procedure and the utilization of inkjet printing for the application of micro etching masks (MEMs) onto a surface-treated hydrophobic PDMS substrate. With this innovative technique, the successful printing of thin film MEMs is enabled. After surface plasma treatment, a pixelated haze distribution is achieved. The novelty that distinguishes this work from conventional mechanoresponsive smart windows lies in the uniform modification of optical properties upon the applied strain. In the fabricated device, the regions with different haze levels are precisely patterned. Consequently, the haze level of the smart window is locally varied, similar to the pixels in displays. This means modification of the haze level modification without external mechanical stress is achieved. The results of this work represent a significant stride forward in maximizing the potential applicability of the manufactured smart window for high dynamic range signage displays.

Parts of the results presented in this chapter have previously been published in the journal Advanced Materials Technologies [198].

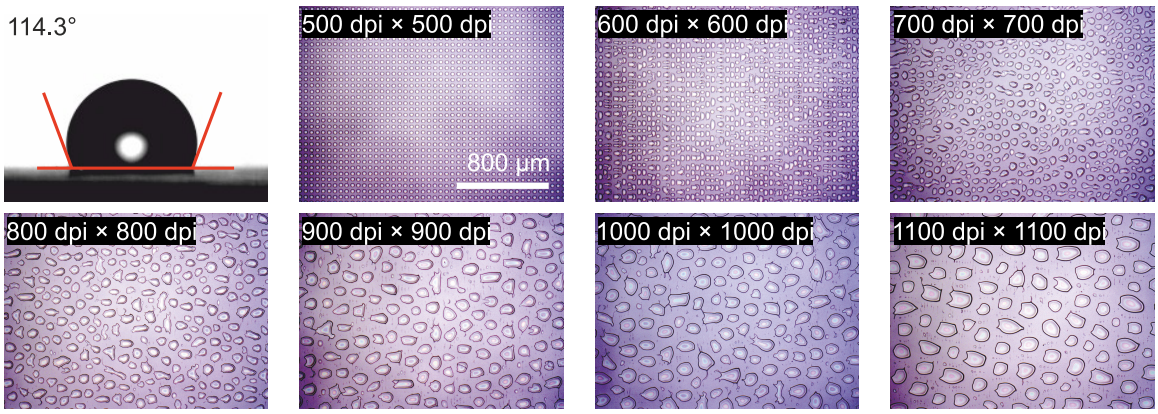

Figure 7.2: Poor thin film formation on the pristine PDMS surface. The static water contact angle shows 114° on the pristine PDMS surface. Printing PMMA ink on pristine PDMS cannot form a homogeneous layer only with an increased printing resolution (dpi).

7.1 Surface hydrophilization of polydimethylsiloxane

Achieving successful inkjet printing of a thin film on a substrate requires a suitable match between the ink and surface properties. Specifically, the ink should exhibit good affinity for the surface, a characteristic often assessed through static contact angle measurements. Generally, a high contact angle indicates poor affinity, while a low value signifies adequate affinity between the ink and the surface. PDMS is known for its hydrophobic surface. A static water contact angle (SWCA) measurement was performed on a PDMS substrate, resulting in an SWCA of 114.3°, as depicted in Figure 7.2. This reading confirms the expected hydrophobic surface property. To inkjet print a thin film on the PDMS surface, an ink formulation comprising PMMA, 1,3-dimethoxybenzene, and hexylbenzene is utilized. The printing resolutions for both the x- and y-axis are set to 500 dpi×500 dpi, 600 dpi×600 dpi, 700 dpi×700 dpi, 800 dpi×800 dpi, 900 dpi×900 dpi, 1000 dpi×1000 dpi, and 1100 dpi×1100 dpi, respectively. Figure 7.2 shows that without appropriate surface treatment, no thin film can be printed on pristine PDMS, regardless of the dpi used. This untreated surface results in isolated grains caused by poor affinity between the ink and the surface.

To modify the surface property for inkjet printing a thin film, a thermal-enhanced surface modification process is employed to deposit an ultra-thin PVA layer onto pristine PDMS. PVA is a versatile polymer with a wide range of applications due to its favorable properties. It is a hydrophilic polymer that is water soluble and is widely used for adjusting the surface free energy [199]. Inkjet printing a continuous PVA thin film directly onto the pristine PDMS presents challenges due to wetting issues. Existing methods for PVA deposition, such as silanization [200], chemical cross-linking [201], and plasma pretreatment [202], have limitations from case to case. Silanization and chemical cross-linking involve the use of hazardous acids, while UV/Ozone plasma pretreatment results in forming an undesired SiO_x layer, which induces surface cracks and inadequate haze into the device. Consequently, achieving a homogeneous PVA layer on the PDMS surface through a non-destructive, environmentally friendly, and cost-effective approach remains an un-

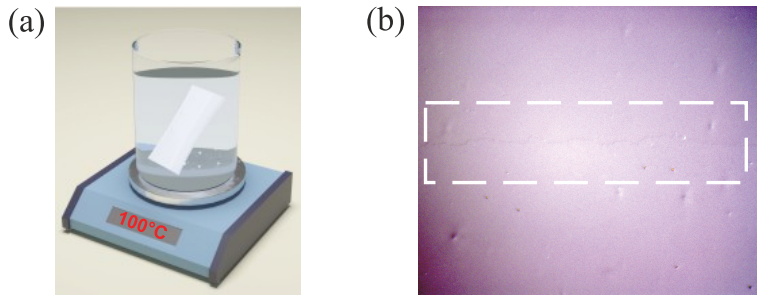

Figure 7.3: Thermal-enhanced treatment of PDMS surface. (a) The schematic illustration of the approach to treat the PDMS surface. The PDMS slice is immersed in the PVA water solution at an elevated temperature. (b) The optical image shows the PVA ultra-thin layer coated on the PDMS slice surface. Inside the dashed frame is the border of the coated and uncoated PDMS slice surface.

explored area. Moreover, the resulting layer should ideally be ultra-thin and durable over the long term, with high surface coverage and minimal surface roughness—particularly crucial for optical applications. Such a hydrophilic buffer layer could enable the direct printing of on-surface MEMs with uniform morphology. Additionally, it favors the selective microstructure patterning to modify the optical properties in smart windows locally.

The preparation for the final polyvinyl alcohol (PVA) solution is as follows: PVA is purchased from (Alfa Aesar). 98–99% of the PVA is hydrolyzed, and the PVA molecules are in a high molecular weight, according to the information from the supplier. To completely dissolve the PVA in water, a weighed amount of PVA is added in a certain amount of distilled water in a beaker, where the water is heated to 100 °C. The water is continuously heated and stirred at 100 °C for 15 minutes, and then the temperature is reduced to 95 °C for another 1 hour until all the PVA is dissolved. During this process, the water inevitably evaporates. To maintain the original amount of water, a small amount of water needs to be carefully added into the beaker to compensate for the water amount that evaporates. The PVA concentration in the final solution is 0.2 wt%.

The surface modification of PDMS starts with immersing the PDMS slice in the PVA water solution at 100 °C. The total time for the water immersion treatment is one hour. After that, the PDMS slice stays in the solution until the temperature goes down to room temperature. Subsequently, the treated sample is subjected to drying under a nitrogen flow. Figure 7.3 (a) shows the schematic of treating the PDMS in temperature-elevated water. A hot plate is used to heat the PVA water solution, and a thermocouple (not shown in the figure) is immersed in the liquid for real-time temperature measurement. After the treatment, the microscope is used to observe the PVA layer. To better assess the results, tape is used to remove part of the PVA layer so that a border of coated and uncoated surfaces can be seen. This border can be clearly observed in the differential interference contrast mode of the microscope. The area contained inside the dashed frame can be seen in Figure 7.3 (b). The lower region is coated with PVA, and the upper region is the uncoated PDMS. The coated PVA layer is expected to be very thin. Therefore, the microscope cannot provide a very high contrast between the coated and uncoated surfaces. Other characterization tools need to be used, which will be discussed later.

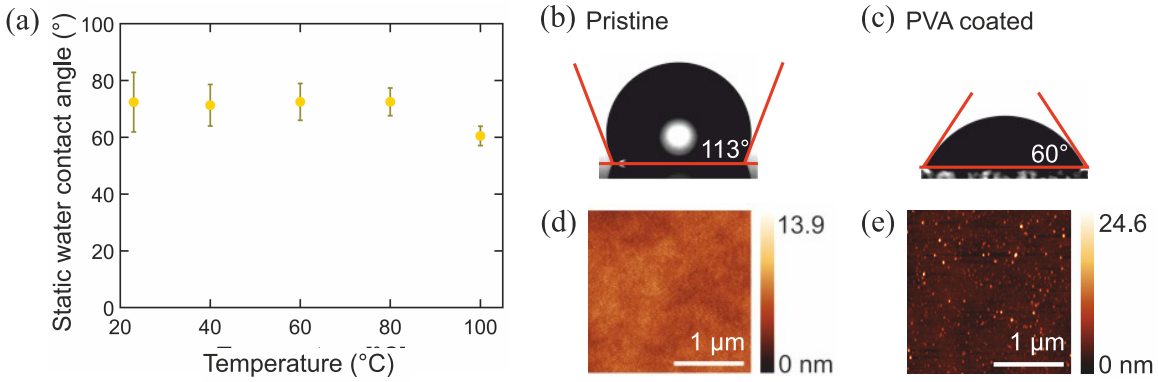

Figure 7.4: Surface property characterization of the PVA-solution-treated PDMS slice. (a) Static water contact angle measurement of PDMS slices. The PDMS slices are treated in PVA water solutions with different temperatures. (b) and (c) are the optical images showing the static water contact angle measured on the pristine and 100 °C PVA-solution-treated PDMS surfaces, respectively. (d) and (e) are the atomic force microscope images of the pristine and 100 °C PVA-solution-treated PDMS surfaces, respectively.

To find the optimum condition of the treatment, different temperatures are applied to the solution to treat the individual samples. The tested values are temperatures—room temperature (23 °C ±1 °C), 40 °C, 60 °C, 80 °C, and 100 °C. After the surface treatment, SWCA is measured to find the best temperature. Two criteria need to be applied, i.e., the SWCA measurement should be conducted multiple times and at different locations on the same sample. The reason for the multiple measurements is apparent since an average value should be used. The reason for the multiple locations on the same sample is that it is essential to verify the homogeneity of the PVA coating. A relatively smaller standard deviation of the final results indicates a better homogeneity of the coating. In this work, 40 water SCAs are measured on each individually treated sample. In Figure 7.4 (a), the results are plotted. It can be seen that with the temperature increasing from 23 °C to 80 °C, the average SWCAs show similar values. A decrease in the SWCA can be seen in the sample that is treated at 100 °C. This matches the research conducted by other groups [203]. It is because when treating the PDMS slice at 100 °C, the hydroxyl group (-OH) is activated on the slice surface, where the -OH originates from the residual -SiH functional groups in the PDMS. Respective standard deviations in Figure 7.4 (a) decrease with the temperature. It suggests that the PVA coating homogeneity is improved by the temperature. Figure 7.4 (b) and (c) show the SWCA on the pristine and 100 °C PVA water-solution-treated PDMS slices, respectively. A noticeable decrease from 113° to 60° of water SWCA is observed before and after coating with PVA. The atomic force microscope is used to characterize the surface roughness of the PDMS substrate. Figure 7.4 (d) and (e) show the measured results, where the peak-to-valley roughness shows only a slight increase when comparing the surface before and after the treatment. The treated surface exhibited a root mean square (RMS) roughness of approximately 1.4 nm, signifying a notably smooth layer.

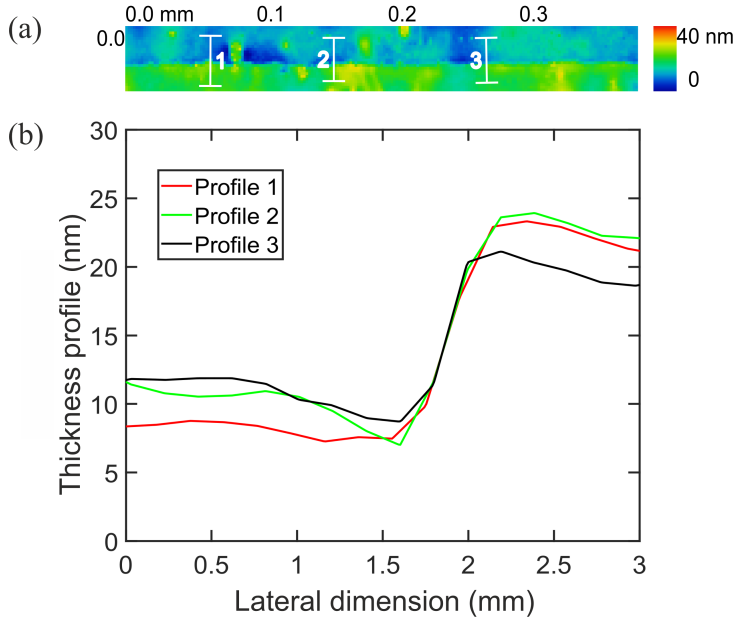

Figure 7.5: Characterization of the thickness of the coated PVA layer on PDMS slice. (a) Image of the surface morphology measured by the white light interferometer. Paths 1, 2, and 3 are used in profile determination. (b) Thickness profile of the coated PVA thin layer.

It is crucial to determine the thickness of the PVA layer quantitatively. Generally, either the atomic force microscope or the white light interferometer can be used for the thickness characterization. In this work, the thickness of the coated PVA layer is measured by the white light interferometer as a non-contact approach. The test sample is the one treated at a temperature of 100 °C in the PVA water solution. The measurement area is at the aforementioned border. By doing this, a profile can be generated to determine the thickness. The measured result can be found in Figure 7.5, where (a) is a two-dimensional color map showing the layer morphology and (b) is the profile extracted from three paths depicted in (a). The path length for determining the PVA layer thickness is 3 mm. From Figure 7.5 (b), it can be seen that the thickness of the coated PVA is around 10 nm. Given this thickness value, the layer can be treated as an ultra-thin membrane. The robustness of the coating is important in terms of long-term stability, as well as against the subsequently covered inks during printing. Therefore, the stability test is conducted. The coated PDMS slice has been stored in the ambient for 100 days. The SWCA characterization is conducted before and after. There is almost no difference being observed, indicating a high robustness of the PVA coating in air. Similarly, the test has also been performed by immersing the coated PDMS slice in room-temperature water. After 100 days, the SWCA increases from around 60° to 66.5°. As mentioned above, PVA is a water-soluble polymer. The increase in the SWCA is an expected result. However, a change below 10% in this case is still impressive. This high robustness can be attributed to the bonding of the PVA molecules with the hydroxyl group, resulting in a firmly adhesive thin layer [203]. It needs to be noted that depositing a thicker PVA layer on the PDMS shall be avoided. It is

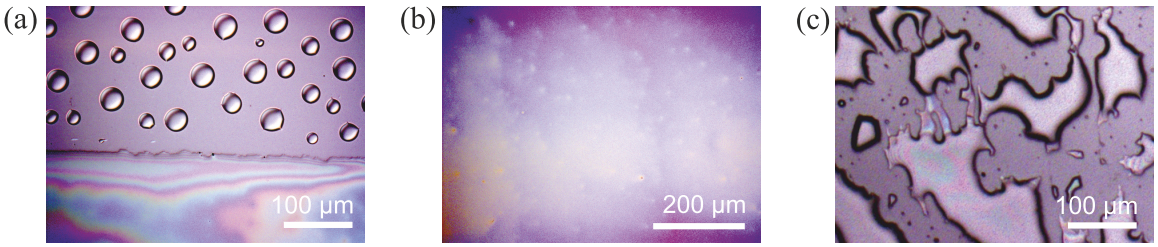

Figure 7.6: Comparison of the thin film formation on the PDMS treated by different parameters. Optical images of PDMS surface printed with PMMA, where (a) only the lower half is coated by PVA, (b) the entire surface is covered by PVA, and (c) the PDMS was treated with PVA solution at room temperature.

because the thicker the coated layer is, the more the unwanted haze will be induced. The haze arises from the crystalization nature of the PVA molecules to induce local grains, as can be seen in Figure 7.4 (e). Since the PDMS is designed to be used as a smart window, a remarkably controllable optical property is demanded. Therefore, precise control of direct transmission and scattering is essential. Mitigating any degradation in these optical properties resulting from uncontrollable factors is of paramount importance.

To give a better overview of the quality of the deposited thin film, Figure 7.6 presents the results based on three treatment parameters. Figure 7.6 (a) shows the printed PMMA thin film on the PDMS surface with and without the PVA thin layer. In the upper region, the PVA is removed, and in the lower region, the PVA layer is deposited with a solution temperature of 100 °C. It can be seen that without the PVA layer on the PDMS, no thin film is formed. Figure 7.6 (b) is a zoomed-in image of the formed PMMA thin film. There are no voids or gaps observed on the scale of micrometer. Therefore, it is evident that the deposition approach leads to a proper adjustment of the affinity between the inks and substrate. A reference sample was also investigated compared to the solution with the elevated temperatures. In Figure 7.6 (c), the PMDS slice is treated with a PVA solution at room temperature. With the same ink and printing parameters, the PMMA thin film is formed with poor quality. Compared to a bare PDMS surface, where only the isolated islands are formed, disconnected segments are formed. It implies that some PVA molecules are attached to the PDMS even when treated at room temperature. However, the coverage is low compared to using elevated temperatures.

7.2 Inkjet printing of micro etching masks (MEMs)

Various fabrication processes, such as photolithography, plasma etching, and physical vapor deposition, require the use of masks. Masks are used to shield specific surfaces from photons, ions, and particles during these processes. Consequently, they prevent any chemical or physical modification and impact in the protected areas. In ion reactive etching, masks, typically made from photoresist, are firmly affixed to the surface, effectively preserving the area beneath. These photoresist masks are typically fabricated using photo-lithography. Given the capability of inkjet printing to deposit surface structures with a feature size of several tens of micrometers, the direct printing of masks is

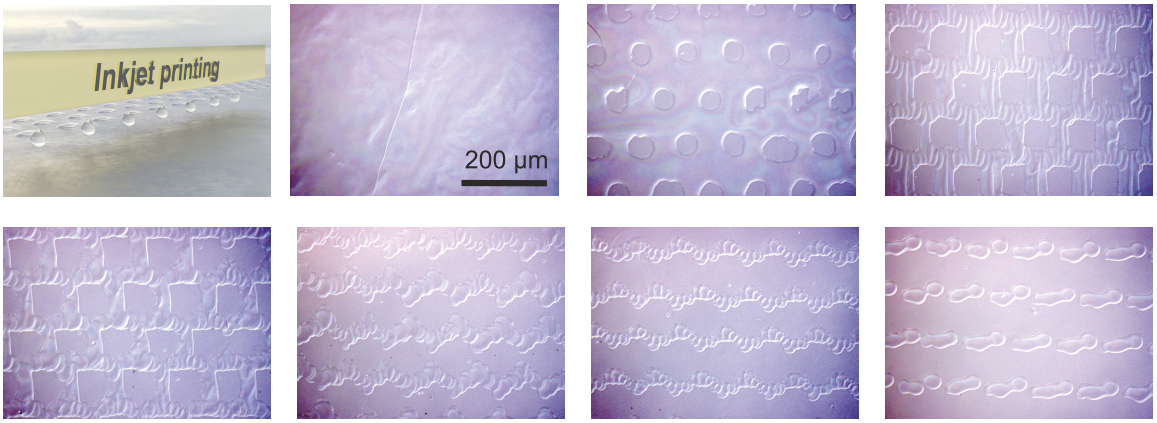

Figure 7.7: Inkjet-printed micro-etching-masks (MEMs) on PVA-treated PDMS surface. The MEMs are printed with different designed patterns. The coverage of these seven masks is 100%, 87.5%, 75%, 62.5%, 50%, 37.5%, 25%, 12.5%, and 0%, respectively, from the left of the first row to the right of the second row.

highly attractive. In this study, plasma treatment is necessary to induce the nano and microstructures, which is discussed in the next section. Selectively treating the surface is realized by surface micro etching masks (MEMs). Poly(methyl methacrylate) (PMMA) is the material for the MEMs, and the ink is inkjet printed on the PDMS slice. The surface covered by the MEMs is free from the treatment.

The PMMA ink is prepared as follows: Before the plasma treatment of the PDMS, poly(methyl methacrylate) (PMMA) is printed as an etching mask to protect and surface selectively. PMMA is purchased from PSS GmbH. The molecular weight is 65 kDa. The PMMA is dissolved in 1,3-d. After the solution is clear, 10 vol% hexylbenzene (97%, purchased from Sigma-Aldrich) is added to the solution. The solution is continuously steered at 50 °C for 10 hours before use. The final concentration of the PMMA ink is 80 mg/ml.

After the PMMA ink is formulated, printing is subsequently carried out by the inkjet printer using a single nozzle, employing a 1 pL cartridge. The print head temperature is maintained at 32 °C, and the jetting frequency is set up to 2.5 kHz, controlled by a custom-optimized waveform with a maximum voltage of 19 V. Digital patterns for micro-etching-masks, with a resolution of 1200 dpi, are generated via halftone reprography and subsequently utilized as the printing recipes. Following the printing process, the micro etching masks are allowed to dry in air under ambient conditions.

In Figure 7.7, a schematic shows the inkjet printing process of MEM printing. Using different printing resolutions and designed printing patterns, MEMs can be fabricated on the surface-treated PDMS in different shapes. Here, seven different MEMs are printed, with different coverage on the PDMS surfaces. The coverage is designed to be 100%, 87.5%, 75%, 62.5%, 50%, 37.5%, 25%, 12.5%, and 0%, respectively, for each mask from the left of the first row to the right of the second row. The printing pattern of the mask is converted by the halftone method based on the greyscale setting. For inkjet printing, the printing pattern processed in the control software is a binary pattern, i.e., the areas in the pattern recognized by the printer are either white or black. Only the black area means

the printer needs to eject inks, and the surface will be printed with materials. Greyscale is defined by the ratio of black and white in an image. The range of greyscale is typically 0 to 255. For instance, when the image is 100% white, the greyscale is 255, while a greyscale of 0 indicates the image is 100% black. If the PDMS surface needs to be 100% covered by the MEM, the printing image used in the inkjet printing control software should be 100% black. The corresponding greyscale is 0.

In the approach provided above, the MEM coverage on the PDMS can be controlled by the setting of the greyscale. That is to say, the coverage of the PMMA mask can be tuned by adjusting the greyscale of the digitally designed image. This gives two substantial advantages in fabricating the MEMs. First, the drop-on-demand technical advantage of inkjet printing allows the MEMs to be printed in a fairly flexible manner. Second, by adjusting the greyscale of the designed pattern in a high resolution, the MEMs coverage can be adjusted in a very fine way. This further can offer a very high dynamic range control of optical haze in a smart window, which is discussed in the next section.

7.3 Plasma-assisted surface nanostructuring

PDMS is a highly suitable material for mechanoresponsive smart windows due to its excellent optical transmission and stretchability. One versatile approach to modulate the optical properties of PDMS is inducing microstructures through surface wrinkles [8]. This can be easily achieved by creating a strain difference between the top SiO_x layer and the pristine PDMS underneath.

SiO_x layer can be introduced by treating the PDMS surface with ultra-violet/O_2 plasma. The thickness of the SiO_x layer can vary depending on the treatment parameters. Different time, gas pressure, power, and gas ratios can lead to different thicknesses. In this regard, the strain difference on the interface of the stiff SiO_x layer and the elastic PDMS can vary and result in different surface structures upon stretching. There are two common ways to fix the pristine PDMS slice before the plasma treatment, i.e., with or without stretching the substrate. It is obvious that when the PDMS sample is treated in the plasma with a stretched state, surface wrinkles are induced when the slice is subsequently released. Because the upper SiO_x layer is less elastic compared to the PDMS slice beneath. The second case is that when the PDMS slice is treated in an unstretched state, the mi-

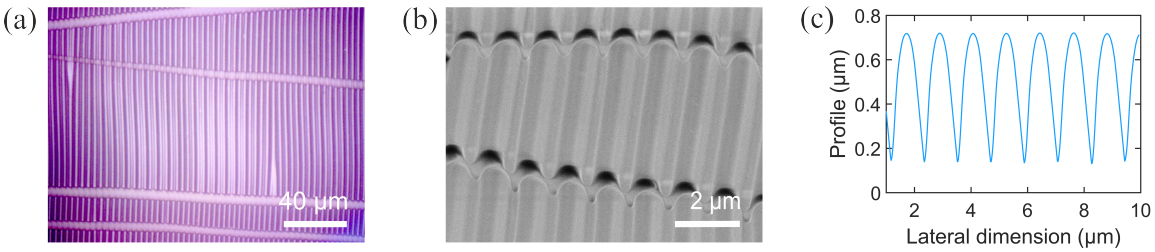

Figure 7.8: Characterization of the surface micro-wrinkles induced by plasma treatment. (a) Optical image of the wrinkles. (b) SEM image of the wrinkles. (c) Surface profile measured by AFM.

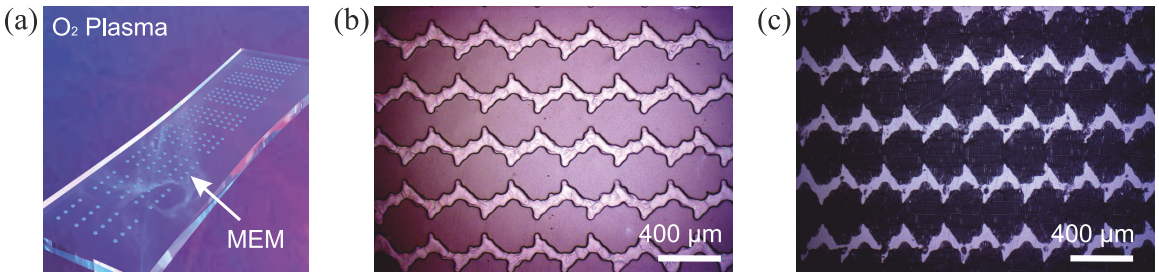

Figure 7.9: Plasma-assisted surface structuring. (a) Schematic of a PDMS slice being treated in plasma. The slice is stretched during the treatment. MEMs are inkjet printed on the PDMS surface. (b) Optical image of printed MEMs. (c) Optical image of surface-treated PDMS slice in the released state.

crostructure is only induced by stretching the PDMS slice. The reason here is also easily understandable since the SiO_x layer is not elastic. Upon stretching the sample, the SiO_x layer is separated into pigments, and cracks can be formed.

In this work, the surface micro-wrinkles are applied to modulate the optical performance of the smart window. The PDMS slice is stretched during the plasma treatment. In Figure 7.8 (a), an optical image shows the micro-wrinkles arranged in a quasi-periodic manner when the treated PDMS slice is in the released state. The micro-wrinkles are aligned in the vertical direction, which is perpendicular to the stretching direction. Here, the stretching ratio is used to describe how much the PDMS slice is stretched. It is defined by the ratio of the length between the stretched state and the released state. For the sample in Figure 7.8 (a), the stretching ratio is 1.6. In the same image, several cracks can be observed also in the horizontal direction. This is because when the PDMS slice is stretched, there is deformation in the vertical direction, similar to a passively induced stretch in the vertical direction. However, this leads to a reduction of the length of the sample in the vertical direction. After the sample is treated and released, the length of the sample in the vertical direction returns to the original, and the stiff SiO_x layer is pulled apart by the elastomer. Therefore, the cracks in the horizontal direction are induced. Nevertheless, the developed smart window in this work mainly relies on the micro-wrinkles to modulate the optical behavior. The cracks in the horizontal direction only induce a limited amount of optical haze.

Figure 7.8 (b) shows the SEM image of the induced micro-wrinkles. It can be seen that the wrinkles are arranged in a period of about 1.3 μm. The thickness is in the order of a hundred nanometer. AFM is also utilized to characterize the surface profile of the generated wrinkles. The peak-to-valley difference is approximately 500 nm, as shown in Figure 7.8 (c).

As mentioned in the last section, the PMMA MEMs are printed to protect the PDMS surface beneath during the plasma treatment. Therefore, the MEMs-covered area is wrinkle-free. This means that the wrinkles are selectively induced onto the PDMS surface. Consequently, the two-dimensional wrinkle patterning is realized. Figure 7.9 (a) shows the schematic of a stretched PDMS slice being treated in the oxygen plasma. The surface of the PDMS is printed with MEMs. Figure 7.9 (b) is an optical image showing the printed PMMA MEM. Before and during the printing process, the surface needs to be stretched so

the MEMs are not deformed. It can be found that the MEMs are printed in good quality. After the plasma treatment, removal of the MEMs, and the release of the PDMS, wrinkles can be seen on the surface. In Figure 7.9 (c), the bright region was covered with MEMs, which is free from the treatment. The dark region was exposed to the plasma, where wrinkles are induced. Since the wrinkles lead to a high deflection of the transmitted light, scattering or haze takes place. Therefore, less light goes into the objective of the microscope, and the surface with microstructures is darker. The area covered by the MEMs is well preserved when comparing Figure 7.9 (b) and (c).

Using this developed method, two-dimensional haze distribution can be realized. It should be noted that until now, the smart window is in a static state. That is to say, the haze is modulated purely by the control of the MEMs patterns. Compared to the conventional mechanoresponsive smart windows, the haze or the transmission needs to be manipulated by stretching the finished sample. In this work, without the mechanical stress, the haze level can already be controlled by design. It is also the novelty of this work that the haze can be modulated both in a static and dynamic mode, which is discussed in the following sections.

7.4 Haze control in static mode

In this section, the haze modulation in a static mode is presented. The obvious consequence of inducing the haze in a transparent substrate is the reduction of direct transmission. This means an increase in the haze will lead to a blur when watching another object through the substrate. This is one of the concepts of developing a smart window, which modulates the information visibility by manipulating the haze level.

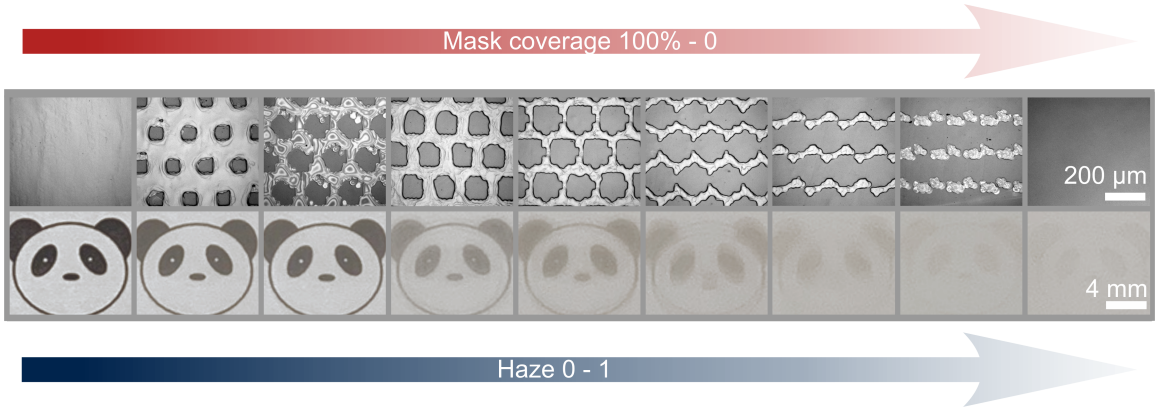

Figure 7.10: Haze modulation in the static state. The first row shows nine different MEMs printed on PVA-treated PDMS slices. The MEMs are printed with the mask coverage from 100% to 0. The second row shows the nice PDMS slices placed on a piece of paper. The PDMS slices are treated by plasma and in the released state. The paper beneath the PDMS slices is printed with a black-and-white image of a panda face using an office printer. The image becomes more and more blurred due to the increased haze level.

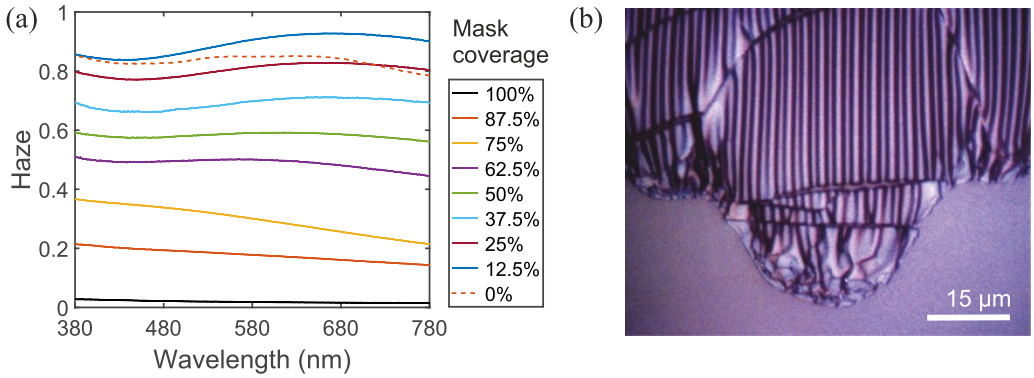

Figure 7.11: Quantitative analysis of haze level. (a) Measured haze level of each treated PDMS slice with different MEMs. Individual MEM is designed to have different surface coverage. (b) An optical image shows the edge of the micro pattern.

Here, nine pieces of PDMS slices treated with different MEMs are placed on a piece of paper. The morphologies of the MEMs are shown in the first row of Figure 7.10 (a). From the left to the right side, the mask coverage on the PDMS is decreasing from 100% to 0. As a result, the surface ratio treated by plasma becomes larger from the left to the right side. This results in an increase in the haze level in the same direction. On the paper beneath the PDMS slices, a panda face image was printed by a normal office printer. The color is black and white. As expected, with the increased haze from the left to the right side, the panda's face becomes more and more blurred.

Given that the design of the MEMs is related to the greyscale level in the initial design, in Figure 7.10, nine greyscale values are used, which are calculated by $2^n - 1$. The n used to design the MEMs is 0 to 8 with a step of 1. However, it should be noted that more greyscale values can be used for designing the MEMs. Regardless of the printing resolution of the inkjet printing, the number of the total greyscale level is infinite as long as the step between every single value is infinitely small. Therefore, a continuous haze modulation can be realized based on this strategy. Back to real life, an ultra-small step between the neighboring haze levels is unnecessary because it is not recognizable by human eyes. In this work, the comparison of the haze level is therefore limited to nine values, which already shows good visual results for modulating the visibility.

To quantitatively characterize haze levels, the spectral dependency of haze is measured for each released PDMS slice in the visible wavelength range, i.e., 380 nm to 780 nm. The results are displayed in Figure 7.11 (a), which indicates a consistent increasing tendency in the haze levels with a decreased mask surface coverage. As the coverage decreases, the haze level approaches 1, signifying the minimal amount of the direct transmission of light.

However, a reduction in haze is observed at a coverage of 0 (depicted by the dashed line in the figure) when compared to a coverage of 12.5%. It does not follow the increasing tendency as expected because more surface micro-wrinkles are induced in coverage of 0 compared to the case with 12.5%. This phenomenon could be attributed to the maximized

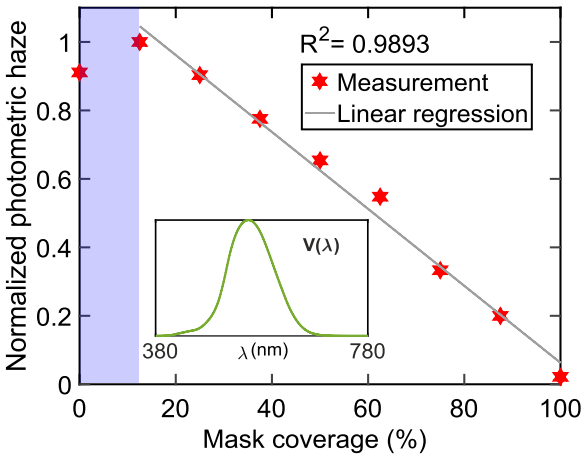

Figure 7.12: Quantitative analysis of the normalized photometric haze level. The photometric haze level shows a high linear dependency on the surface coverage of the MEM. A high coefficient of determination is calculated as 0.9893.

micro-wrinkle density when the mask coverage approaches 0, resulting in the distribution of micro-wrinkles becoming continuous over the entire surface. Consequently, the role of optical scattering originating from the boundary between the structured and pristine surface becomes less pronounced. This interpretation finds support in Figure 7.11 (b), presenting an optical image of the micro-wrinkle pattern generated by a mask coverage of 50%. It can be seen that at the edge of the structure, the density of the irregular micro-wrinkles is higher than the center area of the structured patterns. The previous results show that this irregular microstructure can induce more light scattering compared to other more regular regions [204].

Moreover, to account for the spectral sensitivity of human perception, the haze spectra corresponding to each surface coverage value of the MEM are weighted using the standard photopic luminous efficiency function V(λ). Integration over the visible light range produces a value, which is referred to as photometric haze in this work. The resulting values from various surface coverages are depicted in Figure 7.12. A linear relationship is evident within the coverage range of 12.5% to 100%, with a noticeable deviation in monotonicity at coverage equals 0. In order to achieve precise control over haze in the final smart window, all the following MEMs are designed with mask coverage located within this linear region. The coverage range below 12.5%, highlighted as the violet zone in Figure 7.12, is excluded to maintain the desired linear haze controllability. Notably, a linear regression within the coverage range of 12.5% to 100% yields a high coefficient of determination (R_2 = 0.9893), demonstrating excellent quantitative control of photometric haze through linear coverage tuning.

7.5 Haze control in dynamic mode

It is attractive to achieve the highly adjustable haze level in a smart window by adjusting the design of the MEMs. That is to say, by tuning the greyscale in a small but realistic step,

Figure 7.13: Dynamic modulation of a haze-induced PDMS slice. Using a MEM with gradient surface coverage, a continuous haze distribution is achieved in a released PDMS slice (left). By stretching the PDMS slice, the film becomes transparent (right).

the haze level can be manipulated in a manner that the dynamic range is fairly high. This is similar to a display that offers different light levels in the same image. In this manner, the greyscale used for designing the MEMs can increase from 0 to 255, with a step of 1. This eventually leads to 256 different MEMs that can be used to generate 256 different haze levels. However, to have a distributed and different haze level from site to site, it is preferred not to apply the MEMs one after another to the different locations. Since this will bring a huge amount of effort and is technically exhausting, inkjet printing, again, shows its ability to address this issue. As already known, inkjet printing shows a high degree of freedom in patterning. This means the MEMs can be integrated as one design with a proper pattern. However, it has a feature size requirement, i.e., the MEM should have a minimum feature size larger than several tens of micrometers, which is a typical minimum feature size that can be printed in inkjet printing. Hence, the MEMs for the smart window in this work are designed to be printable.

Here, integrated MEMs can be digitally designed as long as the local greyscale is decided. Then the image can be converted into a binary image using the halftone algorithm. After this, the image is processed in the control software, and the printer is ready to print. This is a similar process to the printing of a single MEM. Therefore, the developed method is highly versatile and practical.

To show a substantial haze depth and linear haze tunability on a single PDMS slice, a MEM with a gradient surface coverage (ranging from 100% to 12.5%) is printed on a PVA-treated PDMS slice. Considering the previous discussion on the photometric haze. The coverage does not reduce below 12.5%. The resulting film, after the plasma treatment, is displayed on the left side of Figure 7.13, showing a gradual increase in haze levels from left (fully transparent) to right (high haze level). Furthermore, the entire PDMS slice can be rendered transparent through stretching, as demonstrated on the right side of the same figure. This dual haze modulation, referring to site-to-site and mechanoresponsive haze tunability, holds potential for applications in smart window signage displays, enabling the transmission of information with a high dynamic range.

7.6 Pixelated haze and the display function

The concept of realizing a two-dimensional haze control in a static smart window and the dual-mode modulation with and without mechanical stretching has been demonstrated.

Figure 7.14: Fabricated smart window with a pixelated and high dynamic range of haze. (a) The original rose image used. (a) Fabricated smart window with a well-replicated rose image in a released state. (c) The fabricated smart window at a large viewing angle preserving a good displaying quality.

Moreover, a high dynamic haze level is also achieved. The next step is to address the topic of how to realize pixelation properly. Up until now, the conventional smart window usually only showed the capability to manipulate the transmission in an entire window. No pixelated smart window has been investigated by far. It is scientifically and technically interesting to enable the smart window with display functionality. A similar product is called electronic paper.

To realize the pixelation of haze in a smart window, precise control of the MEM patterning is required. In this work, a real image is used as the final picture presented by the smart window with a display functionality. Figure 7.14 (a) shows a photo of roses, which was first transformed into a greyscale image using halftone reprography. As previously motioned, it is the first step of designing the MEM. Following this, the MEM was inkjet printed based on digital design, and the PDMS is selectively covered by the mask. The optical image of the resulting smart window in its released state is depicted in Figure 7.14 (b) against a black background. It should be highlighted that the pattern observed in the smart window display accurately replicates the rose photo. This indicates a precise design and deposition of the MEMs as well as a proper surface micro-structuring by plasma treatment. Furthermore, to underscore the viability of viewing the presented image even from a considerably large angle, similar to electronic paper, an optical image was captured from the side of the fabricated smart window (approximately 60° to the surface normal) under normal sunlight illumination, as portrayed in Figure 7.14 (c). This image reveals the reflective scattering view of the smart window enabled with a high dynamic range haze. Evidently, the rose pattern is distinctly discernible, preserving the original image quality to a significant degree. The pixelation of the haze is properly achieved without deteriorating the original image quality. This exemplary performance underscores the potential of the fabricated smart window for application in display scenarios that demand a high dynamic range.

With the results achieved, it is worth investigating the integrated MEM and the generated surface structures a bit deeper. In Figure 7.15, the details of the printed MEM and the micro-wrinkles are presented. Figure 7.15 (a) is the fabricated smart window showing the rose in the released state. Three sites in the image are picked and zoomed in for the details. The sites are marked with frames with different colors to distinguish each other. Figure 7.15 (b), (c), and (d) show the PMMA MEM. When comparing the MEM with the rose image, it can be seen that the darker the color in the rose image is, the higher

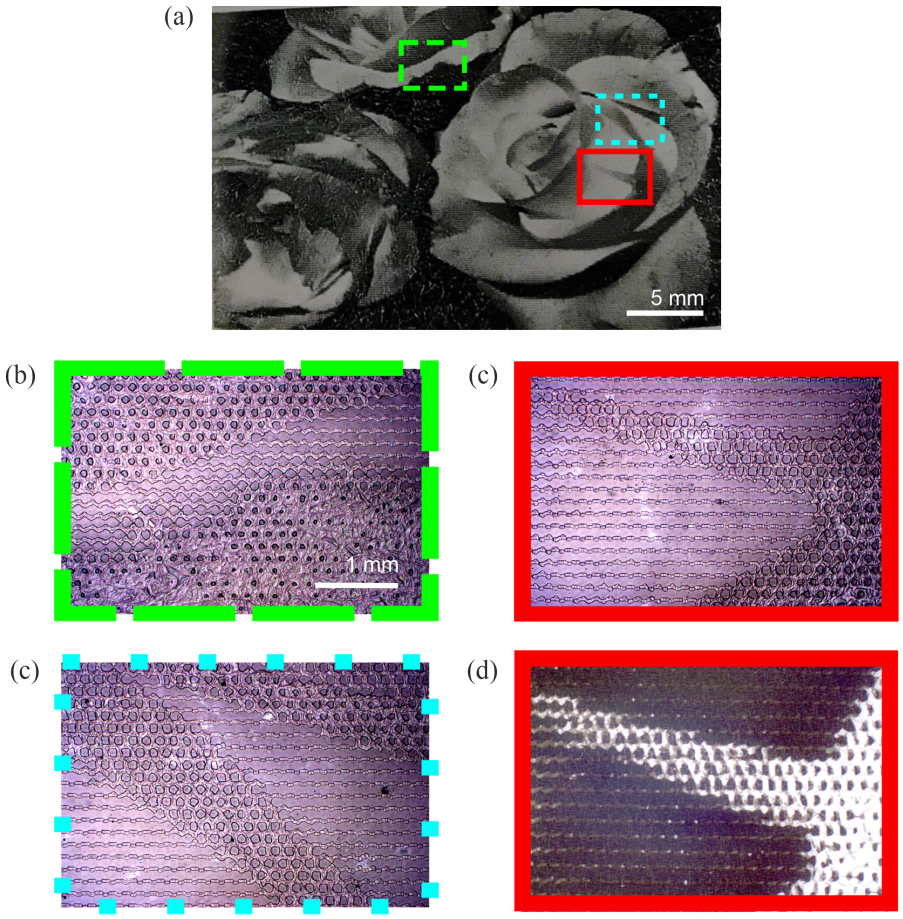

Figure 7.15: Optical image of the details of the printed MEMs and induced micro-wrinkles. (a) Fabricated smart window. The presented pattern is based on the original rose image. (b), (c), and (d) Zoomed-in images of the printed MEM. (e) Zoomed-in image of the region that has been treated by plasma. It is the same region as marked in (c). The scale bar applies for (b) to (e).

the coverage of the MEM is. With a transition of brightness in the rose image, the mask changes the pattern accordingly. Figure 7.15 (d) shows the treated surface resulting from the mask-covered region in (c). In the image, it can be clearly seen that the region with different haze is precisely distributed, followed by the design of the MEM. Compared with a normal display, which presents the image pixel by pixel, the fabricated smart window shows a similar function replying to the pixelation of the haze.

7.7 Summary and discussion

In summary, the work in this chapter presents a versatile approach for the development of a smart window capable of integrating signage functionality. The method involves a water-based and thermally enhanced process to modify the surface of polydimethylsilox-

ane (PDMS) utilizing a boiling process in an aqueous polyvinyl alcohol (PVA) solution. This modification process allows for the precise deposition of polymethyl methacrylate (PMMA) layers on the PDMS films using inkjet printing. The PMMA-based micro-etching mask (MEM), designed with spatial patterning and digital encoding, is then directly inkjet printed onto the modified PDMS substrate, demonstrating remarkable flexibility and precision.

In contrast to traditional mechanoresponsive smart windows, the progress in this work extends beyond the modulation of haze solely under strain, encompassing management of the haze in the static state as well. The developed approach enables precise micro-wrinkle patterning and controlled light scattering based on the edge effect, resulting in a highly controllable spatial distribution of light. The work successfully demonstrates continuous and linear tunability of the photometric haze using the developed technique. Leveraging these capabilities, an energy-efficient smart window display with a high dynamic range is fabricated, achieving a large haze depth and pixelation.

8 3D nanostructure with tailored plasmonic resonance for SERS

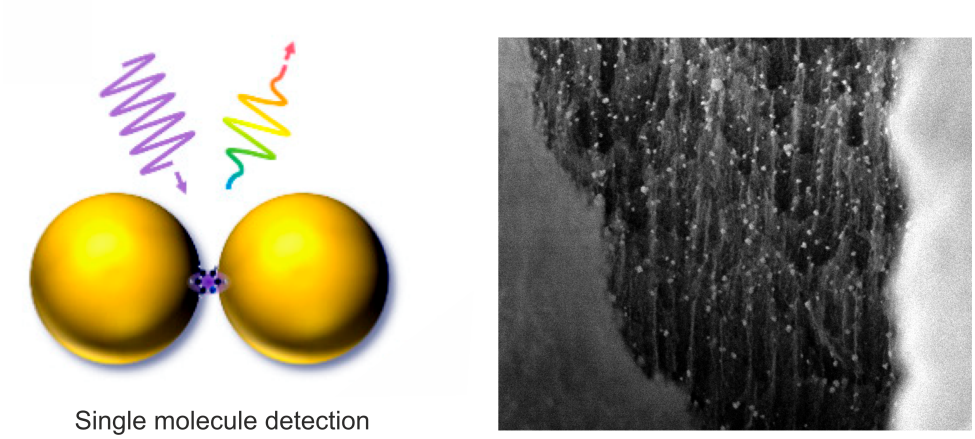

Figure 8.1: Localized surface plasmonic resonance (left) and 3D SERS substrate for material detection (right).

In this chapter, the work on the fabrication of 3D nano-platforms to utilize as surface-enhanced Raman scattering (SERS) substrates is presented. Novel 3D substrates have been developed for on-chip SERS sensing, demonstrating superiority over existing SERS sensors. Strong light-matter interaction is achieved by tailoring the localized surface plasmon resonance (LSPR) in the fabricated device. The results give a remarkable SERS enhancement factor in the order of 10^9*, allowing the detection at the single-molecule level. Experimental validation of this capability is conducted by detecting an analyte with a picomolar per liter concentration,* 10^{-12} *M, of methylene blue (MB).*

To achieve this, a dedicated method is developed to embed gold nanoparticles (AuNPs) into the fabricated 3D nanoporous silicon (np-Si) substrates. The AuNPs enhance the localized electrical field through the excitation of the LSPR. Meanwhile, the dielectric environment of the np-Si serves to further confine this enhancement locally. The 3D-structured nanonetwork offers a large surface area exposed to the LSPR, offering a high density of hot spots. In addition, LSPR peaks have been tailored to match the incident excitation laser wavelength. This optimization results in an elevated electrical field of LSPR, which amplifies the intensity of Raman scattering. Consequently, analyte molecules adsorbed on the nanopores acquire a significantly increased probability of interacting with the intensively confined LSPR, leading to surface-enhanced Raman scattering.

Parts of the results presented in this chapter have previously been published in the journal Nanoscale Horizons [205].

8.1 Fabrication of nanoporous silicon

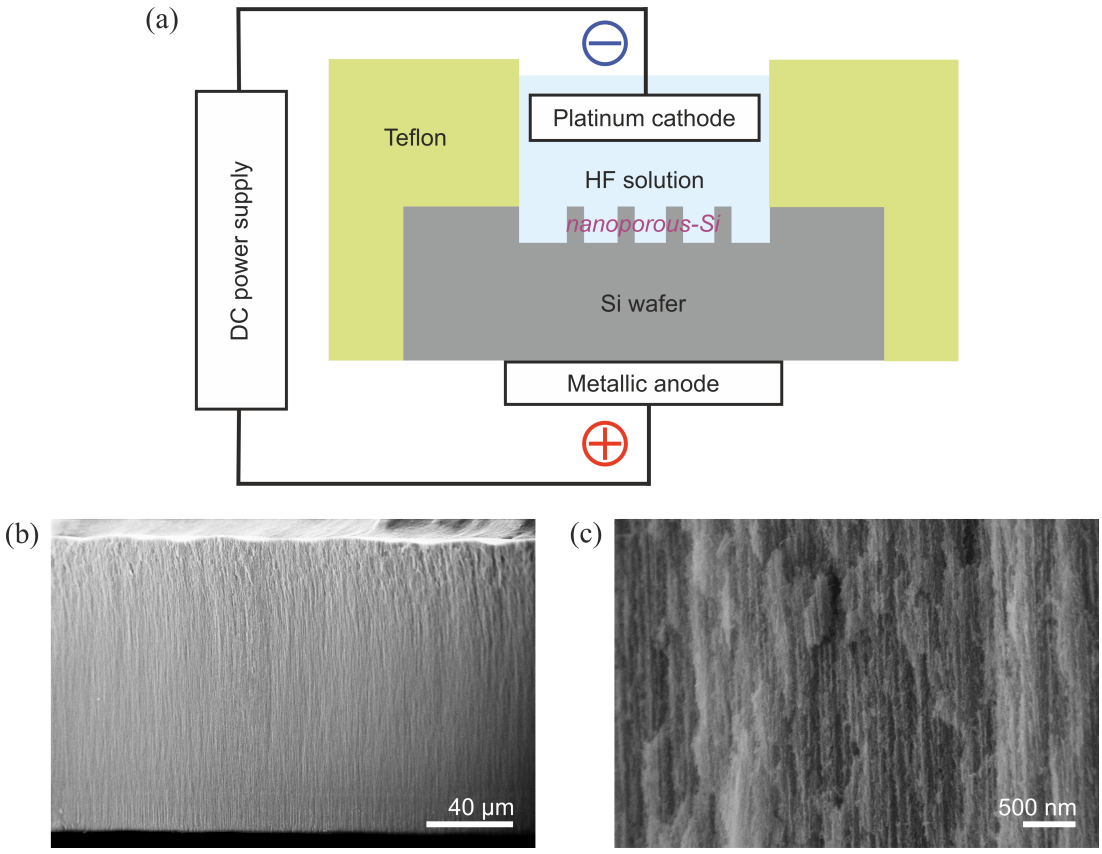

Figure 8.2: Fabrication of nanoporous silicon substrate. (a) Schematic illustration of the electrochemical anodization process. (b) SEM image of the cross-section of the nanoporous silicon substrate, where the sample contains the nanoporous channels from the top to the bottom. The thickness is approximately 150 μm. (c) SEM image of a zoomed-in view of the cross-section of the fabricated nanoporous silicon substrate.

The nanoporous silicon (np-Si) network is chosen as the 3D platform because of its cost-effectiveness, well-established fabrication process, and extensively reported optical and electronic properties. Additionally, np-Si serves as a natural matrix for the growth of metallic nanoparticles within its nanosized channels. These channels are interconnected and provide a substantial surface area.

A common method to fabricate the np-Si is electrochemical anodization of the boron-doped silicon wafers, as shown in Figure 8.2 (a). The wafer is fixed in a teflon-made reactor. A 1:1 ratio mixture of methanol and 40% hydrofluoric acid is used as the electrolyte for etching the Si. The metallic anode, usually made of aluminum, is connected to the bottom side of the Si wafer. The cathode, made of platinum, is immersed in the electrolyte. The external DC power supply provides a current density of 100 mA cm^{-2}, creating an electric field and current flow between the two electrodes. By applying the current for 8 seconds, a np-Si layer with roughly 550 nm can be generated. Nanoporous channels are

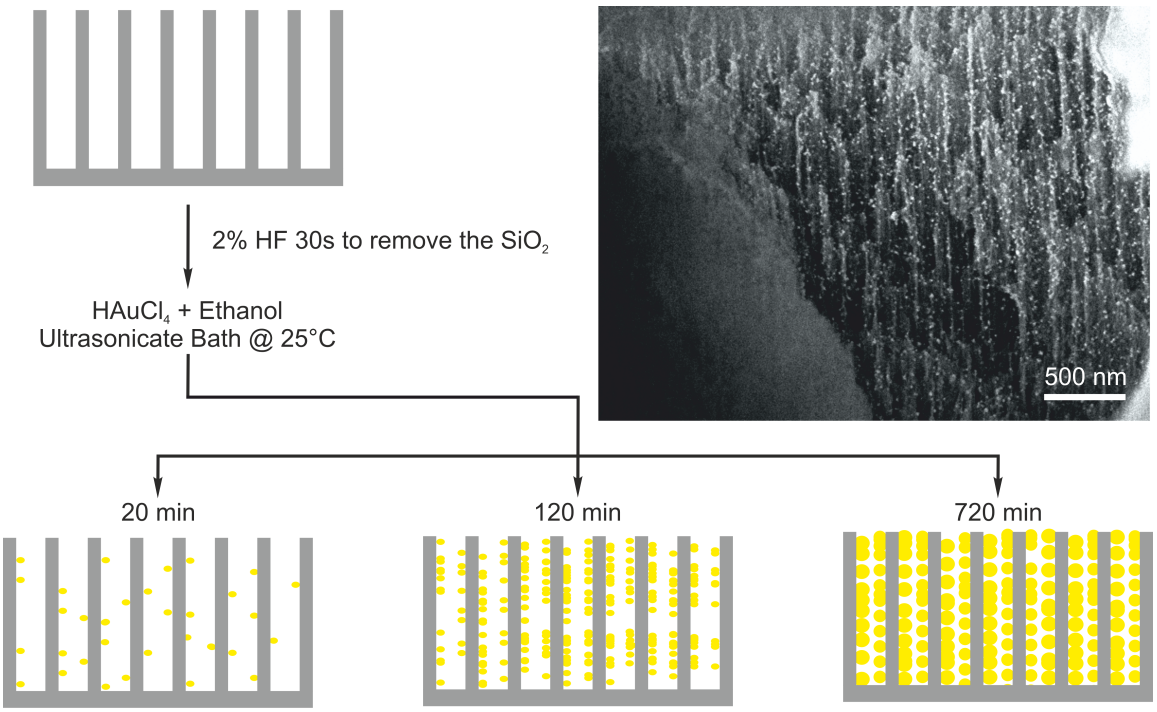

Figure 8.3: Deposition of gold nanoparticles in the nanoporous channels. The process of the ultrasonicated-assisted process is depicted in the left side of the image. The essential parameters used in the process are listed along the steps. A cross-sectional SEM image is inserted on the right side of the figure, where gold nanoparticles can be seen as small bright dots embedded in the nanoporous channels.

induced and vertically aligned in the fabricated np-Si layer. With a longer time of current flow, the entire Si wafer can be made into nanoporous, consisting of numerous vertically aligned nanochannels. An SEM cross-sectional image, Figure 8.2 (b), shows that a wafer with a thickness of around 150 μm is completely turned into a nanoporous structure. It is achieved after a longer period of electrochemical anodization. A zoomed-in SEM image of the cross-section is shown in Figure 8.2 (c). The vertical nanochannels can be found well-aligned, and the size of the channels is in the order of around 100 nm.

8.2 Gold nanoparticle embedding

Since the surface-to-volume ratio in the fabricated np-Si sample is fairly large, the inner wall of the nanochannel is easily oxidized, generating a thin layer of SiO_2. This native layer serves as an inert protection layer that affects the subsequent deposition of metallic nanoparticles. This is because, in conventional methods, the borohydride is usually applied as the gold-ion reducing agent. In this work, to make the fabrication method more straightforward for large-scale production, fewer chemicals are used. Instead of using the assistant reducing agents, the gold atoms are reduced by the metastable Si-H_x termina-

tion. The reaction is initiated near the native np-Si surface as this procedure: $[AuCl_4]^-$ + H^+ + $3e^-$ = Au + $4Cl^-$ + H^+.

Therefore, before the deposition of gold nanoparticles, this undesired SiO_2 layer needs to be removed. The schematic in Figure 8.3 (a) shows the process of deposition of gold nanoparticles (AuNPs), which starts with removing the unwanted oxidized layer. In this work, the np-Si substrate with a thickness of 550 nm is used for all following characterization as well as in the SERS sensing. The np-Si substrate first undergoes a pre-treatment with a 2% HF solution for 30 seconds to remove the native oxide from the pore surfaces. Dangling bonds with hydrogen are saturated at the surface after this treatment. Subsequently, the sample is immersed in a $HAuCl_4$–ethanol solution, where gold ion reduction takes place at the pore channel surfaces. The AuNPs spontaneously grow and form the isolated particles eventually to clusters depending on the immersion time. To enhance the penetration of the $HAuCl_4$–ethanol solution into the nanoporous channels, an ultrasonic bath is utilized during substrate immersion. This not only facilitates the flow into the channels but also prevents the aggregation of Au clusters formation on the top surface, which could block the inlet of the channels and solution penetration and eventually, the deposition of AuNPs in the deeper side of the channel.

Due to the limited diffusion rate of the solution within np-Si nano-channels, the growth of AuNPs already occurs from the top of the nanochannels before the solution reaches the bottom of the substrate. Effective control over the reduction rate by adjusting concentration and temperature is pivotal to facilitate solution penetration to the deeper part of the channels. This is essential to prevent the formed AuNPs from blocking the pore channels. In the previous work, $HAuCl_4$ solution with a concentration below 1 mM at room temperature achieved an equilibrium between diffusion and reduction rates [206]. Elevated temperatures led to cluster formation on the surface, hindering solution infiltration into the pores and impeding uniform growth of AuNPs across the layer thickness. The AuNPs deposition can be achieved by two strategies, i.e., first varying the temperature of the solution while keeping the solution concentration, infiltration rate, and processing time constant; second, controlling the other factors but only varying the processing time. Given the fact that varying the solution temperature leads to a change in the rheology of the liquid, which further impacts the infiltration rate, the deposition of AuNPs is conducted by only varying the processing time. Hence, the np-Si substrate is immersed for 20, 120, and 720 minutes, as shown in Figure 8.3 (a). The 3D structure in grey color indicates the np-Si, and the small dots in yellow represent AuNP. As a trend, the density and the size of the nanoparticles become larger with the immersion time. The temperature during the process remains at 25 °C.

On the other side, variations in AuNP density and size can be achieved by adjusting the $HAuCl_4$ solution concentration. In this work, by applying various combinations of the concentrations and the duration of the processing time, different gold volume fractions are achieved. The results are presented in Table 8.1. The gold volume fraction is estimated using a developed simulation model [206], which is based on the angular-dependent reflectance characterization. After deposition of the AuNPs, the samples are rinsed in ethanol and dried with nitrogen flow.

np-Si substrate	Concentration (mM)	Process time (min)	Gold volume fraction
No. 1	0.5	10	2%
No. 2	1	20	5%
No. 3	1	120	8%
No. 4	1	720	13%

Table 8.1: Parameters of the process and information of the fabricated samples.

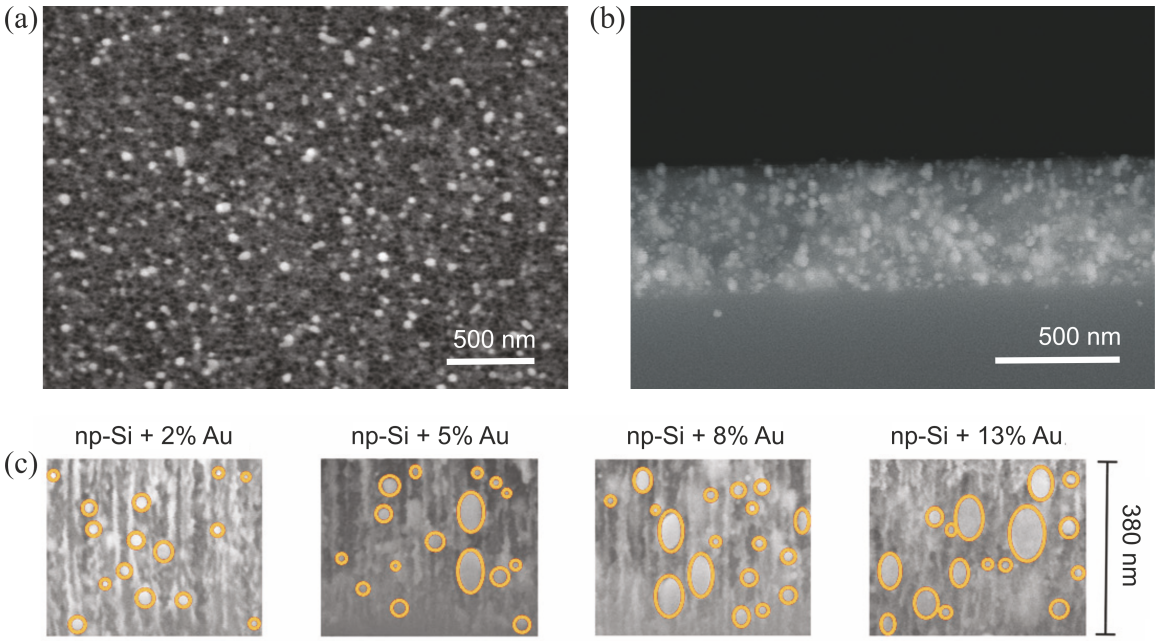

Figure 8.4: Characterization of gold embedded nanoporous silicon substrate. (a) and (b) SEM images of the top surface and the cross-section of the sample possessing a gold volume fraction of 13%. (c) Cross-sectional SEM image of samples fabricated with different gold volume fractions.

8.3 Tunable plasmonic resonance

Figure 8.4 (a) and (b) show the top and cross-sectional SEM images of a fabricated sample. It can be seen in the top-view image that there are no big gold clusters accumulating on the surface of the substrate. The AuNPs exhibit discrete distribution, with particle sizes varying from one to another. The cross-sectional image reveals that the AuNPs are embedded along the vertical channels, distributing in both the top and bottom regions. These findings confirm a uniform dispersion of particles throughout the depth of the 550 nm-thick np-Si substrate without any noticeable severe aggregation.

To quantitatively determine the size of the embedded AuNPs, np-Si substrates fabricated with different parameters are characterized by SEM. The cross-sectional images are presented in Figure 8.4 (c). For all these SEM images, the total vertical length is 380 nm, as depicted on the right side of the figure. The contours of the AuNPs are highlighted

Substrate	$\bar{r}$ (nm)	Average particle spacing (nm)	Calculated number density (m^{-3})
np-Si + 2% Au	8.1	20	9×10^{21}
np-Si + 5% Au	14.5	1.3	4×10^{21}
np-Si + 8% Au	19.5	1.25	2.6×10^{21}
np-Si + 13% Au	26.1	1.05	1.7×10^{21}

Table 8.2: Information of the embedded gold nanoparticles.

in yellow. As a tendency, the size of the AuNPs increases with the immersion time. The estimated volume fraction of the gold (x% Au) for each sample is indicated above each SEM image. Individual particle size can be analyzed by the open-source software ImageJ. Therefore, for each immersion time, the respective mean particle size can be calculated accordingly. With the increased immersion time, the AuNPs tend to form elliptical shapes due to the preferential growth direction imposed by the pore channel walls. Here, the mean particle radius $\bar{r}$ (nm) of each set of parameters is calculated and listed in Table 8.2. The table also summarizes additional information, such as average particle spacing and the calculated number density. With the growth of the particle size, the spacing and the density of particles decline as expected.

To further inspect the particle density difference between samples, a dark-field microscope (DFM) is utilized to collect the scattered light from the nanoparticles. Since the size distribution of the AuNPs is wide, it leads to a broadened scattering spectrum. The DFM used in this work detects the optical information by capturing the optical image with a CCD camera. Therefore, the result is "only" a "color" image. No spectra information is recorded and analyzed. The "color" in the obtained image depends on the color filters in the CCD camera, which are red, green, and blue filters. These color filters are arranged in a proper way and cover individual light-sensitive units, i.e., pixels. As a general phenomenon, the color of light scattered by nanoparticles is primarily determined by the size, shape, and spacing of the nanoparticles. Larger sizes typically result in light with longer wavelengths, often causing a red-shift. Different shapes result in various performances in the emitting light. Here, the shape of the AuNPs is close to the sphere. Therefore, this factor is eased in analysis. The spacing between the different particles, on the other hand, is widely varied. Hence, the color in the captured image is partially affected. This is because the change of the spacing from one to ten nanometers leads to a different plasmon coupling between the metallic nanoparticles [207].

Figure 8.5 shows the recorded DFM images. The relation between the increased immersion time and the particle density is revealed in the images. A 650 nm long pass filter is applied in front of the CCD camera. This blocks other scattered light with shorter wavelengths. The CCD camera used in this work is limited for sensing the visible wavelength range only. It needs to be noted that the intensity of the scattered light is proportional to the scattering cross-section of the particle, which is correlated to the size of the nanoparticles. It needs to be noted that the size of the red dots in the images is not the real size of the nanoparticles. Moreover, as mentioned above, the DFM images only cover the visible

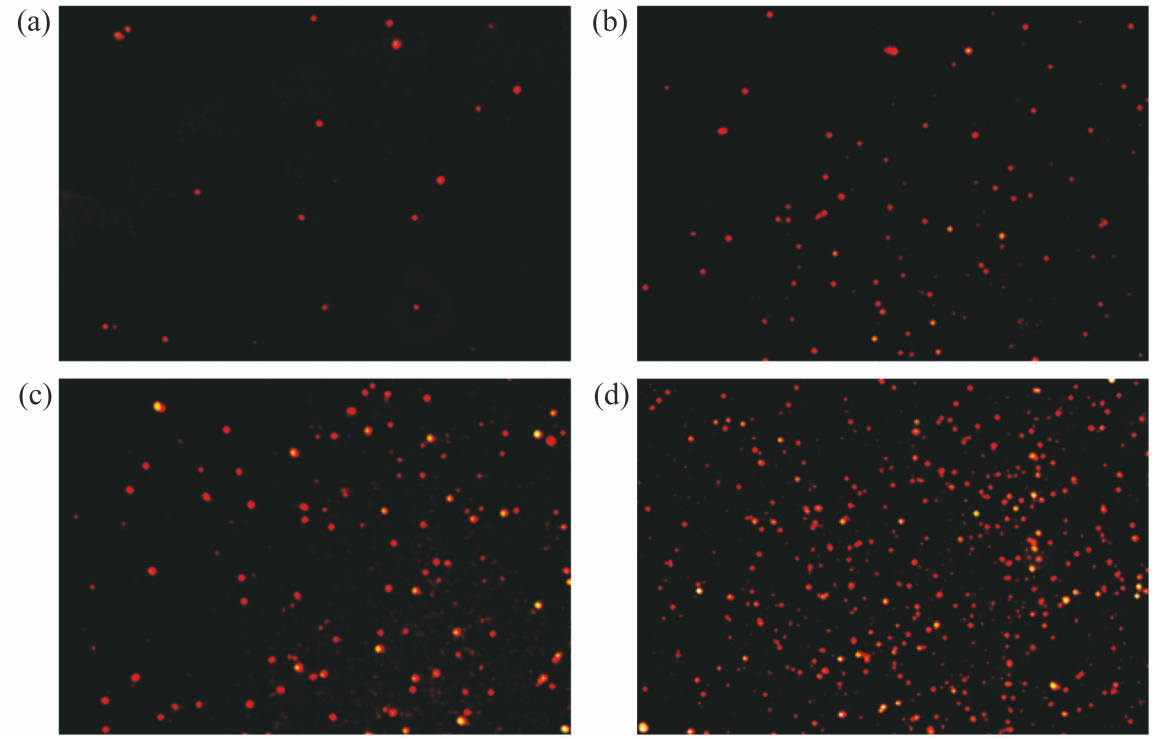

Figure 8.5: Optical images obtained by the dark-field microscope. The images show the top surfaces of the samples. The red dots indicate the scattered light by the nanoparticles. (a), (b), (c), and (d) are the samples with different immersion time lengths, resulting in different volume fractions of Au, i.e., (a) 2%, (b) 5%, (c) 8%, (d) 13%.

wavelength range. To further explore the optical properties of the LSPR, a UV-vis-NIR scanning spectrometer is used for characterization.

The purpose of quantitatively measuring the optical performance of the gold-embedded np-Si is to determine the LSPR peaks. From the theory and empirical work reported [19], the change of the refractive index in the medium around the gold nanoparticles leads to a shift in the resonance peak [208]. For instance, the surrounding environment of the AuNPs in this work is a mixture of air and np-Si. The effective refractive index of this mixture is larger than that of pure air, which is around 1. Additionally, with the decrease in the interparticle spacing, the LSPR peak shifts as well. In principle, when the neighboring AuNPs are brought into proximity, the plasmon resonance shows coupled modes[209]. Therefore, the red-shift of the LSPR of AuNPs is a consequence of the increased effective refractive index and the coupling of plasmon modes. This tendency can be verified by characterizing the individual LSPR peaks in various fabricated samples.

In Figure 8.6, the scattering reflection spectra of the AuNP-embedded np-Si substrates are presented. Measurements are conducted on samples with varying Au volume fractions, including an additional reference sample without any AuNPs. It can be seen that the reference sample shows an almost flat curve when no AuNPs are embedded. The small fluctuation on the measured curve is caused by the limited surface roughness of the np-Si

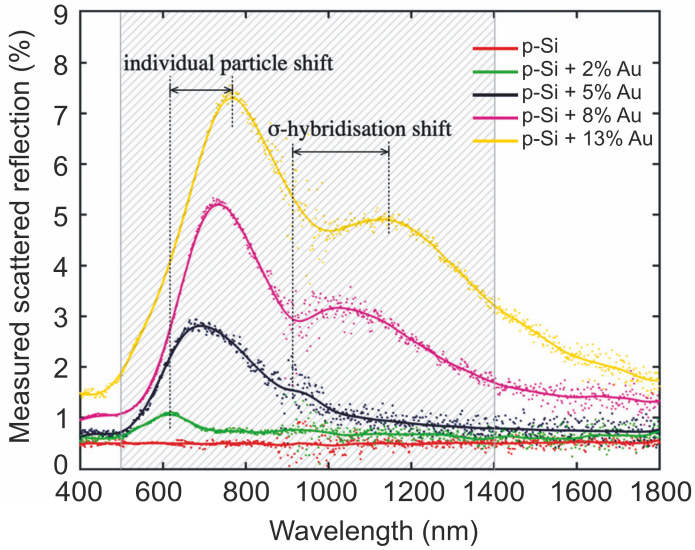

Figure 8.6: Measured scattered reflection of np-Si samples with different volume fractions of gold. The peaks of the curve indicate the peak of localized surface plasmon resonance. Depending on the size and spacing of the gold nanoparticles, single and hybridized plasmon resonance modes are observed.

itself. Since the pore size is much smaller than the wavelength, the scattering ability of the surface exists but is limited. Consequently, there are no scattering centers available to deflect incident photons from their original trajectory. With a small fraction of AuNPs, such as 2%, a peak rises at the wavelength of 610 nm. This is attributed to the LSPR. With an increase in the volume fraction of gold, the resonance peak shifts further into the near-infrared region, accompanied by the emergence of a second scattering band that covers wavelengths between 1000 and 1300 nm. Two principal physical effects contribute to the alteration of the spectrum with an increasing Au fraction within the material.

Firstly, the plasmon resonance undergoes a red-shift as the size of AuNPs increases, as already discussed above. Moreover, this shift of the resonance peak is accompanied by a change in the local environment. As the size of an AuNP becomes larger, it extends towards the opposite wall along the nanochannel, occupying the available space. Consequently, the size of the particle influences the proportions of silicon and air in its vicinity. Particles that are smaller and in sphere shapes leave more unfilled space (air) in the channel. Conversely, larger and elliptical particles increase their contact area with silicon due to their shape, filling the channel. Consequently, larger particles are locally surrounded by an environment with a higher effective dielectric function, causing a red shift in their LSP resonance peak compared to smaller AuNPs.

Secondly, plasmon coupling between adjacent AuNPs can lead to the splitting of the plasmon mode. Analysis based on AuNPs density and mean radius suggests that, for the lowest fraction, the mean spacing between adjacent AuNPs is relatively large, exceeding 10 nm. Under these circumstances, the LSPR field diminishes due to the rapid decay of the plasmon field. It typically declines with the factor of $1/e$ in an interparticle distance of 5 nm [206]. With small particle sizes and low density, the AuNPs can be treated as individual

and isolated nanoparticles. In this case, the displacement of the collective electrons is homogeneous, resulting in a dipolar charge distribution over the nanoparticle surface. Therefore, the displacement of charges yields only one resonance, which is determined by particle properties such as shape and displacement. However, higher Au volume fractions result in larger particles, and the spacing between particles is reduced to a point where the coupling effect becomes significant. This pronounced coupling leads to an extra plasmon resonance referring to the σ-hybridization of two individual AuNPs with collinear and unidirectional fields [210]. The energy of this mode is lower than the primary mode raised by a single AuNP due to the attractive nature of plasmon-plasmon interaction. Therefore, the resonance peak observed is located at longer wavelengths compared to an individual particle case. Since AuNPs within the np-Si substrate possess various sizes and spacings, the scattering spectra measured are a composite of weighted contributions from single and hybridized plasmon resonance modes.

This successful realization of actively controlling the LSPR opens diverse application fields, for instance, pH value measurement [211–213], integrate plasmonic circuits [214], plasmonic switches [215], color filters and polarizers [214], electrochromic smart windows [216–219], and SERS detectors [220]. The core of this work on SERS detector development is to demonstrate a fabrication method that, through a straightforward adjustment in the manufacturing parameters, the plasmon resonance is properly tailored. There are several advantages of this achievement. Firstly and most importantly, by tuning the LSPR peaks to match the wavelength of the excitation laser, the plasmonic field can be enhanced to the maximum extent. Therefore, the sensitivity of the SERS detection is optimized. Secondly, a SERS substrate with an LSP resonance that is easily modified is more versatile and can be used with universal laser sources. Thus, the resulting system can be more affordable and compact, for instance, diode lasers. Thirdly, the fabrication method of 3D np-Si-based SERS substrate has a high scalability. Furthermore, the np-Si is bio-compatible, which largely increases the number of use cases. In the next section, the superiority of AuNPs embedded in a 3D np-Si substrate is demonstrated by using it as a highly sensitive SERS detector.

8.4 SERS for detection of molecules with ultra-low concentration

The np-Si with a gold volume fraction of 13% is used as a SERS substrate. The LSP resonance in this substrate is close to 808 nm, which is the central wavelength emitted by a laser used for demonstration. During the conduction of the SERS detection of the analyte with low concentration, methylene blue (MB) was utilized as a probe molecule due to its absorption peak being away from the excitation wavelength, minimizing the parasitic luminescence background [221]. The Raman spectra of three samples are compared, as shown in Figure 8.8 (a). The samples are bare np-Si, AuNPs embedded np-Si substrate without MB, and AuNPs embedded np-Si substrate after soaking in 1 μM MB. A sharp Raman signal at 520 cm^{-1} is observed in each sample, corresponding to the intrinsic TO phonon mode of silicon [222]. In the SERS substrates without MB molecules, the signal

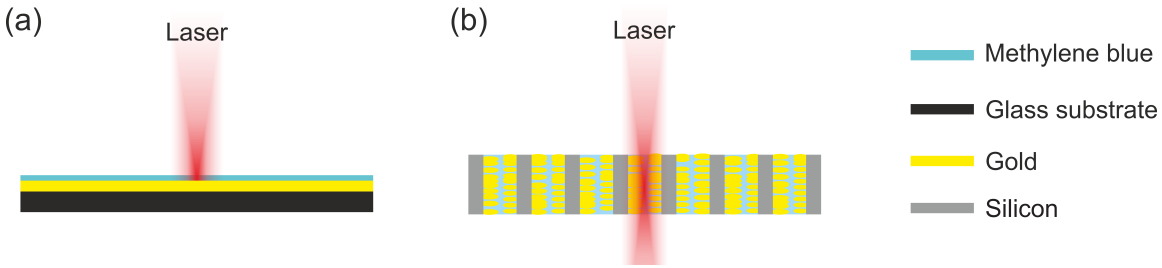

Figure 8.7: Schematic of laser illumination on reference and SERS samples. (a) The reference sample. The laser illumination area is confined to a 2D circular surface area. (b) The SERS sample. The laser-illuminated region is a 3D volume.

is almost flat when ignoring the peak of 520 cm^{-1}. This performance proves the usage of these silicon-based SERS substrates in various chemical and biological detection, which require ultra-low background noise. In contrast, the substrate with MB molecules shows clear Raman peaks corresponding to the laser excitation. The typical Raman peaks of MB molecules are observed, which are 450, 770, and 1150 cm^{-1} [223–228].

To demonstrate the ultra-high sensitivity of the SERS substrates, a series of samples were soaked in MB solution within a concentration range between 1 μM and down to an ultra-low level of 1 pM, and measured for SERS signal intensity as depicted in Figure 8.8 (b). Remarkably, even at a concentration as low as 1 pM, the Raman scattering peak of MB molecule at 450 cm^{-1} remained detectable. Furthermore, increasing the MB molecule concentration makes the spectral fingerprints more visible.

The Raman intensity of three representative peaks at 450, 770, and 1150 cm^{-1} (corresponding to short, middle, and long spectral regions, respectively) is plotted as a function of MB concentration, as shown in Figure 8.8 (c). It is clear that the intensity increase for these peaks with concentration behaves identically. This suggests that the enhancement of the Raman signal on the fabricated SERS substrate is not spectrally selective. This performance enables a big advantage in the quantitative analysis of molecule concentration based on Raman signal intensity. Additionally, each spectral fingerprint can simultaneously refer to the others during analysis, enhancing the reliability of the results.

8.5 Determining the enhancement factor of SERS

The enhancement factor (EF) serves as a crucial parameter for the quantitative assessment of the performance of the SERS substrates. In this study, the EF is calculated as the following equation:

$$EF = \frac{I_{SERS}/N_{SERS}}{I_{Ref}/N_{Ref}} \tag{8.1}$$

where I_{SERS} and I_{Ref} are the detected Raman signal intensities with and without surface enhancement, respectively, while N_{SERS} and N_{Ref} represent the corresponding number of analyte molecules exposed to the laser beam. The radius of the laser spot, r, can be calculated as [229]:

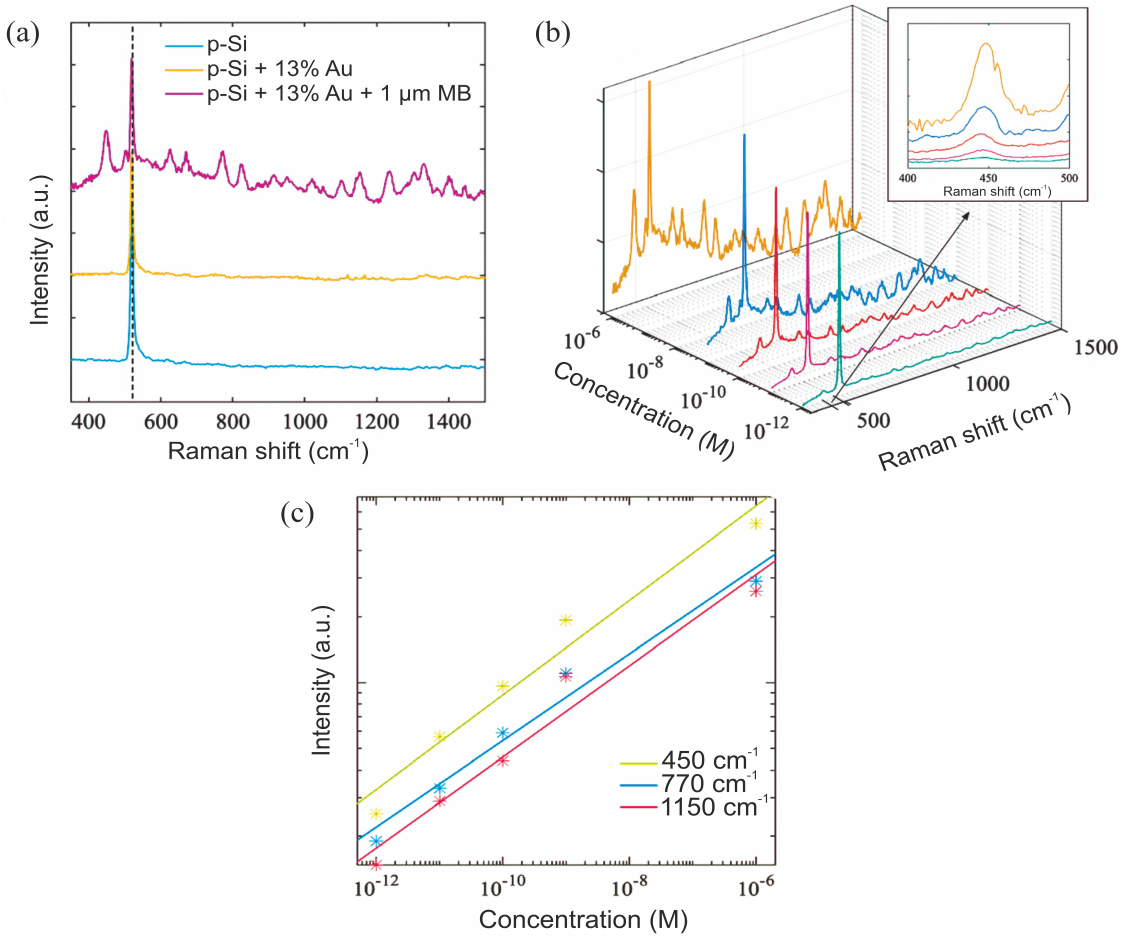

Figure 8.8: Detection of methylene blue molecules by SERS substrate. (a) Raman spectra of np-Si, AuNPs embedded np-Si, and AuNPs embedded np-Si + 1 μM MB, respectively. The 520 cm^{-1} peaks are raised from the TO phonon mode of the silicon. The baseline of each Raman spectrum is rearranged for better comparison. (b) Raman spectra of AuNPs embedded np-Si with different concentrations of MB molecules, varying from 1 pM to 1 μM. The insert is the zoomed-in view of the 450 cm^{-1} peak. (c) Linear relationship of the concentration and Raman intensity of three Raman peaks at 450, 770, and 1150 cm^{-1}, respectively.

$$r = \frac{1.22\lambda}{2NA} \tag{8.2}$$

where λ is the wavelength of the laser and NA is the numerical aperture of the objective used in SERS measurement. In this work, the wavelength of the laser is 808 nm, and the NA is 0.6. Therefore, r is calculated to be around 0.8 μm.

For the reference measurement of I_{Ref}, an Au thin film of around 100 nm is thermally deposited onto a glass substrate with a size of 1 cm^2. 2 mL MB solution with a concentration of 100 mM is uniformly coated over the surface. Since the laser cannot transmit through the optically thick Au layer, the effective illuminated area is, therefore, calculated as a 2D surface. In this work, the shape of this area is approximated as a circular shape.

$I_{\mathbf{SERS}}$	$N_{\mathbf{SERS}}$	$I_{\mathbf{Ref}}$	$N_{\mathbf{Ref}}$	**EF**
0.196	24	4.063	2.4×10^{12}	4.8×10^{9}

Table 8.3: Summary of the essential numbers for estimating the enhancement factor.

Accordingly, the area is determined by the radius of the laser spot. Consequently, in the reference measurement, the number of MB molecules, N_{Ref}, amounts to 2.4×10^{12} in the laser-illuminated area.

In the SERS measurements, the sample is soaked in 2 mL MB solution with a concentration of 1 pM, which is the minimum detectable concentration. The sample size is 1 cm^2 with a thickness of 550 nm, yielding a total volume V_{total} of $5.5\times10^{-11}m^3$. Since the SERS substrate is made for 3D detection, an illuminated volume should be considered instead of a flat area. Here, the illuminated 3D volume is assumed to be a cylinder, where the illuminated volume, V_{illu}, is calculated as:

$$V = \pi r^2 H \tag{8.3}$$

where r is the radius of the laser spot and H is the sample thickness. Therefore, V_{illu} is calculated as around $1.1\times10^{-18}m^3$. Assuming the MB molecules are fully adsorbed by the SERS substrate and uniformly distributed volumetrically, the number of illuminated MB molecules N_{SERS} is calculated as:

$$N_{SERS} = N_A \times 2 \times 10^{-3}(L) \times 10^{-12}(M) \times \frac{V_{illu}}{V_{total}} \tag{8.4}$$

where N_A is the Avogadro constant, which is 6.02214076×10^{23} mol^{-1}. Therefore, the N_{SERS} is 24 accordingly.

To yield a more reliable EF, the intensity of I_{SERS} and I_{RS} are calculated by integrating the Raman intensity at 450, 770 and 1150 cm^{-1}. The overall I_{SERS} and I_{Ref} obtained are 0.196 and 4.063, respectively (arbitrary unit). Consequently, according to Equation 8.1, the EF is yielded as 4.8×10^{9}. The essential numbers for the calculation and the estimated EF are summarized in Table 8.3

This ultra-high EF reveals that the developed SERS substrate is highly suitable for single-molecule detection. The notably high EF in the SERS substrate can be attributed to the unique sponge-like morphological structure of np-Si. In contrast to the planar substrates, the 3D structure provides a tremendous surface area for analyte adsorption and hot spot growth. Table 8.4 shows a comparison of EF of SERS from different works. Various levels of EF can be achieved based on device designs and metallic materials.

8.6 Summary and discussion

In this chapter, 3D np-Si substrates are fabricated, followed by embedding AuNPs in the created porous matrix. The tailoring of the LSP resonance is successfully achieved by adjusting the fabrication parameters. It is realized by controlling the volume fraction of the AuNP in the SERS substrate. This tailorable resonance is further used for SERS

Sample	EF	References
AuNP cluster	*10^9*	*This work*
Single AuNP	10^4	Litti et al. [230]
Aggregate AuNPs	10^5	Litti et al. [230]
Aggregate AuNPs	10^6	Habermehl et al. [231]
Au nanoarray	10^7	Wei et al. [232]
Au nanopillar array	10^7	Liu et al. [233]
Au nanostar	10^8	Hrelescu et al. [234]
AgNP cluster	10^8	Mao et al. [235]

Table 8.4: Comparison of enhancement factors from different works.

detection by properly matching the resonance peak with the incident excitation laser wavelength. The results demonstrate the high versatility of the developed method and SERS substrate.

Different characterization tools, such as SEM, DFM, and UV-vis-NIR spectroscopy, are used to determine the LSP resonance raised by the induced AuNPs. SERS measurement is conducted to explore the minimum detectable concentration of MB molecules. Consequently, the sensitivity of the SERS substrate is defined by the EF of the Raman signal. Remarkably, the EF is estimated in the order of 10^9, which fulfills the requirement of single molecule detection [235]. This substantial amplification is likely attributed to the unique properties of np-Si, which can accommodate a significant number of metal particles engaged in interactions throughout the entire volume of the substrate.

The work in this chapter falls within the scope of exploring the sensing ability of fabricated photonic nanostructures. It involves the modification and precise control of the optical properties of the fabricated device. By showcasing single-molecule detection based on surface-enhanced Raman spectroscopy, it provides a comprehensive approach encompassing design, fabrication, and application.

9 Conclusion and outlook

In this chapter, conclusions of the conducted work and realized results are presented. It consists of three parts of work, i.e., the inkjet-printed optical interference filters, the pixelized haze-controlled smart window, and the highly sensitive SERS substrates. Individual outlook on each work is provided for further development.

9.1 Conclusion

Research on photonic nanostructures has stimulated advances in a broad range of science and technologies. A strong driving force behind devoting numerous efforts to this research field is that it enables the precise control of many properties of light and matter that cannot be easily addressed on the macro-scale. Fabrication of novel photonic nanostructures, or photonic nanostructures fabricated by advanced approaches, is key to the current challenges. It is a highly interdisciplinary subject, which could involve optics, photonics, fluid dynamics, semiconductor physics, thermodynamic physics, chemical engineering, and biological engineering.

In this dissertation, different photonic nanostructures are designed and fabricated. Light management and optical sensing using developed nanostructures are demonstrated. The work explores two physical domains, i.e., optical interference and scattering. Three fields are investigated, i.e., optical filters, smart windows, and chemical sensors based on surface-enhanced Raman scattering.

Inkjet-printed optical interference filters

Optical interference filters consist of multilayers. Fabricating such filters requires a highly precise control of layer thickness. The thickness of individual layers is usually in the range of several tens to hundreds of nanometers, with required thickness tolerance within 3% of each layer. Most high-end optical interference filters are made in vacuum chambers to achieve a precisely controlled layer deposition. The layer number of these high-quality filters starts from several tens. With a traditional solution-based process, achieving the required layer numbers while delivering a good optical property is challenging.

In this dissertation, optical interference filters have been fabricated using the inks and printing process that were developed. The work starts by characterizing the surface energy of the SiO_2 and TiO_2 surfaces, which are the layers used in the multilayer structure. Based on the surface properties, inks with selected organic vehicles are developed. The printability of the inks is assessed by two approaches depending on various rheological parameters. Subsequently, the SiO_2 and TiO_2 thin films are inkjet printed. By controlling the printing resolution, the thickness of the thin film is precisely controlled, with a

standard deviation below 1% of the layer thickness. The corresponding refractive index and extinction coefficient are measured for each thin film. According to the results, the inkjet-printed thin films show their suitability for use in producing optical filters.

Optical interference can be fabricated in periodic and non-periodic structures depending on the designed optical properties and applications. The resulting spectral differences between these two structures are the ripples and overall transmission or reflection. Applying non-periodic layer stacking can suppress the problems mentioned. However, controlling the thickness and printing process takes more effort because it is not simply the repetition of layer stacking but the deposition of the layer with the exact thickness obtained from the simulation. In this work, non-periodic layer assemblies have been realized based on the precise layer thickness control and highly repeatable printing process. The ripples in the transmission curve are suppressed as expected. Based on the rational work above, various optical interference filters are inkjet printed. Lonapass, shortpass, bandpass, and dichroic filters are fabricated by full inkjet printing in ambient conditions. The optical properties of the printed filters are well-replicated from the simulation with small deviations. This is a breakthrough in fabricating the optical interference filter. The developed method not only eliminates cost-intensive machines and conditions for production but also provides new possibilities for filter fabrication. Examples of the advantages are maskless production of filter arrays, rapid prototyping and iterations, fast and affordable customization, and scalability. The printed filters mentioned above are in a size of 20×20 cm^2. Upscaling the filters is also achieved by printing the dichroic filter with a size up to A4 (210×297 cm^2). The optical uniformity of this filter is characterized. The results show small standard deviations of the cut-on, cut-off, and center wavelengths. The order of the deviation is within several nanometers. Furthermore, lateral patterning of the filters is demonstrated. The filters are presented in a logo form. Besides, the inkjet printing process, initially developed for printing on glass, has been successfully transferred to a flexible foil substrate. Later, the printed filters and the commercial products are compared. The optical quality of the inkjet-printed filters is satisfactory, and further strategies to improve the performance are provided. Moreover, the durability of the printed filters is characterized where adhesion and abrasion tests are conducted. The results show a satisfactory surface quality of the fabricated filters. The work on inkjet-printed optical interference filters provides an industrially applicable route to produce filters in a novel and cost-effective way.

Optical scattering control and pixelation in smart windows

The optical scattering raised from the nano- and microstructures is investigated. The effective scattering centers are induced on elastic polydimethylsiloxane (PDMS) slices, enabling the device to function as a mechanoresponsive smart window. The induced optical scattering is tunable and can be manipulated by applying external stress.

Nowadays, most smart windows switch their states globally. The optical behavior needs to be modified when applications such as information conveying or presenting a high dynamic image are required. In this work, a smart window with a high dynamic range is demonstrated with a signage displaying function. This is achieved by inducing various optical scattering levels on different unit surfaces, i.e., pixel by pixel. The nano-

and microstructures of each pixel are precisely defined by inkjet-printed etching masks with the subsequent plasma surface treatment. The material used for etching masks is poly(methyl methacrylate). In order to modify the affinity between the surface and the applied ink during inkjet printing, an essential ultra-thin buffer is deposited on the PDMS surface. The newly developed aqua-based surface coating method enables successful and precise micropattern printing for further plasma etching. This surface modification, or hydrophilization, is a crucial step to allow the realization of pixelated optical scattering. The qualitative characterization of the optical scattering is conducted by a defined parameter called haze. It shows a high linear relationship between the haze and the parameter used in mask design, i.e., the greyscale, which determines the input for the printing process. In this way, the optical performance is precisely controlled by the digital printing process. The work on the smart window develops a novel method of surface hydrophilization, allowing a precise deposition of micro-sized etching masks. Different nano- and microstructures are induced for individual pixel areas, enabling the mechanoresponsive smart windows a high dynamic range for signage display.

Surface-enhanced Raman scattering for high sensitivity optical sensing

Raman scattering is an inelastic optical scattering commonly used in chemical sensing. To increase the sensitivity, surface-enhanced Raman scattering (SERS) microscopy is investigated in this work. The significantly enhanced Raman signal is achieved by two factors, i.e., the 3D sensing substrate and the tailored localized surface plasmonic resonance (LSPR).

This work includes embedding the gold nanoparticles in a 3D nanoporous silicon substrate. The nanonetwork in the 3D substrate offers an enormous surface area for gold nanoparticle deposition. Consequently, a high density of hot spots for detecting molecules with an ultra-low concentration is achieved. To maximize the sensitivity of the SERS sensor, the LSPR is tailored in a manner that the resonance is pushed close to the excitation laser wavelength. This is achieved by carefully controlling the size of the gold nanoparticles and their distribution in the 3D nanoporous silicon substrate. The high sensitivity of the SERS substrate is validated by measuring the methylene blue molecules with down to picomole per liter concentration, showing a SERS enhancement factor in the order of 10^9. The work on developing SERS substrates with a tunable plasmonic resonance offers a cost-effective, highly sensitive, and scalable device for the optical sensing of chemical components.

9.2 Outlook

The devices developed in this work have demonstrated convincing and satisfactory results for their intended applications. Considering the growing interest in photonic research, this work is expected to accelerate advancements in nanofabrication for light management and optical sensing. Additionally, new opportunities are anticipated as a result of these developments:

Inkjet-printed optical filters

The core of this work is inkjet printing, an advanced fabrication approach for optical interference filters. Inkjet printing offers several technical advantages, such as the ability to operate in ambient conditions, cost-effective production, rapid prototyping, and significant flexibility in lateral patterning, substrate selection, and printing of various filter sizes. These benefits extend beyond optical interference filters and can be harnessed for the fabrication of other photonic devices, including microlasers and optical sensors. For example, Bragg mirrors, commonly employed in vertical-cavity surface-emitting lasers (VCSELs) [236], can be produced using inkjet printing. Multispectral and hyperspectral cameras, requiring different spectral channels, can utilize an optical filter array [237]. Inkjet-printed optical interference filters are also adaptable for anti-reflection purposes, presenting a cost-effective alternative to conventional manufacturing methods [238]. Furthermore, the larger-scale, in-ambient fabrication enabled by inkjet printing opens possibilities for energy-efficient coatings on windows and buildings [239].

Light property control in smart windows

Surface property modification for printing

An ultra-thin buffer layer or membrane has a broad spectrum of applications and can be incorporated into various systems [240]. It co-exists with other functional layers to modify the property of the device. In general solution processing of thin films, the property adjustment of layer property is often integral. Adding an ultra-thin layer without deteriorating the original properties of the layers is desired. The developed method in this work of depositing an ultra-thin film to enhance the wettability of the printed inks on the substrate can be employed and adapted to many other applications. For instance, it can be applied to microfluid systems where a high affinity between the channel wall and the liquid is needed [241] as well as for bio and medical applications [242]. Therefore, the utilization of the developed approach shall be extended.

Pixelated smart windows

The mechanoresponsive smart window belongs to the category of smart windows. The pixelation of this type of device is achieved. Despite that, microsize deposition enabled by inkjet printing can be explored for other types of smart windows. In principle, it can be used in all types of smart windows, including electrochromic, thermochromic, magnetic-chromic, and radiative-chromic ones. This is because all these devices require the integration of functional materials or layers. Importantly, many functional materials, such as liquid crystals or thermoresponsive gels, are in a liquid phase. These materials are not feasible to deposit using vacuum-based methods but are highly suitable for inkjet printing. Therefore, further exploration of the fabrication of smart devices using developed inkjet printing for pixelated patterning is expected.

Optical sensing using Raman scattering

The developed SERS sensor is highly sensitive to chemical methylene blue detection. It is achieved by combining a 3D structure with a tailored plasmonic resonance. Two perspectives can be considered to broaden the application of the developed methods further.

First, developing various SERS substrates for different excitation laser sources. With the increased demand for environmental and medical technologies, a large number of optical sensors are needed. Sensors based on lasers offer outstanding detection abilities, with diode lasers showing their advantages in compact-sized systems. To assess the sensitivity of the sensor to different laser excitations, further work needs to be conducted to adjust the plasmonic resonance to match the light source.

Second, tailoring the plasmonic resonance peak in the SERS substrate requires a large amount of empirical effort. The adequate processing parameters are a result of fine-tuning of experimental conditions. Therefore, it is highly attractive to develop a SERS substrate that a plasmonic resonance peak can be actively tuned [243]. Depending on the tunable range, it can either fine-tune the peak to compensate for the offset between the laser wavelength and plasmonic resonance peak to maximize sensitivity or vary the resonance peak over a relatively large range, allowing the use of the SERS substrate with several laser sources.

Bibliography

[1] Paras N. Prasad. *Nanophotonics*. Hoboken NJ: Wiley, 2004. ISBN: 9780471649885.

[2] John Collins, Baldassare Di Bartolo, and Luciano Silvestri, eds. *Nano-Structures for Optics and Photonics: Optical Strategies for Enhancing Sensing, Imaging, Communication and Energy Conversion*. 1st ed. 2015. NATO Science for Peace and Security Series B. Dordrecht: Springer Netherlands and Imprint: Springer, 2015. ISBN: 9789401791335.

[3] Daniel Thangadurai, T et al. *Nanostructured Materials*. 1st edition 2020. Engineering Materials. Cham: Springer International Publishing, 2020. ISBN: 9783030261450.

[4] F. Träger. *Springer handbook of lasers and optics*. 2nd ed. Dordrecht and New York: Springer, 2012. ISBN: 978-3-642-19409-2.

[5] Peter. Török and Fu-Jen. Kao, eds. *Optical Imaging and Microscopy: Techniques and Advanced Systems*. 2nd ed. 2007. Vol. 87. Springer Series in Optical Sciences. Berlin, Heidelberg: Springer Berlin Heidelberg and Imprint: Springer, 2007. ISBN: 978-3-540-69565-3.

[6] Bruce J. Berne. *Dynamic Light Scattering: With Applications to Chemistry, Biology, and Physics*. Dover Publications, 2013. ISBN: 9780486320243.

[7] Yujie Ke et al. "Smart Windows: Electro–, Thermo–, Mechano–, Photochromics, and Beyond". In: *Advanced Energy Materials* 9.39 (2019). ISSN: 1614-6832. DOI: 10.1002/aenm.201902066.

[8] Philseok Kim et al. "Rational Design of Mechano-Responsive Optical Materials by Fine Tuning the Evolution of Strain-Dependent Wrinkling Patterns". In: *Advanced Optical Materials* 1.5 (2013), pp. 381–388. ISSN: 2195-1071. DOI: 10.1002/adom.201300034.

[9] Judith Langer et al. "Present and Future of Surface-Enhanced Raman Scattering". In: *ACS nano* 14.1 (2020), pp. 28–117. DOI: 10.1021/acsnano.9b04224.

[10] Sarah M. Stranahan and Katherine A. Willets. "Super-resolution optical imaging of single-molecule SERS hot spots". In: *Nano letters* 10.9 (2010), pp. 3777–3784. DOI: 10.1021/nl102559d.

[11] Eleonora Petryayeva and Ulrich J. Krull. "Localized surface plasmon resonance: nanostructures, bioassays and biosensing–a review". In: *Analytica chimica acta* 706.1 (2011), pp. 8–24. DOI: 10.1016/j.aca.2011.08.020.

[12] Ana Isabel Pérez-Jiménez et al. "Surface-enhanced Raman spectroscopy: benefits, trade-offs and future developments". In: *Chemical science* 11.18 (2020), pp. 4563–4577. ISSN: 2041-6520. DOI: 10.1039/d0sc00809e.

[13] Wolfram Hergert and Thomas Wriedt. "The Mie Theory". In: 169 (2012). DOI: 10.1007/978-3-642-28738-1.

[14] Aso Rahimzadegan et al. "Minimalist Mie coefficient model". In: *Optics express* 28.11 (2020), pp. 16511–16525. DOI: 10.1364/OE.390331.

[15] Alex Zunger et al. "Raman Scattering in Materials Science". In: 42 (2000). DOI: 10.1007/978-3-662-04221-2.

[16] Song-Yuan Ding et al. "Electromagnetic theories of surface-enhanced Raman spectroscopy". In: *Chemical Society reviews* 46.13 (2017), pp. 4042–4076. DOI: 10.1039/c7cs00238f.

[17] Kristen H. Burns, Prasenjit Srivastava, and Christopher G. Elles. "Absolute Cross Sections of Liquids from Broadband Stimulated Raman Scattering with Femtosecond and Picosecond Pulses". In: *Analytical chemistry* 92.15 (2020), pp. 10686–10692. DOI: 10.1021/acs.analchem.0c01785.

[18] Erik Martinsson and Daniel Aili. "Refractometric Sensing Using Plasmonic Nanoparticles". In: *Encyclopedia of Nanotechnology*. Ed. by Bharat Bhushan. Dordrecht: Springer Netherlands, 2014, pp. 1–11. ISBN: 978-94-007-6178-0. DOI: 10.1007/978-94-007-6178-0{\textunderscore}100984-1.

[19] Katherine A. Willets and Richard P. van Duyne. "Localized surface plasmon resonance spectroscopy and sensing". In: *Annual review of physical chemistry* 58 (2007), pp. 267–297. ISSN: 0066-426X. DOI: 10.1146/annurev.physchem.58.032806.104607.

[20] Paola Lova, Giovanni Manfredi, and Davide Comoretto. "Advances in Functional Solution Processed Planar 1D Photonic Crystals". In: *Advanced Optical Materials* 6.24 (2018), p. 1800730. ISSN: 2195-1071. DOI: 10.1002/adom.201800730.

[21] Emilia Palo and Konstantinos S. Daskalakis. "Prospects in Broadening the Application of Planar Solution–Based Distributed Bragg Reflectors". In: *Advanced Materials Interfaces* 10.19 (2023). ISSN: 2196-7350. DOI: 10.1002/admi.202202206.

[22] Mei Fang et al. "Design and tailoring of inks for inkjet patterning of metal oxides". In: *Royal Society open science* 7.4 (2020), p. 200242. ISSN: 2054-5703. DOI: 10.1098/rsos.200242.

[23] W. Y. Padrón-Hernández et al. "Stable inks for inkjet printing of TiO2 thin films". In: *Materials Science in Semiconductor Processing* 81 (2018), pp. 75–81. ISSN: 13698001. DOI: 10.1016/j.mssp.2018.03.015.

[24] Miguel Anaya et al. "Solution processed high refractive index contrast distributed Bragg reflectors". In: *Journal of Materials Chemistry C* 4.20 (2016), pp. 4532–4537. ISSN: 2050-7526. DOI: 10.1039/C6TC00663A.

[25] Leonid M. Goldenberg, Victor Lisinetskii, and Sigurd Schrader. "Fast and simple fabrication of organic Bragg mirrors—application to plastic microchip lasers". In: *Laser Physics Letters* 10.5 (2013), p. 055808. ISSN: 1612-2011. DOI: 10.1088/1612-2011/10/5/055808.

[26] Barbara Brudieu et al. “Sol-Gel Route Toward Efficient and Robust Distributed Bragg Reflectors for Light Management Applications”. In: *Advanced Optical Materials* 2.11 (2014), pp. 1105–1112. ISSN: 2195-1071. DOI: 10.1002/adom.201400292.

[27] Venkatesh Yepuri, R. S. Dubey, and Brijesh Kumar. “Rapid and economic fabrication approach of dielectric reflectors for energy harvesting applications”. In: *Scientific reports* 10.1 (2020), p. 15930. ISSN: 2045-2322. DOI: 10.1038/s41598-020-73052-w.

[28] Diógenes Frederichi, Mara Heloisa Neves Olsen Scaliante, and Rosangela Bergamasco. “Structured photocatalytic systems: photocatalytic coatings on low-cost structures for treatment of water contaminated with micropollutants-a short review”. In: *Environmental science and pollution research international* 28.19 (2021), pp. 23610–23633. DOI: 10.1007/s11356-020-10022-9.

[29] Carina Bronnbauer et al. “Printing of Large-Scale, Flexible, Long-Term Stable Dielectric Mirrors with Suppressed Side Interferences”. In: *Advanced Optical Materials* 6.1 (2018), p. 1700518. ISSN: 2195-1071. DOI: 10.1002/adom.201700518.

[30] Carina Bronnbauer et al. “Printable Dielectric Mirrors with Easily Adjustable and Well-Defined Reflection Maxima for Semitransparent Organic Solar Cells”. In: *Advanced Optical Materials* 3.10 (2015), pp. 1424–1430. ISSN: 2195-1071. DOI: 10.1002/adom.201500216.

[31] César Omar Ramírez Quiroz et al. “Coloring Semitransparent Perovskite Solar Cells via Dielectric Mirrors”. In: *ACS nano* 10.5 (2016), pp. 5104–5112. DOI: 10.1021/acsnano.6b00225.

[32] Shuai Gao et al. “Time-Resolved Analysis of Dielectric Mirrors for Vapor Sensing”. In: *ACS applied materials & interfaces* 10.42 (2018), pp. 36398–36406. DOI: 10.1021/acsami.8b11434.

[33] Aleksandr V. Yakovlev et al. “Inkjet Color Printing by Interference Nanostructures”. In: *ACS nano* 10.3 (2016), pp. 3078–3086. DOI: 10.1021/acsnano.5b06074.

[34] Aleksandr V. Yakovlev et al. “Inkjet printing of TiO2/AlOOH heterostructures for the formation of interference color images with high optical visibility”. In: *Scientific reports* 6 (2016), p. 37090. ISSN: 2045-2322. DOI: 10.1038/srep37090.

[35] Muhammad Ali Shah et al. “Classifications and Applications of Inkjet Printing Technology: A Review”. In: *IEEE Access* 9 (2021), pp. 140079–140102. DOI: 10.1109/ACCESS.2021.3119219.

[36] Laxmidhar Nayak et al. “A review on inkjet printing of nanoparticle inks for flexible electronics”. In: *Journal of Materials Chemistry C* 7.29 (2019), pp. 8771–8795. ISSN: 2050-7526. DOI: 10.1039/C9TC01630A.

[37] Ludvik Martinu and Daniel Poitras. “Plasma deposition of optical films and coatings: A review”. In: *Journal of Vacuum Science & Technology A: Vacuum, Surfaces, and Films* 18.6 (2000), pp. 2619–2645. ISSN: 0734-2101. DOI: 10.1116/1.1314395.

[38] Wei Ma et al. "Flexible, self-standing and patternable P(MMA-BA)/TiO2 photonic crystals with tunable and bright structural colors". In: *Dyes and Pigments* 160 (2019), pp. 740–746. ISSN: 01437208. DOI: 10.1016/j.dyepig.2018.08.061.

[39] Tristan S. Kleine et al. "One Dimensional Photonic Crystals Using Ultrahigh Refractive Index Chalcogenide Hybrid Inorganic/Organic Polymers". In: *ACS Macro Letters* 7.7 (2018), pp. 875–880. ISSN: 2161-1653. DOI: 10.1021/acsmacrolett.8b00245.

[40] J. R. Castro Smirnov, Mauricio E. Calvo, and Hernán Míguez. "Selective UV Reflecting Mirrors Based on Nanoparticle Multilayers". In: *Advanced Functional Materials* 23.22 (2013), pp. 2805–2811. ISSN: 1616-301X. DOI: 10.1002/adfm.201202587.

[41] Silvia Colodrero et al. "Efficient Transparent Thin Dye Solar Cells Based on Highly Porous 1D Photonic Crystals". In: *Advanced Functional Materials* 22.6 (2012), pp. 1303–1310. ISSN: 1616-301X. DOI: 10.1002/adfm.201102159.

[42] Mauricio E. Calvo and Hernán Míguez. "Flexible, Adhesive, and Biocompatible Bragg Mirrors Based on Polydimethylsiloxane Infiltrated Nanoparticle Multilayers". In: *Chemistry of Materials* 22.13 (2010), pp. 3909–3915. ISSN: 0897-4756. DOI: 10.1021/cm1001016.

[43] Olalla Sánchez-Sobrado, Mauricio E. Calvo, and Hernán Míguez. "Versatility and multifunctionality of highly reflecting Bragg mirrors based on nanoparticle multilayers". In: *Journal of Materials Chemistry* 20.38 (2010), p. 8240. ISSN: 0959-9428. DOI: 10.1039/c0jm01508c.

[44] Nuria Hidalgo, Mauricio E. Calvo, and Hernán Míguez. "Mesostructured thin films as responsive optical coatings of photonic crystals". In: *Small* 5.20 (2009), pp. 2309–2315. DOI: 10.1002/smll.200900411.

[45] Johannes Kobler et al. "Vapor-sensitive bragg mirrors and optical isotherms from mesoporous nanoparticle suspensions". In: *ACS nano* 3.7 (2009), pp. 1669–1676. DOI: 10.1021/nn800911c.

[46] Daniel P. Puzzo et al. "Color from colorless nanomaterials: Bragg reflectors made of nanoparticles". In: *Journal of Materials Chemistry* 19.21 (2009), p. 3500. ISSN: 0959-9428. DOI: 10.1039/b903229k.

[47] Mitsuteru Kimura, Kazuaki Okahara, and Toshihiko Miyamoto. "Tunable multilayer-film distributed-Bragg-reflector filter". In: *Journal of Applied Physics* 50.3 (1979), pp. 1222–1225. ISSN: 0021-8979. DOI: 10.1063/1.326154.

[48] Yanfeng Gao et al. "Nanoceramic VO2 thermochromic smart glass: A review on progress in solution processing". In: *Nano Energy* 1.2 (2012), pp. 221–246. ISSN: 22112855. DOI: 10.1016/j.nanoen.2011.12.002.

[49] S.-Y. Li, G. A. Niklasson, and C. G. Granqvist. "Thermochromic fenestration with VO2-based materials: Three challenges and how they can be met". In: *Thin Solid Films* 520.10 (2012), pp. 3823–3828. ISSN: 00406090. DOI: 10.1016/j.tsf.2011.10.053.

[50] M. Panagopoulou et al. “Thermochromic performance of Mg-doped VO2 thin films on functional substrates for glazing applications”. In: *Solar Energy Materials and Solar Cells* 157 (2016), pp. 1004–1010. ISSN: 09270248. DOI: 10.1016/j.solmat.2016.08.021.

[51] Jingting Zhu et al. “Vanadium Dioxide Nanoparticle-based Thermochromic Smart Coating: High Luminous Transmittance, Excellent Solar Regulation Efficiency, and Near Room Temperature Phase Transition”. In: *ACS applied materials & interfaces* 7.50 (2015), pp. 27796–27803. DOI: 10.1021/acsami.5b09011.

[52] Yuliang Chen et al. “Free-standing SWNTs/VO 2 /Mica hierarchical films for high-performance thermochromic devices”. In: *Nano Energy* 31 (2017), pp. 144–151. ISSN: 22112855. DOI: 10.1016/j.nanoen.2016.11.030.

[53] Fei Guo et al. “Printed Smart Photovoltaic Window Integrated with an Energy-Saving Thermochromic Layer”. In: *Advanced Optical Materials* 3.11 (2015), pp. 1524–1529. ISSN: 2195-1071. DOI: 10.1002/adom.201500314.

[54] Yu Xie et al. “A Phase-Changing Polymer Film for Broadband Smart Window Applications”. In: *Macromolecular rapid communications* 41.16 (2020), e2000290. DOI: 10.1002/marc.202000290.

[55] Gengyao Wei et al. “Thermal-responsive PNIPAm-acrylic/Ag NRs hybrid hydrogel with atmospheric window full-wavelength thermal management for smart windows”. In: *Solar Energy Materials and Solar Cells* 206 (2020), p. 110336. ISSN: 09270248. DOI: 10.1016/j.solmat.2019.110336.

[56] Yang Liu et al. “Flexible Normally Transparent Smart Window Modulating Near–Infrared Penetration under Ambient Conditions”. In: *Advanced Materials Interfaces* 9.19 (2022). ISSN: 2196-7350. DOI: 10.1002/admi.202200338.

[57] Shancheng Wang et al. “Scalable thermochromic smart windows with passive radiative cooling regulation”. In: *Science (New York, N.Y.)* 374.6574 (2021), pp. 1501–1504. DOI: 10.1126/science.abg0291.

[58] Shancheng Wang et al. “Thermochromic smart windows with highly regulated radiative cooling and solar transmission”. In: *Nano Energy* 89 (2021), p. 106440. ISSN: 22112855. DOI: 10.1016/j.nanoen.2021.106440.

[59] Jianing Li et al. “Dynamic Refractive Index-Matching for Adaptive Thermoresponsive Smart Windows”. In: *Small* 18.28 (2022), e2201322. DOI: 10.1002/smll.202201322.

[60] Sai Liu et al. “Organic Hybrid Perovskite (MAPbI 3−x Cl x) for Thermochromic Smart Window with Strong Optical Regulation Ability, Low Transition Temperature, and Narrow Hysteresis Width”. In: *Advanced Functional Materials* 31.26 (2021). ISSN: 1616-301X. DOI: 10.1002/adfm.202010426.

[61] Dongxu Ma et al. “Solar Light Management Enabled by Dual-Responsive Smart Window”. In: *ACS applied materials & interfaces* 14.50 (2022), pp. 56065–56073. DOI: 10.1021/acsami.2c15767.

[62] Yilin Ding et al. "Different ion-based electrolytes for electrochromic devices: A review". In: *Solar Energy Materials and Solar Cells* 248 (2022), p. 112037. ISSN: 09270248. DOI: 10.1016/j.solmat.2022.112037.

[63] Qingke Wang et al. "Robust and stable dual-band electrochromic smart window with multicolor tunability". In: *Materials horizons* 10.3 (2023), pp. 960–966. DOI: 10.1039/d2mh01365g.

[64] Pengyang Lei et al. "An Electrochromic Nickel Phosphate Film for Large-Area Smart Window with Ultra-Large Optical Modulation". In: *Nano-micro letters* 15.1 (2023), p. 34. DOI: 10.1007/s40820-022-01002-4.

[65] Shengliang Zhang et al. "Amorphous and Porous Tungsten Oxide Films for Fast–Switching Dual–Band Electrochromic Smart Windows". In: *Advanced Optical Materials* 11.1 (2023). ISSN: 2195-1071. DOI: 10.1002/adom.202202115.

[66] Giang Thi Phan et al. "Fast-switching electrochromic smart windows based on NiO-nanorods counter electrode". In: *Solar Energy Materials and Solar Cells* 231 (2021), p. 111306. ISSN: 09270248. DOI: 10.1016/j.solmat.2021.111306.

[67] Lirong Yu et al. "Highly Transparent Conjugated Polymer as the Counter Electrode in Electrochromic Smart Windows". In: *Advanced Optical Materials* 10.23 (2022). ISSN: 2195-1071. DOI: 10.1002/adom.202201423.

[68] He Zhang et al. "A stable, self-regulating, flexible, ITO-free electrochromic smart window for energy-efficient buildings". In: *Cell Reports Physical Science* 3.12 (2022), p. 101193. ISSN: 26663864. DOI: 10.1016/j.xcrp.2022.101193.

[69] Hyunmin Cho et al. "Selective Photo-thermal Conversion of Tungsten Oxide Sol Precursor for Electrochromic Smart Window Applications". In: *Acta Materialia* 201 (2020), pp. 528–534. ISSN: 13596454. DOI: 10.1016/j.actamat.2020.10.040.

[70] Jingwei Chen et al. "Scalable Inkjet Printing of Electrochromic Smart Windows for Building Energy Modulation". In: *Advanced Energy and Sustainability Research* 3.5 (2022). ISSN: 2699-9412. DOI: 10.1002/aesr.202100172.

[71] Qi Zhao et al. "Printing of WO3/ITO nanocomposite electrochromic smart windows". In: *Solar Energy Materials and Solar Cells* 194 (2019), pp. 95–102. ISSN: 09270248. DOI: 10.1016/j.solmat.2019.02.002.

[72] Tingke Rao et al. "Fluoride-Assisted Preparation of Plasmonic Oxygen-Deficient MoO 3−x Nanowires for Dual-Band Electrochromic Smart Windows". In: *Journal of The Electrochemical Society* 169.6 (2022), p. 066506. ISSN: 0013-4651. DOI: 10.1149/1945-7111/ac741e.

[73] Shengliang Zhang et al. "Plasmonic Oxygen-Deficient TiO2-x Nanocrystals for Dual-Band Electrochromic Smart Windows with Efficient Energy Recycling". In: *Advanced materials* 32.43 (2020), e2004686. DOI: 10.1002/adma.202004686.

[74] C. M. Lampert. "Large-Area Smart Glass And Integrated Photovoltaics". In: *Photovoltaic and Photoactive Materials — Properties, Technology and Applications*. Ed. by J. M. Marshall and D. Dimova-Malinovska. Dordrecht: Springer Netherlands, 2002, pp. 1–10. ISBN: 978-1-4020-0824-5. DOI: 10.1007/978-94-010-0632-3{\textunderscore}1.

[75] D. J. Gardiner, S. M. Morris, and H. J. Coles. "High-efficiency multistable switchable glazing using smectic A liquid crystals". In: *Solar Energy Materials and Solar Cells* 93.3 (2009), pp. 301–306. ISSN: 09270248. DOI: 10.1016/j.solmat.2008.10.023.

[76] Daniela Cupelli et al. "Self-adjusting smart windows based on polymer-dispersed liquid crystals". In: *Solar Energy Materials and Solar Cells* 93.11 (2009), pp. 2008–2012. ISSN: 09270248. DOI: 10.1016/j.solmat.2009.08.002.

[77] Sucheol Park and Jin Who Hong. "Polymer dispersed liquid crystal film for variable-transparency glazing". In: *Thin Solid Films* 517.10 (2009), pp. 3183–3186. ISSN: 00406090. DOI: 10.1016/j.tsf.2008.11.115.

[78] Yura Kim et al. "Optical properties and optimized conditions for polymer dispersed liquid crystal containing UV curable polymer and nematic liquid crystal". In: *Current Applied Physics* 15.3 (2015), pp. 292–297. ISSN: 15671739. DOI: 10.1016/j.cap.2014.12.027.

[79] Hyun-Keun Kwon et al. "Optically Switchable Smart Windows with Integrated Photovoltaic Devices". In: *Advanced Energy Materials* 5.3 (2015), p. 1401347. ISSN: 16146832. DOI: 10.1002/aenm.201401347.

[80] Hitesh Khandelwal et al. "Electrically switchable polymer stabilised broadband infrared reflectors and their potential as smart windows for energy saving in buildings". In: *Scientific reports* 5 (2015), p. 11773. ISSN: 2045-2322. DOI: 10.1038/srep11773.

[81] Jiaqi Wang et al. "Normally Transparent Tribo-Induced Smart Window". In: *ACS nano* 14.3 (2020), pp. 3630–3639. DOI: 10.1021/acsnano.0c00107.

[82] Won–Jin Yoon et al. "A Single–Step Dual Stabilization of Smart Window by the Formation of Liquid Crystal Physical Gels and the Construction of Liquid Crystal Chambers". In: *Advanced Functional Materials* 30.4 (2020). ISSN: 1616-301X. DOI: 10.1002/adfm.201906780.

[83] Huanxin Liu et al. "Triboelectric-optical responsive cholesteric liquid crystals for self-powered smart window, E-paper display and optical switch". In: *Science bulletin* 66.19 (2021), pp. 1986–1993. DOI: 10.1016/j.scib.2021.05.016.

[84] Weihao Meng et al. "Photothermal Dual Passively Driven Liquid Crystal Smart Window". In: *ACS applied materials & interfaces* 14.24 (2022), pp. 28301–28309. DOI: 10.1021/acsami.2c07462.

[85] Ke Wang et al. "A facile fabrication strategy for anisotropic photonic crystals using deformable spherical nanoparticles". In: *Nanoscale* 11.30 (2019), pp. 14147–14154. DOI: 10.1039/c9nr04735b.

[86] Hye-Na Kim et al. "Multistate and On-Demand Smart Windows". In: *Advanced materials* 30.43 (2018), e1803847. DOI: 10.1002/adma.201803847.

[87] Dengteng Ge et al. “A robust smart window: reversibly switching from high transparency to angle-independent structural color display”. In: *Advanced Materials* 27.15 (2015), pp. 2489–2495. ISSN: 0935-9648. DOI: 10.1002/adma.201500281.

[88] Ying-Jun Quan et al. “Stretchable Biaxial and Shear Strain Sensors Using Diffractive Structural Colors”. In: *ACS nano* 14.5 (2020), pp. 5392–5399. DOI: 10.1021/acsnano.9b08953.

[89] Pengfei Zhao et al. “Stretchable photonic crystals with periodic cylinder shaped air holes for improving mechanochromic performance”. In: *Smart Materials and Structures* 28.7 (2019), p. 075037. ISSN: 0964-1726. DOI: 10.1088/1361-665X/ab1fb8.

[90] Donghwi Cho et al. “High-Contrast Optical Modulation from Strain-Induced Nanogaps at 3D Heterogeneous Interfaces”. In: *Advanced science* 7.11 (2020), p. 1903708. ISSN: 2198-3844. DOI: 10.1002/advs.201903708.

[91] Baolai Jiang et al. “A General and Robust Strategy for Fabricating Mechanoresponsive Surface Wrinkles with Dynamic Switchable Transmittance”. In: *Advanced Optical Materials* 6.13 (2018). ISSN: 2195-1071. DOI: 10.1002/adom.201800195.

[92] Juhee Son et al. “A Mechanoresponsive Smart Window Based on Multifunctional Luminescent Solar Concentrator”. In: *Solar RRL* 7.17 (2023). ISSN: 2367-198X. DOI: 10.1002/solr.202300445.

[93] Songshan Zeng et al. “Bio-inspired sensitive and reversible mechanochromisms via strain-dependent cracks and folds”. In: *Nature communications* 7 (2016), p. 11802. DOI: 10.1038/ncomms11802.

[94] Zemin Mao et al. “Dynamic Mechanochromic Optics with Tunable Strain Sensitivity for Strain–Responsive Digit Display”. In: *Advanced Optical Materials* 8.24 (2020). ISSN: 2195-1071. DOI: 10.1002/adom.202001472.

[95] Pan Wu et al. “Mechanochromic and thermochromic shape memory photonic crystal films based on core/shell nanoparticles for smart monitoring”. In: *Nanoscale* 11.42 (2019), pp. 20015–20023. DOI: 10.1039/c9nr05361a.

[96] Jiaqi Wang et al. “A fully self-powered, ultra-stable cholesteric smart window triggered by instantaneous mechanical stimuli”. In: *Nano Energy* 85 (2021), p. 105976. ISSN: 22112855. DOI: 10.1016/j.nanoen.2021.105976.

[97] Donghwi Cho et al. “Mechanoresponsive scatterers for high-contrast optical modulation”. In: *Nanophotonics* 11.11 (2022), pp. 2737–2762. DOI: 10.1515/nanoph-2021-0642.

[98] Bo Chen et al. “Review on Mechanoresponsive Smart Windows: Structures and Driving Modes”. In: *Materials (Basel, Switzerland)* 16.2 (2023). ISSN: 1996-1944. DOI: 10.3390/ma16020779.

[99] James Goebl et al. “Magnetically tunable colloidal micromirrors”. In: *Nanoscale horizons* 1.1 (2016), pp. 64–68. DOI: 10.1039/c5nh00035a.

[100] Zining Yang, Jun Kyu Park, and Seok Kim. “Magnetically Responsive Elastomer-Silicon Hybrid Surfaces for Fluid and Light Manipulation”. In: *Small* 14.2 (2018). DOI: 10.1002/smll.201702839.

[101] Jianing Li et al. “Transmittance Tunable Smart Window Based on Magnetically Responsive 1D Nanochains”. In: *ACS applied materials & interfaces* 12.28 (2020), pp. 31637–31644. DOI: 10.1021/acsami.0c08402.

[102] Fudong Li et al. “Near-infrared light-responsive dynamic wrinkle patterns”. In: *Science Advances* 4.4 (2018), eaar5762. ISSN: 2375-2548. DOI: 10.1126/sciadv.aar5762.

[103] Minghao Wang et al. “Organic–inorganic semi-interpenetrating networks with orthogonal light- and magnetic-responsiveness for smart photonic gels”. In: *Nature communications* 14.1 (2023), p. 1000. DOI: 10.1038/s41467-023-36706-7.

[104] Bin Ai et al. “Advanced Colloidal Lithography Beyond Surface Patterning”. In: *Advanced Materials Interfaces* 4.1 (2017), p. 1600271. ISSN: 21967350. DOI: 10.1002/admi.201600271.

[105] Bihter Daglar et al. “Soft biomimetic tapered nanostructures for large-area antireflective surfaces and SERS sensing”. In: *Journal of Materials Chemistry C* 1.47 (2013), p. 7842. ISSN: 2050-7526. DOI: 10.1039/c3tc31616e.

[106] Hyeong Min Jin et al. “Ultralarge Area Sub-10 nm Plasmonic Nanogap Array by Block Copolymer Self-Assembly for Reliable High-Sensitivity SERS”. In: *ACS applied materials & interfaces* 10.51 (2018), pp. 44660–44667. DOI: 10.1021/acsami.8b17325.

[107] Tao Li et al. “Wafer-Scale Nanopillars Derived from Block Copolymer Lithography for Surface-Enhanced Raman Spectroscopy”. In: *ACS applied materials & interfaces* 8.24 (2016), pp. 15668–15675. DOI: 10.1021/acsami.6b05431.

[108] Jae Hee Shin et al. “Fabrication of 50 nm scale Pt nanostructures by block copolymer (BCP) and its characteristics of surface-enhanced Raman scattering (SERS)”. In: *RSC Advances* 6.75 (2016), pp. 70756–70762. DOI: 10.1039/C6RA08608J.

[109] F. de Angelis et al. “Breaking the diffusion limit with super-hydrophobic delivery of molecules to plasmonic nanofocusing SERS structures”. In: *Nature Photonics* 5.11 (2011), pp. 682–687. ISSN: 1749-4885. DOI: 10.1038/nphoton.2011.222.

[110] Jing Liu et al. “Ag-NP@Ge-nanotaper/Si-micropillar ordered arrays as ultrasensitive and uniform surface enhanced Raman scattering substrates”. In: *Nanoscale* 7.43 (2015), pp. 18218–18224. DOI: 10.1039/c5nr06001j.

[111] Jian-An Huang et al. “Ordered Ag/Si nanowires array: wide-range surface-enhanced Raman spectroscopy for reproducible biomolecule detection”. In: *Nano letters* 13.11 (2013), pp. 5039–5045. DOI: 10.1021/nl401920u.

[112] Xuan He et al. “Ultrasensitive detection of explosives via hydrophobic condensation effect on biomimetic SERS platforms”. In: *Journal of Materials Chemistry C* 5.47 (2017), pp. 12384–12392. ISSN: 2050-7526. DOI: 10.1039/C7TC04325B.

[113] Daren Xu et al. “Droplet-Confined Electroless Deposition of Silver Nanoparticles on Ordered Superhydrophobic Structures for High Uniform SERS Measurements”. In: *ACS applied materials & interfaces* 9.25 (2017), pp. 21548–21553. DOI: 10.1021/acsami.7b04240.

[114] Katherine N. Kanipe et al. "Large Format Surface-Enhanced Raman Spectroscopy Substrate Optimized for Enhancement and Uniformity". In: *ACS nano* 10.8 (2016), pp. 7566–7571. DOI: 10.1021/acsnano.6b02564.

[115] Hui He et al. "Electrophoretic fabrication of silver nanostructure/zinc oxide nanorod heterogeneous arrays with excellent SERS performance". In: *Journal of Materials Chemistry C* 3.8 (2015), pp. 1724–1731. ISSN: 2050-7526. DOI: 10.1039/C4TC02677B.

[116] Shilian Dong et al. "Springtail-Inspired Superamphiphobic Ordered Nanohoodoo Arrays with Quasi-Doubly Reentrant Structures". In: *Small* 16.19 (2020), e2000779. DOI: 10.1002/smll.202000779.

[117] Chuanwei Cheng et al. "Fabrication and SERS performance of silver-nanoparticle-decorated Si/ZnO nanotrees in ordered arrays". In: *ACS applied materials & interfaces* 2.7 (2010), pp. 1824–1828. DOI: 10.1021/am100270b.

[118] Moon-Keun Lee et al. "Novel 3D arrays of gold nanostructures on suspended platinum-coated carbon nanotubes as surface-enhanced Raman scattering substrates". In: *Materials Letters* 81 (2012), pp. 9–12. ISSN: 0167577X. DOI: 10.1016/j.matlet.2012.04.124.

[119] Yingqi Zhao et al. "Plasmonic nanopillar array embedded microfluidic chips: an in situ SERS monitoring platform". In: *Journal of Materials Chemistry A* 3.12 (2015), pp. 6408–6413. ISSN: 2050-7488. DOI: 10.1039/C4TA07076C.

[120] Yingqi Zhao et al. "Quantitative analysis of multiplex-components and double stranded DNA by wide-range surface-enhanced Raman spectroscopy based on ordered Ag/Si nanowire arrays". In: *Journal of Materials Chemistry A* 2.26 (2014), p. 10218. ISSN: 2050-7488. DOI: 10.1039/c4ta00904e.

[121] Dongdong Lin et al. "Large-Area Au-Nanoparticle-Functionalized Si Nanorod Arrays for Spatially Uniform Surface-Enhanced Raman Spectroscopy". In: *ACS nano* 11.2 (2017), pp. 1478–1487. DOI: 10.1021/acsnano.6b06778.

[122] Yang Liu et al. "Vertically aligned nanostructures for a reliable and ultrasensitive SERS-active platform: Fabrication and engineering strategies". In: *Nano Today* 37 (2021), p. 101063. ISSN: 17480132. DOI: 10.1016/j.nantod.2020.101063.

[123] Xuan He et al. "Ultrasensitive detection of explosives via hydrophobic condensation effect on biomimetic SERS platforms". In: *Journal of Materials Chemistry C* 5.47 (2017), pp. 12384–12392. ISSN: 2050-7526. DOI: 10.1039/C7TC04325B.

[124] Zhongbo Li et al. "Controllable fabrication of Ag-nanoplate-decorated PAN-nanopillar arrays and their application in surface-enhanced Raman scattering". In: *RSC Advances* 7.84 (2017), pp. 53157–53163. DOI: 10.1039/C7RA11102A.

[125] Daren Xu et al. "Droplet-Confined Electroless Deposition of Silver Nanoparticles on Ordered Superhydrophobic Structures for High Uniform SERS Measurements". In: *ACS applied materials & interfaces* 9.25 (2017), pp. 21548–21553. DOI: 10.1021/acsami.7b04240.

[126] Hui He et al. “Electrophoretic fabrication of silver nanostructure/zinc oxide nanorod heterogeneous arrays with excellent SERS performance”. In: *Journal of Materials Chemistry C* 3.8 (2015), pp. 1724–1731. ISSN: 2050-7526. DOI: 10.1039/C4TC02677B.

[127] Stephen J. Bauman et al. “Tunable SERS Enhancement via Sub-nanometer Gap Metasurfaces”. In: *ACS applied materials & interfaces* 14.13 (2022), pp. 15541–15548. DOI: 10.1021/acsami.2c01335.

[128] Amanda J. Haes and Richard P. van Duyne. “A unified view of propagating and localized surface plasmon resonance biosensors”. In: *Analytical and bioanalytical chemistry* 379.7-8 (2004), pp. 920–930. DOI: 10.1007/s00216-004-2708-9.

[129] Alberto Comin and Liberato Manna. “New materials for tunable plasmonic colloidal nanocrystals”. In: *Chemical Society reviews* 43.11 (2014), pp. 3957–3975. DOI: 10.1039/c3cs60265f.

[130] Maowen Song et al. “Colors with plasmonic nanostructures: A full-spectrum review”. In: *Applied Physics Reviews* 6.4 (2019). DOI: 10.1063/1.5110051.

[131] Yannic Brasse et al. “Mechanotunable Plasmonic Properties of Colloidal Assemblies”. In: *Advanced Materials Interfaces* 7.5 (2020). ISSN: 2196-7350. DOI: 10.1002/admi.201901678.

[132] Lin Cui, Jingang Wang, and Mengtao Sun. “Graphene plasmon for optoelectronics”. In: *Reviews in Physics* 6 (2021), p. 100054. ISSN: 24054283. DOI: 10.1016/j.revip.2021.100054.

[133] Kristen D. Alexander et al. “Tunable SERS in gold nanorod dimers through strain control on an elastomeric substrate”. In: *Nano letters* 10.11 (2010), pp. 4488–4493. DOI: 10.1021/nl1023172.

[134] Haipeng Li et al. “SERS Hotspot Engineering by Aerosol Self-Assembly of Plasmonic Ag Nanoaggregates with Tunable Interparticle Distance”. In: *Advanced science* 9.22 (2022), e2201133. ISSN: 2198-3844. DOI: 10.1002/advs.202201133.

[135] Bhavya Sharma et al. “High-performance SERS substrates: Advances and challenges”. In: *MRS Bulletin* 38.8 (2013), pp. 615–624. ISSN: 0883-7694. DOI: 10.1557/mrs.2013.161.

[136] Bhavya Sharma et al. “SERS: Materials, applications, and the future”. In: *Materials Today* 15.1-2 (2012), pp. 16–25. ISSN: 13697021. DOI: 10.1016/S1369-7021(12)70017-2.

[137] N. C. Raut and K. Al-Shamery. “Inkjet printing metals on flexible materials for plastic and paper electronics”. In: *Journal of Materials Chemistry C* 6.7 (2018), pp. 1618–1641. ISSN: 2050-7526. DOI: 10.1039/C7TC04804A.

[138] Jia Li, Fabrice Rossignol, and Joanne Macdonald. “Inkjet printing for biosensor fabrication: combining chemistry and technology for advanced manufacturing”. In: *Lab on a chip* 15.12 (2015), pp. 2538–2558. DOI: 10.1039/c5lc00235d.

[139] Ali Sajedi-Moghaddam, Elham Rahmanian, and Naimeh Naseri. "Inkjet-Printing Technology for Supercapacitor Application: Current State and Perspectives". In: *ACS applied materials & interfaces* 12.31 (2020), pp. 34487–34504. DOI: 10.1021/acsami.0c07689.

[140] Seungjun Chung, Kyungjune Cho, and Takhee Lee. "Recent Progress in Inkjet-Printed Thin-Film Transistors". In: *Advanced science* 6.6 (2019), p. 1801445. ISSN: 2198-3844. DOI: 10.1002/advs.201801445.

[141] Ke Yan et al. "Inkjet printing for flexible and wearable electronics". In: *APL Materials* 8.12 (2020), p. 120705. DOI: 10.1063/5.0031669.

[142] Brian Derby. "Additive Manufacture of Ceramics Components by Inkjet Printing". In: *Engineering* 1.1 (2015), pp. 113–123. ISSN: 20958099. DOI: 10.15302/J-ENG-2015014.

[143] Lei Wu et al. "Emerging Progress of Inkjet Technology in Printing Optical Materials". In: *Advanced Optical Materials* 4.12 (2016), pp. 1915–1932. ISSN: 2195-1071. DOI: 10.1002/adom.201600466.

[144] Gerard Cummins and Marc P.Y. Desmulliez. "Inkjet printing of conductive materials: a review". In: *Circuit World* 38.4 (2012), pp. 193–213. ISSN: 0305-6120. DOI: 10.1108/03056121211280413.

[145] Joseph T. Delaney, Patrick J. Smith, and Ulrich S. Schubert. "Inkjet printing of proteins". In: *Soft Matter* 5.24 (2009), p. 4866. ISSN: 1744-683X. DOI: 10.1039/b909878j.

[146] Hesam Maleki and Volfango Bertola. "Recent advances and prospects of inkjet printing in heterogeneous catalysis". In: *Catalysis Science & Technology* 10.10 (2020), pp. 3140–3159. ISSN: 2044-4753. DOI: 10.1039/d0cy00040j.

[147] B.-J. de Gans, P. C. Duineveld, and U. S. Schubert. "Inkjet Printing of Polymers: State of the Art and Future Developments". In: *Advanced Materials* 16.3 (2004), pp. 203–213. ISSN: 0935-9648. DOI: 10.1002/adma.200300385.

[148] Peihua Yang and Hong Jin Fan. "Inkjet and Extrusion Printing for Electrochemical Energy Storage: A Minireview". In: *Advanced Materials Technologies* 5.10 (2020), p. 2000217. ISSN: 2365-709X. DOI: 10.1002/admt.202000217.

[149] Xiaojin Peng et al. "Perovskite and Organic Solar Cells Fabricated by Inkjet Printing: Progress and Prospects". In: *Advanced Functional Materials* 27.41 (2017), p. 1703704. ISSN: 1616-301X. DOI: 10.1002/adfm.201703704.

[150] Ronan Daly et al. "Inkjet printing for pharmaceutics - A review of research and manufacturing". In: *International journal of pharmaceutics* 494.2 (2015), pp. 554–567. DOI: 10.1016/j.ijpharm.2015.03.017.

[151] Xiaonao Liu et al. "Recent advances in inkjet printing synthesis of functional metal oxides". In: *Particuology* 19 (2015), pp. 1–13. ISSN: 16742001. DOI: 10.1016/j.partic.2014.05.001.

[152] Saeideh Kholghi Eshkalak et al. "A review on inkjet printing of CNT composites for smart applications". In: *Applied Materials Today* 9 (2017), pp. 372–386. ISSN: 23529407. DOI: 10.1016/j.apmt.2017.09.003.

[153] Qiaoshuang Zhang et al. “Fabrication of Bragg Mirrors by Multilayer Inkjet Printing”. In: *Advanced Materials* 34.33 (2022), e2201348. ISSN: 0935-9648. DOI: 10.1002/adma.202201348.

[154] Qiaoshuang Zhang et al. “Fabrication of Microlens Arrays with High Quality and High Fill Factor by Inkjet Printing”. In: *Advanced Optical Materials* 10.14 (2022), p. 2200677. ISSN: 2195-1071. DOI: 10.1002/adom.202200677.

[155] Lifu Shi et al. “In Situ Inkjet Printing Strategy for Fabricating Perovskite Quantum Dot Patterns”. In: *Advanced Functional Materials* 29.37 (2019), p. 1903648. ISSN: 1616-301X. DOI: 10.1002/adfm.201903648.

[156] Aleksandra Samusjew et al. “Inkjet Printing of Soft, Stretchable Optical Waveguides through the Photopolymerization of High-Profile Linear Patterns”. In: *ACS applied materials & interfaces* 9.5 (2017), pp. 4941–4947. DOI: 10.1021/acsami.6b13272.

[157] Theodore A. Cohen et al. “Direct Patterning of Perovskite Nanocrystals on Nanophotonic Cavities with Electrohydrodynamic Inkjet Printing”. In: *Nano letters* 22.14 (2022), pp. 5681–5688. DOI: 10.1021/acs.nanolett.2c00473.

[158] Xiantao Jiang et al. “Inkjet-printed MXene micro-scale devices for integrated broadband ultrafast photonics”. In: *npj 2D Materials and Applications* 3.1 (2019). DOI: 10.1038/s41699-019-0117-3.

[159] Florian Vogelbacher et al. “Integrated silicon nitride organic hybrid DFB laser with inkjet printed gain medium”. In: *Optics express* 27.20 (2019), pp. 29350–29356. DOI: 10.1364/OE.27.029350.

[160] Yidenekachew J. Donie et al. “Phase-Separated Nanophotonic Structures by Inkjet Printing”. In: *ACS nano* 15.4 (2021), pp. 7305–7317. DOI: 10.1021/acsnano.1c00552.

[161] Frederic S. F. Brossard et al. “Inkjet-Printed Nanocavities on a Photonic Crystal Template”. In: *Advanced Materials* 29.47 (2017). ISSN: 0935-9648. DOI: 10.1002/adma.201704425.

[162] Wenyi Li et al. “Inkjet Printing of Patterned, Multispectral, and Biocompatible Photonic Crystals”. In: *Advanced materials* 31.36 (2019), e1901036. DOI: 10.1002/adma.201901036.

[163] Ling Bai et al. “Bio-inspired vapor-responsive colloidal photonic crystal patterns by inkjet printing”. In: *ACS nano* 8.11 (2014), pp. 11094–11100. DOI: 10.1021/nn504659p.

[164] Jue Hou et al. “Four-Dimensional Screening Anti-Counterfeiting Pattern by Inkjet Printed Photonic Crystals”. In: *Chemistry, an Asian journal* 11.19 (2016), pp. 2680–2685. DOI: 10.1002/asia.201600433.

[165] Brian Derby. “Inkjet Printing of Functional and Structural Materials: Fluid Property Requirements, Feature Stability, and Resolution”. In: *Annual Review of Materials Research* 40.1 (2010), pp. 395–414. ISSN: 1531-7331. DOI: 10.1146/annurev-matsci-070909-104502.

[166] Cristina Rodriguez-Rivero, José Rafael Castrejón-Pita, and Ian M. Hutchings. "Aerodynamic Effects in Industrial Inkjet Printing". In: *Journal of Imaging Science and Technology* 59.4 (2015), pp. 040401-1-040401–10. DOI: 10.2352/J.ImagingSci.Technol.2015.59.4.040401.

[167] Clayton T. Crowe. *A guide for learning engineering fluid mechanics: Practice problems with solutions*. 9th ed / Clayton T. Crowe ... [et al.] Hoboken, N.J.: Wiley and Chichester : John Wiley [distributor], 2009. ISBN: 978-0470-25977-1.

[168] Sina Ebnesajjad. "Surface Tension and Its Measurement". In: *Handbook of Adhesives and Surface Preparation*. Elsevier, 2011, pp. 21–30. ISBN: 9781437744613. DOI: 10.1016/B978-1-4377-4461-3.10003-3.

[169] T. Young. "III. An essay on the cohesion of fluids". In: *Philosophical Transactions of the Royal Society of London* 95 (1805), pp. 65–87. ISSN: 0261-0523. DOI: 10.1098/rstl.1805.0005.

[170] Paul C. Duineveld et al. "Ink-jet printing of polymer light-emitting devices". In: *Organic Light-Emitting Materials and Devices V*. Ed. by Zakya H. Kafafi. SPIE Proceedings. SPIE, 2001, p. 59. DOI: 10.1117/12.457460.

[171] Brian Derby. "Inkjet Printing of Functional and Structural Materials: Fluid Property Requirements, Feature Stability, and Resolution". In: *Annual Review of Materials Research* 40.1 (2010), pp. 395–414. ISSN: 1531-7331. DOI: 10.1146/annurev-matsci-070909-104502.

[172] Yuanyuan Liu and Brian Derby. "Experimental study of the parameters for stable drop-on-demand inkjet performance". In: *Physics of Fluids* 31.3 (2019), p. 032004. ISSN: 1070-6631. DOI: 10.1063/1.5085868.

[173] R. Bhola and S. Chandra. "Parameters controlling solidification of molten wax droplets falling on a solid surface". In: *Journal of Materials Science* 34.19 (1999), pp. 4883–4894. ISSN: 00222461. DOI: 10.1023/A:1004680315199.

[174] Robert D. Deegan et al. "39827 // Capillary flow as the cause of ring stains from dried liquid drops". In: *Nature* 389.6653 (1997), pp. 827–829. ISSN: 0028-0836. DOI: 10.1038/39827.

[175] F. Giorgiutti-Dauphiné and L. Pauchard. "Drying drops : Drying drops containing solutes: From hydrodynamical to mechanical instabilities". In: *The European physical journal. E, Soft matter* 41.3 (2018), p. 32. DOI: 10.1140/epje/i2018-11639-2.

[176] A. Friederich, J. R. Binder, and W. Bauer. "Rheological Control of the Coffee Stain Effect for Inkjet Printing of Ceramics". In: *Journal of the American Ceramic Society* 96.7 (2013), pp. 2093–2099. ISSN: 00027820. DOI: 10.1111/jace.12385.

[177] Anke Teichler, Jolke Perelaer, and Ulrich S. Schubert. "Inkjet printing of organic electronics – comparison of deposition techniques and state-of-the-art developments". In: *Journal of Materials Chemistry C* 1.10 (2013), p. 1910. ISSN: 2050-7526. DOI: 10.1039/c2tc00255h.

[178] Qihao Jin et al. "Inkjet-printed optical interference filters". In: *Nature communications* 15.1 (2024), p. 3372. DOI: 10.1038/s41467-024-47086-x.

[179] R.O.F. Verkuijlen et al. “Surface modification of polycarbonate and polyethylene naphtalate foils by UV-ozone treatment and microPlasma printing”. In: *Applied Surface Science* 290 (2014), pp. 381–387. ISSN: 01694332. DOI: 10.1016/j.apsusc.2013.11.089.

[180] Detlef Lohse. “Fundamental Fluid Dynamics Challenges in Inkjet Printing”. In: *Annual Review of Fluid Mechanics* 54.1 (2022), pp. 349–382. ISSN: 0066-4189. DOI: 10.1146/annurev-fluid-022321-114001.

[181] Brian Derby. “Additive Manufacture of Ceramics Components by Inkjet Printing”. In: *Engineering* 1.1 (2015), pp. 113–123. ISSN: 20958099. DOI: 10.15302/J-ENG-2015014.

[182] Stephen D. Hoath, ed. *Fundamentals of inkjet printing: The science of inkjet and droplets*. Weinheim, Germany: Wiley-VCH Verlag, 2016. ISBN: 978-3-527-33785-9.

[183] Baoxing Zhao et al. “Effect of annealing temperature on the structure and optical properties of sputtered TiO2 films”. In: *Journal of Alloys and Compounds* 509.9 (2011), pp. 4060–4064. ISSN: 09258388. DOI: 10.1016/j.jallcom.2011.01.020.

[184] Supachai Sompech, Thananchai Dasri, and Sukhontip Thaomola. “Preparation and Characterization of Amorphous Silica and Calcium Oxide from Agricultural Wastes”. In: *Oriental Journal of Chemistry* 32.4 (2016), pp. 1923–1928. ISSN: 0970020X. DOI: 10.13005/ojc/320418.

[185] A. H. Mayabadi et al. “Evolution of structural and optical properties of rutile TiO2 thin films synthesized at room temperature by chemical bath deposition method”. In: *Journal of Physics and Chemistry of Solids* 75.2 (2014), pp. 182–187. ISSN: 00223697. DOI: 10.1016/j.jpcs.2013.09.008.

[186] Y. F. You et al. “Structural characterization and optical property of TiO2 powders prepared by the sol–gel method”. In: *Ceramics International* 40.6 (2014), pp. 8659–8666. ISSN: 02728842. DOI: 10.1016/j.ceramint.2014.01.083.

[187] Muhammad H. Asghar et al. “Modeling and preparation of practical optical filters”. In: *Current Applied Physics* 9.5 (2009), pp. 1046–1053. ISSN: 15671739. DOI: 10.1016/j.cap.2008.11.007.

[188] H. A. Macleod. *Thin-film optical filters*. 4th ed. Series in optics and optoelectronics. Boca Raton, Fla.: CRC and London : Taylor & Francis [distributor], 2010. ISBN: 978-1-4200-7302-7.

[189] Honghua U. Yang et al. “Optical dielectric function of silver”. In: *Physical Review B* 91.23 (2015). ISSN: 1098-0121. DOI: 10.1103/PhysRevB.91.235137.

[190] Yuko Tachibana et al. “Optical properties of multilayers composed of silver and dielectric materials”. In: *Thin Solid Films* 442.1-2 (2003), pp. 212–216. ISSN: 00406090. DOI: 10.1016/S0040-6090(03)00984-2.

[191] Mohd Sharizal Alias et al. “High Reflectivity YDH/SiO2 Distributed Bragg Reflector for UV-C Wavelength Regime”. In: *IEEE Photonics Journal* 10.2 (2018), pp. 1–8. DOI: 10.1109/JPHOT.2018.2804355.

[192] Xiang-Yu Guan et al. “Broadband high-reflective distributed Bragg reflectors based on amorphous silicon films for semiconductor laser facet coatings”. In: *Applied optics* 54.5 (2015), pp. 1027–1031. DOI: 10.1364/AO.54.001027.

[193] Nithin Poonkottil et al. “Low Temperature Area Selective Atomic Layer Deposition of Ruthenium Dioxide Thin Films Using Polymers as Inhibition Layers”. In: *Advanced Materials Interfaces* 10.9 (2023). ISSN: 2196-7350. DOI: 10.1002/admi.202201934.

[194] Xiaoxiao Zhao and Michael C. Murphy. “A High-adhesion Binding Strategy for Silica Nanoparticle-based Superhydrophobic Coatings”. In: *Colloids and surfaces. A, Physicochemical and engineering aspects* 625 (2021). ISSN: 0927-7757. DOI: 10.1016/j.colsurfa.2021.126810.

[195] Rui Zhu et al. “Improved adhesion of interconnected TiO2 nanofiber network on conductive substrate and its application in polymer photovoltaic devices”. In: *Applied Physics Letters* 93.1 (2008). ISSN: 0003-6951. DOI: 10.1063/1.2907317.

[196] Zahra Sekhavat Pour et al. “Effects of surface treatment of TiO2 nanoparticles on the adhesion and anticorrosion properties of the epoxy coating on mild steel using electrochemical technique”. In: *Progress in Organic Coatings* 119 (2018), pp. 99–108. ISSN: 03009440. DOI: 10.1016/j.porgcoat.2018.02.019.

[197] Erika Iveth Cedillo-Gonzalez et al. “Improvement of the Adhesion Between TiO2 Nanofilm and Glass Substrate by Roughness Modifications”. In: *Physics Procedia* 40 (2013), pp. 19–29. ISSN: 18753892. DOI: 10.1016/j.phpro.2012.12.003.

[198] Qihao Jin et al. “High Dynamic Range Smart Window Display by Surface Hydrophilization and Inkjet Printing”. In: *Advanced Materials Technologies* 7.5 (2022), p. 2101026. ISSN: 2365-709X. DOI: 10.1002/admt.202101026.

[199] Tatiana Trantidou et al. “Hydrophilic surface modification of PDMS for droplet microfluidics using a simple, quick, and robust method via PVA deposition”. In: *Microsystems & nanoengineering* 3 (2017), p. 16091. DOI: 10.1038/micronano.2016.91.

[200] Ling Yu et al. “Poly(vinyl alcohol) functionalized poly(dimethylsiloxane) solid surface for immunoassay”. In: *Bioconjugate chemistry* 18.2 (2007), pp. 281–284. ISSN: 1043-1802. DOI: 10.1021/bc060108p.

[201] Detlev Belder et al. “Cross-linked poly(vinyl alcohol) as permanent hydrophilic column coating for capillary electrophoresis”. In: *ELECTROPHORESIS* 22.17 (2001), pp. 3813–3818. ISSN: 0173-0835. DOI: 10.1002/1522-2683(200109)22:17{\textless}3813::AID-ELPS3813{\textgreater}3.0.CO;2-D.

[202] Tianxi He et al. “A modified microfluidic chip for fabrication of paclitaxel-loaded poly(l-lactic acid) microspheres”. In: *Microfluidics and Nanofluidics* 10.6 (2011), pp. 1289–1298. ISSN: 1613-4982. DOI: 10.1007/s10404-010-0760-7.

[203] Joong Yull Park et al. “Surface chemistry modification of PDMS elastomers with boiling water improves cellular adhesion”. In: *Sensors and Actuators B: Chemical* 173 (2012), pp. 765–771. ISSN: 09254005. DOI: 10.1016/j.snb.2012.06.096.

[204] Stéphane Béfahy et al. “Thickness and elastic modulus of plasma treated PDMS silica-like surface layer”. In: *Langmuir : the ACS journal of surfaces and colloids* 26.5 (2010), pp. 3372–3375. DOI: 10.1021/la903154y.

[205] Rihan Wu et al. “Gold nanoplasmonic particles in tunable porous silicon 3D scaffolds for ultra-low concentration detection by SERS”. In: *Nanoscale horizons* 6.10 (2021), pp. 781–790. DOI: 10.1039/d1nh00228g.

[206] Rihan Wu et al. “Localized Plasmon Field Effect of Gold Clusters Embedded in Nanoporous Silicon”. In: *Advanced Optical Materials* 9.9 (2021). ISSN: 2195-1071. DOI: 10.1002/adom.202002119.

[207] Hiang Kwee Lee et al. “Designing surface-enhanced Raman scattering (SERS) platforms beyond hotspot engineering: emerging opportunities in analyte manipulations and hybrid materials”. In: *Chemical Society reviews* 48.3 (2019), pp. 731–756. DOI: 10.1039/c7cs00786h.

[208] Cecilia Noguez. “Surface Plasmons on Metal Nanoparticles: The Influence of Shape and Physical Environment”. In: *The Journal of Physical Chemistry C* 111.10 (2007), pp. 3806–3819. ISSN: 1932-7447. DOI: 10.1021/jp066539m.

[209] Wen Bo Zhao et al. “Localized surface plasmon resonance coupling in Au nanoparticles/phosphorus dendrimer multilayer thin films fabricated by layer-by-layer self-assembly method”. In: *Journal of Materials Chemistry* 19.14 (2009), p. 2006. ISSN: 0959-9428. DOI: 10.1039/b814116a.

[210] P. Nordlander et al. “Plasmon Hybridization in Nanoparticle Dimers”. In: *Nano Letters* 4.5 (2004), pp. 899–903. ISSN: 1530-6984. DOI: 10.1021/nl049681c.

[211] Jiwon Lee et al. “pH-tunable plasmonic properties of Ag nanoparticle cores in block copolymer micelle arrays on Ag films”. In: *Journal of Materials Chemistry A* 3.22 (2015), pp. 11730–11735. ISSN: 2050-7488. DOI: 10.1039/C5TA02085A.

[212] Ihor Tokarev and Sergiy Minko. “Tunable plasmonic nanostructures from noble metal nanoparticles and stimuli-responsive polymers”. In: *Soft Matter* 8.22 (2012), p. 5980. ISSN: 1744-683X. DOI: 10.1039/c2sm25069a.

[213] Iryna Tokareva et al. “Nanosensors based on responsive polymer brushes and gold nanoparticle enhanced transmission surface plasmon resonance spectroscopy”. In: *Journal of the American Chemical Society* 126.49 (2004), pp. 15950–15951. ISSN: 1520-5126. DOI: 10.1021/ja044575y.

[214] Nina Jiang, Xiaolu Zhuo, and Jianfang Wang. “Active Plasmonics: Principles, Structures, and Applications”. In: *Chemical reviews* 118.6 (2018), pp. 3054–3099. DOI: 10.1021/acs.chemrev.7b00252.

[215] Yuanhai Lin et al. “A cross-stacked plasmonic nanowire network for high-contrast femtosecond optical switching”. In: *Nanoscale* 8.3 (2016), pp. 1421–1429. DOI: 10.1039/c5nr06464c.

[216] Teresa E. Williams et al. "NIR-Selective electrochromic heteromaterial frameworks: a platform to understand mesoscale transport phenomena in solid-state electrochemical devices". In: *Journal of Materials Chemistry C* 2.17 (2014), p. 3328. ISSN: 2050-7526. DOI: 10.1039/c3tc32247e.

[217] Guillermo Garcia et al. "Near–Infrared Spectrally Selective Plasmonic Electrochromic Thin Films". In: *Advanced Optical Materials* 1.3 (2013), pp. 215–220. ISSN: 2195-1071. DOI: 10.1002/adom.201200051.

[218] Anna Llordés et al. "Tunable near-infrared and visible-light transmittance in nanocrystal-in-glass composites". In: *Nature* 500.7462 (2013), pp. 323–326. ISSN: 0028-0836. DOI: 10.1038/nature12398.

[219] Guillermo Garcia et al. "Dynamically modulating the surface plasmon resonance of doped semiconductor nanocrystals". In: *Nano letters* 11.10 (2011), pp. 4415–4420. DOI: 10.1021/nl202597n.

[220] Amane Shiohara, Yusong Wang, and Luis M. Liz-Marzán. "Recent approaches toward creation of hot spots for SERS detection". In: *Journal of Photochemistry and Photobiology C: Photochemistry Reviews* 21 (2014), pp. 2–25. ISSN: 13895567. DOI: 10.1016/j.jphotochemrev.2014.09.001.

[221] F. Pahang et al. "Fluorescence properties of methylene blue molecules coupled with metal oxide nanoparticles". In: *OSA Continuum* 3.3 (2020), p. 688. DOI: 10.1364/OSAC.387557.

[222] Agnieszka Kaminska et al. "Chemically bound gold nanoparticle arrays on silicon: assembly, properties and SERS study of protein interactions". In: *Physical chemistry chemical physics : PCCP* 10.28 (2008), pp. 4172–4180. ISSN: 1463-9076. DOI: 10.1039/b803007c.

[223] Kyu–Dong Shim and Eue–Soon Jang. "SERS Signal Enhancement of Methylene Blue–embedded Agglomerated Gold Nanorod@SiO 2 Core@Shell Composites". In: *Bulletin of the Korean Chemical Society* 39.8 (2018), pp. 936–940. ISSN: 1229-5949. DOI: 10.1002/bkcs.11528.

[224] Sannak Dutta Roy et al. "Charge transfer mechanism and the adsorptive stance of methylene blue on gold nanocolloids: a vis–à–vis aftermath". In: *Journal of Raman Spectroscopy* 48.1 (2017), pp. 38–45. ISSN: 0377-0486. DOI: 10.1002/jrs.4981.

[225] Chunying Li et al. "Analysis of trace methylene blue in fish muscles using ultrasensitive surface-enhanced Raman spectroscopy". In: *Food Control* 65 (2016), pp. 99–105. ISSN: 09567135. DOI: 10.1016/j.foodcont.2016.01.017.

[226] Chunying Li et al. "Analysis of trace methylene blue in fish muscles using ultrasensitive surface-enhanced Raman spectroscopy". In: *Food Control* 65 (2016), pp. 99–105. ISSN: 09567135. DOI: 10.1016/j.foodcont.2016.01.017.

[227] Chavis Srichan et al. "Highly-Sensitive Surface-Enhanced Raman Spectroscopy (SERS)-based Chemical Sensor using 3D Graphene Foam Decorated with Silver Nanoparticles as SERS substrate". In: *Scientific reports* 6 (2016), p. 23733. ISSN: 2045-2322. DOI: 10.1038/srep23733.

[228] Roberta R. Naujok, Robert V. Duevel, and Robert M. Corn. "Fluorescence and Fourier Transform surface-enhanced Raman scattering measurements of methylene blue adsorbed onto a sulfur-modified gold electrode". In: *Langmuir : the ACS journal of surfaces and colloids* 9.7 (1993), pp. 1771–1774. DOI: 10.1021/la00031a026.

[229] Wai Hin Lee et al. "A Raman spectro-microscopic investigation of ETFE-based radiation-grafted anion-exchange membranes". In: *RSC Adv* 7.75 (2017), pp. 47726–47737. DOI: 10.1039/C7RA09650J.

[230] Lucio Litti and Moreno Meneghetti. "Predictions on the SERS enhancement factor of gold nanosphere aggregate samples". In: *Physical chemistry chemical physics : PCCP* 21.28 (2019), pp. 15515–15522. ISSN: 1463-9076. DOI: 10.1039/c9cp02015b.

[231] Anne Habermehl et al. "Lab-on-Chip, Surface-Enhanced Raman Analysis by Aerosol Jet Printing and Roll-to-Roll Hot Embossing". In: *Sensors (Basel, Switzerland)* 17.10 (2017). DOI: 10.3390/s17102401.

[232] Alexander Wei et al. "Tunable Surface-Enhanced Raman Scattering from Large Gold Nanoparticle Arrays". In: *ChemPhysChem* 2.12 (2001), p. 743. ISSN: 14394235. DOI: 10.1002/1439-7641(20011217)2:12<743::AID-CPHC743>3.0.CO;2-1.

[233] Xin Liu et al. "Tailored surface-enhanced Raman nanopillar arrays fabricated by laser-assisted replication for biomolecular detection using organic semiconductor lasers". In: *ACS nano* 9.1 (2015), pp. 260–270. DOI: 10.1021/nn506589a.

[234] Calin Hrelescu et al. "Single gold nanostars enhance Raman scattering". In: *Applied Physics Letters* 94.15 (2009). ISSN: 0003-6951. DOI: 10.1063/1.3119642.

[235] Peng Mao et al. "Broadband single molecule SERS detection designed by warped optical spaces". In: *Nature communications* 9.1 (2018), p. 5428. DOI: 10.1038/s41467-018-07869-5.

[236] Yi-Yang Xie et al. "Metasurface-integrated vertical cavity surface-emitting lasers for programmable directional lasing emissions". In: *Nature nanotechnology* 15.2 (2020), pp. 125–130. DOI: 10.1038/s41565-019-0611-y.

[237] Yaniv Oiknine, Isaac August, and Adrian Stern. "Multi-aperture snapshot compressive hyperspectral camera". In: *Optics letters* 43.20 (2018), pp. 5042–5045. DOI: 10.1364/OL.43.005042.

[238] Yaniv Oiknine, Isaac August, and Adrian Stern. "Multi-aperture snapshot compressive hyperspectral camera". In: *Optics letters* 43.20 (2018), pp. 5042–5045. DOI: 10.1364/OL.43.005042.

[239] Bjørn Petter Jelle, Simen Edsjø Kalnæs, and Tao Gao. "Low-emissivity materials for building applications: A state-of-the-art review and future research perspectives". In: *Energy and Buildings* 96 (2015), pp. 329–356. ISSN: 03787788. DOI: 10.1016/j.enbuild.2015.03.024.

[240] Weiyin Su et al. "Polysaccharides-based ultra-thin membrane with high haze, conductivity, and recyclability". In: *Chemical Engineering Journal* 472 (2023), p. 144933. ISSN: 13858947. DOI: 10.1016/j.cej.2023.144933.

[241] S. H. Lee, K. M. Jang, and S. Y. Yang. "Study of Thin Films Containing Polyelectrolyte and Block Copolymer for Nano-Filtration Using in Microfluidics". In: *Procedia Engineering* 44 (2012), pp. 918–920. ISSN: 18777058. DOI: 10.1016/j.proeng.2012.08.621.

[242] Venkat K. Vendra, Lin Wu, and Sitaraman Krishnan. "Polymer Thin Films for Biomedical Applications". In: *Nanotechnologies for the Life Sciences*. Ed. by Challa S. S. R. Kumar. Wiley, 2007. ISBN: 9783527313013. DOI: 10.1002/9783527610419.ntls0179.

[243] Nina Jiang, Xiaolu Zhuo, and Jianfang Wang. "Active Plasmonics: Principles, Structures, and Applications". In: *Chemical reviews* 118.6 (2018), pp. 3054–3099. DOI: 10.1021/acs.chemrev.7b00252.

Acknowledgments

Throughout this journey, I received assistance from many individuals. I would like to express my sincere gratitude to these kind and supportive people.

First and foremost, I would like to express my sincere gratitude to my family. While such acknowledgments often find their place at the end of dissertations, I feel more like to begin by thanking my family. Their consistent support has been a cornerstone in my life. My parents' values and guidance since childhood have shaped my understanding of the significance of pursuing what brings genuine joy. I am sincerely grateful for the nurturing environment they created, allowing me to explore and embrace my passions. I extend my gratitude to my beloved girlfriend, whose unwavering support has been the cornerstone of my journey. With her by my side, every step of this adventure has become a treasure, weaving together the most precious and beautiful moments of my life. This journey will persist for countless compelling reasons, illuminating every facet of life along the way.

Second, I would like to express my gratitude to Prof. Dr. Uli Lemmer for his great support and thoughtful guidance throughout this endeavor. Uli's advice and technical expertise have proven invaluable, playing a substantial role in the success of my work.

Special thanks go to Prof. Dr. Wilhelm Stork for serving as the second referee for my dissertation.

I would also like to thank all my current and former co-workers at the Light Technology Institute, especially Qiaoshuang Zhang, Junchi Chen, Hang Hu, Yang Li, Robert Huber, Guillaume Gomard, Tim Gehring, Santiago Eizaguirre, Jan Dycke, Isabel Allegro, Kai Xia, and Biruk Alemu for our collaborations and enjoyable scientific activities.

Appreciation extends to my friends who once worked at KIT as visitors. A thank you goes to Prof. Yuqing Wang, who returned to Germany in 2023 to share and engage in discussions about her groundbreaking work.

Another big thank you to Qiaoshuang, Andres, and Gerda, who dedicated considerable effort to the application process for our EXIST proposal.

My sincere thanks to Dr. Rainer Kling for collaborating on plasma physics and project management before I started as a doctoral student.

I extend my appreciation to the LTI workshop for their crucial assistance in manufacturing the parts utilized in my experiments.

Lastly, I would like to express my gratitude to all the students that I supervised. I appreciate their trust in me during the preparation of their theses and their support in my research.